A Thesis for the Degree of Ph.D. in Engineering

Dispersion engineering of high-*Q* optical microresonators for frequency comb generation

July 2020

Keio University

Graduate School of Science and Technology
School of Integrated Design Engineering

FUJII, Shun

Keio University

Graduate School of Science and Technology
School of Integrated Design Engineering

Dispersion engineering of high-Q optical microresonators for frequency comb generation

by

Fujii, Shun

A Thesis Submitted
in Partial Fulfillment of
the Requirements for the Degree
Doctor of Philosophy

Approved, Thesis Committee:

Tanabe, Takasumi

Kannari, Fumihiko

Tsuda, Hiroyuki

Watanabe, Shinichi

Nic Chormaic, Sile

Abstract

Since the development of laser technology, light-matter interactions, and relevant applications have been intensively studied. In particular, the optical microresonator is known to be a device that enables the ultimate enhancement of optical density by confining light with a small mode volume, resulting in the appearance of various optical nonlinearities. Recently, a microresonator-based optical frequency comb, which is known as a microcomb, has been attracting a lot of attention.

One requirement for the development of a microcomb is dispersion engineering. Specifically, dispersion plays a vital role as regards the phase-matching condition for optical parametric oscillation. Proper control of microresonator dispersion has the potential to allow the expansion of the microcomb bandwidth and the mode-locking operation.

This thesis describes a study of the dispersion engineering of high-Q optical microresonators, which influences optical frequency comb generation, featuring monolithic whispering gallery mode microresonators. This study demonstrates the expansion of the microcomb bandwidth based on sophisticated dispersion engineering, which became possible by employing high-Q microresonators fabricated with precision machining.

Chapter 1 provides the background and objective of this thesis.

Chapter 2 introduces the fundamental theory of third-order nonlinearity, fabrication, and the pros and cons of different high-Q microresonators from the perspective of microcomb formation.

Chapter 3 explains basic theory, calculation, and measurement with regard to the dispersion of a microresonator for a frequency comb. In particular, it highlights the relationship between a microcomb and higher-order dispersion, and reveals the dispersion geometry design strategy.

Chapter 4 discusses the ultraprecision machining fabrication of dispersion-engineered optical microresonators with a Q exceeding 10^8. Moreover, an octave-wide optical parametric oscillation was demonstrated in a machined magnesium fluoride resonator.

Chapter 5 describes a blue light emission realized via cascade four-wave mixing and third-harmonic generation in dispersion-engineered on-chip silica microresonators. This chapter also reveals that precise dispersion engineering can be used to generate visible light deterministically.

Chapter 6 describes the numerical modeling of the anti-mode crossing-induced

microcomb generation. It is shown that this model is particularly powerful for simulating mode-locked pulse formation in a normal-dispersion regime in a rigorous way.

Chapter 7 summarizes the thesis and describes the future outlook.

Contents

Abstract **5**

1 Introduction and motivation **11**
1.1 Introduction to optical microresonators 11
1.2 Introduction to microresonator frequency comb 12
1.3 Research overview related to the thesis 13
1.4 Thesis outline and objective 17

2 Microresonator based optical frequency comb **21**
2.1 Fundamentals of optical microresonators 21
2.1.1 Basic characteristics of microresonators 21
2.1.2 Theory of optical coupling to microresonator 24
2.1.3 Scheme for coupling to microresoantor 26
2.1.4 Quality factor measurement 30
2.1.5 Fabrication of microresonators used in this work 31
2.2 Optical nonlinearity in microresonators 34
2.2.1 Third-order nonlinearities in microressonators 34
2.2.2 Thermal nonlinearity in optical microresonators 42
2.3 Optical frequency comb 44
2.3.1 Optical frequency comb in mode-locked lasers 44
2.3.2 Application of optical frequency combs 45
2.4 Microresonator frequency comb 46
2.4.1 Nonlinear coupled mode equation 47
2.4.2 Lugiato-Lefever equation 47
2.4.3 Microcomb generation via cascaded four-wave mixing . . . 49
2.4.4 Temporal dissipative Kerr soliton formation 53
2.4.5 Novel microresonator frequency comb 58
2.4.6 Application of microresonator frequency combs 58

3 Dispersion engineering and measurement for microresonator frequency comb **61**
3.1 Microresonator dispersion 61
3.1.1 Theoretical description of dispersion 61
3.1.2 Dispersion in optical microresonators 63
3.1.3 Material dispersion 65

3.1.4 Geometric dispersion 66
3.2 Microresonator dispersion engineering 69
3.2.1 Structure design of microresonators 69
3.2.2 Calculated dispersion of whispering gallery mode microresonators 70
3.2.3 Calculated dispersion of waveguide mode microresonators 75
3.2.4 Review of a strategy of dispersion engineering 75
3.3 Measurement of microresonator dispersion 75
3.3.1 Objective of dispersion measurement 75
3.3.2 Laser wavemeter based method 76
3.3.3 Mode-locked frequency comb based method 78
3.3.4 Calibrated fiber-based interferometer method 79
3.3.5 Electro-optic modulator comb based method 82
3.4 Role of microresonator dispersion in microcombs 83
3.4.1 Anomalous group velocity dispersion and dispersive waves 83
3.4.2 Normal group velocity dispersion 85
3.5 Summary 86

4 All-precision-machining fabrication of dispersion engineered crystalline microresonator for microcomb generation 87
4.1 Introduction and motivation 88
4.2 Investigation of critical depth of cut 88
4.2.1 Miller index and crystal plane 88
4.2.2 Definition of critical depth of cut 89
4.2.3 Orthogonal cutting experiment 89
4.3 Ultra-precision cylindrical turning 93
4.3.1 Procedure of cylindrical turning 93
4.3.2 Surface roughness measurement 97
4.3.3 Fabrication and cleaning of microresonators 99
4.4 Quality factor and dispersion measurement 100
4.4.1 Spherical-shaped WGM microresonator 100
4.4.2 Triangular-shaped WGM microresonator 102
4.5 Dispersion engineering and numerical simulation of octave-wide parametric oscillation 102
4.6 Experimental demonstration in a dispersion engineered crystalline microresonator 104
4.6.1 Characterization of crystalline magnesium fluoride microresonator 104
4.6.2 Observation of octave-wide optical parametric oscillations and clustered combs 107
4.7 Discussion and summary 109
4.7.1 Towards further Q-factor improvement in ultraprecision machining 109

4.7.2 Conversion efficiency and measurable power of parametric oscillation . . . 112
4.7.3 Summary . . . 113

5 Third-harmonic blue light emission via Kerr clustered combs and dispersive waves 115
5.1 Introduction and motivation . . . 115
5.2 Analysis of phase-matching condition for efficient third-harmonic generation . . . 116
5.2.1 Phase-matched transverse mode in visible wavelength . . . 116
5.2.2 Mode analysis in blue light wavelength regime . . . 116
5.3 Dispersion engineering and numerical simulation in a silica microtoroid . . . 118
5.4 Experimental demonstration in a silica toroid microresonator . . . 120
5.4.1 Mode identification using dispersion measurement . . . 120
5.4.2 Observation of blue light emission and broadband visible light emission . . . 121
5.5 Discussion and summary . . . 126

6 Numerical investigation of Kerr frequency comb generation in mode coupled microresonators 127
6.1 Introduction and motivation . . . 127
6.2 Theoretical analysis . . . 132
6.2.1 Supermode resonance by anti-mode crossing effect . . . 132
6.2.2 Phase-matching condition by anti-mode crossing in normal dispersion microresonators . . . 133
6.3 Numerical simulation . . . 136
6.3.1 Nonlinear coupled mode equations with mode coupling effect . . . 136
6.3.2 Numerical simulation on FSR-selectable comb and deterministic dark pulse formation . . . 138
6.3.3 Mode coupling induced oscillating behavior in 1-FSR comb generation . . . 140
6.4 Discussion and summary . . . 142
6.4.1 Discussion . . . 142
6.4.2 Summary . . . 142

7 Summary and outlook 145
7.1 Summary . . . 145
7.2 Outlook . . . 146

Appendix A Gain transition between four-wave mixing and Raman effect in silica microresonators 149
A.1 Theory and analysis of FWM and Raman gain in a silica microresonator . . . 149

A.2 Numerical simulation based on Lugiato-Lefever equation 152
A.3 Experimental observation in silica microtoroid 153
A.4 Summary 154

Appendix B Impact on microcomb formation in a clockwise and counter-clockwise mode coupled microresonator 155
B.1 Numerical simulation based on coupled Lugiato-Lefever equations 155
B.2 Experimental observation of CW-CCW mode coupled Kerr frequency comb 158
B.3 Summary 160

List of publications and presentations 175

Acknowledgment 179

Chapter 1

Introduction and motivation

1.1 Introduction to optical microresonators

A laser named as an acronym for "light amplification by stimulated emission of radiation" is one of the greatest inventions in human history. In 1960, the first laser was demonstrated by Theodore H. Maiman [1] based on the theoretical studies by Charles H. Townes and Arthur L. Schawlow [2]. Compared to the conventional light source, such as a lamp and light bulb, the emitted light from lasers shows spatial and temporal coherent properties, making it possible to provide various applications. In 2020, lasers have become an essential technology for our lives and celebrate its 60th anniversary.

A resonator, sometimes called a cavity, is the main element that composes the laser, based on a cylinder with two highly refractive mirrors to confine light. This type is the most conventional resonator known as a Fabry-Pérot resonator, and it serves as a feedback system that light goes through a gain medium for several times. The light trapped in the resonator travels back and forth between two reflectors, as being amplified through the round trip. This mechanism is known as stimulated emission, which creates coherent new photons as the photons of incident waves. In general, one mirror is partially transparent to let output from the resonator escape. In addition to Fabry-Pérot, a spherical shape is also an attractive candidate for optical resonators. The light travels along the resonator's circumference, whereas it is technically difficult to form such types of resonators with mirrors. Alternatively, dielectric materials offer a fascinating way to confine the light into tiny space by utilizing the difference of refractive indices. In these types of resonators, there is no limit for the direction of laser emission. Moreover, it is possible to reduce the size of the resonator by using droplets, polymers, and glasses to micro-meter scale [3]. This light guiding structure is the original idea of microresonators mainly discussed in this thesis.

Whispering gallery mode (WGM) resonators confine light by total internal reflection where the refractive index of the resonator materials is higher than that of surrounding materials. WGM is originated from the sound waves in the whispering gallery of St Paul's Cathedral in London. In the case of WGM, the

light must be kept on a circular trajectory along the resonator's circumference. The light guided on the resonator is inherently lossy due to material absorption, scattering, radiation, etc. Therefore, utilizing low loss optical materials is straightforward to fabricate high quality (Q) factor WGM microresonators. Another approach for achieving ultrahigh-Q is to reduce the surface roughness. The first demonstration of ultrahigh-Q WGM microresonator was reported in 1989 [4] by melting the tip of silica optical fiber using laser annealing, which forms spherical shape resonator exhibiting small roughness thanks to the surface tension of melted silica. There is a wide variety of material candidates for WGM microresonators including fused silica [4–6], fluoride materials [7], polymer [8], sapphire [9], silicon [10], and lithium niobate [11]. Besides the choice of materials, various kinds of resonator shapes have been proposed [12], such as microtoroids [5], microdisks [13], microrods [14, 15], and microbubbles [16].

In contrast to WGM microresonators, waveguide resonators have a different structure to confine the propagated light. The core region, which is a rectangular shape typically, is surrounded by cladding material, guiding the light as a waveguide mode. The waveguide resonator is no longer necessarily a circular trajectory because of its tight confinement by surrounding structure from all sides [12]. Waveguide resonators are commonly-used platforms since they have a small footprint and can be fabricated by CMOS-compatible processes, which enables the achievement of precise structure control and integration of external waveguides on the same chip. The variety of waveguide resonators include silicon (Si) [17], silicon nitride (Si_3N_4) [18], high-index doped silica (Hydex) [19], aluminium nitride (AlN) [20], aluminium gallium arsenide (AlGaAs) [21], and diamond [22].

The applications of optical microresonators cover numerous fields including signal processing [23], high-precision sensing [24], cavity quantum electrodynamics (QED) [25, 26], cavity optomechanics [27] and frequency comb generation [28]. Even though there are several potential applications, this thesis focuses the light on the microresonator-based frequency comb.

1.2 Introduction to microresonator frequency comb

An optical frequency comb has a set of equidistantly spaced optical frequency lines, which looks like *a comb* in the frequency domain, and the mutually coherent comb lines correspond to ultrashort optical pulses in the time domain [29–31]. The evolution of the optical frequency comb has drastically developed the research fields of ultrafast lasers and have created novel ideas and applications [32]. In 2005, the Nobel Prize in physics was awarded to two scientists, Theodor W. Hänsch and John L. Hall, for the contribution to the development of optical frequency comb technique [33]. The optical frequency comb simultaneously links several frequency scales; optical frequencies (∼sub-PHz), comb bandwidth (∼THz), repetition rate (∼GHz), and carrier offset frequency (∼MHz). Therefore, an optical frequency comb provides *a frequency ruler* cov-

ering from radio-frequency (RF) to optical frequency domain, which strongly impacts on optical frequency metrology. Absolute frequency measurement is one example. Before the development of optical frequency comb, measuring the optical frequency required a complex frequency chain system and many professional scientists. Nevertheless, the present systematic frequency comb technique enabled the obtainment of the frequency information in a few seconds on a small table.

The microresonator based frequency comb has been explored by T. Kippenberg *et al.* in 2007 for the first time [34]. A strongly enhanced optical field inside a high-Q optical microresonator enables the conversion of a CW laser pump to the broadband and equally spaced comb via cascaded four-wave mixing (FWM) [28, 35–38]. The critical difference from the conventional laser is that a passive microresonator device generates new frequencies as a result of nonlinear frequency conversion thanks to Kerr nonlinearity. Since the mode spacing of frequency comb is scaled down with the cavity size, microresonator frequency comb has readily achieved the large mode spacing exceeding several tens to hundreds of GHz, which has been an unexplored domain for the conventional frequency comb sources. Besides, the tiny mode volume of microresonator, which sometimes can be integrated on a chip, also contributed to reducing the required pump power to generate a frequency comb. Microresonator frequency combs rely on Kerr nonlinearity of dielectric microresonator material, and therefore, they are called Kerr frequency comb or microcomb [39].

However, as opposed to the conventional mode-locked lasers, the output of microcomb in the time domain does not necessarily guarantee optical pulse formation. In order to achieve a mode-locked state in a continuously driven nonlinear resonator, it is needed to satisfy several conditions governed by a mean field model describing a dissipative system [40]. The first observation of temporal soliton in optical microresonators, which is called a dissipative Kerr soliton (DKS), has been reported in 2013 [41]. This discovery made it possible to explore a high-coherence, stable soliton microcomb, as a result of the balance between parametric gain and loss and between dispersion and nonlinearity [40]. By now, DKSs have been successively demonstrated in a wide variety of microresonators, ranging from silica [42], MgF_2 crystalline [41], silicon nitride [43, 44], silicon [45], aluminum nitride [46], and lithium niobate [47]. Different platforms have different advantages (e.g., high Q-factor, nonlinearity, chip-integration), and many groups are developing and proposing new materials and structures for microresonators.

1.3 Research overview related to the thesis

Ultra-precision machining of crystalline microresonators

The development of ultra-high quality factor (Q) optical microresonators enabled us to explore a universe of optics. In particular, crystalline microresonators

offer potential applications such as laser stabilization, quantum manipulation, and optical frequency comb owing to extremely long photon storage time. Indeed, several applications rely on the ultrahigh-Q up to 10^9 and corresponding to a resonance linewidth of hundreds of kilohertz. The fundamental limit of the Q-factor in crystalline resonators is $\sim 10^{13}$ [48] ($Q > 10^{11}$ as observed in the experiment [49]), and this value surpasses that of resonators made with other materials (e.g., silica, silicon, etc.). Especially, magnesium fluoride (MgF_2) and calcium fluoride (CaF_2) are Kerr nonlinear materials that are commonly used for fabricating crystalline microresonators thanks to their quality, commercial availability, and optical properties. Very recently, lithium niobate ($LiNbO_3$) and lithium tantalate ($LiTaO_3$) crystals exhibiting the second-order nonlinearity are attracting interest with respect to the variety of optical properties (e.g., Pockels effect, piezoelectric effect, etc.).

A polishing and machining process is usually employed to fabricate the crystalline microresonators, which are particularly non-integrated and bulk resonators. They are accomplished either with a motion-controlled machine or manually. A hard diamond tool enables us to fabricate WGM structures initially, but it is needed to employ subsequent manual polishing with diamond slurry to improve the Q-factor of the microresonator. Precision machining readily overcomes the geometrical limitation of the manual process; therefore, precise computer-controlled machining has achieved the pre-designed, sophisticated mode structures, for example, single-mode [50,51] and dispersion engineered resonators to generate broadband microresonator frequency combs [52–54]. However, a significant challenge remains because it is essential to employ additional hand polishing after the diamond turning process due to the relatively low Q of $10^6 \sim 10^7$ at best when using machining alone [50,52,53,55]. This value is not usually sufficient to generate a Kerr frequency comb in which the threshold power follows the scaling factor $\sim V/Q^2$ [56]. Indeed, the additional polishing improves the Q; nevertheless, a subsequent polishing deforms the precisely fabricated structures in spite of the engineered dispersion realized by the programmed motion of the lathe [50]. Then, a strong motivation of this study is to fabricate ultrahigh-Q crystalline microresonators with only precision machining.

Although an automated ultra-precision machining technique is highly compatible with dispersion engineering, the achievement of ultrahigh-Q factor has been the bottleneck encountered with conventional fabrication techniques. Therefore, the reliable production of high-Q crystalline microresonators by using precision machining is highly required so far. Such a technique also supports recent advances in the integration of crystalline microresonators with photonic waveguides towards a wide range of future applications [57–60].

Large frequency shift optical parametric oscillation and clustered comb

As an independent study on the fabrication of high-Q microresonators, phase-matched FWM in optical microresonators driven by a continuous wave (CW) laser has been attracting interests. Not only in regard to a microresonator frequency comb in an anomalous dispersion regime, but also comb generation in a weak normal dispersion regime is proceeding recently. Since normal dispersion usually does not allow modulation instability (MI) near the pump, phase-matched FWM is generally considered to occur only in an anomalous dispersion system. In the case of fiber optics, nevertheless, a unique phase-matching scheme assisted by higher-order dispersions has been employed to achieve the resonant MI process even in the normal dispersion regime [61]. It is namely that higher-order dispersion, particularly even orders of dispersion, enables the phase-matching process far from the pump mode, and moreover, the large frequency shift oscillation frequencies can be widely tunable depending on pump frequency. Since it is necessary to pump near the zero-dispersion wavelength, standard silica fibers [61, 62] and photonic crystal fibers [63] have been employed as the platform.

Recent studies have demonstrated the large frequency shift optical parametric generation and subsequent comb generation via a FWM process in an optical microresonator system including MgF_2 [64–66], silica (SiO_2) [67], aluminum nitride (AlN) [68], and silicon nitride (Si_3N_4) [69] ring resonators. The micro-comb, characterized by FWM generation with large shift parametric sidebands, is called Kerr clustered combs since the pump and primary sidebands form *comb clusters* around them. Such clustered combs have the potential to utilize a microresonator comb source covering the visible to mid-infrared wavelength region when only tuning a single CW laser frequency to pump the resonances. Moreover, the oscillation wavelength is also highly tunable, relying on the microresonator dispersion; and thus, this study is compatible with the technique of cavity geometric dispersion engineering. For both cases of a pure parametric oscillation with a pair of signal and idler light and a clustered comb, the oscillation wavelengths are essential and interesting subjects for investigation with regard to dispersion engineering in optical microresonators. A bandwidth expansion of the frequency shift via the phase-matched FWM process is one of the recent hot topics in the field of microresonator dispersion engineering, so many studies have been reported using various platforms and wavelength bands. Despite a number of experimental demonstration, the dispersion engineering, from the standpoint of precise fabrication, has not been well explored yet. In particular, the precise fabrication of whispering gallery mode resonators (e.g., crystalline-based and fused silica-based) is a critical issue regarding dispersion engineering of higher-order dispersion.

Visible light emission via second and third-harmonic generation

Optical microresonators have attracted considerable interest as compact platforms in the field of nonlinear harmonic generation for obtaining visible light from infrared light. There have been many studies on harmonic frequency conversion by using optical microresonators since such frequency-mixing processes via second- and third-order optical nonlinearities occur efficiently in microresonators as a result of large optical field enhancement owing to a high-Q and a small mode volume. In particular, the second-harmonic process [i.e., second-harmonic generation (SHG), and sum-frequency generation (SFG)] and third-harmonic process [i.e., third-harmonic generation (THG), and third-order sum-frequency generation (TSFG)] enable a direct frequency up-conversion to the visible wavelength regime from the near-infrared wavelength regime.

The first demonstration of continuous wave (CW) third-harmonic emission in an optical microresonator was reported in 2007 by using a silica toroid WGM microresonator [70]. The work by T. Carmon *et al.* triggered many studies on the visible light emission via frequency up-conversion in optical microresonators for the past decades. Not only a harmonic generation from a pump light but also multi-color emission via TSFG has been demonstrated in a silica microresonator [71], and comb-like spectrum generation at visible wavelengths has been reported using waveguide resonators [72–74]. Since microcomb generation is usually inhibited due to strong material dispersion at the visible wavelength regime, these frequency up-conversion processes have been expected to realize a visible microcomb with near-infrared pumping.

In addition, interactions between several nonlinear processes are attracting a lot of attention. For example, a silica microtoroid easily emits multi-color visible light (e.g., blue, green, yellow, and red) with a high pump power. However, third-harmonic generation permits only green light (517 nm) with 1550 nm pumping. These are mysterious and interesting observations, and they provide the motivation to discover what is occurring inside the resonator.

Normal dispersion Kerr frequency comb and dark pulse formation

A study on normal dispersion microresonator frequency combs began following intensive research on Kerr comb generation with anomalous dispersion. This is because the nonlinear propagation, particularly in single-mode optical fibers, usually exhibits modulation instability (MI) only with anomalous dispersion. This limitation can be unleashed by using a cavity system; however, most microcomb studies have been conducted using microresonators exhibiting anomalous dispersion since the phase-matching condition for optical parametric oscillation is easy to satisfy in this regime. Still, there have been several demonstrations of Kerr comb generation in the normal dispersion regime, and they offer practical

advantages over anomalous dispersion microcombs. One of them is a conversion efficiency, which is known as a weakness of the microcomb. In contrast to a bright soliton pulse in anomalous dispersion, a mode-locked state in normal dispersion (i.e., a dark pulse) makes it possible to realize a much higher conversion efficiency than 30% in the infrared wavelength regime [75]. Also, it admits more deterministic approaches to mode-locking state [76]. Notably, its better power efficiency and low noise figure are highly attractive for a specific application such as a light source of coherent optical telecommunications.

Thus far, reliable approaches to obtaining normal dispersion microcombs are as follows: engineering the geometric dispersion to overcome strong material dispersion, utilizing the anti-mode crossing effect to induce a local anomalous dispersion, and the use of both techniques. Notably, the utilization of avoided mode crossing is more attractive with a view to the controllability of a mode spacing of the comb. Subsequently, many works have focused on revealing the underlying physics of Kerr frequency comb generation in the normal dispersion regime [76–78]. These works paved the way for normal dispersion microcomb to extend the spectral bandwidth and to realize stably propagating pulse operation. However, the complex dynamics of normal dispersion microcombs has not been well understood, including the development of numerical modeling and analysis.

1.4 Thesis outline and objective

This thesis investigates the dispersion engineering of high-Q optical microresonators for optical frequency comb generation. Dispersion engineering, based on the design and fabrication of microresonators, is a crucial technique for obtaining a mode-locked state, namely a dissipative Kerr soliton, and for expanding the bandwidth of microresonator frequency combs. The thesis addresses this issue with a view to designing the geometry of microresonators. Since the goal of this thesis is to study dispersion engineering and its application to microresonator frequency combs, the fundamental theory, techniques and strategy are introduced in Chapter 2 and Chapter 3. The developed simulation method and dispersion measurement techniques described in Chapter 3 are used to design and evaluate microresonator dispersion. Then, the role of dispersion in microcomb generation is briefly described. The author uses precision machining for crystalline microresonator fabrication since it is a powerful tool for dispersion engineering. Chapter 4 mainly describes fabrication using precision machining with the goal of realizing dispersion-engineered microcomb applications. Ultraprecision machining has a great advantage as regards geometry controllability because it is a fully computer-controlled system. However, a low Q-factor imposed by large surface roughness is a critical limitation in relation to nonlinear optics applications. To overcome this problem, the author confronts the optimization of the fabrication conditions to make it possible to manage both a high Q and geometry dispersion engineering. As a result, parametric oscillation is demonstrated in a machine-made crystalline resonator in which the dispersion

is evaluated with the techniques described in Chapter 3. The phase-matching scheme described in Chapter 4 can be applied to silica-based resonators. Here, the author highlights phenomena in a silica microtoroid resonator that have been observed but not explained. The emission of various colors, in particular blue light, is explained well by dispersion engineering and the coexistence of third-order nonlinear effects. This study provides a deep insight into cascaded parametric oscillation in optical microresonators. Although "geometry" dispersion engineering is the main concern of this thesis, another dispersion engineering method is also dealt with in Chapter 6, namely anti-mode-crossing induced microcomb generation. The use of mode coupling eases the difficulty of geometry dispersion engineering, particularly in a strong normal dispersion regime, and this approach paves the way to deterministic mode-locking operation. Rigorous modeling and a more practical simulation are the objectives of this chapter. The chapter overviews are as follows,

Chapter2
High-Q optical microresonators have been developed along with an evolution of microresonator frequency combs. Dynamics and underlying physics of microcombs have been revealed owing to great efforts over the years, which also contributed to induce the big wave in the field of nonlinear optics as well as nanophotonics. Chapter 2 introduces the study on optical microresonator based frequency comb generation while reviewing the background, theory, simulations, fabrication, and experiments with essential previous literature.

Chapter 3
Dispersion engineering is one of the essential techniques for microcomb generation. Chapter 3 describes how to simulate and design the microresonator dispersion precisely, featuring whispering gallery mode microresonators that exhibit a significant difference in the strategy of resonator geometry design from waveguide resonators. Besides, the precise dispersion measurement methods will be introduced with the comparative experiment. A role of dispersion, particularly of higher-order dispersion, in the Kerr frequency comb spectrum, is highlighted in this chapter.

Chapter 4
Chapter 4 presents ultrahigh-Q crystalline microresonator fabrication for the first time by the all-precision machining process. A cutting condition has been thoroughly addressed by considering crystal anisotropy, resulting in Q exceeding 100 million with a machining process solely. This work makes a major breakthrough for dispersion engineering due to the fabrication accuracy and freedom of geometry design, both of which are the critical drawbacks of the conventional fabrication method. This chapter also describes the other significant demonstration, namely an octave-wide optical parametric oscillation in crystalline microresonators. With a continuous-wave pump, oscillation frequencies were widely

tuned, and subsequent comb clusters around 1.1 μm and 2.4 μm wavelengths were also observed for the first time in this work.

Chapter 5
Third-harmonic generation can be observed in optical microresonators, even though the process is independent of four-wave mixing. However, mutual interaction among other $\chi^{(3)}$-nonlinearity processes allows the bandwidth extension of the optical spectrum. This chapter reports a continuous blue light emission via third-harmonic generation, for the first time, upon a dispersion engineered optical parametric generation. A chain of $\chi^{(3)}$ process enables generating broadband optical spectrum covering visible to near-infrared wavelengths in a chip-integrated microresonator with only a continuous-wave pump.

Chapter 6
Dispersion engineering is a key technique for microresonator frequency comb generation including but not limited to geometric tailoring, a variety of resonator material, and a fusion of them. A mode coupling induced resonance shift makes it possible to create anomalous dispersion in a specific region, which becomes a starting point of four-wave mixing. This method enables a normal dispersion mode-locked comb generation, namely dark-pulse generation, deterministically. This chapter proposes a rigorous model of Kerr comb generation in mode coupled microresonators, and numerically investigates the behavior with the analysis of phase-matching condition from the standpoint of dispersion engineering.

Chapter 7
This chapter summarizes the thesis and gives an outlook with a view to plotting a new landscape for the microresonator frequency comb.

Chapter 2

Microresonator based optical frequency comb

2.1 Fundamentals of optical microresonators

2.1.1 Basic characteristics of microresonators

Resonance frequencies

Optical microresonators have equidistantly spaced resonance frequencies determined by:

$$\omega_m = \frac{2\pi mc}{n_{\text{eff}}L} \tag{2.1}$$

$$\lambda_m = \frac{n_{\text{eff}}L}{m} \tag{2.2}$$

where m is the mode number ($m \in \mathbb{N}$), ω_m is the angular frequency of the m-th mode (λ_m is the wavelength), n_{eff} is the effective index, L is the roundtrip length of the resonator, and c is the speed of light. Here, the roundtrip time t_R is expressed as the inverse of the free-spectral range (FSR) of the resonator $t_R = 1/FSR$. Figure 2.1 shows schematics of optical microresonators with a roundtrip length L and corresponding optical resonances. It should be noted that the FSR is the frequency-dependent value due to the material and geometric dispersion of the medium.

Microresonator dispersion

The dispersion of the microresonator is determined by both contributions of the material dispersion and geometric dispersion. Material dispersion expresses the dependence of the refractive index on frequency, and geometric dispersion includes the effect of the resonator structure. Total microresonator dispersion appears as the deviation of resonance frequencies from equidistance and results

in frequency-dependent mode spacings. The resonance frequencies of arbitrary mode ω_μ can be expressed with a relative mode number μ ($\mu \in \mathbb{Z}$) as,

$$\omega_\mu = \omega_0 + D_1\mu + D_2\mu^2 + D_3\mu^3 + \cdots . \tag{2.3}$$

The equidistant frequency grid (FSR) at the center frequency ω_0 corresponds to $D_1/2\pi$, and D_2 describes the deviation of FSR in terms of the center frequency. Also, D_2 and D_3 correspond to the second- and third-order dispersion, respectively. Dispersion has a critical influence on the frequency comb generation, particularly its bandwidth, and phase-matching condition. The further details of microresonator dispersion will be introduced in Chapter 3.

Quality factor and decay rate

Quality factor is an important parameter to characterize the property of the resonator. The intensity of light stored in the resonator shows an exponential decay, passing through a medium mainly due to material absorption and scattering loss. Here, an attenuation coefficient α of the electric filed amplitude with respect to 1-roundtrip in the resonator is introduced:

$$\alpha = \exp(-\alpha_r \cdot L) \tag{2.4}$$

where α_r is the attenuation per unit of length, and the attenuation per unit of time is described as $\alpha_t = c\alpha_r$. Cavity lifetime τ_p is defined as the time at which the electric field amplitude decays to $1/\sqrt{e}$ of the original amplitude (electric field intensity decays to $1/e$ ($\sim 37\%$) with respect to the original intensity) as follows,

$$\tau_p = \frac{1}{2\alpha_t} = \frac{1}{2c\alpha_r}. \tag{2.5}$$

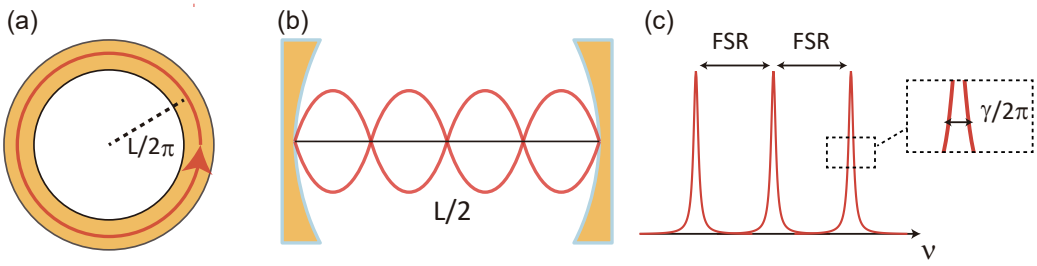

Fig. 2.1: (a) Ring-type optical microresonator with a round-trip length L. (b) Fabry-Pérot resonator with a round-trip length of $2L$, consisting of two reflective mirrors. (c) Resonant spectrum characterized by an equidistant free-spectral range (FSR) and full-width of half-maximum (FWHM) linewidth.

Thus, the decay of electric field amplitude at an arbitrary time is described as,

$$\alpha = \exp\left(-\frac{t}{2\tau_p}\right). \tag{2.6}$$

Quality factor is well related to the above discussion in terms of decay time of the optical field, and can be evaluated by the relation between the stored energy E_{cav} and dissipated energy per oscillation cycle E_{diss}, which corresponds to dissipated power $P_{\text{diss}} = \nu E_{\text{diss}}$ (ν is the frequency):

$$Q = 2\pi\frac{E_{\text{cav}}}{E_{\text{diss}}} = 2\pi\nu\frac{E_{\text{cav}}}{P_{\text{diss}}} = \omega\tau_p = \frac{\omega}{\gamma}. \tag{2.7}$$

The optical resonance has a certain linewidth given by the cavity decay rate γ. The decay rate corresponds to the full-width of half-maximum (FWHM) of the linewidth in frequency domain, and relates to the cavity lifetime as $\gamma = \tau_p^{-1}$. Besides, the linewidth is also given by $\Delta\lambda = (c/2\pi\nu^2)\gamma$ in the unit of wavelength. The resonance linewidth can be directly obtained from the resonator transmission spectrum in the experiment, and the cavity lifetime is also a measurable parameter in time domain measurements.

Table. 2.1: Comparison of basic characteristics of different microresonators.

Q-factor	$\gamma/2\pi$	$\Delta\lambda$	lifetime τ_p
1×10^6	193.4 MHz	1.55 pm	0.823 ns
2×10^6	96.71 MHz	0.775 pm	1.646 ns
5×10^6	38.68 MHz	0.310 pm	4.114 ns
1×10^7	19.34 MHz	0.155 pm	8.23 ns
2×10^7	9.671 MHz	77.5 nm	16.46 ns
5×10^7	3.868 MHz	31.0 nm	41.14 ns
1×10^8	1.934 MHz	15.5 nm	82.3 ns
2×10^8	967.1 kHz	7.75 nm	164.6 ns
5×10^8	386.8 kHz	3.10 nm	411.4 ns

Effective mode area

The effective mode area is derived from the mode profile of the intensity orthogonal to the propagation direction:

$$A_{\text{eff}} = \frac{(\int |E|^2 dA)^2}{\int |E|^4 dA}, \tag{2.8}$$

where $|E|^2$ is light intensity ($|E|$ is the magnitude of the electric field) and A is defined as the integral area. The effective mode volume is given by $V_{\text{eff}} = A_{\text{eff}}L$. The effective mode volume is related to the threshold power for nonlinear frequency conversion.

2.1.2 Theory of optical coupling to microresonator

Coupled mode equation

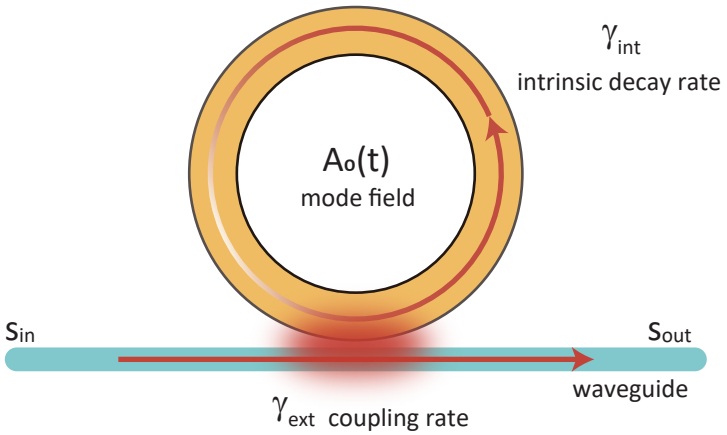

Fig. 2.2: Waveguide-microresonator optical coupling system via evanescent field. $A_0(t)$ is the intracavity optical field, s_{in} and s_{in} denote the input and output fields, respectively. γ_{int} and γ_{ext} are the intrinsic decay rate and coupling rate, respectively.

A coupled mode equation describes an optical coupling between a resonator and an external coupler through an evanescent field as shown in Fig. 2.2. When adopting slowly varying envelope approximation, the time evolution of a light field at the resonance frequency ω_0, $\tilde{A}_0(t)$, can be written as [79, 80]

$$\frac{d\tilde{A}_0(t)}{dt} = -\frac{\gamma}{2}\tilde{A}_0(t) - j\omega_0\tilde{A}_0(t) + \sqrt{\gamma_{ext}}s_{in}(t)\exp(-j\omega_p t), \tag{2.9}$$

where s_{in} is the driving field and ω_p is the pump frequency. The decay rate γ is given by the sum of the intrinsic decay rate γ_{int} and the coupling rate γ_{ext} to the waveguide. It should be noted that the field amplitude $\tilde{A}_0(t)$ is normalized to the number of intracavity photon at the resonance as $|\tilde{A}_0(t)|^2$. Here, Eq. (2.9) can be rewritten by adopting the phase transformation $A_0(t) = \tilde{A}_0(t)\exp(j\omega_p t)$ as follows,

$$\frac{dA_0(t)}{dt} = -\left(\frac{\gamma}{2} + j(\omega_0 - \omega_p)\right)A_0(t) + \sqrt{\gamma_{ext}}s_{in}(t). \tag{2.10}$$

Assuming the steady state ($dA_0(t)/dt = 0$), the field amplitude is expressed as,

$$A_0 = \frac{\sqrt{\gamma_{ext}}}{\gamma/2 + j(\omega_0 - \omega_p)}s_{in}, \tag{2.11}$$

hence, the number of photons stored inside the resonator is given with the photon flux in the waveguide $|s_{in}^2|$:

$$|A_0|^2 = \frac{\gamma_{ext}}{\gamma^2/4 + (\omega_0 - \omega_p)^2}|s_{in}|^2. \tag{2.12}$$

The relation between the driving field and the transmission field is described as

$$s_{\text{out}} = -s_{\text{in}} + \sqrt{\gamma_{\text{ext}}} A_0 \tag{2.13}$$

and the transmittance defined as $t = s_{\text{out}}/s_{\text{in}}$ and $T = |s_{\text{out}}/s_{\text{in}}|^2$ yield

$$t = \frac{s_{\text{out}}}{s_{\text{in}}} = \frac{(\gamma_{\text{ext}} - \gamma_{\text{int}})/2 - j(\omega_0 - \omega_p)}{(\gamma_{\text{ext}} + \gamma_{\text{int}})/2 + j(\omega_0 - \omega_p)}, \tag{2.14}$$

$$T = \left| \frac{s_{\text{out}}}{s_{\text{in}}} \right|^2 = \frac{(\gamma_{\text{ext}} - \gamma_{\text{int}})^2/4 + (\omega_0 - \omega_p)^2}{(\gamma_{\text{ext}} + \gamma_{\text{int}})^2/4 + (\omega_0 - \omega_p)^2}. \tag{2.15}$$

From the view of energy conservation, the difference between the output photons $|s_{\text{out}}|^2$ and the input photons yields the dissipated photons inside the resonator as,

$$\begin{aligned} |s_{\text{out}}|^2 = |s_{\text{in}}|^2 - \gamma_{\text{int}}|A_0|^2 &= \left(1 - \frac{\gamma_{\text{int}}\gamma_{\text{ext}}}{\gamma^2/4 + (\omega_0 - \omega_p)^2}\right)|s_{\text{in}}|^2 \\ &= \frac{(\gamma_{\text{ext}} - \gamma_{\text{int}})^2/4 + (\omega_0 - \omega_p)^2}{(\gamma_{\text{ext}} + \gamma_{\text{int}})^2/4 + (\omega_0 - \omega_p)^2}|s_{\text{in}}|^2, \end{aligned} \tag{2.16}$$

which is consistent with Eq. (2.15). When zero detuning ($\omega_0 - \omega_p = 0$) is assumed, the maximum dip of transmission T_0 is expressed as,

$$T_0 = \left(\frac{Q_{\text{int}} - Q_{\text{ext}}}{Q_{\text{ext}} + Q_{\text{int}}}\right)^2. \tag{2.17}$$

Here, $T_0 = 0$, which means the full extinction of transmittance, occurs under the critical coupling condition $Q_{\text{int}} = Q_{\text{ext}}$ ($\gamma_{\text{int}} = \gamma_{\text{ext}}$), and then the loaded Q becomes half of the intrinsic and coupling Q (the decay rate γ becomes twice the intrinsic decay rate γ_{int} and coupling rate γ_{ext}). The optical coupling condition is classified into three conditions: under coupling $Q_{\text{int}} < Q_{\text{ext}}$ ($\gamma_{\text{int}} > \gamma_{\text{ext}}$), over coupling $Q_{\text{int}} > Q_{\text{ext}}$ ($\gamma_{\text{int}} < \gamma_{\text{ext}}$), and critical coupling described above. The coupling ratio is defined as $\eta = \gamma_{\text{ext}}/\gamma$, namely $\eta = 0.5$ for critical coupling condition. In general, the coupling ratio can be controlled by changing the gap between the resonator and the waveguide. Figure 2.3 shows the minimum transmission for different coupling rates and the corresponding normalized transmission.

Furthermore, T_0 can be rewritten in terms of Q-factor,

$$T_0 = \left|1 - 2\frac{Q_{\text{tot}}}{Q_{\text{int}}}\right|^2, \tag{2.18}$$

$$Q_{\text{int}} = \frac{2}{1 \pm \sqrt{T_0}} Q_{\text{tot}}, \tag{2.19}$$

where the sign expresses under coupling (plus) and over coupling (minus), respectively. It should be noted that Q_{tot} is given by $Q_{\text{int}}Q_{\text{ext}}/(Q_{\text{int}} + Q_{\text{ext}})$. These relations give the intrinsic and coupling Q from the result of the measurement of the transmission spectrum.

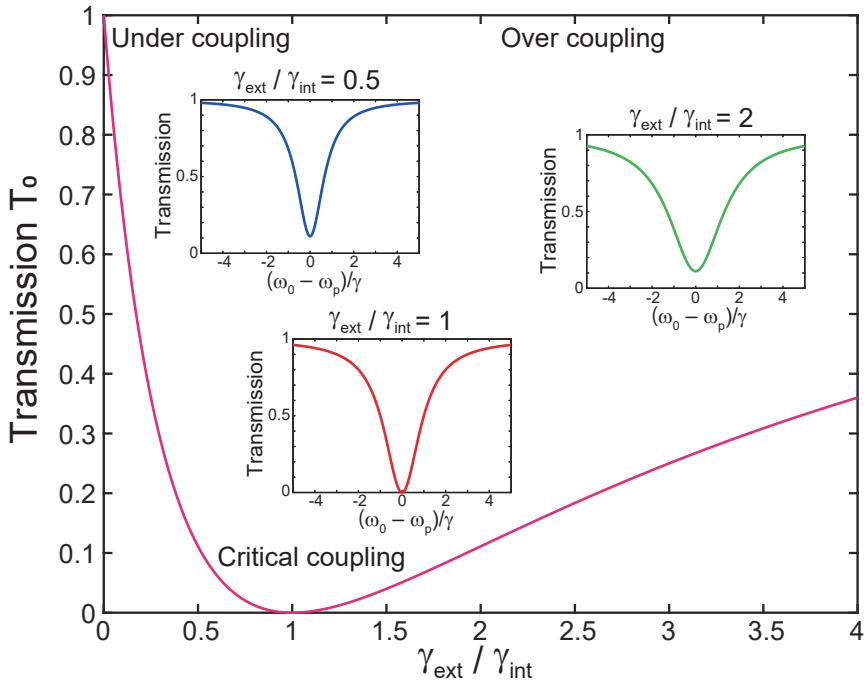

Fig. 2.3: Minimum transmission T_0 for different $\gamma_{\text{ext}}/\gamma_{\text{int}}$. $\gamma_{\text{ext}}/\gamma_{\text{int}} = 1$ corresponds to critical coupling condition, and $\gamma_{\text{int}} > \gamma_{\text{ext}}$ ($\gamma_{\text{int}} < \gamma_{\text{ext}}$) are under (over) coupling condition. Insets show normalized transmission for each coupling condition.

Circulating power and Finesse

The photon number translates into the intracavity circulating power by multiplying the photon energy $\hbar\omega_p$ and devision by the roundtrip time t_R:

$$P_{\text{cav}} = \hbar\omega_p |A_0|^2 / t_R = \frac{\gamma_{\text{ext}}}{\gamma^2/4 + (\omega_0 - \omega_p)^2} \cdot \frac{P_{\text{in}}}{t_R}, \tag{2.20}$$

where $\hbar$ is Dirac's constant, and the input power $P_{\text{in}} = \hbar\omega_p |s_{\text{in}}|^2$. The finesse $\mathscr{F}$ is defined as the ratio between the mode spacing (FSR) and linewidth, and the circulating power P_{cav} under the case of zero detuning and critical coupling is described as

$$\mathscr{F} = \frac{FSR}{\gamma/2\pi}, \tag{2.21}$$

$$P_{\text{cav}} = \frac{\mathscr{F}}{\pi} P_{\text{in}}, \tag{2.22}$$

which corresponds to the enhancement factor in terms of intracavity power.

2.1.3 Scheme for coupling to microresoantor

In contrast to the case of a Fabry-Pérot resonator, which has a partially transmitting mirror for output, an evanescent field is used in order to couple the light into

the microresonators. There are several methods for achieving efficient coupling, such as prism coupling, angle cleaved (pigtailed) fiber coupling, side polished fiber coupling, waveguide coupling, and tapered fiber coupling. In particular, prism and tapered fiber coupling are widely employed to couple the light into WGM microresonators due to their low-loss nature and high-coupling efficiency. In the case of waveguide resonators, an integrated waveguide in the same chip is used as a coupler. Here, these three methods are reviewed.

Tapered optical fiber coupling

One of the significant advantages of the tapered fiber coupling is a low propagation loss [81–83]. Figure 2.4 shows schematics and the setup of tapered fiber coupling. The tapered fiber is fabricated by heating and stretching a standard optical fiber with a diameter of ∼125 μm. Since this process is adiabatically operated above the melting point of silica, the additional loss is suppressed after the fabrication. For stretching the fiber, there are several types of heaters, such as propane/oxygen gas, hydrogen gas, and a ceramic microheater. Typically, the conventional single-mode fiber (SMF-28) clamped by fiber brackets is prolonged during the heating by moving two translation stages, and the cladding and core (slightly higher refractive index) region become one material whose refractive index is much larger than that of the surrounding air. After starting the taper stretching, the cladding modes are excited, resulting in oscillations in the transmission signal. The oscillation stops when the tapered fiber becomes single-mode again, and it indicates the end of the fabrication for a single-mode tapered fiber. The loss of the tapered fiber is less than one percent if the parameters, such as stretching speed, the temperature of the heater, and the alignment of the fiber, are appropriately optimized. The single-mode condition for an optical fiber is given by

$$V_{\text{fiber}} = \frac{\pi \phi_{\text{fiber}} \sqrt{n_i^2 - n_o^2}}{\lambda} < 2.405, \tag{2.23}$$

where ϕ_{fiber} is the diameter of the fiber, λ is wavelength, and n_i, n_o are the refractive indice of core and cladding material, respectively. From the relation, ϕ_{fiber} equals 1.15 μm with $n_i = 1.44$, $n_o = 1.0$, and $\lambda = 1.55$ μm under the single mode condition.

Another advantage of a tapered fiber is the tunability of the propagation constant and coupling strength. The former is controlled by the diameter of the tapered region by optimizing tapering conditions or changing the fiber position of coupling to the resonator. The latter corresponds to changing the gap between the tapered fiber and the resonator. The careful tuning of the coupling condition enables high ideality of light coupling (i.e., critical coupling) [80].

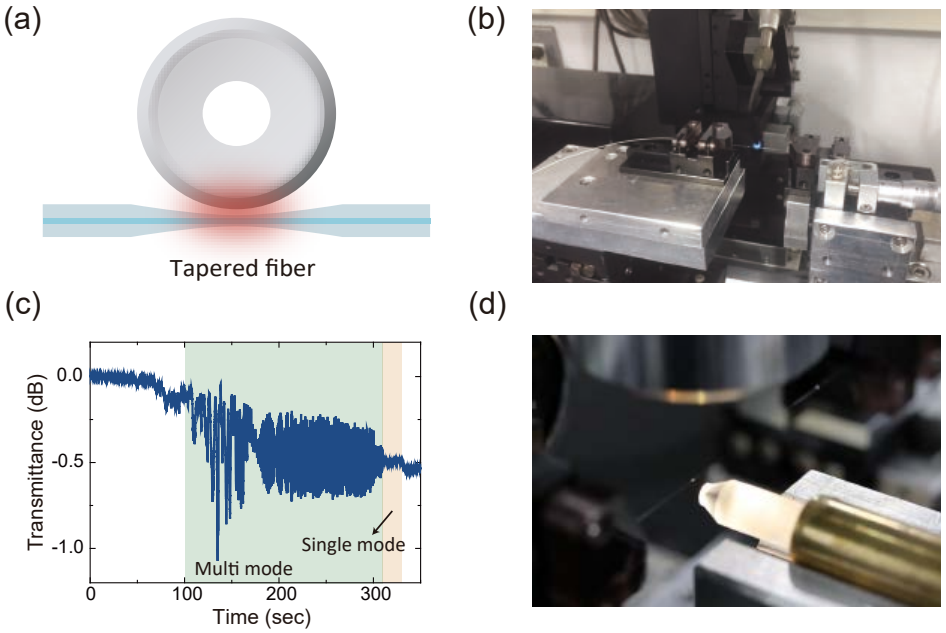

Fig. 2.4: (a) Schematic of tapered optical fiber coupling system. (b) Setup for tapered fiber fabrication. (c) Transmission for tapered fiber fabrication while translation stages are pulling heated optical fiber. (d) Experimental tapered fiber coupling system. Coupling strength is determined by a gap between a tapered fiber and a microresonator.

Prism coupling

Prism coupling has been initially proposed for the light coupling to a silica microsphere [84]. The incident light from the slope face of a prism undergoes total internal reflection on the coupling face, and couples into a resonator via an evanescent field as presented in Fig. 2.5. The transmission goes again to free space through the prism. AN objective lens or gradient-index (GRIN) lens is usually used to focus the spot on the coupling point. The angle of the incident beam must be satisfied with the condition of total internal reflection, and it critically affects the coupling efficiency [85]. The advantages of prism coupling are the robustness and the compatibility of high refractive index resonator material. It is clear that bulky optical elements ensure the robustness of the system, although careful free space alignment of the beam is necessary. There are several choices of prism materials, including BK7 [84], SF11 [86], diamond [87], silicon [88], rutile [89], and sapphire [90], for the case of couping with high refractive index resonators, which have the difficulty of coupling even with a silica optical tapered fiber. The coupling efficiency reaches as high as 80% by optimizing the alignment, whereas operating in the strongly overcoupled regime is not easily achieved.

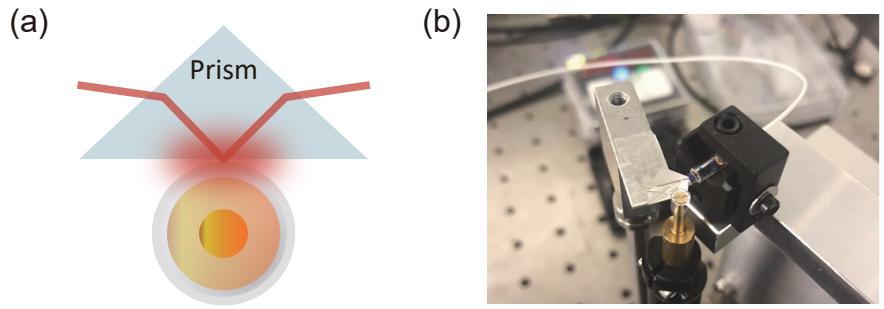

Fig. 2.5: (a) Schematic of prism coupling system. The incident light is coupled into the resonator via an evanescent field. (b) Setup for prism coupling using a GRIN lens as a beam focuser. Output beam can be detected with either a free space photodetector or a fiber collimator.

Waveguide coupling

Waveguide coupling is a way to couple the light into waveguide resonators (e.g., silicon nitride microring) that are fully integrated. Figure 2.6 shows a schematic and micrograph of waveguide coupling. This scheme maintains a stable coupling condition, which can be prepared in the fabrication step by designing the waveguide dimension (e.g., straight bus and pulley-style) and the gap between the waveguide and resonator such that the resonator structure is designed [57, 91]. On the other hand, there is less tunability of coupling strength after the fabrication because it is not possible to change the gap in the same manner as a tapered fiber and prism coupling.

Recent studies have demonstrated highly efficient coupling between a WGM microresonator and waveguide coupler [57–60]. Even though the integration of WGM resonators to a photonic chip is a challenge because of the significant difference of refractive index, the manipulation of photonic waveguides allows for efficient coupling to a wide range of microresonators, including crystalline and fused silica materials.

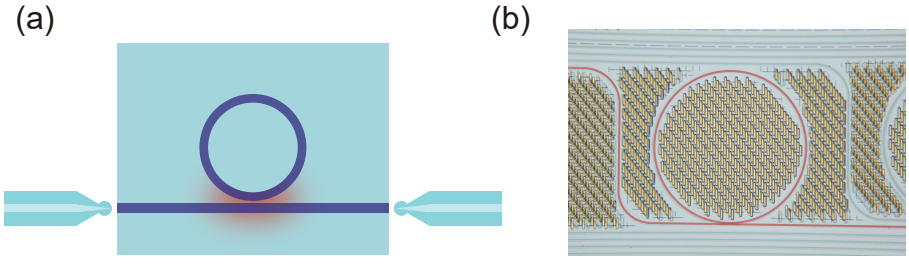

Fig. 2.6: (a) Schematic of a waveguide coupling system. The incident light is injected into the waveguide by using a lensed fiber or a focusing lens. (b) Micrograph of a waveguide integrated silicon nitride microresonator. The bus waveguide and the microring are highlighted in red.

2.1.4 Quality factor measurement

Measurement of quality factor is one of the most fundamental experiments to evaluate a microresonator. The optical resonances are detected by measuring the transmittance through the coupler using a photodetector, and the linewidth corresponds to the quality factor of the resonance mode (frequency domain measurement). However, particularly in the case of ultrahigh-Q, the observed transmittance directly reflects a cavity lifetime, namely time-domain measurement. The commonly used experimental setup is presented in Fig. 2.7. Here, two measurement methods and the results are introduced.

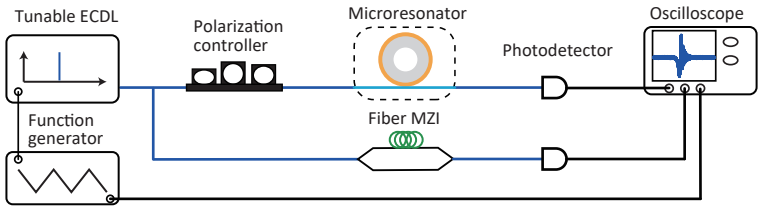

Fig. 2.7: Experimental setup for Q-factor measurement. A fiber Mach-Zehnder interferometer (MZI) is used to calibrate the frequency axis of a recorded spectrum. ECDL, external cavity diode laser.

Frequency domain measurement

The resonance mode typically shows a Lorentzian shape as a function of the frequency in a transmission spectrum [Fig. 2.8(a)]. Therefore, it is a useful way to record the transmission while the laser frequency is scanned using a frequency tunable laser, and theoretical Lorentz fitting gives the linewidth of a particular resonance. Then, the frequency (wavelength) axis should be correctly calibrated since the axis works as a ruler for the recorded spectrum. There are several ways to make the frequency axis; however, it is simple to use the output signal of a tunable laser, which gives reliable information about frequency. Such a function is often available in a commercial laser system (e.g., Santec TSL series laser, New focus Velocity series laser). Otherwise, the interference signal from the Mach-Zehnder interferometer (MZI) and a phase-modulator would be useful choices with respect to simplicity and accuracy.

Time domain measurement

The quality factor can be measured in the time domain by monitoring the transmission from the resonator. When the laser frequency is scanned quickly across the resonance, the scanning laser and the output from the resonator interfere with each other due to their long photon time. This phenomenon induces an oscillation signal of the transmitted light that decays exponentially. Another

approach is to use a squared modulation signal as input instead of continuous-wave light. By applying the square modulation, the squared pulse kicks the input out at the end of the pulse. Afterward, the stored light flows out from the resonator, exhibiting exponential decay as the previous case. The fitted exponential function gives the cavity lifetime, as shown in Fig. 2.8(b). Since a long photon lifetime is a key to obtaining a clear signal, these measurements are compatible with ultrahigh-Q resonators ($Q \gg 10^8$).

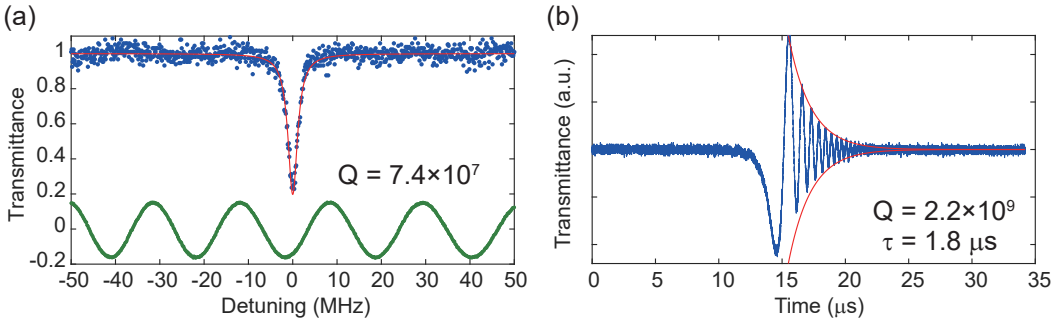

Fig. 2.8: (a) Q-factor measurement in the frequency domain. The blue dots and the solid red line represent the experimental and the fit, respectively. The frequency axis is calibrated by using a fiber MZI spectrum (green) with an FSR of 20 MHz. The FWHM of the transmission spectrum $\gamma/2\pi$ yields a Q of 7.4×10^7. (b) Measurement result in the time domain, called cavity ring-down method. The fitted curve (red line) represents the cavity decay rate, yielding ultrahigh-Q of 2.2×10^9.

2.1.5 Fabrication of microresonators used in this work

Silica toroid microresonators

A fused silica toroid microresonator (microtoroid) works as one of the platforms in this thesis. A silica microtoroid has the major advantages of small mode volume and high Q-factor, which reduces the threshold power for nonlinear frequency conversion, and moreover, it is possible to integrate onto a silicon chip [5]. Figure 2.9(a) shows the fabrication steps for the microtoroids. The main process can be classified into the following four steps: 1. Photolithography with an oxidized silicon wafer, 2. Hydrofluoric acid (HF) wet etching, 3. Xenon difluoride (XeF_2) dry etching, 4. Carbon dioxide (CO_2) laser reflow.

First, an oxidized silicon wafer with a thickness of the oxidized layer on the order of a few micrometers is prepared. The thickness of the oxidized silica layer is related to the final size of the resonator because it influences the flow of heat radiation in the laser reflow process. The next step is the UV-photolithography process, which forms a circular resist pattern with a desired diameter on the substrate, and HF etching is subsequently applied to the sample in order to remove unnecessary silica layer except for the protected pattern with circular re-

sist. A XeF_2 dry etching is performed to undercut disk structure thanks to the high etch selectivity of silicon compared to silica, namely 1000:1. After this process, a disk structure supported by a silicon post can be formed on a silicon wafer. The formed silica disk can be already used as a microresonator (i.e., microdisk), whereas the final process of CO_2 laser reflow melts and shrinks the outer edge of the silica disk. As a result, a microtoroid resonator with a donut-shaped toroidal structure can be formed, and it exhibits a high-Q due to its smooth surface. The degradation of Q occurs mainly due to OH^- bonds within the SiO_2. In order to circumvent the OH^- bonding, laser reflow under a nitrogen environment is a way to achieve ultrahigh-Q up to 10^9, which corresponds to the absorption limit of fused silica. Figures 2.9(b) and 2.9(c) show SEM images of a silica microdisk and a microtoroid, respectively[*a].

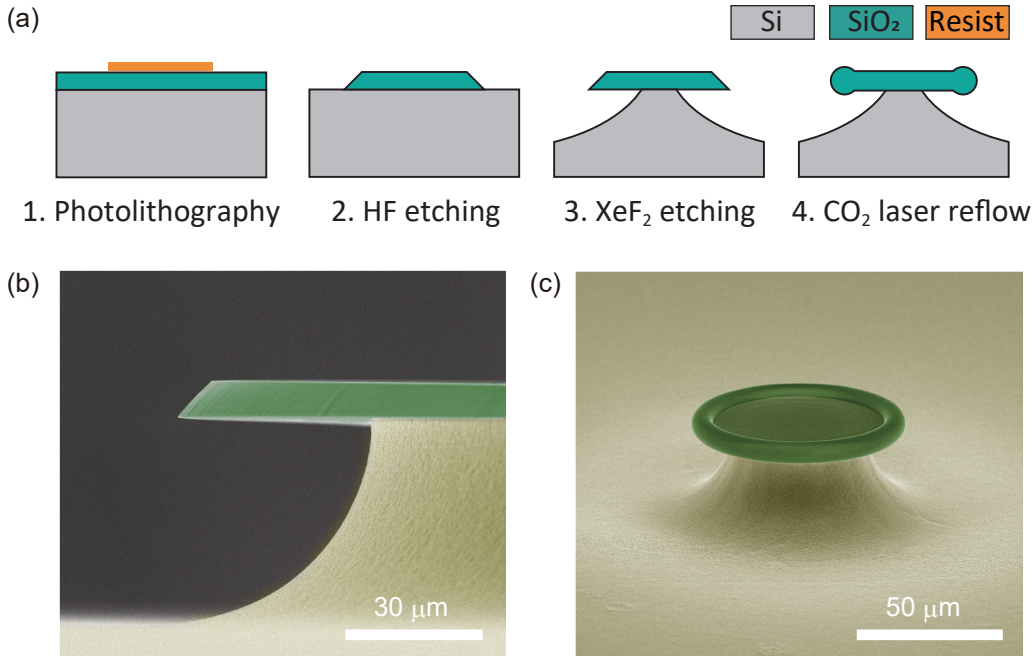

Fig. 2.9: (a) Fabrication process of a silica toroid microresonator. (b) Scanning electron microscope (SEM) image showing a microdisk resonator. The thickness of the silica disk is 8 μm. (c) SEM image of a silica microtoroid fabricated from a silicon wafer with an oxidized SiO_2 thickness of 2 μm. A CO_2 laser reflow forms the toroidal cross-sectional shape by melting the outer edge of the SiO_2 disk.

Crystalline fluoride microresonators

Crystalline fluoride microresonators have been developed as an attractive platform, exhibiting an exceptionally high Q value compared with other resonator

[*a]The silica microresonators in Fig. 2.9 were fabricated by R. Imamura.

materials (e.g., silica, silicon, etc.). The limit of Q-factor in crystalline microresonators is exceptionally high, up to $\sim 10^{13}$, which is imposed by material absorption [48], and moreover, they have a broad transparent window in the visible to mid-infrared wavelength region, which expands the available bandwidth for several applications. On the other hand, these crystalline resonators are of millimeter-scale dimension, and hence generally incompatible with chip integration. Crystalline fluoride materials, including magnesium fluoride (MgF_2) and calcium fluoride (CaF_2) are major candidates for fabricating WGM microresonators due to their crystal quality and commercial availability.

The crystalline microresonators are usually fabricated by abrasive polishing after creating the resonator form with a diamond paper or diamond turning. A hard diamond tool enables us to fabricate WGM structures, and a gradual manual, sometimes mechanical, polishing process with diamond slurry greatly improves the Q-factor of the microresonators. An alternative method is computer-controlled precise machining. Such precision lathes readily overcome the geometrical limitation of handicraft, and they have substantial advantages with respect to designing the resonator structure. However, there remains a significant challenge so far because it is difficult to achieve high-Q by diamond turning solely due to the large surface roughness on the scale of a few micron. Figures 2.10 presents hand-polished and a precision-machined MgF_2 crystalline resonators[*b].

Chapter 4 reports a novel approach of diamond turning and crystalline microresonator fabrication with a Q exceeding 10^8 by *all-precision-machining* process.

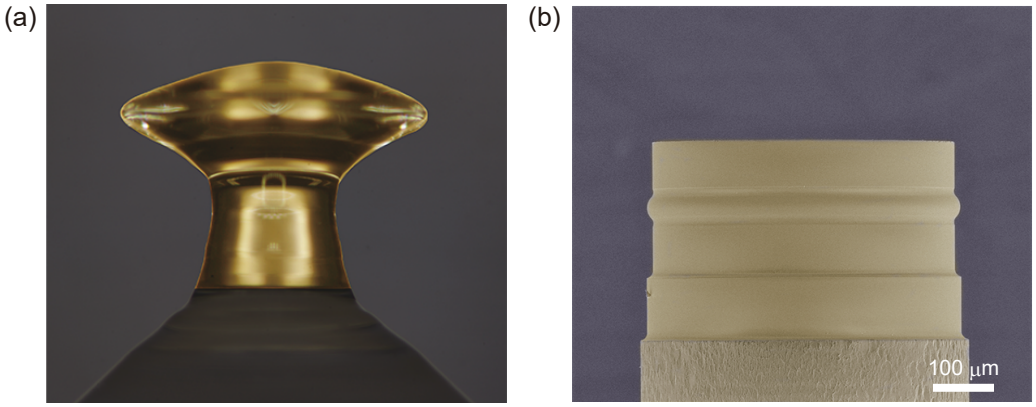

Fig. 2.10: (a) Magnesium fluoride (MgF_2) crystalline microresonator fabricated by a manual polishing process. A diameter of the resonator is approximately 2.8 mm. (b) A precision machined (MgF_2) crystalline microresonator. A resonator diameter is approximately 500 μm.

[*b]The hand-polished MgF_2 resonator was diligently fabricated by K. Wada; the precision-machined MgF_2 resonator was fabricated in collaboration with Kakinuma group (Keio University).

Silicon nitride microresonators

Silicon nitride (Si_3N_4) microresonators are fabricated in a CMOS-compatible process, and the planar resonator structure is formed by chemical vapor deposition on a SiO_2 substrate. The general fabrication steps and micrographs are shown in Fig. 2.11[*c]. The advantage of Si_3N_4 microresonators is integration on a chip with a waveguide coupler and the high refractive index and small mode area, which compensates the relatively low Q-factor compared with a silica and fluoride crystalline microresonators. Furthermore, electron-beam (EB) lithography makes it possible to design the waveguide shape precisely and assure the reproducibility. Recently, high-Q Si_3N_4 microresonators up to 10^7 have been demonstrated by addressing the fabrication technique and procedure [92–94].

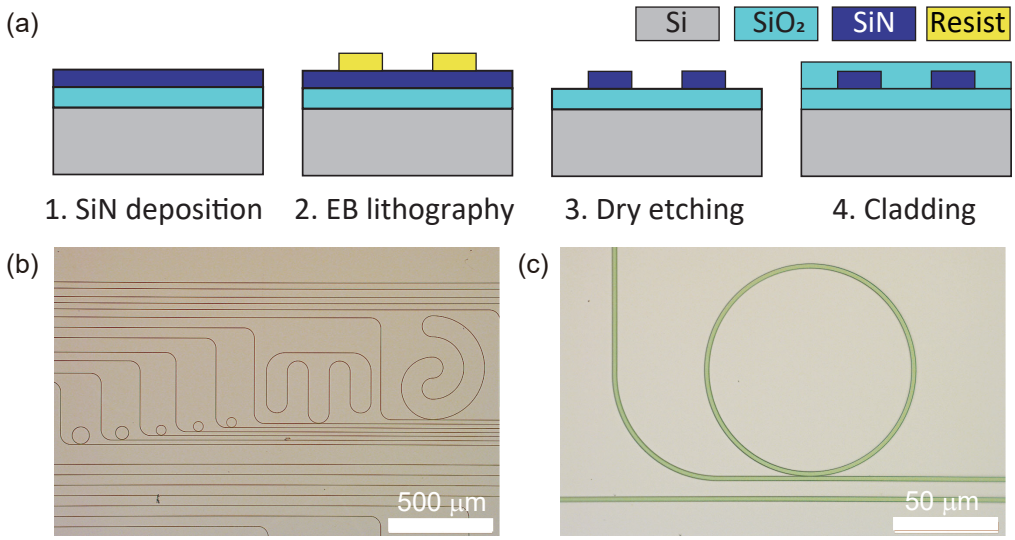

Fig. 2.11: (a) Fabrication process of a silicon nitride (SiN) microresonator. After the deposition of SiN to the desired thickness, lithography and etching processes pattern the designed waveguide with a SiN layer. A silica cladding can be performed to protect the resonator from the surrounding environment. (b) and (c) Micrographs showing SiN waveguide and microring after dry etching (reactive ion etching, RIE) process.

2.2 Optical nonlinearity in microresonators

2.2.1 Third-order nonlinearities in microressonators

Optical nonlinearity, in particular the response of nonlinear medium to an externally applied electrical (optical) field $E(z,t)$, can be described with the time dependent polarization $P(z,t)$ in scalar formulation as [95]:

[*c]The micrographs of SiN resonators were kindly provided by S. Zhang and P. Del'Haye (Max Planck Institute for the Science of Light).

Table. 2.2: Comparison of material properties used in this thesis. The values of MgF_2 are for ordinary polarized mode.

	Fused SiO_2	MgF_2	CaF_2	Si_3N_4
Typical Q	10^7-10^8	10^8-10^9	10^8-10^9	10^6-10^7
Typical FSR [GHz]	20-1000	15-100	15-100	50-1000
Transparency [μm]	0.3-2.6	0.13-8.0	0.15-8.5	0.40-7.5
n	1.44	1.37	1.43	1.98
n_2 [$\times 10^{-20}$ m^2/W]	2.2	0.9	1.9	25
$(1/L)dL/dT$ [$\times 10^{-6}$ /K]	0.55	9.0	18.9	3.3
$(1/n)dn/dT$ [$\times 10^{-6}$ /K]	7.3	0.6	−8.0	30

$$P = \varepsilon_0(\chi^{(1)}E + \chi^{(2)}E^2 + \chi^{(3)}E^3 + \cdots), \tag{2.24}$$

where ε_0 is the vacuum permittivity, $\chi^{(1)}$, $\chi^{(2)}$ and $\chi^{(3)}$ are the linear, second- and third-order susceptibility, respectively. Higher-order terms are less important as long as the optical field does not become extremely high-power scale (e.g., ultra-short pulse lasers). The term of second order nonlinearity can be excluded from Eq. (2.24) because of inversion symmetry of the dielectric materials used in this thesis (i.e, silica, MgF_2, CaF_2, and Si_3N_4). Therefore, the nonlinear polarization P_{NL} can be rewritten as,

$$P_{NL} = \varepsilon_0\chi^{(3)}E^3, \tag{2.25}$$

where the electric fields with three different frequencies are introduced as,

$$E = \frac{1}{2}(E_k \exp\{j(k_k z - \omega_k t)\} + E_l \exp\{j(k_l z - \omega_l t)\} + E_m \exp\{j(k_m z - \omega_m t)\} + \text{c.c.}). \tag{2.26}$$

By substituting Eq. (2.26) into Eq. (2.25), nonlinear polarization is described as,

$$P_{NL} = \frac{1}{2}\sum_n P_n(\omega_n)\exp\{j(k_n z - \omega_n t)\} + \text{c.c.}, \tag{2.27}$$

and then P_n consists of a large number of terms (total 44 different frequency components) describing possible interactions,

$$P_n(\omega_n) = \frac{\varepsilon_0\chi^{(3)}}{4}[(3|E_k|^2 + 6|E_l|^2 + 6|E_m|^2)E_k\exp(j\omega_k t) + \ldots \tag{2.28}$$

$$+ 3E_k^2E_l^*\exp\{j(2\omega_k - \omega_l)t\} + 6E_kE_lE_m^*\exp\{j(\omega_k + \omega_l - \omega_m)t\} + \ldots \tag{2.29}$$

$$+ 3E_k^2E_l\exp\{j(2\omega_k + \omega_l)t\} + 6E_kE_lE_m\exp\{j(\omega_k + \omega_l + \omega_m)t\} + \ldots \tag{2.30}$$

$$+ E_k^3\exp\{j(3\omega_k)t)\}]. \tag{2.31}$$

The relation of wavenumber $k_{n,k,l,m}$ can be always written in the same manner as angular frequency $\omega_{n,k,l,m}$ (i.e., phase-matching condition).

Kerr effect (self- and cross-phase modulation)

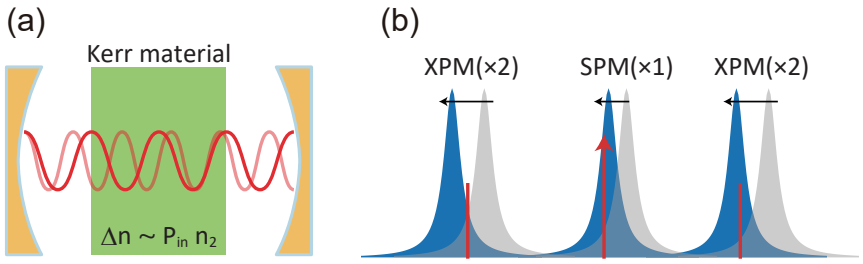

Fig. 2.12: Schematic of optical Kerr effect (self- and cross-phase modulation). (a) An effective refractive index can be modulated by strong pump power via self-phase modulation (SPM) and cross-phase modulation (XPM). (b) In the case of optical resonances, resonance frequencies are shifted by the influence of the nonlinear phase shift.

The optical Kerr effect is a phenomenon in which the nonlinear phase shift is induced by high-intensity light field. Kerr medium, which experiences light propagation, shows an intensity-dependent refractive index, as shown in Fig. 2.12(a). The self-induced phase shift is referred to as self-phase modulation (SPM) and the phase shift induced by different optical fields is referred to as cross-phase-modulation (XPM). Eq. (2.28) represents SPM and XPM, and one can see that the XPM effect works twice as much as the SPM effect. The change of refractive index is expressed with optical light intensity $I_{k,l,m}$ as

$$\Delta n = n_2 I_k + 2n_2(I_l + I_m) \tag{2.32}$$

where n_2 is the nonlinear refractive index defined as,

$$n_2 = \frac{3}{4n_0^2 \varepsilon_0 c}\chi^{(3)}. \tag{2.33}$$

When the light circulates inside a microresonator, the wavelength shift of the pumped resonance via SPM can be described as,

$$\Delta\lambda_m = \frac{\Delta n L}{m} = \frac{n_2 P_{\text{cav}} L}{m A_{\text{eff}}} + \frac{2n_2 P'_{\text{cav}} L}{m A_{\text{eff}}} = \lambda_m \left(\frac{n_2 P_{\text{cav}}}{n A_{\text{eff}}} + \frac{2n_2 P'_{\text{cav}}}{n A_{\text{eff}}} \right) \tag{2.34}$$

where P_{cav} and P'_{cav} represent circulating powers contributing to SPM and XPM, respectively [Fig. 2.12(b)].

Four-wave mixing

Four-wave mixing (FWM) is the optical process to create new photons with annihilation of incident photons. In the case of degenerate FWM, annihilated

two photons with the same frequencies $2\omega_k$ create two photons with different frequencies ω_n and ω_m, namely the first term of Eq. (2.29). Non-degenerate FWM corresponds to the process in which two photons of frequency ω_k and ω_m generate two photons of frequency ω_n and ω_l described in the second term of Eq. (2.29). These processes require the phase matching condition as,

$$k_n = 2k_k - k_l \quad \text{(degenerate)},$$
$$k_n = k_k - k_l + k_m \quad \text{(non-degenerate)}.$$

The threshold pump power for degenerate FWM is given by [56, 96],

$$P_{\text{th}}^{\text{FWM}} = \frac{\gamma^2 n^2 V_{\text{eff}}}{8\eta\omega_0 c n_2}. \tag{2.35}$$

Figure 2.13 shows the observed optical spectrum of FWM in a silica toroid microresonator.

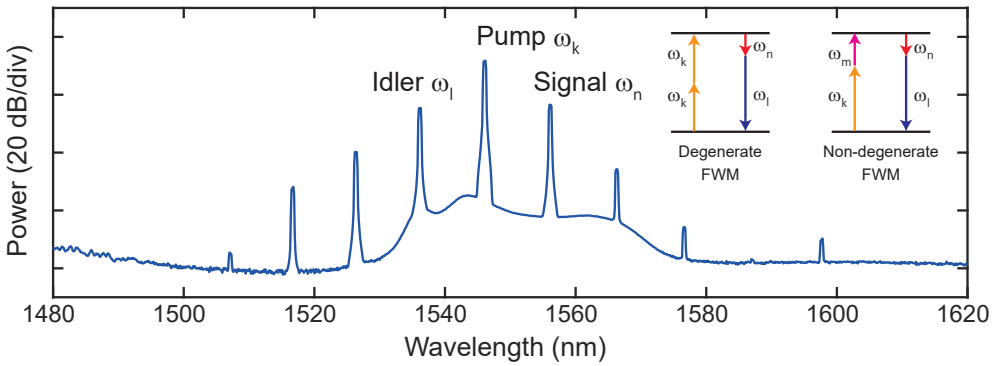

Fig. 2.13: Measured optical spectrum of FWM in a silica microtoroid. Pump light creates primary signal and idler photons via degenerate FWM process, and subsequently sidebands are generated in cascade via non-degenerate process. The inset shows the energy diagram of degenerate and non-degenerate FWM.

Third-order sum-frequency generation

Third-order sum-frequency generation (TSFG) is the phenomenon based on the annihilation of three photons at frequency $2\omega_k$ and ω_l, and the creation of new photon at frequency ω_n described in the first term in Eq. (2.30). There is the other process in which annihilated three photons at three different frequencies ω_k, ω_l, and ω_m create new photon at frequency ω_n, namely second term in Eq. (2.30). Although the number and frequency of photons are the same as the case of FWM, the difference between FWM and TSFG can be seen in the wavevectors.

Third harmonic generation

Third-harmonic generation (THG) occurs when parametric conversion satisfies the condition of Eq. (2.31). Pump light at frequency ω_k is converted into triple-frequency light of $3\omega_k$, where the phase-matching condition is satisfied. THG can be simply interpreted as the combination of three same frequencies in the case of TSFG. Figure 2.14 shows the observed spectra of the pump and THG light.

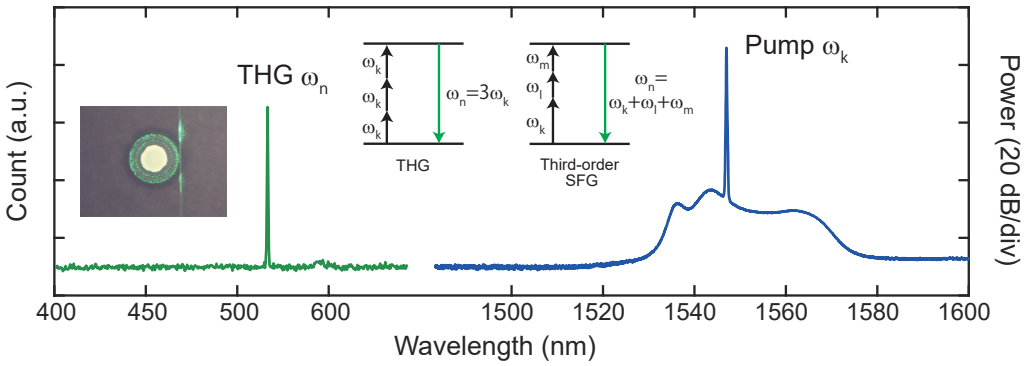

Fig. 2.14: Observed third-harmonic light at 516 nm generated from pump light at 1548 nm in a silica microtoroid. The inset picture shows the captured image with a top camera. The energy diagram of THG and TSFG are also shown in the inset.

Stimulated Raman scattering

Stimulated Raman scattering (SRS) is an inelastic scattering process where photons of pump field ω_p interact with optical phonons Ω_R. In contrast to the Kerr effect, the mechanism of SRS is attributed to the molecular vibration inside the material. SRS can be explained as a nonlinear phenomenon in which the Stokes light multiplies inside the medium under the strong pump condition. It exists in all the dielectric materials, including crystals with all symmetries and glasses, and therefore SRS is a non-negligible optical nonlinear process when describing third-order nonlinear effects in optical microresonators. The energy conservation of SRS can be written as,

$$\omega_S = \omega_p - \Omega_R \tag{2.36}$$

where ω_S and ω_p, respectively, are a Stokes and pump photon, and Ω_R is known as the Raman shift (Stokes shift). The Raman shift Ω_R is typically on the order of 10 THz, and the bandwidth of Raman gain in silica is also large (up to 40 THz), whereas the bandwidth can be much narrower in crystalline materials ($\sim$1 THz). Moreover, SRS is not a parametric process in contrast to FWM and can be generated in both clockwise and counter-clockwise directions. The threshold power

for SRS under the critical coupling condition can be expressed as [97],

$$P_{\text{th}}^{\text{SRS}} \approx \frac{2\pi^2 n^2 V_{\text{eff}}}{g_{\text{R(max)}} \lambda_p \lambda_R Q_p Q_R}, \tag{2.37}$$

where $g_{\text{R(max)}}$ is the maximum Raman gain in units of m/W, λ_p and λ_R are the wavelengths of the pump and Raman modes, Q_p and Q_R are the loaded Q-factor of the pump and Raman modes, respectively. In a fused silica, $g_{\text{R(max)}}$ and Ω_R are approximately 0.6×10^{-13} m/W and 13 THz, respectively. Figure 2.15(a) shows the cascaded SRS light, where each frequency shift corresponds to ∼13 THz, in a silica microresonator. Also, an SRS process can coexist along with FWM generation in the vicinity of the pump [Fig. 2.15(b)]

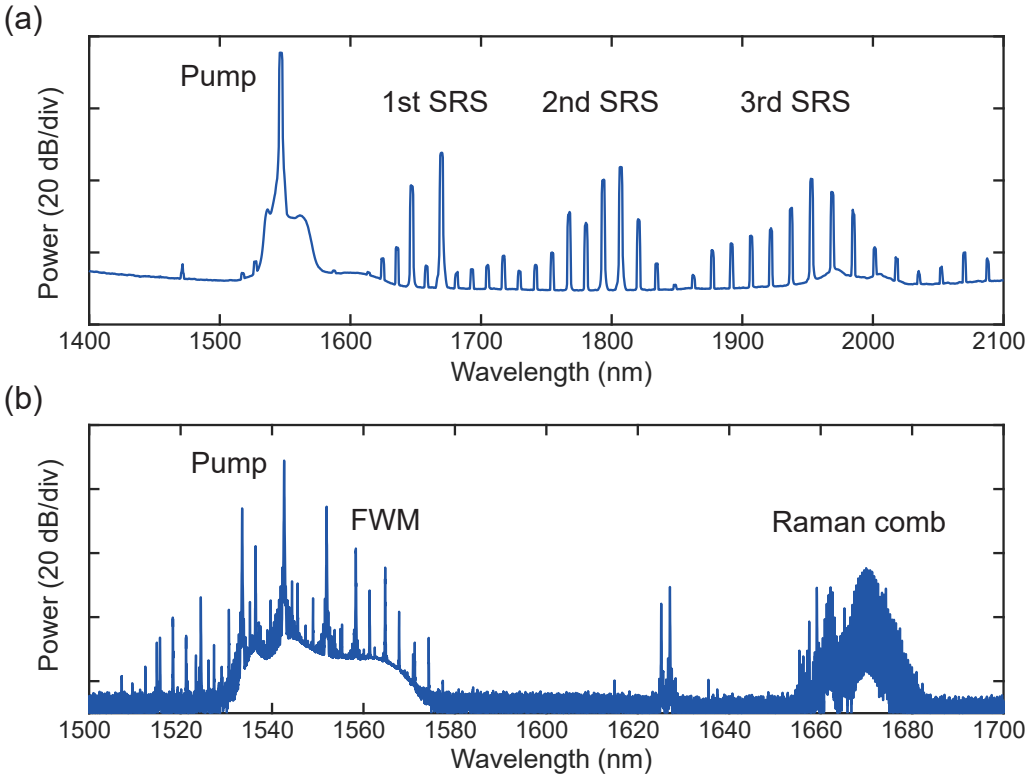

Fig. 2.15: (a) Measured optical spectrum of SRS in a silica toroid microresonator in which cascaded SRS processes are observed. The frequency shift of 1st SRS corresponds to the Raman gain peak at around 13 THz. (b) Observed optical spectrum in a silica rod microresonator. The 1st Raman gain forms an SRS envelope at around 1670 nm, and FWM is simultaneously observed in the vicinity of the pump.

Stimulated Brillouin scattering

Brillouin scattering (SBS) is also an inelastic scattering where acoustic phonons Ω_B take part in the interaction with photons ω_p. The pump light induces a

traveling density wave, which acts as a refractive index grating and scatters the pump laser in a preferable direction (usually 1st Stokes of SBS can be scattered backward). The pump field and induced Stokes fields inside the cavity can be enhanced in a way shown in the following energy diagram,

$$\omega_S = \omega_p - \Omega_B \tag{2.38}$$

where Ω_B is called the Brillouin shift. The Brillouin shift is typically 10 GHz order (e.g., 11 GHz for silica). However, the bandwidth of SBS is very narrow ($\sim$100 MHz) compared to SRS. The threshold power for SBS is given similar to the SRS case [98],

$$P_{\text{th}}^{\text{SBS}} \approx \frac{2\pi^2 n^2 V_{\text{eff}}}{g_{\text{B(max)}} \lambda_p \lambda_B Q_p Q_B}, \tag{2.39}$$

where $g_{\text{B(max)}}$ is the maximum Brillouin gain (e.g., 4.5×10^{-11} m/W for silica), λ_B and Q_B are the wavelength and Q-factor of Brillouin mode, respectively.

Competition and interaction of third-order nonlinearities

In practice, third-order nonlinearities compete and coexist inside the microresonator since the circulating power reaches the threshold and satisfies the phase-matching condition simultaneously. Cascaded and simultaneous frequency conversion processes enable us to generate new light covering a broad bandwidth. The nonlinear processes in optical microresonators are mutually resonant, hence appear as discrete frequency components. In this thesis, the phenomenon described in Chapter 5 is based on the interaction between FWM, THG, and TSFG. In addition to the coexistence of nonlinear interactions, the gain competition is a unique feature in optical microresonators, particularly between Kerr effects and Raman effects. While these processes can coexist in microresonators, the gain competition and thereby the switching occurs in a relatively large-FSR microresonator due to a broad Raman gain in fused silica. As shown in Fig. 2.16, the FWM gain is shifted with increasing the pump power, whereas the position of Raman gain is insensitive to the pump; the difference induces the gain competition and switching in a microresonator system. The investigation on the gain competition in a silica microtoroid is presented in Appendix. A in more detail. Figure 2.17 shows experimentally observed optical spectra in silica microresonators. The coexistence of third-order nonlinearities brings a variety of observed spectra with the only single-frequency pump.

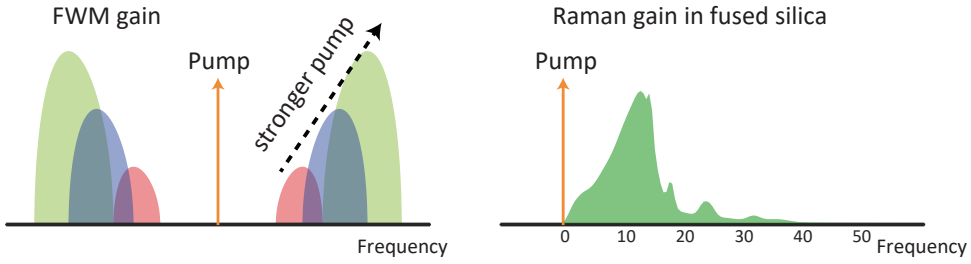

Fig. 2.16: Comparison of FWM gain and Raman gain in fused silica. The gain peak of FWM shifts away from the pump frequency with increasing pump power, but the Raman shift is insensitive to the pump power. The gain competition originates from the difference of the gain profiles.

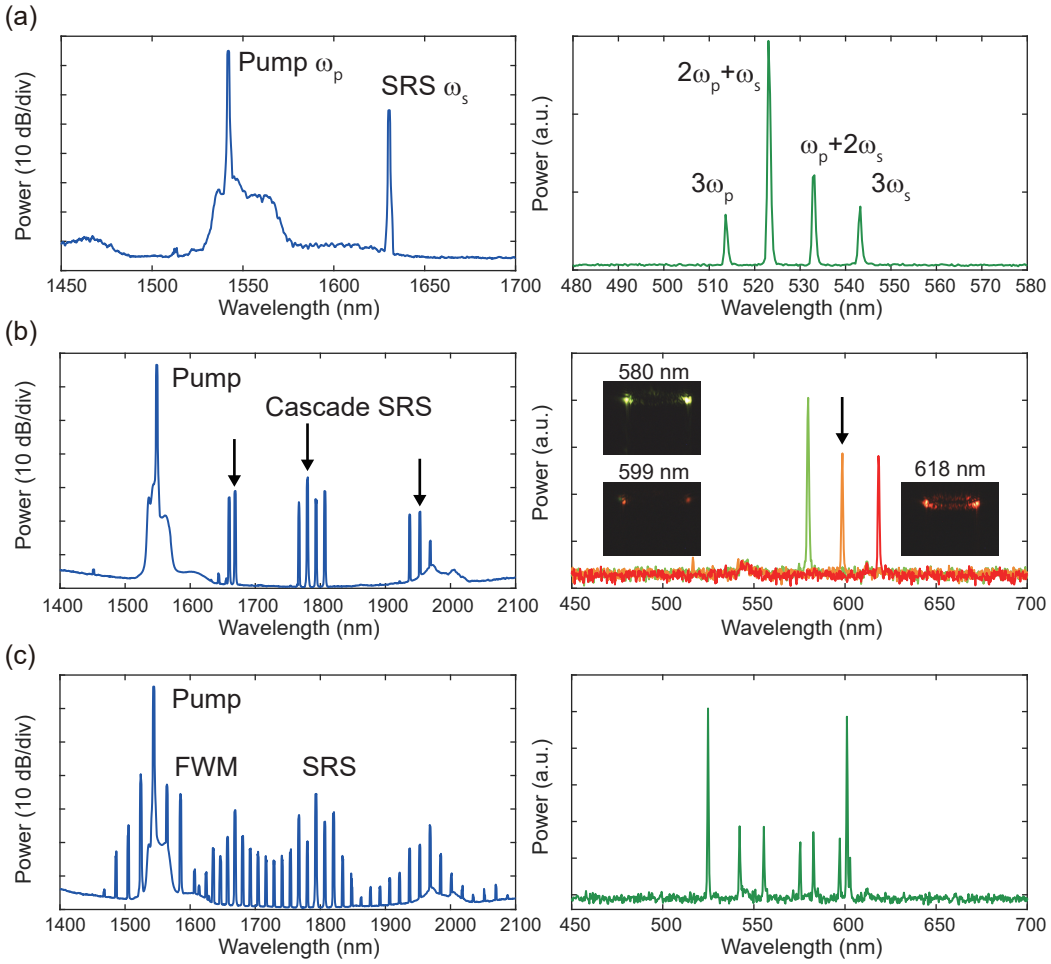

Fig. 2.17: Experimentally observed optical spectra in silica microtoroids. (a) Equidistant THG and TSFG as generated from the pump and SRS light. (b) Cascaded SRS generates multi-color visible light via TSFG. (c) The broad visible light generated from the nonlinear interaction of FWM and SRS in near-infrared regime.

2.2.2 Thermal nonlinearity in optical microresonators

Thermal resonance shift

Stored light inside the resonators heats them up as a result of thermal loss in the same manner as other energy dissipation systems. Thermal effects cannot be neglected in optical microresonators, and have strong influences on resonance shift and stability of the microresonator system. When a high power pump laser is scanned across the resonance, the Lorentzian shaped resonance is distorted by the thermal effects [99]. In particular, when the laser scan is performed from a shorter wavelength (a higher frequency) to a longer wavelength (a lower frequency), the resonance exhibits triangular-shaped transmission instead of Lorentzian resonance dip as shown in Fig. 2.18. This phenomenon indicates that the resonance is pushed by the scanning laser from the original position and suddenly comes back when the laser crosses over the shifted resonance. Such a triangular thermal shift can be observed with a higher pump power experiment and used to stabilize optical coupling, called thermal self-locking described later.

The thermal shift occurs as the result of two contributions, namely thermo-optic and thermal expansion effect. Former effect originates from the change of effective refractive index by the heat (dn/dT), and latter one induces the change of cavity length (dL/dT). The thermal wavelength shift can be estimated as,

$$\Delta\lambda_m \approx \frac{nL}{m}\left(\frac{\Delta L}{L}+\frac{\Delta n}{n}\right)=\lambda_m\left(\frac{1}{L}\frac{dL}{dT}\Delta T+\frac{1}{n}\frac{dn}{dT}\Delta T\right), \tag{2.40}$$

where ΔT represents the induced temperature change of the resonator material.

Thermal stability and instability

As the thermal shift follows Eq. (2.40), the value and sign of thermal coefficients play a critical role in the stability of thermal-locking. In many cases, for commonly-used resonator materials (e.g., silica, MgF_2, Si_3N_4), both thermal coefficients are positive, which means that thermal locking can be achieved in the blue-detuned regime (i.e., pump laser is in the shorter wavelength regime against the resonance). However, for the thermal locking, it should be noted that the laser has to be swept from a shorter wavelength (a higher frequency) side due to the thermal bistability. On the other hand, self-thermal oscillation often happens if two thermal coefficients of the resonator have the opposite sign [100], for instance, PDMS-coated silica, CaF_2, and BaF_2 crystal. Figure 2.19 shows experimentally observed self-thermal oscillation. These features make it challenging to employ the self-thermal locking technique; therefore, another external locking is necessary to stabilize the optical coupling.

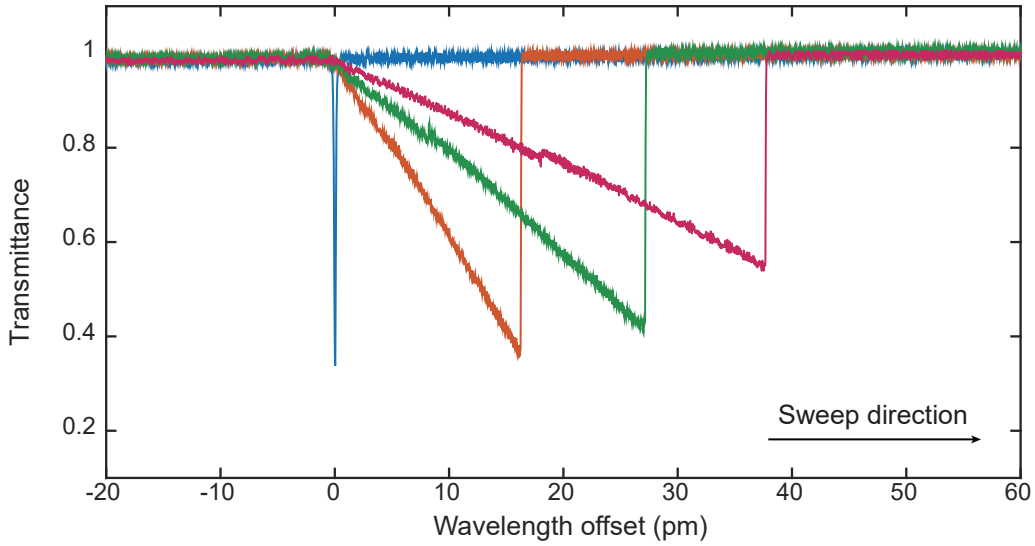

Fig. 2.18: Observed transmission spectra showing thermal resonance shift (thermal triangle) when increasing the input power in a silica microtoroid. During a laser scan from the blue-side, the optical resonance undergoes an effective resonance shift towards the red-side due to the thermal effect and Kerr effect.

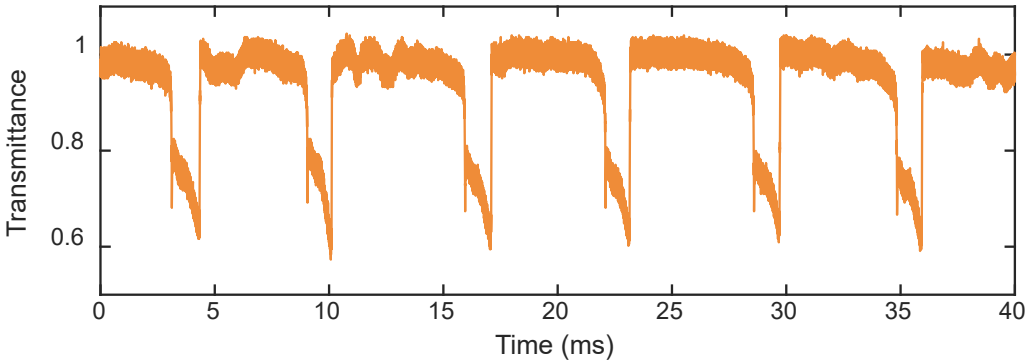

Fig. 2.19: Experimentally observed self-thermal oscillation in a CaF_2 resonator. Even though a pump frequency is kept constant value, the transmission exhibits oscillatory behavior due to the thermal instability. The oscillation period and waveform are sensitive to the coupled power to the resonator.

2.3 Optical frequency comb

2.3.1 Optical frequency comb in mode-locked lasers

A passively mode-locked laser is one of the most conventional optical frequency comb generators by means of a gain medium and a saturable absorber inside the laser cavity [101, 102]. When a pumped gain medium yields an intracavity modulation as a result of laser operation, a saturable absorber exhibits an intensity-dependent transmission. In general, a saturable absorber transmits a high-intensity component of circulating pulse; nevertheless, it absorbs low-intensity light, which corresponds to the foot region of the optical pulse. Such a filtering operation enables us to passively shape the optical pulse with an ultrashort duration on the order of picoseconds or femtoseconds. Schematics of an optical frequency comb in mode-locked lasers are depicted in Fig. 2.20.

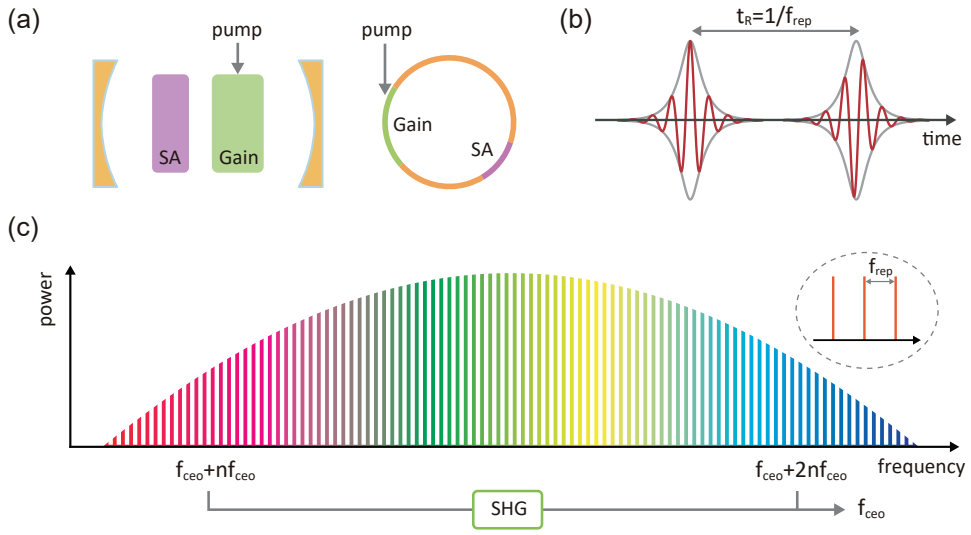

Fig. 2.20: (a) Schematics of conventional mode-locked lasers. The cavity consists of the gain medium, which is externally pumped for lasing operation, and a saturable absorber (SA), working as a passive mode-locker. (b) Optical pulse train generated in a mode-locked laser. A pulse repetition rate of f_{rep} corresponds to the inverse of a round-trip time t_R, and the offset phase shift as regards the pulse envelope is also given by the carrier-envelope offset of f_{ceo}. The red line corresponds to the electric field, and the gray line represents the pulse envelope. (c) A frequency comb spectrum of the mode-locked laser. The comb spectrum and the pulse train of (b) can be mathematically converted by Fourier transform; hence the properties such as the bandwidth and mode spacing are characterized by one-to-one relation. The $f-2f$ self-referencing method to detect the offset frequency of f_{ceo} is realized by generating second harmonics of the low-frequency component of f_n and then mixing with the high-frequency component of f_{2n}.

An optical frequency of frequency comb is defined as,

$$f_m = f_{\mathrm{ceo}} + m f_{\mathrm{rep}}, \tag{2.41}$$

where m is the integer, f_{ceo} and f_{rep} represent the carrier envelope offset frequency and pulse repetition frequency, respectively. The pulse repetition equals the frequency spacing of comb lines, namely the cavity FSR. The offset frequency f_{ceo} can be interpreted as the frequency of the "first" comb line. The repetition frequency f_{rep} is directly measurable with a fast photodetector because the RF beatnote of the overall frequency comb gives the information of f_{rep}. On the other hand, the f_{ceo} measurement is a challenge since f_{ceo} does not appear in the beat signal. However, it has been possible to determine f_{ceo} when the comb bandwidth exceeds one-octave by means of the useful method referred to as $f-2f$ self-referencing [29,30,103]. The lower frequency of the octave spanning comb f_n is converted to a doubled frequency $2f_n$ via second-harmonic generation. When the harmonic light and filtered higher frequency f_{2n} are mixed with a photodetector, the beat signal corresponds to the f_{ceo} as,

$$2f_n - f_{2n} = 2(nf_{\mathrm{rep}} + f_{\mathrm{ceo}}) - (2nf_{\mathrm{rep}} + f_{\mathrm{ceo}}) = f_{\mathrm{ceo}}. \tag{2.42}$$

In practice, an offset frequency can be detected by the $2f$-$3f$ method, which modifies the requirement of octave-spanning. The frequency comb is usually stabilized by locking the two frequencies (i.e., f_{ceo} and f_{rep}) to an external reference clock for the reason of frequency stability and accuracy [103].

Besides the passive mode-locking comb, there have been many developments regarding frequency comb generation. An electro-optic (EO) modulator enables the generation of optical sidebands by amplitude or phase modulation of CW laser, so-called EO comb [104]. Since a modulation frequency is controlled by an external signal generator, precise control of cavity length is no longer necessary; moreover, a high repetition rate (∼several tens of GHz) can be easily obtained with the EO comb. An actively mode-locked laser can be operated by using such a modulator (e.g., electro-optic modulator) instead of a saturable absorber so as to synchronize the cavity loss with the resonator round-trip.

2.3.2 Application of optical frequency combs

Optical frequency combs provide numerous applications owing to mutually coherent time-frequency properties. Excellent fractional uncertainty of 10^{-19} or lower accelerated the use of frequency combs as absolute frequency standards, and nowadays, there are various metrological applications [105]. The optical clock is based on an accurate frequency measurement of a clock laser locked to an atomic transition, and frequency combs are used for precise frequency measurement, namely, laser spectroscopy. The direct link between commonly used frequency references (e.g., cavity, atom, and quartz crystal) and frequency combs enables the improvement of the international definition of the second instead of the natural oscillations of the cesium atom [106]. Indeed, the frequency

comb was adopted in 2009 for the definition of length in Japan. In addition to the use in frequency standards, frequency combs offer direct molecular spectroscopy by exploiting the accuracy of the frequency [107], and particularly, dual-comb spectroscopy overcomes several limitations of conventional methods and is widely adopted in the present [108]. Highly desirable low-phase noise microwave oscillators are also realized by frequency down-conversion of a comb from the optical to radio-frequency domain [109]. Harmonics generated by photodetection of the comb repetition rate directly reflect the excellent phase-noise property of the frequency comb. The fact that frequency comb works as absolute frequency standards indicates the underlying nature of time, speed, and distance. In other words, the accuracy of the frequency comb is not only for the spectral domain but also for the spatial domain. Owing to its mutual relation, ranging and imaging applications have great impacts on the field of metrology.

2.4 Microresonator frequency comb

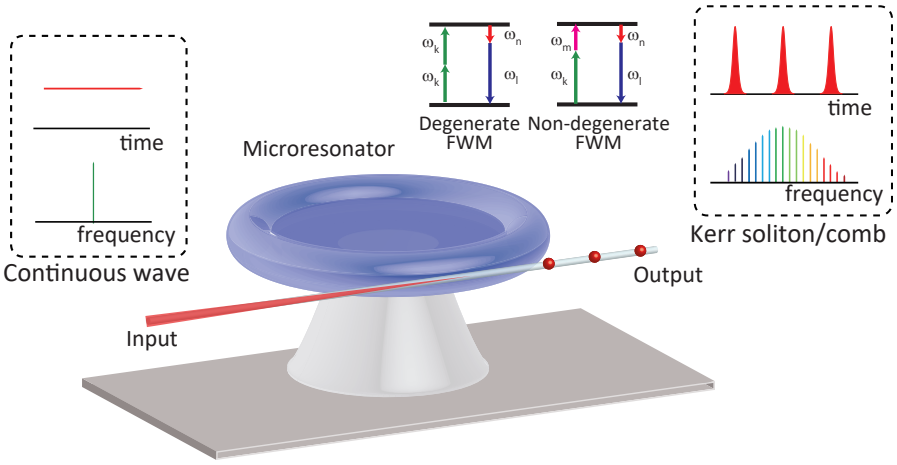

Fig. 2.21: Schematic illustration of the microresonator frequency comb generation. A dielectric microresonator is driven by a CW laser through an external coupler, and a cascade intracavity FWM process outputs the equidistant comb spectrum. The output light forms a pulse train, so-called Kerr soliton with each comb line being mode-locking.

Figure 2.21 illustrates the microresonator frequency comb generation. When a CW laser pumps a dielectric microresonator, the output corresponds to the equidistant comb spectrum, which originates from a cascaded FWM process. The following sections introduce the fundamental physical background and the experimental observation of the microresonator frequency comb. Besides, a brief explanation as regards to novel microcomb generation and applications will be presented.

2.4.1 Nonlinear coupled mode equation

The dynamics of microresonator comb formation can be described with coupled mode equations. The series of equations prepared for each comb mode describe nonlinear interactions between the large comb modes, and thus the evolution of the microresonator frequency comb [96, 110]. This approach is referred to as a nonlinear coupled mode equation (NCME) or spectrotemporal model since it tracks the evolution of individual modes in the time domain. The nonlinear coupled mode equation can be rewritten from Eq. (2.9), by taking a series of resonance modes and the Kerr effect into account,

$$\frac{d\tilde{A}_\mu(t)}{dt} = -\frac{\gamma}{2}\tilde{A}_\mu - i\omega_\mu\tilde{A}_\mu + \delta_{\mu,0}\sqrt{\gamma_{\text{ext}}}s_{\text{in}}\exp(-i\omega_p t) + ig\sum_{\mu_1,\mu_2,\mu_3}\tilde{A}_{\mu_1}\tilde{A}_{\mu_2}\tilde{A}^*_{\mu_3}, \quad (2.43)$$

where $\tilde{A}_\mu$ denotes the optical field of the μ-th comb mode, $\delta_{\mu,0}$ is the Kronecker delta function to validate the driving field (i.e., $\delta_{\mu,0} = 1$ for $\mu = 0$), g is the Kerr nonlinear coefficient given as $(\hbar\omega_0^2 c n_2)/(n_0^2 V_{\text{eff}})$, and ω_μ is the μ-th resonance angular frequency. The last term on the right hand side represents Kerr effects including SPM, XPM, and FWM. When applying a rotating frame $A_\mu(t) = \tilde{A}_\mu \exp\{j(\omega_p + \mu D_1)t\}$, Eq. (2.43) is transformed to,

$$\begin{aligned}\frac{dA_\mu(t)}{dt} = -\frac{\gamma}{2}A_\mu - i(\omega_\mu - \omega_p - \mu D_1)A_\mu + \delta_{\mu,0}\sqrt{\gamma_{\text{ext}}}A_{\text{in}} \\ + ig\sum_{\mu_1,\mu_2,\mu_3}\delta_{\mu-(\mu_1+\mu_2-\mu_3)}A_{\mu_1}A_{\mu_2}A^*_{\mu_3}.\end{aligned} \quad (2.44)$$

The delta function in the nonlinear term stands for the requirement of energy conservation to satisfy the relation $\mu = \mu_1 + \mu_2 - \mu_3$. The driving term $A_{\text{in}} = \sqrt{P_{\text{in}}/\hbar\omega_p}$ stands for the square root of input photon flux, and P_{in} denotes the pump power in watts. Therefore, Eq. (2.44) can be generalized as,

$$\frac{dA_\mu(t)}{dt} = -\frac{\gamma}{2}A_\mu - j(\omega_\mu - \omega_p - \mu D_1)A_\mu + \delta_{\mu,0}\sqrt{\gamma_{\text{ext}}}A_{\text{in}} + jg\sum_{\mu_1,\mu_2}A_{\mu_1}A_{\mu_2}A^*_{\mu_1+\mu_2-\mu}. \quad (2.45)$$

The second term on the right hand side includes both the dispersion term $D_{\text{int}} = (\omega_\mu - \omega_0 - \mu D_1)$ and the pump detuning term $\delta_0 = (\omega_0 - \omega_p)$.

2.4.2 Lugiato-Lefever equation

Instead of considering time domain dynamics of individual modes, the comb formation can be described by tracking the overall intracavity field along the circumference of the resonator, namely the position in the azimuthal coordinate ϕ. This alternative approach is called the spatiotemporal model, which is essentially governed by the Lugiato-Lefever equation [111, 112]. The spatiotemporal

intracavity field $A(\phi,t)$ relates to the optical field of each comb mode $A_\mu(t)$ by a discrete Fourier transform,

$$A(\phi,t)=\sum_\mu A_\mu(t)\exp(j\mu\phi), \tag{2.46}$$

where $A(\phi,t)$ satisfies a periodic boundary condition $A(\phi,t)=A(\phi+2\pi,t)$. Equation (2.45) is transformed into the Lugiato-Lefever equation by taking Eq. (2.46) into account,

$$\begin{aligned}\frac{\partial A(\phi,t)}{\partial t}&=\sum_\mu \frac{\partial A_\mu(t)\exp(i\mu\phi)}{\partial t}\\&=-\frac{\gamma}{2}A_\mu\exp(i\mu\phi)-i\delta_0\sum_\mu A_\mu\exp(i\mu\phi)-i\sum_\mu D_{\text{int}}A_\mu\exp(i\mu\phi)\\&\quad+\sqrt{\gamma_{\text{ext}}}A_{\text{in}}+ig\sum_\mu\sum_{\mu_1,\mu_2}A_{\mu_1}A_{\mu_2}A^*_{\mu_1+\mu_2-\mu}\exp(i\mu\phi).\end{aligned} \tag{2.47}$$

Equation (2.47) can be simplified using Eq. (2.46) as,

$$\frac{\partial A(\phi,t)}{\partial t}=-\left(\frac{\gamma}{2}+i\delta_0\right)A-i\sum_{k\geq 2}\frac{D_k}{k!}\left(\frac{\partial}{i\partial\phi}\right)^k A+ig|A|^2A+\sqrt{\gamma_{\text{ext}}}A_{\text{in}}. \tag{2.48}$$

A nonlinear partial differential equation of the form in Eq. (2.48) is equivalent to the general form of the Lugiato-Lefever Equation (LLE) proposed in 1987 [113]. It should be noted that the LLE can be written in a different timescale, called fast time, instead of the azimuthal coordinate. The fast time coordinate $\tilde{t}$ can be replaced by the relation $\tilde{t}=-\phi/D_1$, standing for the relative position of the circulating waveform. They are strictly equivalent in terms of physical understanding, whereas the fast time approach has been developed from the point of view of nonlinear fiber optics.

A master equation for the LLE can be modified in order to consider other nonlinear effects, for instance Raman effect and self-steepening effect [114]. As opposed to the Kerr effect, which is the quasi-instantaneous electronic response, the Raman effect is delayed relative to the incident field owing to the molecular response (non-instantaneous). Therefore, the nonlinear response can be expressed as a function of the fast time coordinate $\tilde{t}$ as [115],

$$R(\tilde{t})=(1-f_R)\delta(\tilde{t})+f_Rh_R(\tilde{t}), \tag{2.49}$$

where f_R is the Raman fractional coefficient, $\delta(\tilde{t})$ is the Kronecker delta, and $h_R(t)$ is the impulse Raman response, which is given as

$$h_R(\tilde{t})=\frac{\tau_1^2+\tau_2^2}{\tau_1\tau_2^2}\exp\left(-\frac{\tilde{t}}{\tau_2}\right)\sin\left(\frac{\tilde{t}}{\tau_1}\right). \tag{2.50}$$

Here, τ_1 and τ_2 represent an inverse Stokes shift $(1/\Omega_R)$ and inverse FWHM bandwidth of Raman gain $(1/\Delta\Omega_R)$ of the material, respectively. Hence, an LLE including the Raman effect is expressed as,

$$\begin{aligned}\frac{\partial A(\phi,t)}{\partial t} = &-\left(\frac{\gamma}{2}+i\delta_0\right)A - i\sum_{k\geq 2}\frac{D_k}{k!}\left(\frac{\partial}{i\partial\phi}\right)^k A \\ &+igA\int R\left(\frac{\phi'}{D_1}\right)|A(\phi-\phi')|^2 d\phi' + \sqrt{\gamma_{\text{ext}}}A_{\text{in}}.\end{aligned} \tag{2.51}$$

By replacing $R(\phi'/D_1)$ with Eq. (2.49), Eq. (2.51) can be rewritten as,

$$\begin{aligned}\frac{\partial A(\phi,t)}{\partial t} = &-\left(\frac{\gamma}{2}+i\delta_0\right)A - i\sum_{k\geq 2}\frac{D_k}{k!}\left(\frac{\partial}{i\partial\phi}\right)^k A + ig(1-f_R)|A|^2 A \\ &+igf_R A\int h_R\left(\frac{\phi'}{D_1}\right)|A(\phi-\phi')|^2 d\phi' + \sqrt{\gamma_{\text{ext}}}A_{\text{in}}.\end{aligned} \tag{2.52}$$

The self-steepening effect, which leads to a delay of pulse peak due to the change of group velocity, can be also added to the master equation Eq. (2.48) [116],

$$\begin{aligned}\frac{\partial A(\phi,t)}{\partial t} = &-\left(\frac{\gamma}{2}+i\delta_0\right)A - i\sum_{k\geq 2}\frac{D_k}{k!}\left(\frac{\partial}{i\partial\phi}\right)^k A \\ &+ig\left(1+\frac{iD_1}{\omega_p}\frac{\partial}{\partial\phi}\right)|A|^2 A + \sqrt{\gamma_{\text{ext}}}A_{\text{in}}.\end{aligned} \tag{2.53}$$

2.4.3 Microcomb generation via cascaded four-wave mixing

Theoretical description of threshold power and initial sideband generation

The primary sidebands of the microcomb are generated via degenerate FWM as the CW pump laser approaches the resonance mode from the blue detuned side. Subsequent cascaded FWM forms the microcomb, which accompanies multiple comb sidebands; nevertheless, a frequency spacing of the generated primary sidebands is determined by the condition of various parameters, including the pump power, pump detuning, dispersion, quality factor, and so on. Here, the simplified coupled-mode equations provide an analytical solution with respect to parametric gain, which critically affects the primary sideband generation [110, 117, 118].

To begin with, a nonlinear coupled mode equation of Eq. (2.45) is transformed to a dimensionless description:

$$\frac{\partial a_\mu}{\partial\tau} = -(1+i\zeta_\mu)a_\mu + i\sum_{\mu_1,\mu_2} a_{\mu_1}a_{\mu_2}a^*_{\mu_1+\mu_2-\mu} + \delta_{\mu,0}f, \tag{2.54}$$

where the normalization and the phase transformation are applied as follows: $\tau = \gamma t/2$, $d_2 = D_2/\gamma$, $\zeta_\mu = 2(\omega_\mu - \omega_p - \mu D_1)/\gamma = \zeta_0 + d_2\mu^2$, $f = \sqrt{8\eta g/\gamma^2}A_{\text{in}}$,

and $a_\mu = A_\mu\sqrt{2g/\gamma}e^{-i(\omega_\mu-\omega_p-\mu D_1)t}$. In order to consider the primary sidebands, namely the signal $a_{+\mu}$ and idler $a_{-\mu}$ light, from the pump light a_0, the sets of the linearized equation are expressed as,

$$\frac{\partial a_0}{\partial \tau} = -(1+i\zeta_\mu - 2i|a_0|^2)a_{+0} + f, \tag{2.55}$$

$$\frac{\partial a_{+\mu}}{\partial \tau} = -(1+i\zeta_\mu - 2i|a_0|^2)a_{+\mu} + ia_0^2 a_{-\mu}^*, \tag{2.56}$$

$$\frac{\partial a_{-\mu}^*}{\partial \tau} = -(1-i\zeta_\mu - 2i|a_0|^2)a_{-\mu}^* - ia_0^{*2} a_{+\mu}, \tag{2.57}$$

where the later two equations yield the eigenvalues:

$$\lambda = -1 \pm \sqrt{|a_0|^4 - (\zeta_\mu - 2|a_0|^2)^2}. \tag{2.58}$$

The positive real part of the eignenvalue corresponds to the parametric gain, and thus the net gain $G = \gamma\sqrt{|a_0|^4 - (\zeta_\mu - 2|a_0|^2)^2}$ has to exceed the cavity loss γ for the parametric oscillation. This relation yields the required minimum power in the pump mode as $|a_0|^2 = 1$, which is always satisfied under laser detuning $\zeta_0 \leq 1$. Next, the steady state solution ($\partial a_0/\partial\tau = 0$) for the pump mode can be described as,

$$(\zeta_0 - |a_0|^2)^2|a_0|^2 + |a_0|^2 = f^2, \tag{2.59}$$

which gives the critical condition with respect to pump power $f^2 = 1$ (i.e., $|a_0|^2 = 1$ and $\zeta_0 = 1$), to be $P_{\text{in}} = (\gamma^2 n^2 V_{\text{eff}})/(8\eta\omega_0 c n_2)$ as defined in Eq. (2.35).

From Eq. (2.59), a laser detuning is expressed as a function of intracavity threshold power $|a_0|^2$:

$$\zeta_0 = |a_0|^2 - \sqrt{f^2/|a_0^2| - 1}. \tag{2.60}$$

Finally, by substituting $\zeta_0 = \zeta_\mu - d_2\mu^2$ at the threshold value of parametric gain, the mode number of the primary sideband is derived as [117],

$$\mu_{\text{th}} = \sqrt{\frac{\gamma}{D_2}\left(\sqrt{\frac{P_{\text{in}}}{P_{\text{th}}} - 1} + 1\right)}. \tag{2.61}$$

Microcomb formation dynamics: the stability and noise

The initial sidebands are generated via degenerate FWM, as described above. Meanwhile, multiple comb sidebands and subsequent broad microcomb evolve via cascaded FWM when driving the resonator with a CW pumping. A pump laser is tuned into a pump resonance from a blue-detuned side to a red-detuned side to achieve stable microcomb generation owing to the self-thermal locking [99]. When approaching zero-detuning, the intracavity power is gradually enhanced,

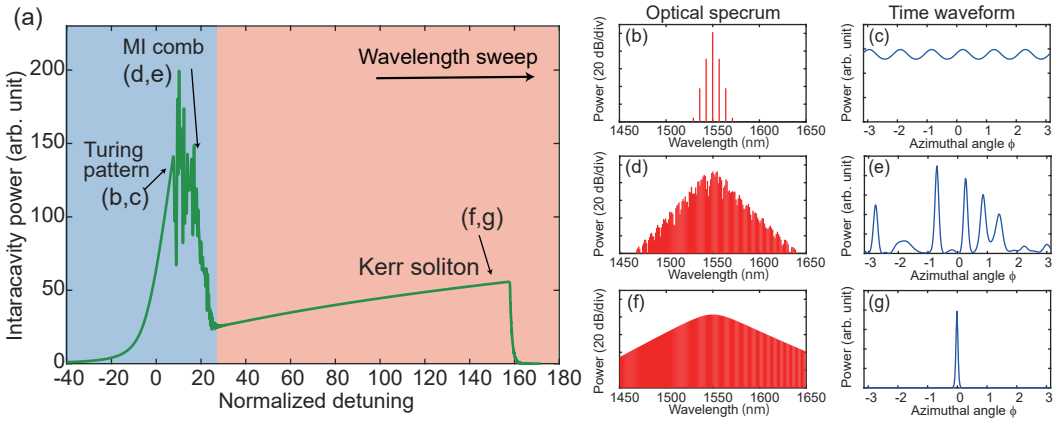

Fig. 2.22: Numerically simulated microcomb formation with laser sweeping. The calculation parameters are as follows: $\gamma = 12.1$ MHz, $\gamma_{\text{ext}} = 6.07$ MHz, $\lambda_p = 1550$ nm, $D_1/2\pi = 145$ GHz, $D_2/2\pi = 550$ kHz, $A_{\text{eff}} = 40$ μm, $n_0 = 1.44$, $n_2 = 2.2 \times 10^{-20}$ m^2/W, and $P_{\text{in}} = 70$ mW. (a) Intracavity power as a function of pump detuning. The blue-shaded and red-shaded area indicate effectively blue-detuned and effectively re-detuned region, respectively. (b, c) Optical spectrum and temporal waveform of Turing pattern comb. (d, e) Corresponding spectrum and waveform of MI comb. (f, g) Corresponding spectrum and waveform of Kerr soliton comb.

resulting in the growing parametric gain. The formation dynamics of microcombs have been studied enough in many earlier works, which provided a detailed understanding with respect to the stability as well as noise formation during microcomb evolution [38, 117, 119]. Here, simple and brief discussions will be introduced as limiting the scope on a more important part for understanding the physics of microcomb.

The primary sidebands are initially generated with a single or multiple-FSR at the effectively blue-detuned region. In this case, the optical spectrum and corresponding time-domain waveform show the symmetric and ordered pattern, so-called Turing pattern (roll) comb. Figure 2.22 represents a numerical simulation showing microcomb formation dynamics during the commonly used laser sweeping method. The Turing pattern is shown in Figs. 2.22(b) and 2.22(c). The higher intracavity power circulates inside the resonator, the more subcombs are subsequently generated while approaching the effectively zero-detuning. Then, the state transits into a chaotic state referred to as a modulation instability (MI) comb due to cascaded subcomb formation, which leads to a broad beatnote in the RF domain. This is a low coherence and high noise comb [Figs. 2.22(d) and 2.22(e)]. Further detuning, however, enables the ultrasmooth spectral comb state at the effectively red-detuned region, and the state is understood to be a dissipative Kerr soliton, as shown in Figs. 2.22(f) and 2.22(g). Kerr soliton is characterized by its high coherence and stability since it is inherently the mode-locked state where the soliton pulse propagates inside the resonator, hence ad-

vantageous for many applications. More details of Kerr solitons are described later. The point, with respect to the stability and noise, is that the Kerr soliton state is considered to be desirable rather than the MI comb, and intensive investigations on soliton formation have been conducted thus far.

Experimental observation of microcomb formation

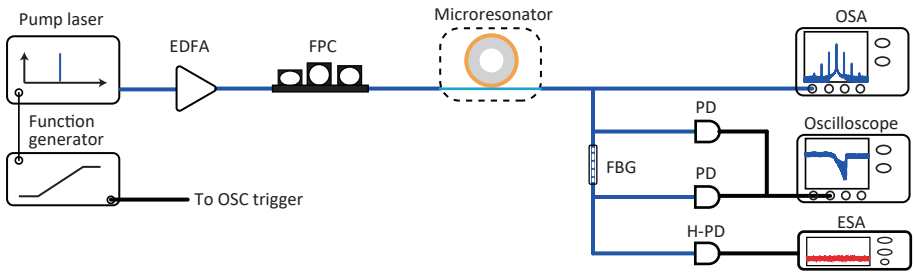

Fig. 2.23: Experimental setup for the microcomb observation. The pump laser frequency is controlled by a ramp signal from a function generator. EDFA, erbium doped fiber amplifier; FPC, fiber polarization controller; OSA, optical spectrum analyzer; ESA, electrical spectrum analyzer; (H)-PD, (High-speed) Photodetector, FBG, fiber Bragg grating.

A commonly used experimental setup for microcomb observation is shown in Fig. 2.23. A pump frequency of a narrow-linewidth CW laser is externally controlled by using a function generator to generate a microresonator frequency comb. The laser power is usually amplified with an optical amplifier, an erbium-doped fiber amplifier (EDFA) for telecom wavelength, and evanescently coupled via an external coupler. A fiber polarization controller (FPC) adjusts the laser polarization in order to excite a desired mode. The transmitted light is monitored by using an optical spectrum analyzer (OSA) and photodetectors (PD) connected to an oscilloscope (OSC) and an electric spectrum analyzer (ESA), which allows us to monitor the transmission and the RF beatnote, respectively. In order to monitor only the comb power, a fiber Bragg grating (FBG) filter is used to exclude the transmitted pump light. A ramp function is often applied to the laser frequency to be scanned, enabling continuous microcomb formation from the blue-detuned region to the red-detuned region.

Figure 2.24 presents the continuous evolution of the microcomb spectrum in a 16.6 GHz FSR MgF_2 resonator while tuning the pump into the resonance. A multiple-mode spaced comb and subsequent subcombs were generated with further detuning, and the comb finally settled into a characteristic, *stratovolcano-like*, MI comb spectrum. Figure 2.25 shows the experimentally observed micocomb spectrum in various platforms. It should be noted that all these combs are operated in the effectively blue-detuned region, namely MI comb. The comb can be stably operated for a long time owing to self-thermal locking, but coherence and noise properties are inherently not good, as described in the previous

section.

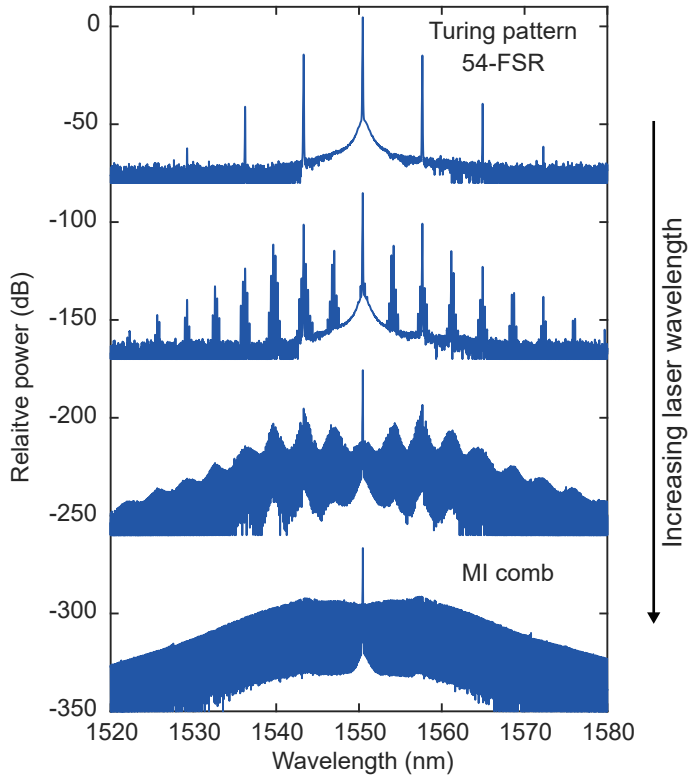

Fig. 2.24: Evolution of the microcomb spectrum in a 16.6 GHz FSR MgF_2 resonator while increasing the pump wavelength with a pump power of 300 mW. Through the generation of Turing pattern comb and subcomb formation, a comb spectrum finally settled into a *stratovolcano-like* MI comb.

2.4.4 Temporal dissipative Kerr soliton formation

Theoretical description of a single soliton solution in microresonators

The analytical solution of a temporal soliton can be derived from an LLE [cf. Eq. (2.48)] in which the loss and external pump terms are excluded, and only second-order dispersion D_2 is taken into account [41]:

$$\frac{\partial A(\phi,t)}{\partial t} - i\frac{D_2}{2}\frac{\partial^2 A}{\partial \phi^2} - ig|A|^2A + i\delta_0 A = 0. \tag{2.62}$$

As the steady-state solution for temporal soliton, the following form is assumed,

$$A(\phi) = B\,\mathrm{sech}(\phi/\phi_s), \tag{2.63}$$

where B and ϕ_s represent the soliton amplitude and pulse width in the azimuthal coordinate, respectively. Then, Eq. (2.62) can be transformed by in-

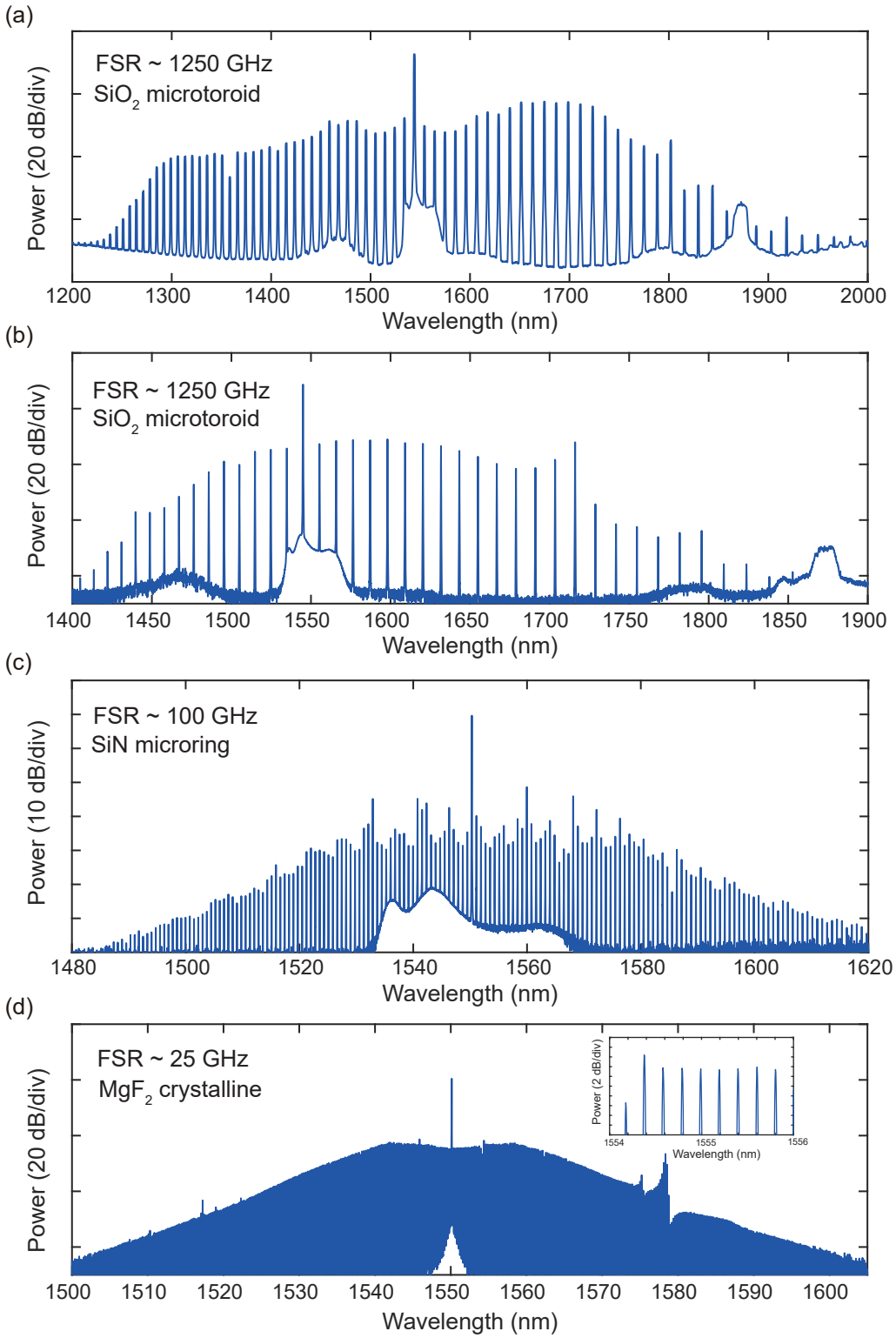

Fig. 2.25: The microresonator frequency comb generation in different platforms and mode spacings. (a) and (b) Two different SiO_2 microtoroids, (c) Si_3N_4 microring, and (d) MgF_2 crystalline microresonator. Inset shows the magnification view from 1554 nm to 1556 nm.

serting Eq. (2.63) as follows:

$$\frac{D_2}{2\phi_s^2}[1-2\mathrm{sech}^2(\phi/\phi_s)]+gB^2\mathrm{sech}^2(\phi/\phi_s)-\delta_0=0. \tag{2.64}$$

Here, the transformed LLE gives the fruitful stationary soliton condition with respect to the dispersion and pump detuning as,

$$D_2 = gB^2\phi_s^2, \tag{2.65}$$

$$\delta_0 = \frac{D_2}{2\phi_s^2} = \frac{gB^2}{2}. \tag{2.66}$$

The above relations can be interpreted as the balance between Kerr nonlinearity, dispersion and pump detuning. Moreover, they indicate that the soliton exists under the condition both of anomalous dispersion ($D_2 > 0$) and a red-detuned pump laser ($\delta_0 > 0$).

The soliton power and pulse duration can be expressed as [42],

$$P_s = \frac{2\eta A_{\mathrm{eff}}}{n_2 Q}\sqrt{-2nc\beta_2\delta_0}, \tag{2.67}$$

$$\tau_s = \sqrt{-\frac{c\beta_2}{2n\delta_0}}, \tag{2.68}$$

where $\beta_2 = -nD_2/cD_1^2$ stands for the group velocity dispersion. The detuning is one of the most important parameters to stabilize the soliton power for a long-term, and the servo control (feedback loop) offers an effective solution to maintain the certain detuning point. The maximum detuning value (normalized by cavity linewidth) for the soliton existence is given by $\delta_{0,\mathrm{max}} = \pi^2 P_{\mathrm{in}}/16P_{\mathrm{th}}$, which suggests that higher pump power contributes to a wider detuning range.

Experimental observation of dissipative Kerr soliton

In order to generate a soliton microcomb, the pump laser has to be positioned in the effectively red-detuned region. Owing to the bistability of nonlinear resonance shifts due to thermal and Kerr nonlinearity, the decreasing laser frequency from the blue-detuned side provides a reliable way to access the soliton existence regime, and this method was employed in the first demonstration of a temporal soliton. However, as opposed to an effectively blue-detuned region, self-stability cannot work in the red-detuned region, and it makes it difficult to obtain the soliton. Moreover, the strong thermal effect plays a critical role in the case of high pump power, and usually has a negative effect for soliton formation. Since the thermal relaxation time occurs quite slowly compared to the Kerr nonlinear shift, the effective detuning can be changed after the appearance of the thermal effect, and hence the laser immediately goes out of resonance. Therefore, it is necessary to optimize the laser tuning parameters (i.e., start/stop frequency,

sweeping speed) for the soliton self-stabilization, which is achieved when the resonator settles in the thermal equilibrium state [41].

Over the years, several methods have been proposed to circumvent thermal effect, for instance, power kicking [120, 121], fast scanning [122], and auxiliary laser pumping [123, 124]. In the power kicking method, the pump power is suddenly reduced just before the soliton formation using an intensity modulator, and it brings a resonance back to the blue-side via thermal cooling. By increasing the pump power again in a particular period (i.e., nanosecond to microsecond timescale), the soliton is thermally stabilized. When the laser scanning is operated faster than the thermal relaxation time, the nonlinear resonance does not experience the thermal effect. This method requires a significantly fast scanning speed, which is usually realized by a single sideband (SSB) modulator driven with voltage controlled oscillator (VCO). The thermal stabilization can be achieved by using the auxiliary laser. When the pump laser excites the soliton, the auxiliary laser set on a different resonance mode helps to keep the temperature of the resonator, which effectively contributes the soliton stabilization. These methods are often used for the resonator exhibiting a strong thermal effect, such as made of silica and silicon nitride. In practice, the active feedback loop is usually combined with the above methods to maintain the soliton. A servo controller provides the feedback signal for one or some of the experimental conditions (i.e., pump power, detuning, coupling). Especially, Pound-Drever-Hall (PDH) method is an effective way owing to the stability and robustness [125].

Figure 2.26 represents an experimentally observed spectrum of a dissipative Kerr soliton in a 4.2 mm diameter MgF_2 crystalline microresonator with a pump power of 270 mW. The spectral fitting of $sech^2$ envelope is indicated as the red line, yielding a 3 dB bandwidth of 2.05 THz. The transmission and comb power during soliton formation are shown in Figs. 2.27(a) and 2.27(b). A stable region (6 ms-10.5 ms) corresponds to a soliton existence range, which can be lengthened or shortened depending on the pump power, polarization, and coupling. Figures 2.27(c) and 2.27(d) show multiple traces of converted comb power that revealed the stochastic behavior of the number of solitons.

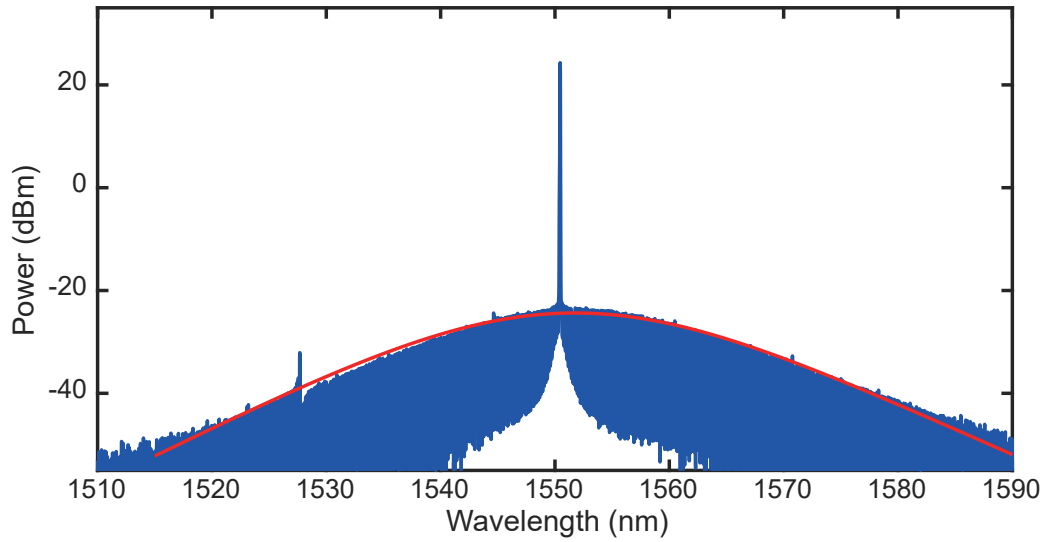

Fig. 2.26: Optical spectrum of a single temporal soliton in a 16.6 GHz FSR MgF_2 resonator. The red line represents the $sech^2$ envelope with a 3 dB bandwidth of 2.05 THz (corresponding to a pulse duration of 153 fs FWHM).

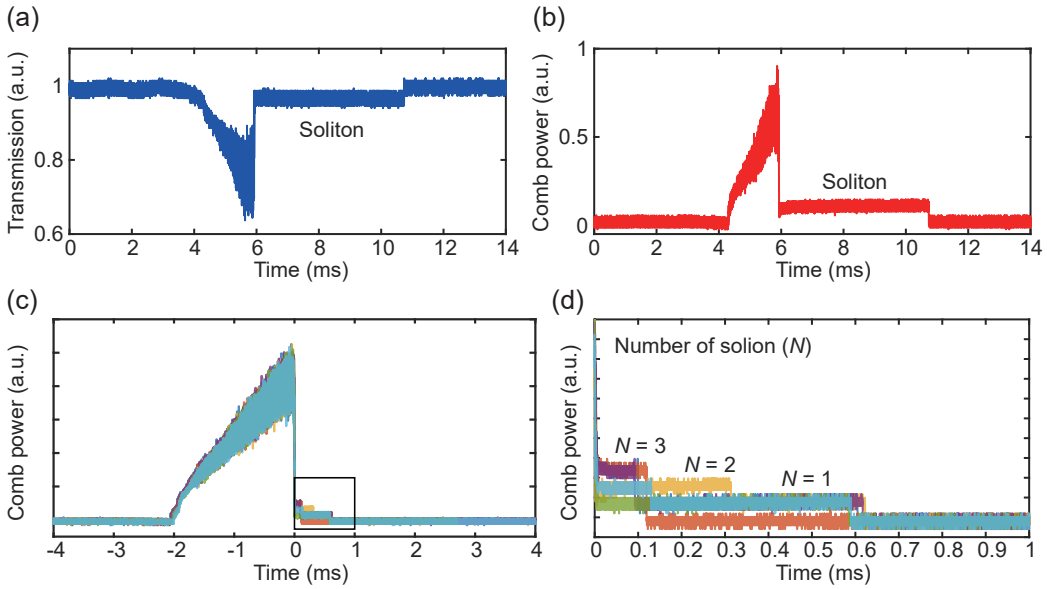

Fig. 2.27: (a), (b) Transmission and converted comb power while scanning a pump laser to generate a soliton, respectively. (c) Multiple traces of comb power, indicating a stochastic behavior of the number of solitons. (d) Magnified view of (c) from 0 ms to 1 ms, where N represents the number of solitons inside the resonator. The traces of intracavity power change for every scan due to passing through a chaotic state. The intracavity power shows discrete changes during the laser scan, the so-called soliton step.

2.4.5 Novel microresonator frequency comb

Recently, novel microcombs have been developed by considering the resonator material, the structure, and the experimental procedure. Designing and engineering microresonator dispersion is a powerful way to tailor a microcomb spectrum, and these techniques have contributed to attaining a broad bandwidth and high-efficient microcomb, even in the normal dispersion. Dispersion engineering is one of the essential subjects in this thesis, and thus intensively highlighted in Chapter 3.

The structure of the microresonator is not necessarily limited to the ring and waveguide type resonators (i.e., WGM, microring). The fiber-based Fabry-Pérot microresonators consist of a single-mode fiber with dielectric Bragg mirror coating. As opposed to CW-driven microresonators, they are driven by optical pulses and thus show great advantages regarding the efficiency and the controllability of soliton repetition rate [126].

Kerr nonlinearity enables microcomb generation via the effect of SPM, XPM and FWM, whereas the second-order nonlinearity leads to cascade parametric frequency conversion processes including optical parametric oscillation (OPO), second-harmonic and sum-frequency generation (SHG/SFG) [127]. Moreover, electro-optic (EO) phase modulation in a lithium niobate (LN) microring resonator overcomes limitations such as the comb power and the mode spacing flexibility [128]. High-Q LN resonators enable the simultaneous generation of Kerr microcombs and second-harmonic combs [47], and even the filtering and modulation of the generated comb line via inherent EO nonlinearity [129].

Even though a significant feature of a microcomb is its high-repetition-rate of pulse owing to the short round-trip length, the mode-locking in the "conventional" micro-lasers, which are based on the gain medium and saturable absorber, offer alternative approaches to realizing a high-repetition-rate mode-locked pulse oscillator. Fabry-Pérot resonators based on erbium-doped single-mode fiber [130], semiconductor saturable absorber mirror (SESAM) [131] and Kerr-lens mode-locking [132] have attained the multi-GHz repetition rate, which is almost comparable value to Kerr nonlinearity based microresonator frequency combs despite the difference of operation mechanism.

2.4.6 Application of microresonator frequency combs

Microresonator frequency combs are inherently characterized by the high repetition rates (large mode spacings), integration (compactness), low-power operation, and broadband spectral bandwidth. In particular, large mode spacing and broad bandwidth are notable advantages for some applications, which have not been sufficiently explored by conventional comb sources. In addition, a soliton microcomb expands the potential for wider application owing to the excellent spectral purity and coherence property.

For example, a microcomb can replace massively arrayed semiconductor lasers as an optical carrier source for the purpose of optical telecommunication. Wave-

length division multiplexing (WDM) is a widely used technique in coherent optical telecommunication [133, 134]; however, it demands precise wavelength alignment for each laser so as to meet the standard frequency grid, the so-called ITU-grid. The microcomb provides equally distant carriers in nature with only a single CW pump laser, and easily satisfies required channel spacing (e.g., 25 GHz, 50 GHz, and 100 GHz) by designing the resonator FSR. Notably, a soliton microcomb can be used as both the transmitter and the local oscillator at the receiver in coherent data transmission without a systematic penalty compared to parallel diode lasers.

Spectroscopy and imaging are widely used techniques in various fields, including fundamental research and industry. These applications naturally require a broadband light source such as an incoherent light emitting diode (LED), and a delayed system to interfere with the light transmitted through a sample with the reference light. Dual-comb spectroscopy significantly improves the scan rate of Fourier-transform spectroscopy owing to its high repetition rate [135, 136]. Although the resolution is restricted by the trade-off relation, the soliton microcomb enables a broadband and high acquisition rate spectroscopy platform. A microcomb generated in the mid-infrared region is of particular interest to molecular spectroscopy [137], and moreover, the visible to near-infrared wavelength around 1.3 μm is more important for biological imaging including optical coherence tomography (OCT) [138]. Recently, soliton microcombs have also been adopted to coherent laser-based distance measurement, so-called LIDAR (light detection and ranging) [139, 140].

The precisely equidistant comb lines can be adapted to the frequency calibration of the spectrometer. Especially, astronomical spectroscopy requires accurate, stable, and a large mode spacing comb because the calibration of the spectrometer is essential to detect a slight variation of stellar spectra. However, conventional comb sources have such dense mode spacing that spectrometers cannot resolve the calibration comb lines; and thus, microcombs are in high demand for astronomical calibration use, namely astrocomb [141, 142].

Soliton microcombs characterized by tens of GHz (i.e., radio-frequency domain) repetition rate have enabled the link between the microwave and the optical domains. The nonlinear spectral broadening and dispersion engineering techniques allow the direct detection of f_{ceo}; furthermore, by exploiting phase coherency of optical and microwave frequencies, many practical applications have been developed including absolute optical frequency measurement [143], optical clock [144], ultrastable microwave generation [145] and integrated optical frequency synthesizer [146].

For a wide variety of applications, the subject of comb power (intensity) cannot be avoided as regards microcombs. Since soliton power is specifically given by Eq. (2.67), it is typically estimated to be at best a few milliwatts. Indeed, the power per comb line is typically given as −40 dBm to 0 dBm, which is consistent with the measured result seen in Fig. 2.26 and elsewhere [42]. The predicted maximum power per comb line increases linearly with the repetition frequency

and inversely with the Q factor; therefore, a high-repetition rate silicon nitride resonator is considered an ideal platform in terms of comb power. On the other hand, a high Q factor greatly reduces the threshold power and the pump power required for soliton stabilization. To date, several state-of-the-art applications have been demonstrated without the amplification of a soliton comb [135,139], whereas some work has been carried out with amplification to power levels of several hundreds of milliwatts using C-band and L-band EDFAs [134,140]. Such amplification is needed to improve the signal-to-noise ratio or the measurement accuracy. However, shot noise or amplified spontaneous emission (ASE) noise from the EDFA fundamentally limits the performance in many applications. It should be noted that the typical average power of the master oscillator of a mode-locked erbium fiber laser ranges from only a few milliwatts to several tens of milliwatts [147]. In this respect, the average power of soliton microcombs is lower than that of typical fiber lasers. However, microcombs have a specific merit with respect to the power per line due to their large mode spacing.

Chapter 3

Dispersion engineering and measurement for microresonator frequency comb

This chapter describes the fundamentals of microresonator dispersion and the engineering including calculation and measurement methods for a microresonator frequency comb[*a].

3.1 Microresonator dispersion

3.1.1 Theoretical description of dispersion

Dispersion plays a critical role in microresonator frequency comb generation and in ultrafast optics. When light travels the same physical path length, dispersion originates from the frequency-dependence of the refractive index, which indicates that different frequency components experience different phase velocities (equivalent to different optical path lengths). A fundamental dispersion relation is derived from the frequency dependence of the propagation constant β of traveling light as follows [114]:

$$\begin{aligned}\beta(\omega) = \frac{\omega}{c} n(\omega) &= \sum_{m=0}^{n} \left(\frac{1}{m!} \left. \frac{d^m \beta}{d\omega^m} \right|_{\omega=\omega_0} (\omega - \omega_0)^m \right) \\ &= \beta_0 + (\omega - \omega_0)\beta_1 + \frac{1}{2}(\omega - \omega_0)^2 \beta_2 + \frac{1}{6}(\omega - \omega_0)^3 \beta_3 + \cdots,\end{aligned} \tag{3.1}$$

where ω and c are angular frequency and light speed in a vacuum, respectively. The linear term $\beta_0 = \omega_0 / v_p$ is given by the phase velocity of the center frequency v_p, and the effective index n_{eff} is also given by $n_{\text{eff}} = c/v_p$. The first order

[*a] Contents presented in this chapter has been published in "Dispersion engineering and measurement of whispering gallery mode microresonator for Kerr frequency comb generation," Nanophotonics, **9**, 5, 1087–1104 (2020).

dispersion β_1 is expressed by group velocity v_g and group index n_g as,

$$\beta_1 = \left.\frac{d\beta}{d\omega}\right|_{\omega=\omega_0} = \frac{1}{v_g} = \frac{n_g}{c} = \frac{1}{c}\left(n_{\text{eff}}(\omega) + \omega\frac{dn_{\text{eff}}}{d\omega}\right). \tag{3.2}$$

The expression as a function of wavelength λ is sometimes helpful:

$$n_g = n_{\text{eff}}(\lambda) - \lambda\frac{dn_{\text{eff}}(\lambda)}{d\lambda}. \tag{3.3}$$

The group velocity is explained as the speed of the envelope of the optical pulse (wave packet). When taking the phase shift $\varphi = \beta L$ into account, the spectral phase after the propagation through a dispersive medium of length L is given by $\Phi(\omega) = \omega t - \beta L$. By substituting Eq. (3.1), the spectral phase can be written as

$$\Phi(\omega) \equiv \omega_0\left(t - \frac{L}{v_p}\right) + (\omega - \omega_0)\left(t - \frac{L}{v_g}\right) + \cdots. \tag{3.4}$$

At the time of $t = L/v_g$, the spectral phases of all the frequency components have constant values without being dependent on frequency, which means that the envelope of optical pulse arrives with a velocity of v_g. Then, the group delay T_g is defined as the first order derivative of the phase-shift φ as,

$$T_g = \frac{d\varphi}{d\omega} = L\frac{d\beta}{d\omega} = \frac{L}{v_g} = \beta_1 L, \tag{3.5}$$

which corresponds to the propagation time of a pulse through an optical medium of length L. The second-order derivative term of Eq. (3.1) represents the change rate in the inverse group velocity in terms of frequency, which corresponds to group velocity dispersion (GVD) β_2:

$$\beta_2 = \left.\frac{d^2\beta}{d\omega^2}\right|_{\omega=\omega_0} = \frac{1}{c}\frac{dn_g}{d\omega} = \frac{1}{c}\left(2\frac{dn_{\text{eff}}}{d\omega} + \omega\frac{d^2n_{\text{eff}}}{d\omega^2}\right). \tag{3.6}$$

It is known that β_2 plays important role in nonlinear pulse propagation such as broadening of the pulse bandwidth. Moreover, the frequency dependency of the group delay is related to group delay dispersion (GDD),

$$\frac{dT_g}{d\omega} = \frac{d^2\varphi}{d\omega^2} = L\frac{d^2\beta}{d\omega^2} = \beta_2 L. \tag{3.7}$$

In addition to the GVD parameter β_2, the dispersion parameter D is a useful expression, particularly in the field of fiber optics, which is derived by the change of group delay T_g per unit length in function to wavelength as,

$$D = \frac{1}{L}\frac{dT_g}{d\lambda} = \frac{d\beta_1}{d\lambda} = \frac{1}{c}\frac{dn_g}{d\lambda} = -\frac{\lambda}{c}\frac{d^2n_{\text{eff}}}{d\lambda^2}. \tag{3.8}$$

D can be expressed with β_2 using Eq. (3.5) as follows:

$$D = \frac{1}{L}\frac{dT_g}{d\lambda} = \frac{d\beta_1}{d\lambda} = \frac{d^2\beta}{d\lambda d\omega} = \frac{d\omega}{d\lambda}\frac{d^2\beta}{d\omega^2} = -\frac{2\pi c}{\lambda^2}\beta_2. \tag{3.9}$$

It should be noted that whether to use β_2 or D to express the group velocity dispersion depends on different preferences in the research community. The parameters β_2 and D are given in units of (ps^2/km) and (ps/(km $\cdot$ nm)), respectively. As a result, the sign of the two dispersion parameters are opposite and given by "β_2>0, D<0" for normal dispersion, and "β_2<0, D>0" for anomalous dispersion. Note that the above definition of normal/anomalous dispersion gives the group velocity dispersion for a particular wavelength. The wavelength dependence of the refractive index $dn/d\lambda$ is also referred to as normal dispersion ($dn/d\lambda$<0) and anomalous dispersion ($dn/d\lambda$>0), whereas this definition does not coincide with group velocity dispersion, and it is sometimes confusing. In general, "dispersion" indicates group velocity dispersion in the community of microresonator frequency comb, and this thesis follows the definition.

3.1.2 Dispersion in optical microresonators

In contrast to optical fibers, optical resonators have discrete resonance frequencies given by,

$$f_m = \frac{mc}{2\pi R'(m)\cdot n'_{\mathrm{eff}}(m)} = \frac{mc}{2\pi R\cdot n_{\mathrm{eff}}}, \tag{3.10}$$

where f_m ($= \omega_m/2\pi$) is the resonance frequency of the m-th longitudinal mode with the azimuthal mode number m. Although the resonance frequency is already defined in Eq.2.1, the above expression provides deeper understanding in "ring"-type optical microresonators. Here it should be noted that both the effective refractive index n'_{eff} and the effective radius of the mode R' are as a function of the azimuthal mode number (frequency). The effective radius R' is usually a constant in standard waveguide devices thanks to strong mode confinement, whereas the value is depending on the frequency in WGM resonators, and this is a unique property of WGM. Nevertheless, the effect of frequency dependence of the R' is included in the frequency-dependent effective refractive index n_{eff} in practice. Therefore, n_{eff} describes the frequency-dependent value, whereas R is a constant corresponding to the actual radius of WGM resonators.

Based on the above discussion, propagation constant of m-th WGM is given as,

$$\tilde{\beta} = \frac{2\pi n_{\mathrm{eff}}}{\lambda_m} = \frac{m}{R}. \tag{3.11}$$

Consequently, the first order dispersion $\tilde{\beta}_1$ and group velocity dispersion $\tilde{\beta}_2$ are given by the free-spectral range (FSR) of the resonator Δf_m around the center mode m_0,

$$\tilde{\beta}_1 = \left.\frac{d\tilde{\beta}}{d\omega_m}\right|_{m=m_0} = \frac{1}{2\pi R}\frac{dm}{df_m} = \frac{1}{2\pi R\cdot\Delta f_m} \tag{3.12}$$

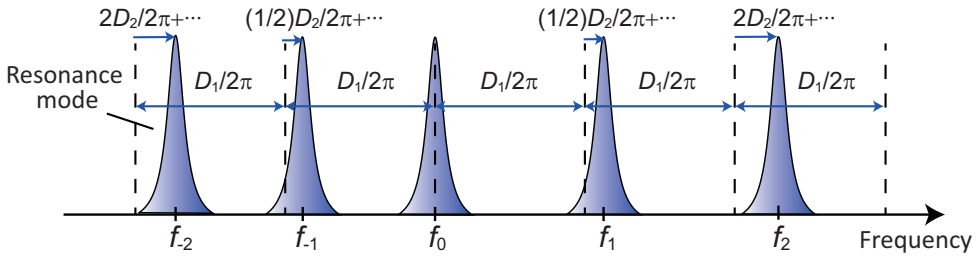

Fig. 3.1: Resonance frequencies taking dispersion into account. The mismatch between the equidistant comb grid (black dashed line) and the resonance mode (blue) corresponds to the microresonator dispersion.

$$\begin{aligned}\tilde{\beta}_2 &= \left.\frac{d^2\tilde{\beta}}{d\omega_m^2}\right|_{m=m_0} = \frac{d\tilde{\beta}_1}{d\omega_m} = \frac{1}{(2\pi)^2 R}\left(\frac{d}{df_m}\frac{1}{\Delta f_m}\right) \\ &= -\frac{1}{4\pi^2 R\cdot\Delta f_m^2}\frac{d\Delta f_m}{df_m} = -\frac{1}{4\pi^2 R\cdot\Delta f_m^3}\cdot\Delta(\Delta f_m).\end{aligned} \tag{3.13}$$

Then $\tilde{\beta}_2$ gives the dispersion parameter $\tilde{D}$ with resonance frequencies from Eq. (3.9) as,

$$\tilde{D} = -\frac{2\pi c}{\lambda^2}\tilde{\beta}_2 = \frac{c}{2\pi\lambda^2 R\cdot\Delta f_m^3}\cdot\Delta(\Delta f_m), \tag{3.14}$$

where a difference approximation for the m-th mode is employed such as, $\Delta f_m = (f_{m+1} - f_{m-1})/2$, and $\Delta(\Delta f_m) = f_{m+1} - 2f_m + f_{m-1}$.

The microresonator dispersion is often expressed as a function of the relative position of the resonance frequencies. The relative mode number μ is defined as the integer mode index as regards the center (pump) mode $\mu = 0$; therefore all the resonance frequencies are given with a Taylor expansion around the center frequency:

$$\begin{aligned}\omega_\mu &= \omega_0 + D_1\mu + \frac{1}{2}D_2\mu^2 + \frac{1}{6}D_3\mu^3 + \frac{1}{24}D_4\mu^4 + \cdots \\ &= \omega_0 + D_1\mu + D_{\text{int}},\end{aligned} \tag{3.15}$$

where $D_1/2\pi$ is the equidistant resonator FSR, $D_2/2\pi$ is the second-order dispersion related to β_2, and $D_3/2\pi$, $D_4/2\pi$, $\cdots$ represent the higher order dispersion in units of (Hz) (D_i is given in (rad/s)). Consequently, the integrated dispersion D_{int} is defined as the deviation of the resonance frequency including all orders of dispersion from the equidistant grid $D_1/2\pi$. The frequency distance between two adjacent resonant modes is called an FSR, which is the general definition (including dispersive effect). However, an equidistant grid with respect to the pump mode $D_1/2\pi$ can be sometimes defined as an FSR. The former includes the frequency offset induced by the dispersion whereas the latter indicates only equal intervals. Although both terms are used to stand for "FSR", this thesis distinguishes the original definition of "FSR" (i.e., longitudinal mode spacing including dispersion) from the "equidistant FSR" (i.e., $D_1/2\pi$).

Figure 3.1 shows a schematic illustration of microresonator dispersion. Higher order dispersions can be omitted if the following relation is valid: $D_2 \gg D_3 \gg D_4 \cdots$. Here, a positive (negative) D_2 corresponds to an anomalous (normal) dispersion, and D_i parameter is related to dispersion β_i as,

$$D_2 = -\frac{c}{n} D_1^2 \beta_2. \tag{3.16}$$

$$D_3 = -\frac{c}{n} D_1^3 \beta_3 + 3\frac{c^2}{n^2} D_1^3 \beta_2 \approx -\frac{c}{n} D_1^3 \beta_3. \tag{3.17}$$

$$D_4 = -\frac{c}{n} D_1^4 \beta_4 + 16\frac{c^2}{n^2} D_1^4 \beta_2 \beta_3 - 33\frac{c^3}{n^3} D_1^4 \beta_2^3 \approx -\frac{c}{n} D_1^4 \beta_4. \tag{3.18}$$

Here, the inverse round trip time t_R^{-1} is equal to $D_1/2\pi$ (corresponding to $ct_R = n_g L$), which means that FSR around the pump mode determines the group velocity of the microresonator system. When taking these relations into account, the resonator FSR depends on the effective radius and group index as,

$$FSR(\omega) = \frac{1}{2\pi R(\omega) \cdot \frac{d\beta}{d\omega}} = \frac{c}{2\pi R(\omega) \cdot n_g(\omega)}. \tag{3.19}$$

The following expressions are useful to understand the relationship between FSR and dispersion straightforwardly:

$$\frac{dFSR}{d\omega} > 0, \ \frac{dFSR}{d\lambda} < 0 : \text{(anomalous dispersion)} \tag{3.20}$$

$$\frac{dFSR}{d\omega} < 0, \ \frac{dFSR}{d\lambda} > 0 : \text{(normal dispersion)} \tag{3.21}$$

3.1.3 Material dispersion

Material dispersion — the frequency dependence of refractive index of a material — plays an important role in the total dispersion of a resonator. The Sellmeier equation proposed in 1872 [148] is used to determine the dispersion in the medium as:

$$n^2(\lambda) = 1 + \sum_i \frac{A_i \cdot \lambda^2}{\lambda^2 - B_i^2} \tag{3.22}$$

where A_i and B_i are the Sellmeier coefficients, and λ is wavelength in units of μm (see Table 3.1). Figure 3.2 shows material dispersion given by Eq. (3.22). Sellmeier coefficients for other optical materials can be found elsewhere [149, 150].

Table. 3.1: Coefficients of Sellmeier equations in microresonator material [149]

Material	A_1	A_2	A_3	B_1 [μm]	B_2 [μm]	B_3 [μm]
SiO_2	0.6961663	0.4079426	0.8974794	0.0684043	0.1162414	9.896161
MgF_2	0.48755108	0.39875031	2.3120353	0.04338408	0.09461442	23.793604
CaF_2	0.5675888	0.4710914	3.8484723	0.050263605	0.1003909	34.649040
Si_3N_4	3.0249	40314		0.1353406	1239.842	

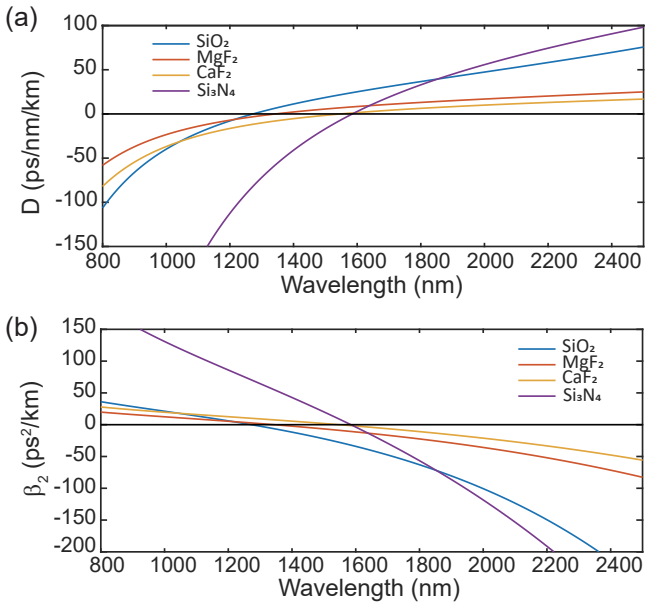

Fig. 3.2: (a) and (b) Material dispersion D and β_2 of various platforms: silica (SiO_2), magnesium fluoride (MgF_2), calcium fluoride (CaF_2), and silicon nitride (Si_3N_4).

3.1.4 Geometric dispersion

Besides the contribution of material dispersion, geometric dispersion has a substantial impact on total dispersion. Geometrical dispersion can be interpreted as follows: an optical mode with a different frequency experiences a different optical path in the waveguide. Since optical microresonators have various kinds of geometry parameters such as resonator diameter and cross-section dimension, it is necessary to take the geometry effect into account carefully. Furthermore, it is known that different spatial modes and different polarization modes can induce additional dispersion effects in terms of geometric dispersion because optical microresonators generally have a multi-mode structure.

Finite-element method analysis

In order to calculate the geometric dispersion of the optical microresonator, two useful methods have been developed. One is an analytical approach via an approximation of the eigenfrequency of resonators [110, 151, 152]. Such an analytical expression offers an accurate simulation of the resonance frequencies and mode field distribution, and it has also been used to calculate geometric dispersion. However, this method has the geometrical limitation of resonators in which an analytical estimation is valid only for simple and symmetric geometries (i.e., spheroids and toroids). The other approach is a finite-element method (FEM) simulation that is widely used to solve the partial differential equations in various mathematical models (e.g., structure analysis, and heat transfer, and electromagnetic potential). The FEM simulation can be performed with commercially available software (e.g., COMSOL Multiphysics) as an eigenvalue solver of axisymmetric structures like optical microresonators [153]. An FEM simulation yields not only the eigenmode frequency corresponding to the resonance frequency but also the mode field distribution, which gives the effective mode area (see Eq.(2.8)) and the mode overlap factor between different transverse modes. Since the whispering galley mode and waveguide mode exhibit different properties with regards to the geometric dispersion, it is straight to introduce independently.

Geometric dispersion in a WGM microresonator

Figure 3.3 shows the examples of mode profile simulation with FEM in a silica microdisk resonator. In the case of a WGM, the effective mode radius readily influences the dispersion since the optical mode approaches the inner region of the resonator (symmetric axis of the resonator) when the wavelength (frequency) is increasing (decreasing). Such a trend of the effective radius corresponds to one side of the geometric dispersion. The change in n_g, which is determined by the sum of n_{eff} and the frequency-dependent variation $\omega(dn_{\mathrm{eff}}/d\omega)$ defined as Eq. (3.2), is interpreted as another side of the geometric dispersion. When the optical mode extends to the lower index region, it results in the reduction in n_{eff} (which promotes normal dispersion). On the other hand, a sudden change in n_{eff} induces an overall increase in n_g, and it helps to contribute anomalous dispersion.

Here, one can see that the effective index is associated with the change in effective radius and the penetration of the mode field into the air cladding region. The former effect is a unique feature in WGM, not present in a waveguide mode. Although these two mutual contributions must be taken into account simultaneously, it is possible to predict the overall microresonator dispersion by understanding the principle of the geometric dispersion of WGM microresonators. This makes a significant difference between WGM resonator and waveguide resonator as regards the dispersion engineering. It should also be noted that transverse electric (TE) and transverse magnetic (TM) polarizations are defined as

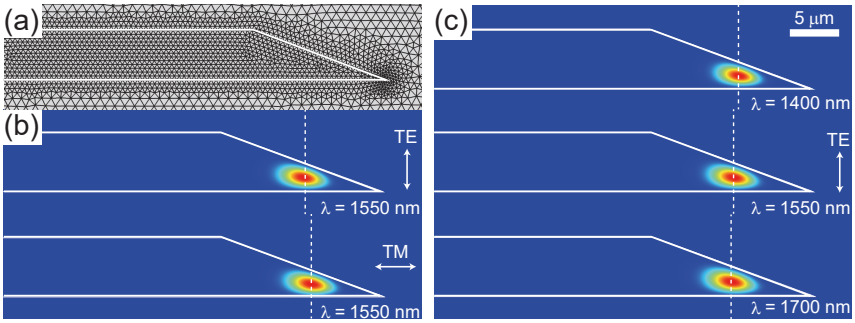

Fig. 3.3: (a) Created mesh cells for axisymmetric microdisk resonator with 40° wedge angle in FEM calculation. (b) Calculated mode profile of fundamental TE and TM modes around 1550 nm. The TM mode slightly extends the outer boundary of the disk resonator. (c) Comparison of mode profiles at three different wavelengths. At longer wavelengths, the center of the optical mode is shifted inside the resonator.

the parallel (orthogonal) direction of the dominant electrical field to the symmetric axis of the WGM microresonator [153, 154]. This definition is opposite to the case of waveguide mode described later.

In order to obtain the total dispersion of WGM microresonators, both material and geometry dispersions should be taken into account in the calculation. Nevertheless, it is not easy to consider these two dispersions separately since the mode field distribution of a WGM resonator is strongly related to the refractive index of the resonator material and the outer field. Therefore, an iterative calculation is an effective way to simulate resonance frequencies accurately. Three steps have been used in the calculation. (1) Input the microresonator structure and the approximate refractive index of the material into an FEM solver. The approximate refractive index can be obtained by Eq. (3.22) or literature. (2) A Sellmeier equation gives the refractive index at the frequency, which is obtained as an eigenfrequency in FEM solver. These procedures are repeated several times. (three or four times are sufficient) (3) Obtain the "exact" resonance frequency taking account of the "exact" refractive index at the frequency. The obtained results are resonance frequencies that include both material and geometry dispersions, which yield the FSR and dispersion through proper data processing. A detailed calculation flow is shown in Fig. 3.4. The setting of the starting eigenfrequency to be searched is essential to avoid an undesired calculation and a failed result. Calculation sometimes diverges due to an error with the solver, and then the calculation should be repeated with a different searching frequency. A judgment algorithm that can be used to check the values is also important for implementing a successful simulation and reducing the redundant computation time. Moreover, the mesh size should be sufficiently fine to obtain exact values even though it is a trade-off against calculation time.

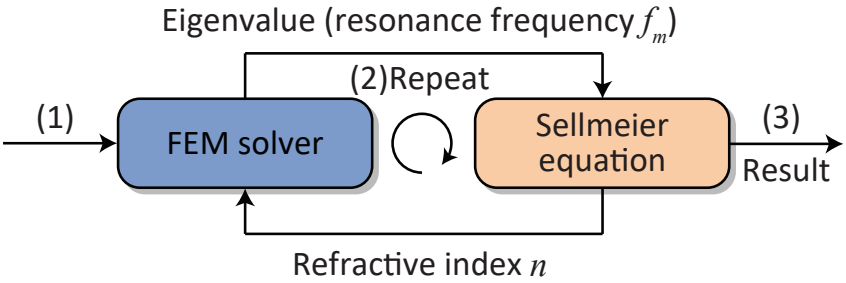

Fig. 3.4: Iterative calculation flow for WGM microresonator dispersion taking account of material and geometry dispersion.

Geometric dispersion in waveguide microresonator

In general, the geometric dispersion of a waveguide (guided-mode) resonator approaches anomalous dispersion near the higher confinement region and normal dispersion near the lower confinement (cut-off) region. This is the simple rule in the case of waveguide resonators, where the effect of frequency-dependent mode radius variation is neglected due to its strong mode confinement. Also, TE and TM polarizations are defined as the electric (magnetic) field being perpendicular to the propagation direction, as is the case of the general definition.

3.2 Microresonator dispersion engineering

3.2.1 Structure design of microresonators

Optical microresonators have wide-ranging combinations of material and geometry; in particular, various choices are available and selected based on the demands for FSR or integration possibility. The host material for resonators determines the Q limitation, and the major trend of the dispersion as material dispersion. Nevertheless, the total dispersion can only be modified by arranging the structural parameters in the monolithic resonators, and thus there are many studies aimed at engineering the resonator dispersion utilizing geometry tailoring [53, 155], layer structure [156], slot waveguide [157], and multi-resonator system [78, 158].

Here, the total dispersions in several kinds of microresonators are briefly introduced. The resonator geometry can be engineered via the structural condition where different structure parameters are used for different resonators. The resonator size (corresponding to radius R) is directly related to the FSR, and thus the FSR can be approximated from the resonator radius and refractive index while other structural parameters can affect both the FSR and dispersion. The following section mainly focuses on presenting the dependence of each geometry parameter on total dispersion and the principle of dispersion engineering.

The modeling of WGM resonators are depicted in Fig. 3.5.

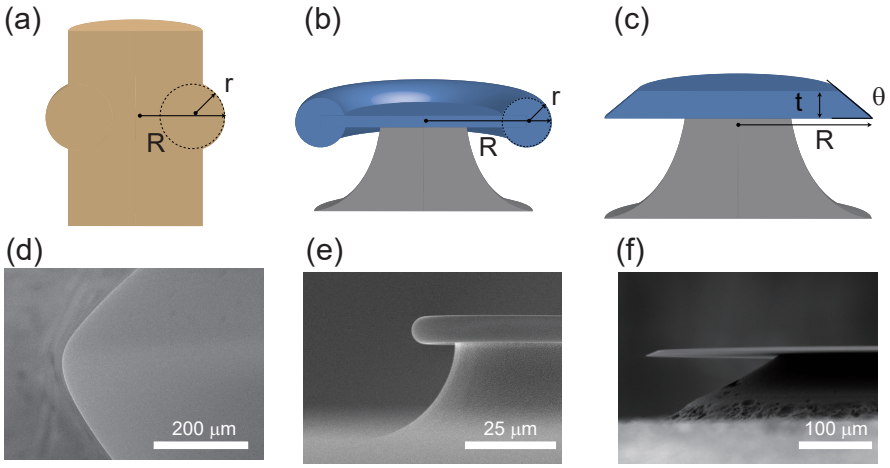

Fig. 3.5: (a) Spheroid (spherical) model, representing a mm-sized microresonator with a resonator radius R and a curvature radius r. (b) Microtoroid model, whose two structural parameters are major radius R and minor radius r. (c) Single-disk model with resonator radius R, thickness t, and wedge angle θ. (d) SEM image of an MgF_2 crystalline resonator. (e) SEM image of a silica microtoroid resonator. (f) SEM image of a silica microdisk resonator.

3.2.2 Calculated dispersion of whispering gallery mode microresonators

Spheroid (spherical) model

Spheroid and spherical cross-sectional shapes are ubiquitous structures in crystalline and silica-based WGM microresonators [14,15]. The spheroid (spherical) structure is characterized by a resonator radius R and a curvature radius r, and microsphere resonator corresponds to the case of the perfect sphere, namely the condition of $R = r$ [4]. Since the fabricated resonator size is in the order of several hundred micrometers to several millimeters, the typical curvature radius becomes several tens/hundreds of micrometers. These features are determined by the fabrication methods such as mechanical and hand polishing with a crystalline resonator, and a carbon dioxide (CO_2) laser cutting process with a silica rod resonator.

Figures 3.6(a) and 3.6(b) shows calculated dispersion D as a function of wavelength for the fundamental TE mode of a MgF_2 resonator with a different resonator radius and curvature radius. Figures 3.6(c) and 3.6(d) shows the corresponding integrated dispersions D_{int}, which indicates the deviation between each resonance frequency and the estimated equidistant FSR $D_1/2\pi$. The resonator radius is changed to 350 μm, 700 μm, 1400 μm, and 2800 μm. One

can see that the dispersion curves gradually get close to the material dispersion with a larger resonator size, enhancing an overall anomalous dispersion. On the other hand, it is clear that the curvature radii from 25 μm to 100 μm are less important as regards overall dispersion, even though a smaller radius contributes slightly to a strong anomalous dispersion as shown in the inset of Fig. 3.6(b). These results suggest important guidelines: (1) the overall dispersion mainly depends on the resonator size, (2) the curvature size plays a less important role in a mm-size spheroid/spherical resonator. The first guideline can be simply understood as a suppression of the geometric effect in a larger size resonator. The second guideline describes that the optical mode is not influenced by a relatively large curvature radius than the resonance wavelength. Nevertheless, this example is only the fundamental mode, and it is known that the radial and polar higher-order modes also contributes to the change of the total dispersion [159].

Microtoroid model

A microtoroid is characterized by a major radius (corresponding to resonator radius) and a minor radius of several tens/hundreds of micrometers and several micrometers, respectively [5]. The results of simulated dispersion in silica microtoroid are shown in Fig. 3.7. A choice of major radii strongly affects the dispersion as with the case of the spheroid model. One can find that the difference between radii of 40 μm and 60 μm are more important as regards realizing an anomalous dispersion in the 1550 nm region. Interestingly, the smaller minor radius contributes to a strong anomalous dispersion as shown in Fig. 3.7(b). This feature indicates that the μm-size of minor radius strongly affects the geometry dispersion. As a result, the change towards an anomalous dispersion with a smaller minor radius is interpreted as follows: geometry dispersion generally contributes to normal dispersion because of a reduction of mode radius, which corresponds to an increasing FSR with a longer wavelength. On the other hand, a change in n_g can compensate for the normal dispersion, and the total dispersion becomes anomalous due to the strong mode confinement. Consequently, the geometry dispersion becomes anomalous overall as the resonator cross-section dimension is compressed. In contrast, the dispersion for $r = 5$ and $r = 6$ exhibits little change compared with that for $r = 3$ and $r = 4$ as shown in Figs. 3.7(b) and 3.7(d). These results indicate that relatively loose mode confinement has less influence on dispersion, namely “mode relaxation” effect.

Single-disk model

A single-disk resonator is characterized by three parameters, namely a resonator radius, a wedge angle, and thickness [13, 160]. Figures 3.8(a) and 3.8(c) show the dispersion with different thicknesses of 4 μm, 6 μm, 8 μm and 10 μm. The disk angle and resonator radius were kept at 40° and $R = 300$ μm, respectively. Here, the dispersion curves increase significantly with a decrease in disk thickness, and does not show any significant change with thicknesses of 8 μm and

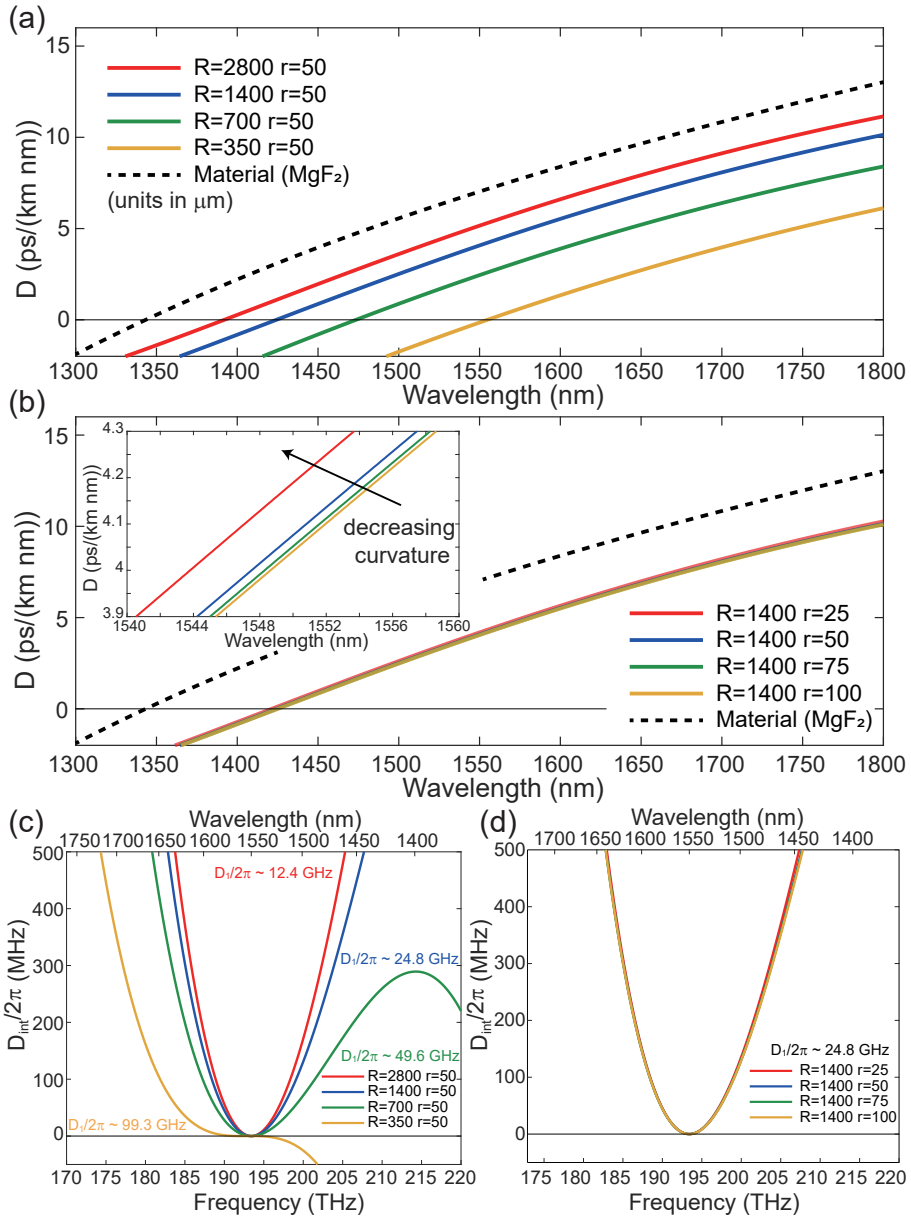

Fig. 3.6: Simulated dispersion of MgF_2 spheroid resonator for different resonator radii R and curvature radii r in μm. (a) Dispersion parameter D for different resonator radii. (b) Dispersion parameter D for different curvature radii. (c) Integrated dispersion D_{int}, which is defined as the deviation of the resonance frequency from an equidistant FSR, for different resonator radii. The positive parabolic function corresponds to anomalous dispersion, and the cubic function curves of the dispersion originate from the effect of third-order dispersion. (d) Integrated dispersion D_{int} for different curvature radii.

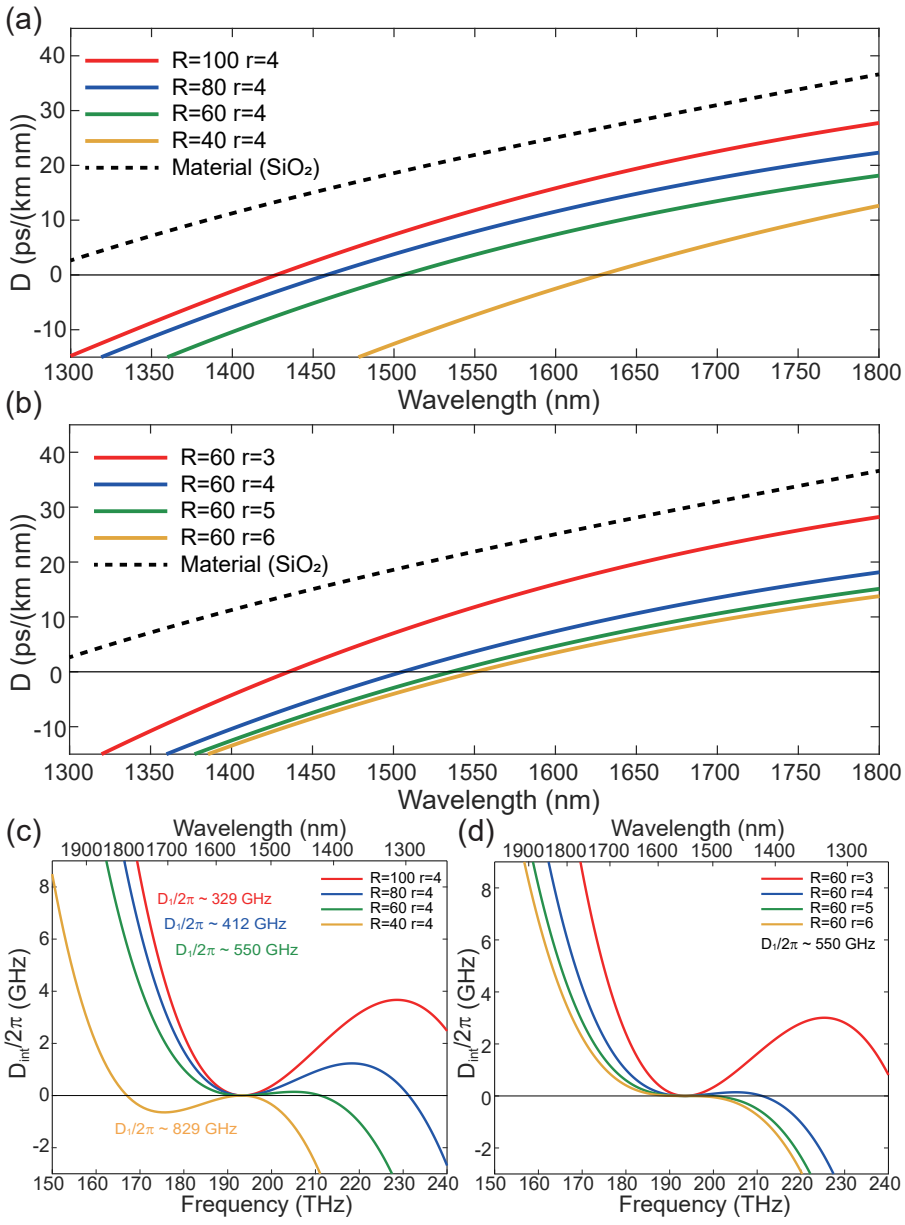

Fig. 3.7: Simulated dispersion of a SiO_2 microtoroid for different resonator radii R and minor radii r in µm. (a) Dispersion parameter D for different resonator radii. (b) Dispersion parameter D for different minor radii. (c) Integrated dispersion D_{int}, for different resonator radii. (d) Integrated dispersion D_{int} for different minor radii.

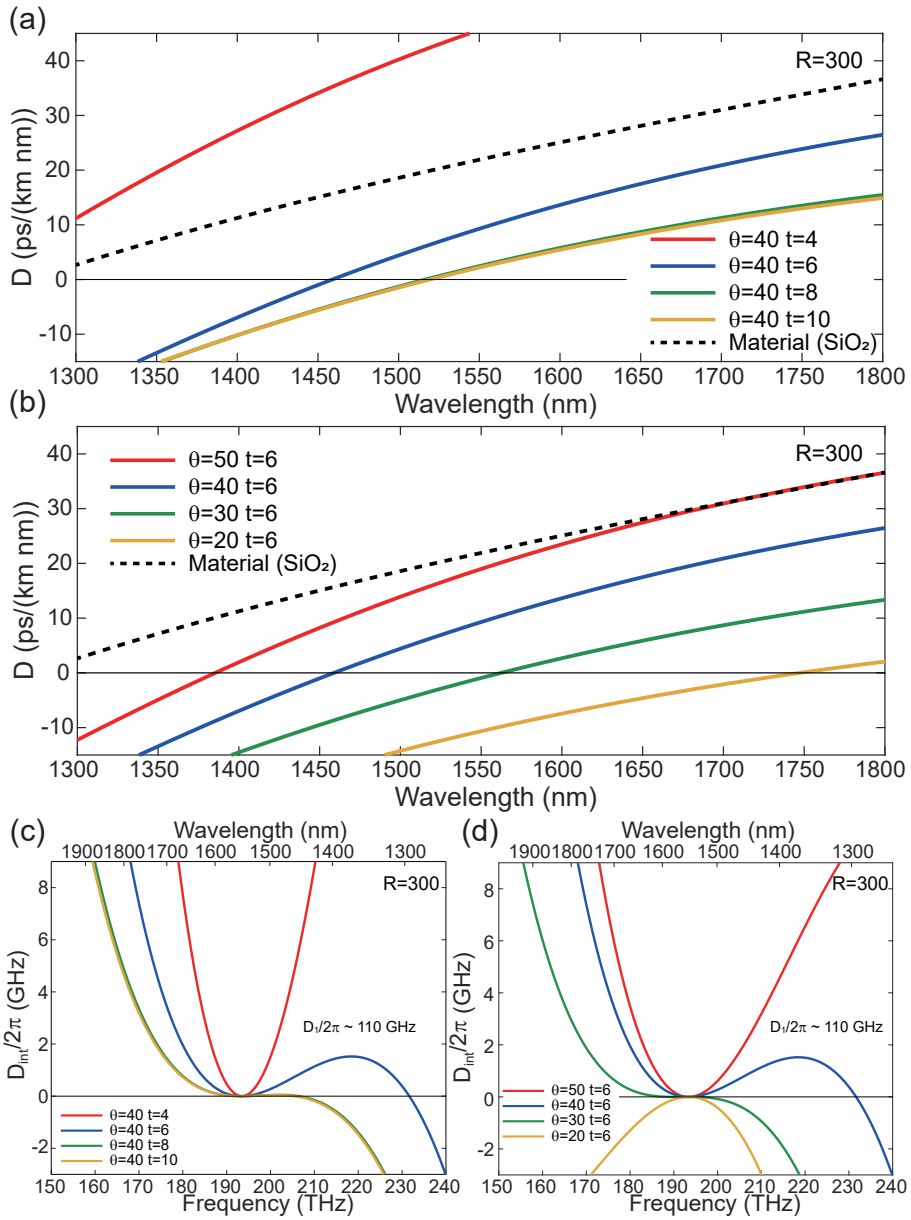

Fig. 3.8: Simulated dispersion of SiO_2 disk of 300 μm radius for different angles θ and thicknesses t μm. (a) Dispersion parameter D for different disk thicknesses. (b) Dispersion parameter D for different disk angles. (c) Integrated dispersion D_{int}, for different disk thicknesses. (d) Integrated dispersion D_{int} for different disk angles.

10 μm. The reason for the former result can be explained with the analogy of "mode compression", and latter observation can be understood with the analogy of "mode relaxation" as with the microtoroid model. Next, the disk angle is changed to 20°, 30°, 40°, and 50° with a fixed thickness of 6 μm and resonator radius of $R = 300$ μm as shown in Fig. 3.8(b) and 3.8(d). The simulation result indicates that the smaller disk angle contributes greatly to the normal dispersion. The faster mode radius reduction mainly explains this effect with a smaller disk angle.

3.2.3 Calculated dispersion of waveguide mode microresonators

3.2.4 Review of a strategy of dispersion engineering

Here the strategy of dispersion engineering is briefly reviewed from the obtained results of dispersion simulation. First, it is clear that the choice of material and type of microresonator is essential with respect to deciding the overall dispersion. Indeed, different material exhibits different dispersion, and the manufacturable structure mutually depends on the material and the resonator size.

In the case of WGM microresonator, a smaller radius resonator is strongly influenced by geometric dispersion approaching a normal dispersion in general. However, the resonator size determines the FSR of a generated comb, and so it is not easy to achieve both a large FSR and a proper anomalous dispersion in terms of microresonator frequency comb generation. The compression of smaller resonator cross-section dimension is an effective way in order to overcome this limitation since the dispersion changes from normal to anomalous in small radius resonators [160, 161]. A criterion for such mode compression is several times the wavelength of the optical mode (i.e., a cross-section dimension of $\lambda \sim 4\lambda$). In addition, the disk angle critically affects the dispersion, which is not observed with spheroid/spherical and microtoroid models. One can understand this case as a rapidly decreasing mode radius with a smaller disk angle than with a larger angle (i.e., contribution to normal dispersion) [155, 162]. These trends can be applied to every type of WGM microresonator, and it will be an important strategy for designing the microresonator structure.

3.3 Measurement of microresonator dispersion

3.3.1 Objective of dispersion measurement

The measurement of microresonator dispersion is one of the essential techniques for the evaluation of fabricated microresonators. In addition to numerical simulation, as described in Section 3.2, a precise measurement of dispersion allows us to find the desired resonance mode from massive resonance frequencies. Measured resonance frequency provides the resonator FSR, second and higher-order

dispersions, and the mode interaction between different transverse modes. However, resonator dispersion measurements must be performed carefully and accurately since the linewidth and the deviation of the mode spacing are in the orders of kHz or MHz, which means that high spectral resolution is required over the measurement bandwidth. In general, it is not easy to guarantee the frequency with such accuracy due to the uncertainty of the measurement, which cannot be neglected in this case. Therefore, the wavelength axis of the measurement data must be calibrated with reliable methods to give precise frequency references. The requirements of dispersion measurement are as follows; (1) measurement bandwidth, (2) accuracy and resolution, (3) system simplicity. There is often a trade-off, and thus it is necessary to choose the method carefully on demand. Here, several dispersion measurement methods are reviewed with the measurement results. Figure 3.9 shows a schematic of the experimental setup for various dispersion measurements.

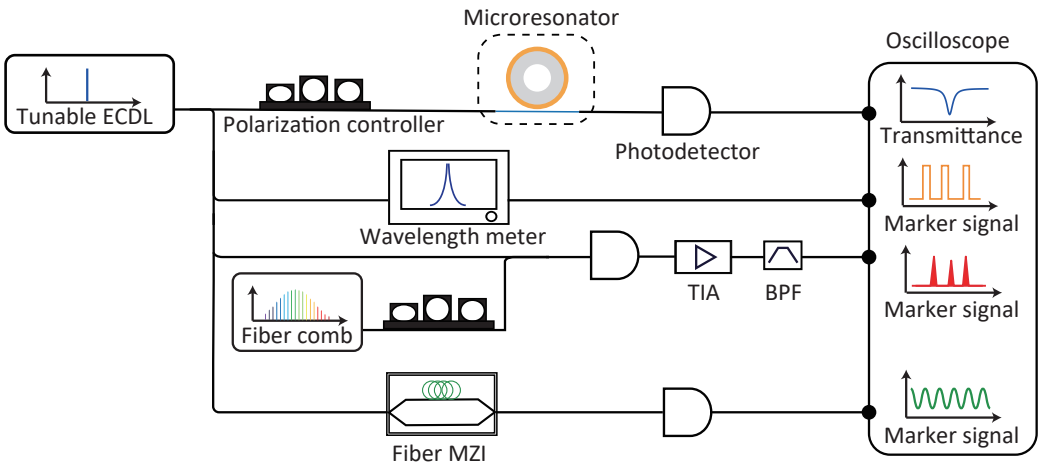

Fig. 3.9: Schematic of the setup used for the microresonator dispersion measurement. The dispersion of crystalline MgF_2 microresonator was measured with three different methods. Both the resonator transmittance and calibration marker are recorded simultaneously with a multi-channel oscilloscope. Each path can be independently used for dispersion measurements, whereas all the signals in the experiment were observed for comparison. ECDL, external cavity diode laser. MZI, Mach-Zehnder interferometer. TIA, transimpedance amplifier. BPF, band-pass filter.

3.3.2 Laser wavemeter based method

The simplest method involves using a wavelength meter to calibrate the actual wavelength of the sweeping laser. The wavelength meter is synchronized with the scanning laser, and the resonance transmission and the output signal from the wavelength meter are obtained simultaneously with a long-memory oscilloscope or other data acquisition (DAQ) system. It is assumed that the wavelength

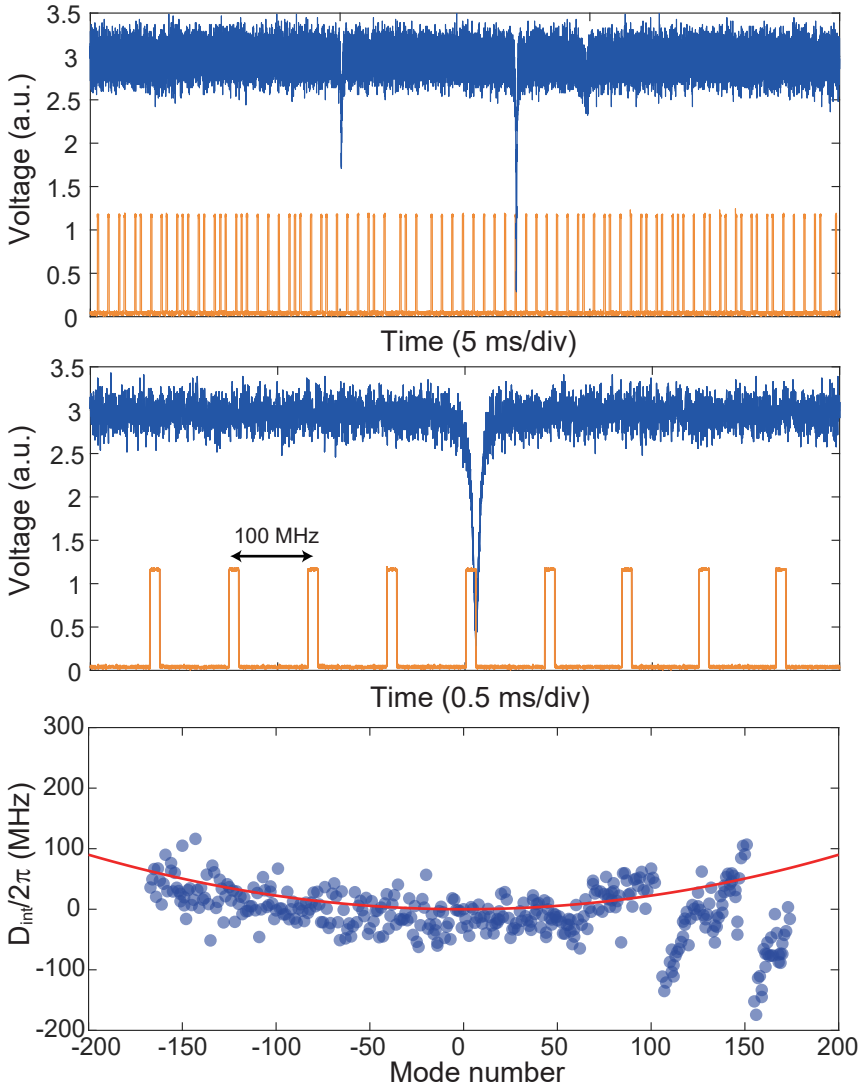

Fig. 3.10: The result of the laser wavelength method. Top: Measured resonator transmission spectrum (blue) and frequency marker signal with wavelength meter (orange). Several different mode families are recorded. Middle: 10× enlarged view of the top. The frequency axis is calibrated by the peaks at a 100 MHz distance. Bottom: Measured dispersion plot of D_{int} (blue dots) versus relative mode number μ. The red line shows a parabolic fitting curve yielding $D_2/2\pi = 4.5$ kHz (FSR ~ 21.6 GHz). The deviations from the fitting are limited by the accuracy of the wavelength meter. Strong mode perturbations around $\mu = 100$ and $\mu = 150$ are caused by anti-mode crossing between different mode families.

meter can be synchronized with the sweeping laser in this measurement. Accordingly, wavelength resolution and accuracy would be limited by the performance of the wavelength meter, which is at best of tens of MHz order in commercially available products. This property lacks wavelength accuracy even though it is critical for the dispersion measurement. The advantage of this method is experimental simplicity, and it requires only a 2-channel oscilloscope (available for maximum performance of memory length). Figure 3.10 shows the experimental dispersion result obtained with a wavelength-meter-based measurement. Here, the trigger outputs based on a built-in-function wavelength meter of the tunable laser (TSL-710, santec) are used as the marker signal.

3.3.3 Mode-locked frequency comb based method

This method was first proposed as frequency comb assisted diode laser spectroscopy [163], and used in many studies [43, 76]. A scanning laser over resonances is partially split and combined with a stabilized frequency comb source, which generates a laser beat signal with equidistant comb lines. The beat signals are electrically filtered with a narrow-band bandpass filter to make calibration markers only when the scanning laser passes through the comb lines. Consequently, the calibration markers are detected when the laser frequency (f_s) matches the difference between a neighboring comb line ($f_c = f_{\mathrm{ceo}} + nf_{\mathrm{rep}}$) and the center of the bandpass filter (f_b) with $0 < f_b < f_{\mathrm{rep}}/2$: $f_s = f_{\mathrm{ceo}} + nf_{\mathrm{rep}} \pm f_b$. The schematic of the operation principle of this method is shown in Fig. 3.11. This method provides reliable information about the scanning laser frequency and the transmission resonance simultaneously within a few seconds. Marker peaks can be processed with a local peak finding algorithm and converted to an accurate frequency axis. The measured results are shown in Fig. 3.12.

The spectral resolution is determined from the scan bandwidth and the memory length of the oscilloscope, and the sweeping speed of the laser should be sufficiently fast to avoid unnecessary measurement error (e.g., the frequency fluctuation of the comb source). Nevertheless, the maximum sweep speed v_s is limited by the bandwidth of electric filters, which have certain response times (estimated from the inverse of the filter bandwidth Γ_{bw}), yielding $v_s = 1/\Gamma_{\mathrm{bw}}^2$. The laser frequency between neighboring calibration markers can be interpolated so that the use of multiple bandpass filters can increase the measurement accuracy. It should be noted that this method uses a multi-channel oscilloscope with a sufficiently long memory because the spectral resolution (scan bandwidth divided by memory length) must be sufficiently finer than the resonance linewidth $\gamma = Q/\nu$. For instance, the detection of a high Q resonance of 10^9 over a 40 nm range needs a memory length of at least $\sim$ 25M point per channel. It should also be noted that this measurement requires a mode-hope-free tunable laser over the scanning range, and the measurement bandwidth is limited by both the laser and the reference frequency comb. The polarization of the fiber comb must be carefully adjusted to interfere with the tunable laser. Otherwise, the marker

signal lacks in the sweeping range. This means that the degree of polarization uniformity and the stability of fiber comb directly links to the noise floor of the marker signal.

Besides, there is a way to use a wavelength meter or frequency-stabilized CW laser in order to generate a reference marker signal to calibrate the absolute wavelength. The uncertainty of the wavelength meter introduces an absolute wavelength offset for the measurement data; however, it is less important for microresonator "dispersion" measurements. This indicates that measurement accuracy does not depend on absolute frequency calibration, but on relative frequency calibration. The bandwidth limitation of the measurement can be overcome by utilizing two widely tunable lasers with different wavelength bands if the reference comb has a broad enough bandwidth over the full measurement range [164].

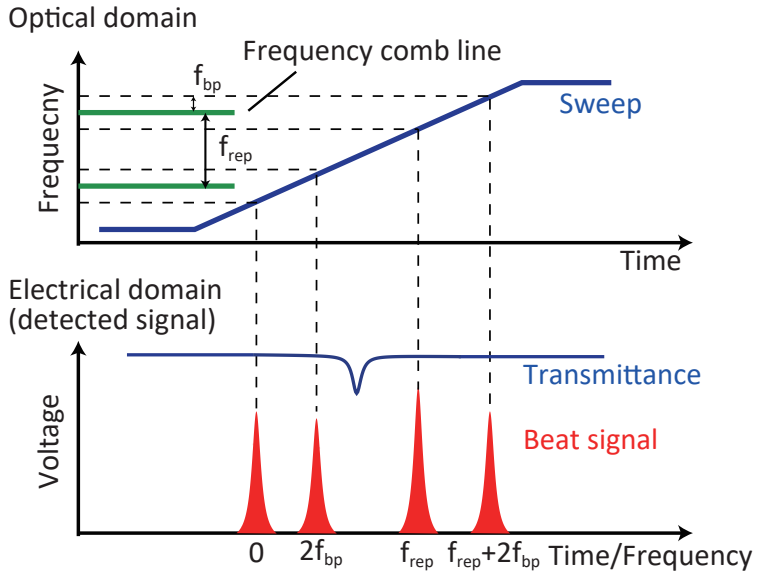

Fig. 3.11: Operating principle of the mode-locked frequency comb-based method. The scanning laser generates beat notes with stabilized fiber comb lines, and the beat signals filtered with a band-pass filter calibrate the time axis to frequency axis.

3.3.4 Calibrated fiber-based interferometer method

A fiber-based interferometer or fiber-loop cavity can be used as a calibration marker [13, 42, 77, 124] instead of beat signals generated with a mode-locked frequency comb. This method offers simple implementation, high accuracy, and broad bandwidth. However, the fiber interferometer composed of optical silica fiber itself inherently exhibits dispersion. Thus, the FSR and dispersion of a

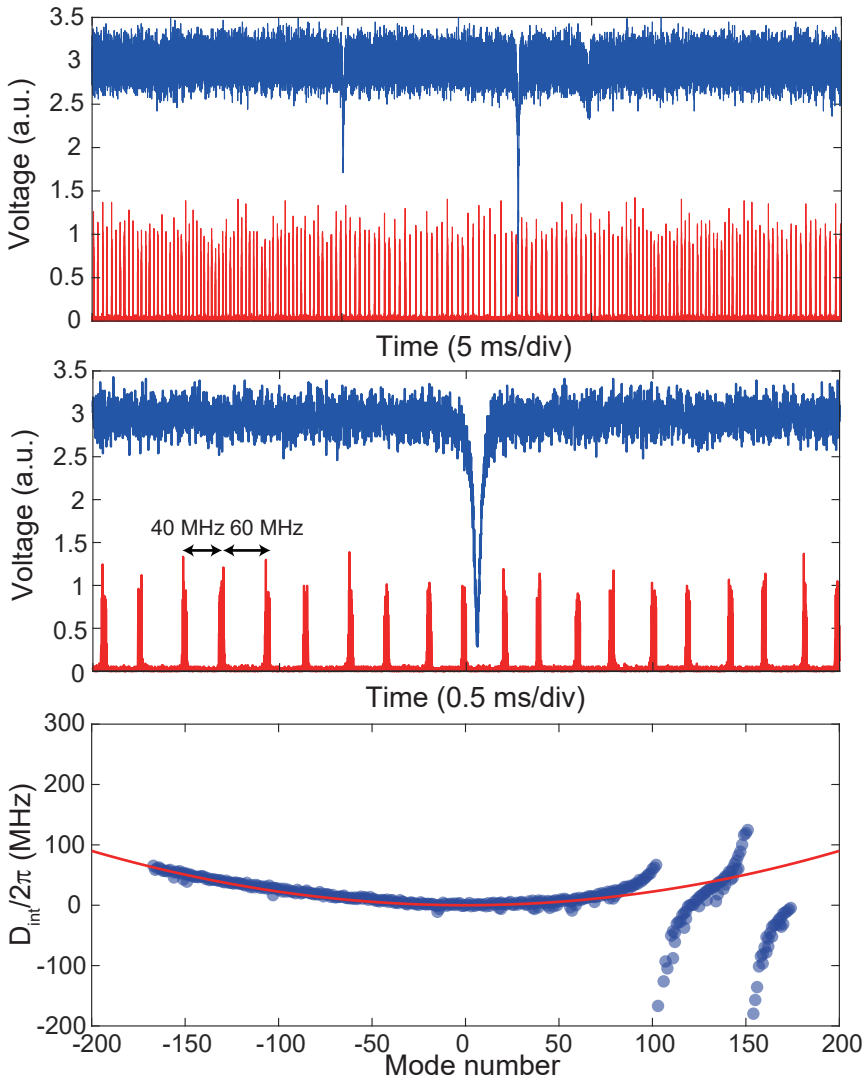

Fig. 3.12: The result of the mode-locked frequency comb based method. Top: Measured resonator transmission spectrum (blue) and beat signal (red) with fiber comb lines, which work as calibration peaks. Middle: 10× enlarged view of the top. The frequency axis is calibrated by the peaks at 40 MHz and 60 MHz with respect to the fiber comb lines with a 100 MHz mode spacing. Bottom: Measured dispersion plot of D_{int} (blue dots) and fitting curve (solid red line). The measurement accuracy is greatly improved compared with the wavelength meter method.

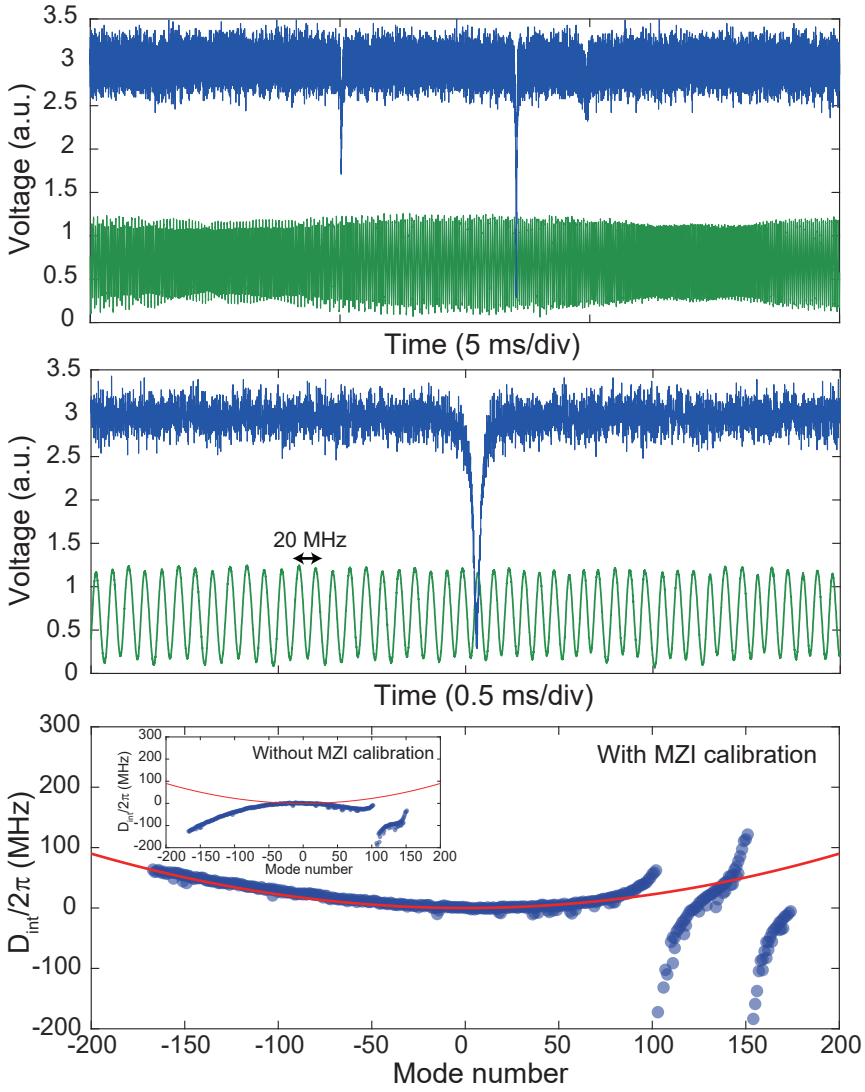

Fig. 3.13: The result of the calibrated fiber MZI method. Top: Measured resonator transmission spectrum (blue) and interferometric signal (green) with a fiber MZI. Middle: 10× enlarged view of the top. The frequency axis is calibrated by the sinusoidal peaks at 20 MHz of the FSR of the MZI. Bottom: Measured dispersion plot of D_{int} (blue dots) and fitting curve (solid red line). With proper dispersion calibration of the fiber MZI, the measured dispersion agrees well with the results obtained with other methods. The inset shows the result without the calibration of MZI, which reflects the inherent dispersion of silica optical fiber, and it hinders the resonator dispersion.

fiber Mach-Zehnder interferometer (MZI) must be carefully measured and calibrated in advance of the resonator dispersion measurement. A fiber MZI is easy to prepare by connecting two 50/50 fiber couplers where one path is several meters longer than the other. The length difference between the two paths ΔL_{fiber} corresponds to the frequency period of a sinusoidal interferometer signal $\Delta f_{\text{MZI}} = c/(n\Delta L_{\text{fiber}})$. When using a 10 m length of delay line (e.g., commercial single-mode silica optical fiber), the interferometric period will be around 20 MHz. The period of the MZI becomes longer on the time axis while the laser is slowly scanned; on the other hand, the MZI will respond as a short period against faster scanning. This time-variant sinusoidal signal gives frequency calibration information, and the number of MZI periods is counted with a similar algorithm to that used with the frequency comb-based method. Measured results are shown in Fig. 3.13. The MZI dispersion can be expressed by a Taylor expanded equation as,

$$\Delta f_{\text{MZI}}(\mu_{\text{MZI}}) = \Delta f_{\text{MZI},0} + d_1\mu_{\text{MZI}} + \frac{1}{2}d_2\mu_{\text{MZI}}^2 \tag{3.23}$$

where $\Delta f_{\text{MZI},0}$ is the FSR of the center mode, $\mu_{\text{MZI}} = 0$, μ_{MZI} is the relative mode number of the MZI period with respect to the center mode, d_1 and d_2 are the first and second-order dispersion, respectively. The calibration of the fiber MZI must be accomplished by the precise measurement of the FSR both near and far from the center mode, and polynomial fitting according to Eq. (3.23). If the dispersion of the fiber MZI, namely, d_1 and d_2, is not considered, the resonator dispersion can be no longer measured, as shown in the inset of the bottom figure of Fig. 3.13. The calibrated fiber MZI should be operated in a stable condition for temperature, pressure, and bending in order to avoid any deviation of the calibration data.

3.3.5 Electro-optic modulator comb based method

An electro-optic modulator (EOM) modulates the scanning laser, and this generates multiple resonances on both sides with a modulation frequency f_{mod}. Such sideband modulation technique can be used in various microresonator researches such as the Pound-Drever-Hall (PDH) technique [125], linewidth estimation [58], electro-optic frequency comb generation [165], and the dispersion measurement described here [155, 162]. If the modulation frequency f_{mod} nearly matches the resonator FSR, three resonance dips can overlap each other in the spectral domain, and then f_{mod} itself gives the FSR of the interest. This method can be adopted for broadband dispersion measurement and is not limited by the tunable range of the mode-hope free laser, from 1400 to 1700 nm, and even around the 2100 nm wavelength region via difference frequency generation [155]. The CW laser sent to the EO modulator with f_{mod} outputs a narrow band EO comb, and the bandwidth can be broadened through multiple amplifiers and highly nonlinear fibers. When the broadened comb lines sweep over

the multiple resonances simultaneously, precisely adjusted f_{mod} will provide the average FSR of the extracted resonances. The uncertainty of this measurement is estimated to be about 100 kHz [162]. It should be noted that there is one limitation regarding resonator FSR since f_{mod} must reach at least 1-FSR from the pump laser. The bandwidth of a commercially available EO modulator is several tens of GHz, and thus this method can only be operated in the measurement of microresonators having the FSR of the same order as a bandwidth of EO modulator used in the experiment.

3.4 Role of microresonator dispersion in microcombs

The microresonator dispersion plays a critical role in the frequency comb spectrum, especially for the position of initial sideband, spectrum shape, and comb bandwidth. Anomalous dispersion is a requirement for phase-matching in terms of FWM under CW pumping condition, and for dissipative Kerr soliton formation as well. Thus, the dispersion tailoring for attaining anomalous dispersion becomes an essential technique to obtain soliton microcomb. On the other hand, microcomb generation in the normal dispersion region has also been experimentally and theoretically studied in the present. Here, the role of dispersion and local dispersion perturbation by avoided mode crossing on the microresonator frequency comb spectrum are briefly reviewed.

3.4.1 Anomalous group velocity dispersion and dispersive waves

Second-order dispersion and dissipative Kerr soliton

In the formation of dissipative Kerr soliton, second-order (quadratic) dispersion compensates Kerr nonlinearity as well as the relation of parametric gain and loss [40, 41]. A nearly pure quadratic dispersion should ideally be achieved around the pump wavelength, and then the DKSs characterized by sech^2-shaped optical spectrum stably maintains the waveform during propagating the resonator [Fig. 3.14(a)]. The steepness of parabolic function corresponds to the value of second-order dispersion D_2, and overall, it determines the comb bandwidth. The detailed description of D_2-dominated soliton with respect to the mathematical form and its formation can be referred to §2.4.4.

Dispersive wave due to higher-order dispersion

Higher-order dispersion makes it possible to extend the comb bandwidth into a wavelength region in which the sign of the integrated dispersion D_{int} changes from positive (negative) to negative (positive). In this case, the comb spectrum is no longer imposed by the limitation by second-order dispersion, and expands even the normal dispersion regime [Figs. 3.14(b) and 3.14(c)]. This process is known as the dispersive wave formation, which can be understood in terms of

soliton-induced Cherenkov radiation [43]. The higher-order dispersion enables to bend D_{int} curve at the far from the pump mode, and leads to the generation of enhanced comb sidebands. The spectral location of the dispersive wave can be approximately estimated by the zero-cross point of D_{int}, namely $D_{\mathrm{int}}(\mu) = 0$, which means that resonator FSR around μ-mode matches to the FSR around pump mode. For instance, the position of dispersive waves μ_{DW} are expressed as,

$$\mu_{\mathrm{DW}} = -\frac{3D_2}{D_3} \tag{3.24}$$

$$\mu_{\mathrm{DW}} = -\frac{3D_3}{D_4} \pm \sqrt{\left(\frac{2D_3}{D_4}\right)^2 - \frac{12D_2}{D_4}}, \tag{3.25}$$

where Eq. (3.24) is valid for $D_4 = 0$. One can see that fourth-order dispersion permits the formation of a dispersive wave with double peaks on both sides with respect to the pump light, whereas third-order dispersion induces only a single peak. The dispersion wave emission induces the oscillatory tail on the CW background of the intracavity waveform, resulting from the modulation by beating of dispersive wave and the pump light. In addition, the dispersive wave formation causes soliton recoil accompanied by a soliton frequency shift relative to the pump frequency. The management of higher-order dispersion offers the potential of spectral extension and power enhancement even in the spectral ends of frequency comb; therefore, they can be used for f-$2f$ or $2f$-$3f$ self-referencing measurement in microresonator frequency comb [143].

Dispersive wave due to avoided mode crossing

Avoided mode crossing or anti-crossing effect is often observed in optical microresonators due to their multi-mode structure. Such mode crossing effects induce a local dispersion perturbation, which influences comb spectra as well as higher-order dispersion. Although it is known that strong avoided-mode-crossing occurring at the vicinity of the pump disturbs soliton formation [166], a local dispersion shift leads to attractive applications including deterministic single soliton generation [167] and dispersive wave emission [168]. In particular, dispersive wave emission induced by avoided mode crossings attracts many interests because the effect of the dispersive wave is well related to unique soliton formation such as a soliton crystal [169]. A modulated CW background results in the creation of a potential grid, which determines temporal and frequency spacing, and then it works as the lattice trapping optical pulse inside the resonators [170]. The local dispersion change associated with avoided mode crossing appears as strong suppression or enhancement of a few comb lines at crossing position, and the excess power due to dispersive wave also makes soliton recoil in the opposite direction against spectral spikes [168].

3.4.2 Normal group velocity dispersion

Phase-matched four-wave mixing by fourth-order dispersion

In the case of normal group velocity dispersion, a microresonator frequency comb cannot usually be observed with a CW pumping because of the absence of modulation instability. However, higher-order dispersion, especially even orders of dispersion, makes it possible to initiate four-wave mixing even in the normal dispersion microresonator. When the resonance mode located in a *weak* normal dispersion regime ($D_2 < 0$), positive fourth-order dispersion ($D_4 > 0$) compensates the normal dispersion and enables a resonant modulation instability (MI) process to occur far from the pump mode [Fig. 3.14(d)]. The parametric sideband generation via phase-matched FWM has been studied in fiber devices, and recently demonstrated in optical microresonators. The position of initial parametric sidebands can be approximately estimated from the zero-cross of the value of frequency difference $(\omega_{0+\mu} + \omega_{0-\mu} - 2\omega_0) = D_2\mu^2 + D_4/12\mu^4$, yielding,

$$\mu_{\mathrm{PS}} = \pm\sqrt{\frac{-12D_2}{D_4}}. \tag{3.26}$$

Here only even orders of dispersion play a role regarding the phase-matching condition even though D_{int} shows the cubic function affected by D_3 (odd orders of dispersion are negligible). This unique phase-matching scheme offers a practical advantage that it enables us to drastically extend the bandwidth of FWM with a combination of dispersion engineering. Moreover, subsequent cascade FWM forms comb clusters around the primary sidebands, called clustered comb [64]. The extension of spectral coverage assisted by fourth-order dispersion will be discussed, in Chapter 4 and Chapter 5 in this thesis.

Normal dispersion microcomb via avoided mode crossing

As described previously, modulation instability induced four-wave mixing is not usually allowed in the normal dispersion regime. Nevertheless, mode-locked frequency combs in normal dispersion were experimentally observed via avoided mode crossing effect, which creates local anomalous dispersion regime in overall normal dispersion system [171, 172]. These mode-locked states are interpreted as dark pulses [76], also called flat-topped pulses or platicons [173]. It should be noted that they can be classified by the pulse duration but not specified so far. The normal dispersion microresonator comb formation is expected to expand the comb bandwidth in a certain wavelength range, where the strong material dispersion dominates the total dispersion (e.g., visible wavelength region), via tailoring of dispersion and mode crossing. In addition, the higher conversion efficiency [75] and FSR controllability [158, 172] are unique features of the normal dispersion microcomb. Such a dark pulse state is also accessible by the bichromatic and amplitude-modulated pump. Chapter 6 highlights on the normal dispersion microcomb and its rigorous modeling and numerical simulation.

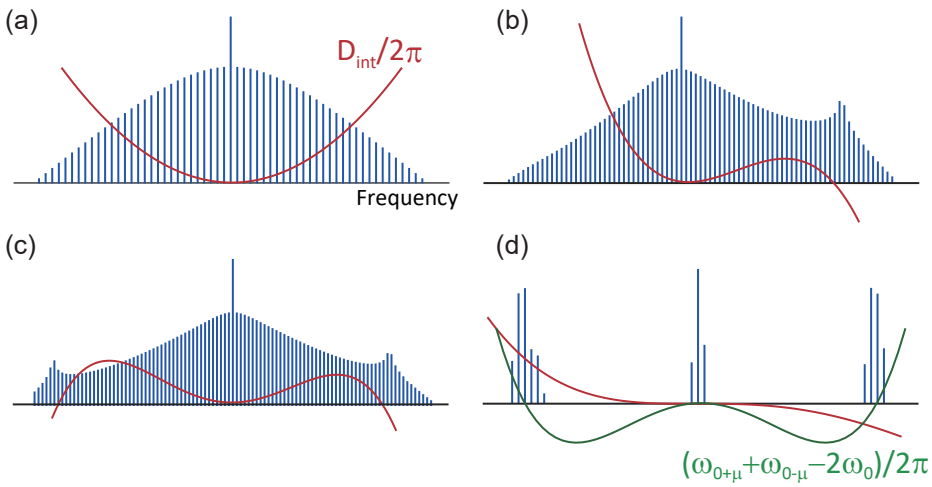

Fig. 3.14: Spectra of Kerr frequency comb (blue line) and corresponding dispersion D_{int} (solid red line). Dissipative Kerr solitons dominated by D_2 (a), with a single peak dispersive wave (b) and double peaks (c) affected by D_3 and D_4, respectively. (d) Clustered comb formed in a normal dispersion regime via D_4. Phase-matching points are indicated by the solid green line.

3.5 Summary

This chapter reviewed microresonator dispersion engineering and described a calculation method and a measurement method with the aim of microresonator frequency comb generation. As this chapter features WGM microresonators that have several kinds of resonator structures and candidate materials, FEM based dispersion simulation and precise dispersion measurement techniques are provided in detail. Moreover, it is revealed that microresonator dispersions, including higher-order dispersion and local dispersion change, influence the optical spectrum of the microresonator frequency comb decisively.

Chapter 4

All-precision-machining fabrication of dispersion engineered crystalline microresonator for microcomb generation

This chapter presents the dispersion-engineered crystalline microresonator fabrication method with ultra-precision machining for microresonator frequency comb generation. The first part mainly focuses on the all-precision-machining fabrication of ultrahigh-Q crystalline optical microresonators. By addressing the cutting condition and crystal anisotropy to overcome the large surface roughness, an ultrahigh-Q exceeding 100 million has been achieved solely by computer-controlled ultraprecision machining. Since the fully programmed-machining readily enables the precise geometry control, this approach promises to accelerate the study of dispersion engineering for microresonator frequency comb generation. The later part reports on the observation of octave-wide optical parametric oscillation (OPO) by a continuous-wave pump, that is, phase-matched FWM in a crystalline microresonator fabricated by ultra-precision machining. The dispersion of a high-Q MgF_2 microresonator was precisely engineered to satisfy the phase-matching condition assisted by higher-order dispersion. Experimental and numerical results presented in this chapter confirm that primary sidebands were generated with a frequency shift up to 140 THz and that secondary sidebands formed a localized comb structure, namely a clustered comb in the vicinity of the primary sidebands[*a*b].

[*a]Contents presented in this chapter have been published in "All-precision-machining fabrication of ultrahigh-Q crystalline optical microresonators," Optica, **7**, 6, 694–701 (2020) and "Octave-wide phase-matched four-wave mixing in dispersion-engineered crystalline microresonators," Optics Letters, **44**, 12, 3146–3149 (2019).

[*b]Fabrication of crystalline microresonators with precision machining is collaboration work with Kakinuma group (Keio Univ.). Note that the author led all the experiments and performed optical measurement and numerical simulation.

4.1 Introduction and motivation

A strong motivation of this work is to fabricate dispersion-engineered ultrahigh-Q crystalline microresonators using all-precision-machining techniques and demonstrate a large frequency shift optical parametric oscillation and a clustered comb, especially exceeding one-octave, using a fabricated resonator. As a resonator material, fused silica has been widely used to study the large frequency shift parametric generation thus far. However, the use of crystalline material (e.g., CaF_2 and MgF_2) as a resonator is straightforward because crystalline materials have a broad transparent window compared to fused silica showing strong optical attenuation due to water absorption band.

This work addresses the single-crystal cutting condition by considering a crystal anisotropy to obtain the ultrahigh-Q with precision machining alone. An orthogonal cutting experiment is performed to reveal the critical depth of cut for different cutting directions. Also, a precise cylindrical turning experiment gives the relationship between crystal anisotropy and surface quality after machining to realize nanometer-scale surface roughness with diamond turning. The experimental demonstration of optical parametric oscillation is performed based on the dispersion engineering technique and numerical simulation with Lugiato-Lefever equation (LLE). Moreover, the control of oscillation frequency by pump frequency tuning is also a challenge in this work.

4.2 Investigation of critical depth of cut

4.2.1 Miller index and crystal plane

The main purpose is to investigate the critical depth of cut; however, it will be helpful to introduce the Miller index at the beginning, which is usually used to define crystal plane and direction in crystallography. A single crystal is composed of infinite unit cells, which correspond to the simplest possible units in the crystal. These unit cells are categorized into seven fundamental patterns, and the ordered structure characterizes various optical and material properties of the crystal, such as refractive index, absorption, cleavage, plastic deformation, and crystal anisotropy [174, 175].

When the three lattice vectors $\boldsymbol{a}$, $\boldsymbol{b}$, and $\boldsymbol{c}$ are used to denote a unit cell, the following notation $[h\ k\ l]$ defines the crystal direction:

$$h\boldsymbol{a} + k\boldsymbol{b} + l\boldsymbol{c}, \tag{4.1}$$

where h, k, and l are relatively prime integer numbers. For instance, $[100]$ denotes the direction along the a-axis. A negative number indicates the opposite direction and is written as $[\bar{1}00]$. The crystal plane is also denoted with such

indices as well as the direction so that $(h\ k\ l)$ gives a plane that intercepts the three points $\boldsymbol{a}/h$, $\boldsymbol{b}/k$, and $\boldsymbol{c}/l$. With a cubic lattice structure, the $[h\,k\,l]$ direction is normal to the $(h\ k\ l)$ plane.

Figures 4.1(a) and 4.1(b) show examples of the Miller index and crystallographic images of CaF_2 and MgF_2 crystal. The difference in crystal structure influences the critical depth of cut and the cutting conditions. CaF_2 exhibits symmetrical cubic structure, whereas MgF_2 has a more complex structure, namely rutile structure. Besides, from the point of view of the optical property, MgF_2 is known as a uniaxial crystal, and it is slightly birefringent depending on the polarization and the direction of the incident light. Therefore, MgF_2 material is often cut with the optical axis perpendicular to the plane of the window to avoid birefringence in commercial products. Such window materials are referred to as c-cut or z-cut, in which the optical axis is normal to the (001) plane.

4.2.2 Definition of critical depth of cut

The critical depth of cut is one important parameter when fabricating a single crystalline microresonator. It is defined by the depth of cut where the transition from ductile-mode to brittle-mode cutting is observed when machining single-crystal material [176]. In the ductile regime, a smooth crack-free surface can be maintained as generating a continuous ribbon chip. This cutting process is considered more suitable for optical applications due to its ultra-smooth surface. On the other hand, the surface in the brittle regime is rougher and contains cracks; hence it is generally inadequate for optical applications. Nevertheless, CaF_2 and MgF_2 crystals are hard and brittle materials and have a crystal anisotropy, so they are challenging to cut. These features make it difficult to manufacture smooth optical elements with a designed shape such as spherical lenses and optical microresonators. In particular, high-Q microresonators require an ultra-smooth surface with a surface roughness of no more than a few nanometers. Thus, the critical depth of cut must be investigated before resonator fabrication to cut the crystal in the ductile mode regime.

4.2.3 Orthogonal cutting experiment

An orthogonal cutting experiment was performed to investigate the critical depth of cut. The experiment was carried out with an ultra-precision machining center (UVC-450C, TOSHIBA MACHINE), and a workpiece holder equipped with a dynamometer to detect the cutting force during the processing. A workpiece is a pre-polished single-crystal MgF_2 substrate with a size of 38 mm×13 mm and a thickness of 1 mm, which was fixed on the workpiece holder with a vacuum chuck. Figure 4.2(a) shows the experimental setup. The experiment was conducted with two different crystal planes, (001) and (010) by cutting in every 30° rotational direction, and the direction of 0° was set at [100] and [001], respectively [Fig. 4.2(b)]. The cutting slope D/L, which gives the cutting depth

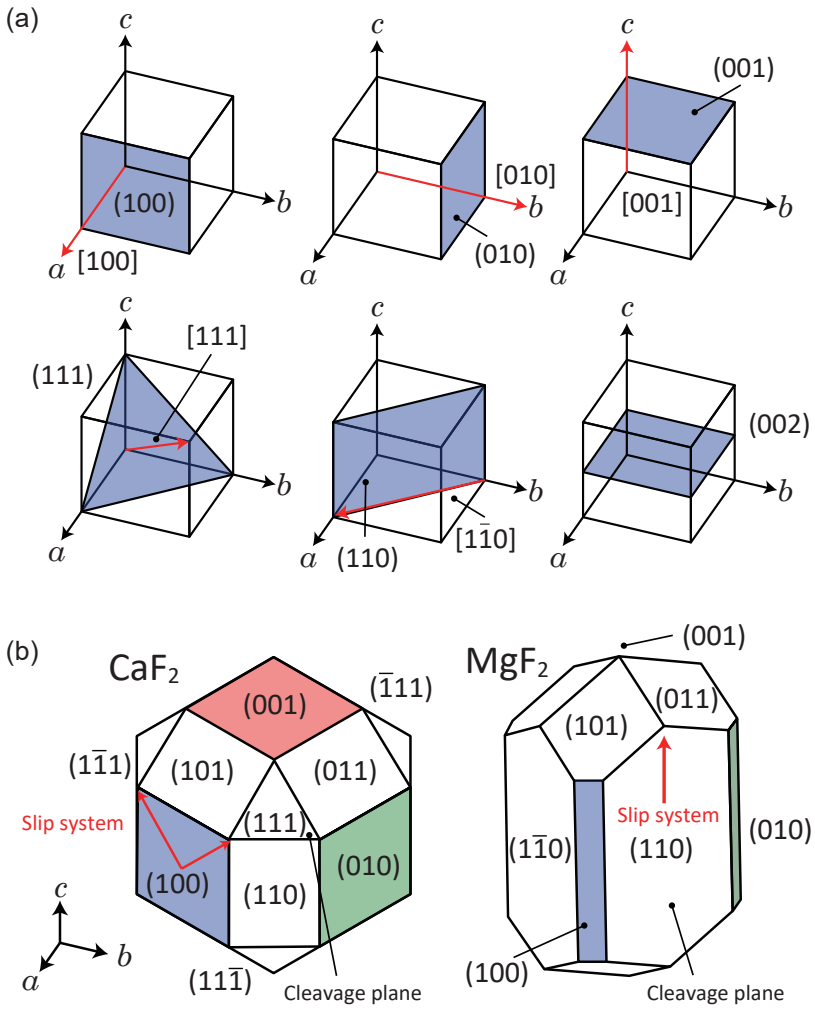

Fig. 4.1: (a) Examples of the Miller index, where $(h\ k\ l)$ and $[h\ k\ l]$ indicate the corresponding plane and direction, respectively. (b) Crystallographic images of CaF_2 and MgF_2 crystal. The red arrows indicate examples of slip system. The structure of CaF_2 is known as the cubic symmetry system, and MgF_2 is characterized by a more complex rutile structure.

to cutting length ratio, and the feed rate, were set at 1/500 and 20 mm/min, respectively, with a numerical control (NC) program. The cutting tool used in the test will be presented in more detail later.

The critical depth of cut, defined as the cutting depth at which the first brittle fracture appeared on the surface, can be measured using a scanning white light interferometer (New View TM6200, Zygo). Figures 4.2(c) and 4.2(d) show a microscope image and the reconstruction image of the machined surface. The black points of Fig. 4.2(d) indicate fractures or cracks that appeared on the surface. Note that MgF_2 has a complex rutile structure with a different crystal plane configuration from CaF_2; hence the two major planes are selected for the test to reveal the effect of crystal anisotropy.

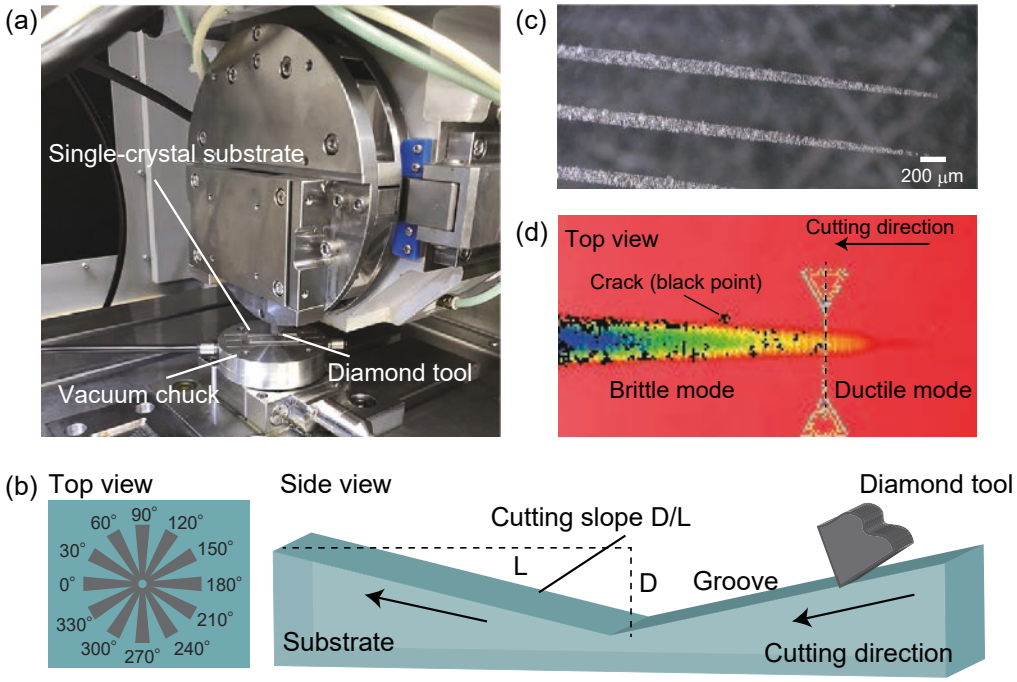

Fig. 4.2: (a) Experimental setup for orthogonal cutting to investigate the critical depth of cut in an MgF_2 single crystal. (b) Schematics of a single-crystal substrate and the cutting direction in the orthogonal cutting experiment. The cutting was performed in every 30° rotation direction (left panel), and the diamond tool cut a V-shaped groove with a slope of D/L (right panel). (c) Microscope image of the machined surface. (d) Reconstructed image of the machined surface using scanning white light interferometer. The critical depth of cut is given by the depth where the first brittle fracture appeared (black point).

Figure 4.3(a) shows scanning electron microscope (SEM) images of the surface condition of the (010) plane after orthogonal machining. Note that the yellow region is the original uncut surface. Even though the only difference is

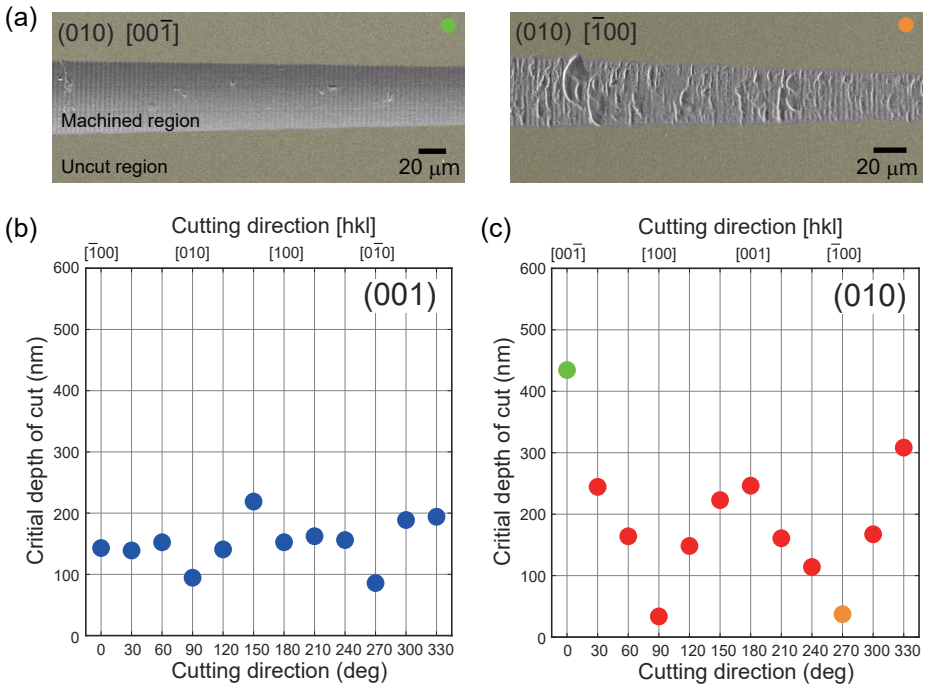

Fig. 4.3: (a) Scanning electron micrographs showing machined surfaces of a (010) plane with [00$\bar{1}$] direction (upper panel) and [$\bar{1}$00] direction (lower panel). The yellow shaded area and the gray area correspond to the original uncut surfaces and machined surfaces, respectively. The difference between the machined surface conditions is attributed to the crystal anisotropy of the MgF_2 crystal. (b) and (c) The measured critical depth of cut versus cutting direction on a (001) and (010) plane, respectively. In comparison with the (001) plane, the (010) plane shows a large variation in cutting direction due to crystal anisotropy. The results of 0° (green dot) and 270° (orange dot) correspond to the upper panel and lower panel in (a), respectively. These results confirmed that the measured critical depths of cut are consistent with images of the machined surface. In order to perform ductile mode cutting, the depth of cut must be kept below the critical depth of cut.

the cutting direction (i.e., $[00\bar{1}]$ and $[\bar{1}00]$), there is a significant impact on the surface quality of the machined region due to the crystal anisotropy. One can see large brittle fractures in the $[\bar{1}00]$ direction, whereas overall, the $[00\bar{1}]$ direction exhibited smooth surfaces. Figures 4.3(b) and 4.3(c) show the variation in the critical depth of cut as a function of cutting direction on each plane. On the (001) plane, the critical depth variation was approximately 120 nm, and the lower bound value was 86 nm in the 270° direction ($[0\bar{1}0]$ direction). On the other hand, the variation with the (010) plane was more significant than that with the (001) plane, and the lower bound also decreased (i.e., worsened). These considerable differences in critical depth of cut are consistent with surface observations, as shown in Fig. 4.3(a).

These results can be explained by taking the tensile model in single-crystal cutting into account, as shown in Fig. 4.4. The difference in critical depth of cut could be considered to originate from the slip system and the cleavage plane, as they are strongly related to the ductile-brittle mode transition. Cutting along the slip plane promotes ductile-mode cutting (i.e., plastic deformation), which contributes to the large critical depth of cut. On the other hand, the cutting force against cleavage induces crystal parting where brittle fractures are easily manifested.

The slip system and cleavage plane of single-crystal MgF_2 are (110)[001] and (110), respectively, as shown in Fig. 4.1; therefore the influence of cutting on the (001) plane on the critical depth of cut is less susceptible to the cutting direction because the cutting on the (001) plane is always perpendicular to both the slip system and the cleavage plane. With the (010) plane, however, a large variation in the cutting direction was observed, because the cutting periodically followed the same direction as the slip system (i.e., 0° and 180°). In contrast, the smallest (i.e., worst) critical depth of cut was obtained for directions of 90° and 270°, corresponding to $[100]$ and $[\bar{1}00]$, respectively. They are in a configuration where the cutting force is applied in a direction almost perpendicular to the cleavage plane (110) and its inversion symmetry $(\bar{1}10)$. As a result, a shallow depth of cut is needed to obtain a ductile mode for these directions. As a result, the experiment indicates that the depth of cut must be less than approximately 50 nm to maintain ductile mode cutting.

4.3 Ultra-precision cylindrical turning

4.3.1 Procedure of cylindrical turning

Based on the results of the orthogonal cutting experiment, cylindrical turning is performed to manufacture a crystalline cylinder workpiece. Since the cutting direction continuously changes in the turning process, the optimum turning parameters have to be investigated to achieve the smooth surface needed for a high-Q microresonator. A MgF_2 cylinder workpiece was prepared with an end-face orientation of (001) because a z-cut (c-cut) resonator is used to avoid optical

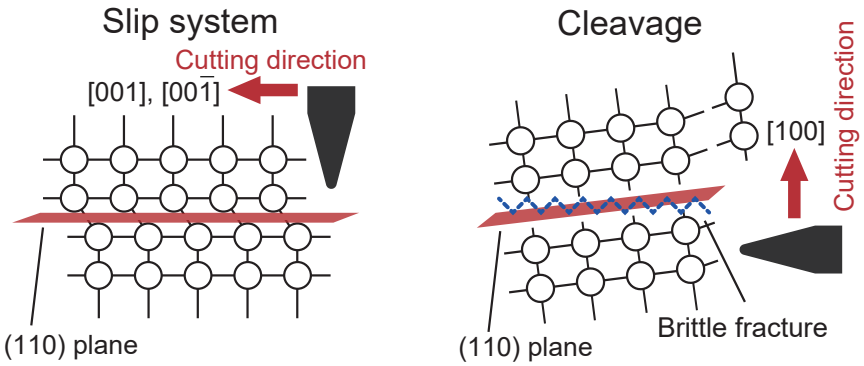

Fig. 4.4: Schematics of tensile stress model in MgF_2 crystal regarding cutting direction. Cutting along the slip system (110)[001] and the inversion symmetry (110)[00$\bar{1}$] promotes ductile mode cutting (left panel). Cleavage and subsequent brittle fractures are induced by the cutting force against cleavage plane (right panel).

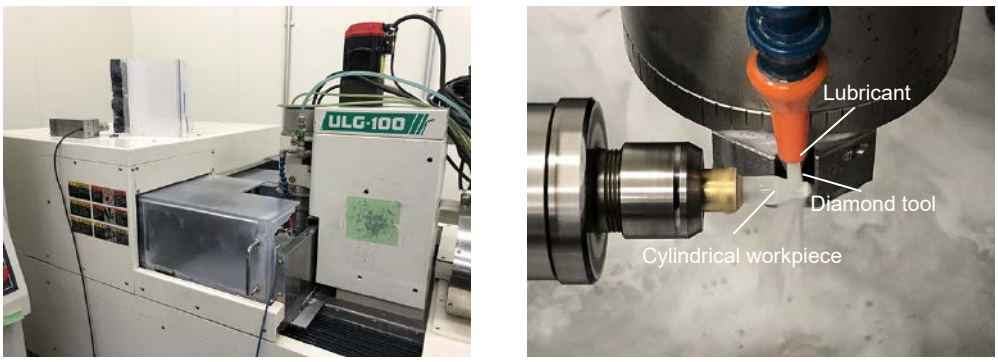

Fig. 4.5: Ultra-precision aspheric surface machine for cylindrical turning. A single crystal workpiece is fixed to a brass jig, and mounted on a vacuum chuck. Lubricant oil is used for manufacturing the microresonator.

birefringence.

Cylindrical turning was performed using an ultra-precision aspheric surface machine (ULG-100E, TOSHIBA MACHINE), as shown in Fig. 4.5. An MgF_2 workpiece with a diameter of 6 mm was fixed to a brass jig and then mounted on a vacuum chuck. The ultra-precision turning was conducted in the following three steps. Rough turning was initially undertaken to form the desired diameter (here 3 mm). It should be noted that this initial rough turning was performed in the brittle regime. Next, pre-finish cutting was conducted to remove the large cracks that occurred in brittle mode cutting with a removal thickness of 8 μm. Finally, finish cutting in the ductile mode completed the ultra-precise turning. The detailed cutting condition for each step is listed Table 4.1.

The effective cutting speed is given by the rotation speed multiplied by $2\pi R$, where R is the radius of the cylinder workpiece, and feed per revolution (mm/rev) is given by the feed rate (mm/min) divided by the rotation speed (min^{-1}). In this work, the rotation speeds were set at 500 min^{-1} and 1000 min^{-1} for 3 mm and 0.5 mm diameter workpieces, respectively. Nevertheless, it should be noted that the rotation speed is less important than the other parameters (i.e., feed rate, depth of cut, and the choice of the diamond tool) as regards machined surface quality [177] as discussed in more detail later.

Table. 4.1: Cutting condition for each step

	Rough turning	Pre-finish turning	Finish turning
Rotation speed (min^{-1})	1000	500 or 1000	500 or 1000
Feed rate (mm/min)	20	0.5	0.1
Depth of cut (nm)	2000	100	50
Removed thickness (μm)	—	8.0	2.0
Diamond tool	Tool #1	Tool #2	Tool #2

Single crystal diamond tool

Figure 4.6(a) shows schematics of the single-crystal diamond tool. Two types of single crystal diamond tools were used in this work, and their properties were as follows: Tool #1 had a 0.2 mm nose radius, a −20° rake angle, and a 10° clearance angle [Fig. 4.6(b)]; Tool #2 had a 0.01 mm nose radius, a 0° rake angle, and a 10° clearance angle [Fig. 4.6(c)]. Tool #1 had a negative rake angle and a large nose radius, which made it suitable for efficiently manufacturing millimeter size workpieces such as crystalline microresonators. Therefore, Tool #1 was used for the orthogonal cutting experiment and the rough turning stage in the ultra-precision turning. On the other hand, for the pre-finish and finish cutting, Tool #2 was used since a sharper edge with a rake angle of 0° enables us to achieve stable cutting because the small rake angle reduced the thrust force on the material [178]. Moreover, in terms of the choice of the cutting tool, a

smaller nose radius makes it possible to have a smaller contact area between tool and material during cylindrical turning, which helps to reduce any excess cutting force and leads to improved surface quality. However, tools with a small nose radius are more fragile, which gives them a short lifespan; hence it will be reasonable to use different tools for the rough turning and finish turning stages.

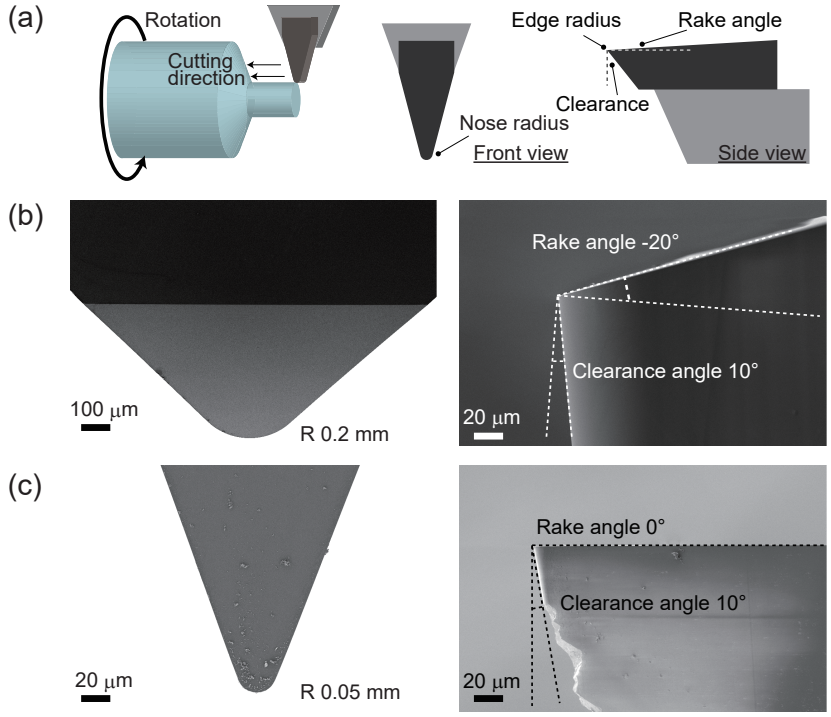

Fig. 4.6: (a) Relationship between cutting direction and tool shape of single crystal diamond tool. (b) SEM image showing Tool #1 used for an orthogonal cutting experiment and rough turning (c) SEM image of Tool #2 used for pre-finish and finish turning.

Cutting condition for single-crystal machining

Although the depth of cut at the finish turning step was readily set at 50 nm based on the result of the orthogonal cutting experiment, other factors, such as the rotation speed, feed rate, and diamond tool, should also be taken into account because these choices determine the effective cutting speed and cutting amount. In particular, previous studies have reported that the feed rate critically affects the quality of the machined surface, as does the combination of the tool radius and depth of cut [177, 179, 180]. These studies suggest that a fast feed rate induces brittle mode cutting if the depth of cut is kept below the critical value. In this work, thus, a relatively slow feed rate ($\leq$ 1 mm/min) is chosen when fabricating a smooth surface.

In addition, it is necessary to consider the relationship between the edge radius of the tool, the undeformed chip thickness, and the critical depth of cut, namely the size effect [181]. If the undeformed chip thickness is much smaller than the edge radius of the tool, the cutting process does not occur (the plowing effect occurs instead). The critical thickness at which material removal begins is called the minimum chip thickness, and chip formation occurs when the undeformed chip thickness reaches this critical value.

Furthermore, the undeformed chip thickness must not exceed the critical depth of cut, which indicates the boundary of the ductile-brittle transition to minimize excess surface roughness. Considering the discussion above, the depth of cut should exceed the tool edge radius and be smaller than the critical depth of cut. The tool edge radii of both Tool #1 and Tool #2 are less than approximately 10 nm. Hence, one can see that a depth of cut of 50 nm is a feasible value from the standpoint of the size effect.

4.3.2 Surface roughness measurement

The machined surfaces were observed using an optical microscope (VHX-5000, Keyence), as shown in Figs. 4.7(a) and 4.7(b). Clear boundaries can be identified in the micrograph images between the rough turning and finish turning regions. The surface roughness after cylindrical turning was measured using a scanning white-light interferometer (New View TM6200, Zygo). Surface measurement was performed at 15° intervals from the orientation flat [100] defined as 0° as shown in Fig. 4.7(c), and the measurement results are presented in Figs. 4.7(d) and 4.7(e). Here, an end-face orientation of an MgF_2 workpiece was (001), namely z-cut orientation. Unsurprisingly, the surface roughness after the rough cutting exceeded 200 nm for the entire cylindrical surface, as shown with red dots in Fig. 4.7(d). The large roughness was caused by the brittle-regime cutting. In contrast, the smoothness improved significantly after the finish cutting, which was performed under the ductile cutting condition. The magnified plot on a linear scale is shown in Fig. 4.7(e). These results confirmed that the turning condition for final cutting enabled us to achieve a smooth surface. Specifically, an excellent RMS roughness of below 2 nm was obtained at 18 observation points. The result also revealed an interesting feature of 90° periodicity, namely that specific observation points exhibited a slightly larger RMS roughness of 7.8 nm on average. Periodicity can also be seen in the micrograph shown in Figs. 4.7(a)-4.7(c); for instance, 135° exhibits a smoother machined surface than that in the 180° direction. This is evidence of the appearance of crystal anisotropy in MgF_2 crystal, as observed in the orthogonal cutting experiment.

Such a periodicity can also be understood from the slip system and cleavage configurations shown in Fig. 4.4. The relatively rough surfaces can be explained in terms of specific directions where the excess cutting force acts on the boundaries of cleavage planes. The 15° asymmetry is due to the rotation direction of the workpiece; the force on the cleavage plane exerts stress only in the clockwise

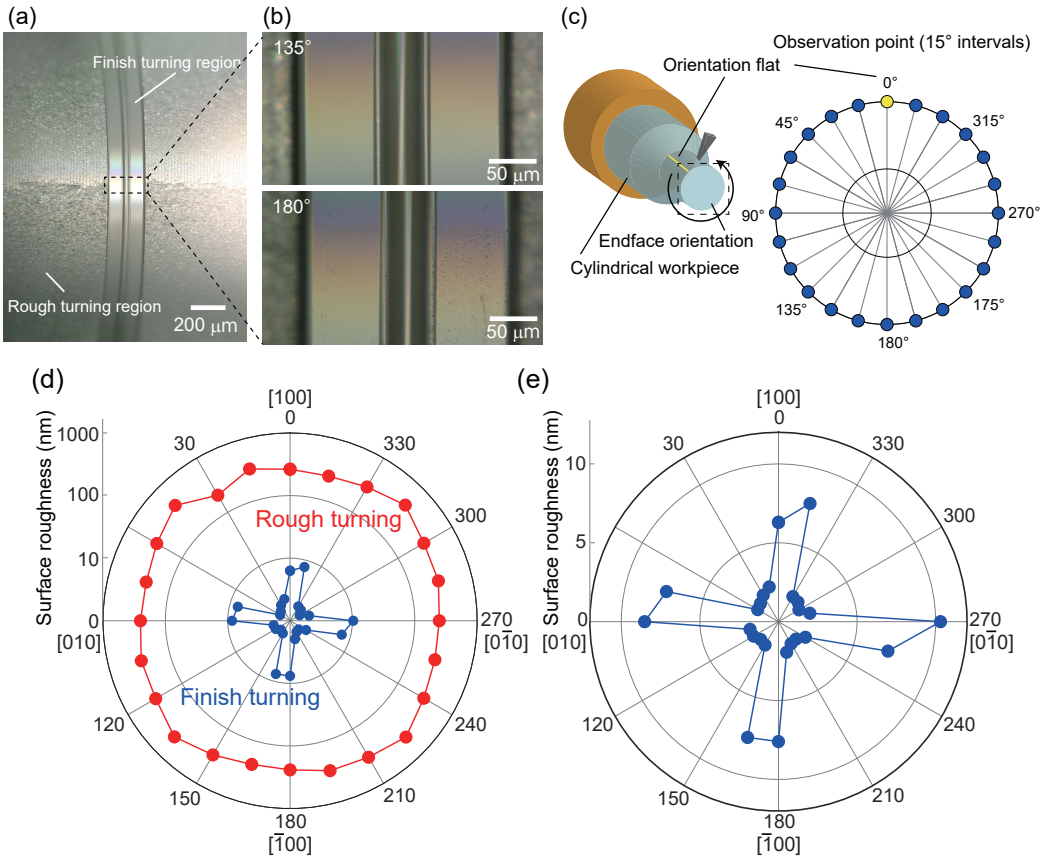

Fig. 4.7: (a) Micrograph showing a machined surface, where clear boundaries are observed between the rough turning and finish turning regions. The horizontal boundary in the rough turning region is evidence of the dependence of the cutting direction on the crystal anisotropy in MgF_2 single crystal. (b) Magnified views of the finish turning region in 135° and 180°, respectively. The machined surface of 135° is smoother than that of 180°, which agrees with the result of the surface roughness (RMS) measurement. (c) Schematic of surface roughness measurement. The yellow line and dot correspond to orientation flat [100] with an endface orientation of (001). The surface roughness at a total of 24 points was measured at 15° intervals. (d) Measured surface roughness (RMS) of the finish turning (red dots) and rough turning (blue dots) regions. A quarter symmetry is clearly observed in the finish turning condition due to crystal anisotropy. (e) The magnified plot on a linear scale of finish turning in (d).

direction (the opposite direction to workpiece rotation). There is nevertheless excellent surface integrity as long as the cutting remains on a cylindrical surface where the cutting force circumvents the crystal anisotropy.

The cylindrical turning presented here is a pre-process in microresonator fabrication. It should be noted that the measured roughness is the result of the implosion of a machined cylinder, not the dimensional resonator surface. However, the results enabled us to predict the surface of the resonator under the employed cutting conditions.

4.3.3 Fabrication and cleaning of microresonators

Crystalline microresonators are fabricated using the same ultra-precision machine as that used in the cylindrical turning experiment (ULG-100E, TOSHIBA MACHINE). Although the resonator diameter is determined after the finish cutting, the diameter can be precisely controlled by measuring the diameter and undertaking additional turning prior to microresonator fabrication. The resonator shape is carefully fabricated by feeding a diamond tool under the critical cutting depth. Here, the turning motion is fully and automatically controlled by the NC program. The manufacturing procedures of spherical and triangular WGM structure are shown in Fig. 4.8, where a finish turning condition was employed at the resonator shaping step. The total fabrication time is about ten hours, from rough turning to final shaping.

Once the fabrication has completed, the cleaning of the microresonator was conducted to remove lubricants and small chips attached to the surface. Proper cleaning is essential for obtaining a high-Q as well as optimized cutting conditions. A lens cleaning tissue is usually used to wipe the resonator, but there is the possibility that it might scratch or damage the resonator surface, which could be a critical problem in terms of degrading the Q-factor. Alternatively, to avoid unwanted damage on the resonator, ultrasonic cleaning can be employed. The cleaning procedure is as follows. First, an acetone solution is used to reduce the amount of oil lubricant. Then, the resonator is cleaned with ethanol or isopropanol. Next, a dust-free dry nitrogen blower treated the resonator surface. Finally, the resonator surface should be carefully observed using a stereomicroscope. This cleaning procedure can be repeated several times to ensure that no particles or chips remained close to the resonator surface.

In the case of the ultrasonic cleaning, the resonator is fixed in position with a jig and cleaned using a commercial ultrasonic cleaner with a frequency of 40 kHz (Bransonic M1800-J, BRANSON). The cleaning has continued for several minutes. After the cleaning, one can observe small particles floating in the solvent, which convinced us that the lubricant or attached specks of dust and particles had been removed from the crystalline microresonator. The use of an ultrasonic cleaner enables us to clean the surface without touching or rubbing it. It is also a great advantage for fully automated fabrication combined with ultra-precision turning.

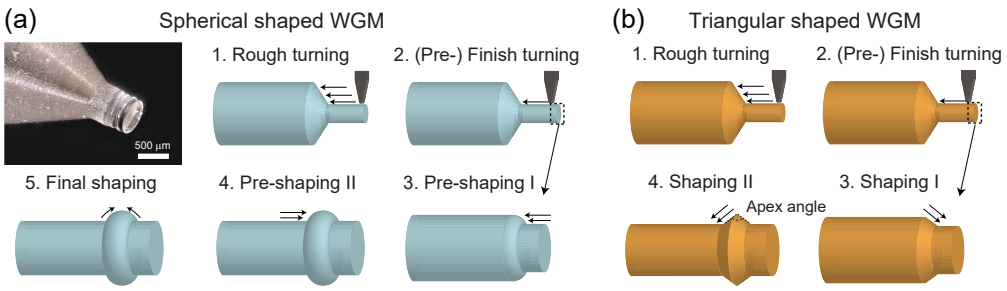

Fig. 4.8: (a) and (b) Fabrication flow of spherical and triangular WGM microresonator when using ultra-precision turning. First, a rough turning determines the approximate diameter of the resonator. Next, pre-finish and finish shaping with ductile mode cutting are used to realize a cylindrical surface that is smooth and entirely crack-free. Finally, fully-programmed shaping steps are performed to fabricate the designed resonator structure.

4.4 Quality factor and dispersion measurement

4.4.1 Spherical-shaped WGM microresonator

First, the Q-factor and dispersion were measured in two different microresonators fabricated with ultraprecision machining, MgF_2 and CaF_2 crystalline resonators. The diameters were 508 µm for MgF_2 resonator, and 512 µm for CaF_2 resonator, whereas they have the same curvature radii of 36 µm. SEM images of the fabricated MgF_2 microresonator are shown in Figs 4.9(a)-4.9(c).

Although the two resonators were fabricated with the same motion program and cutting conditions, their diameters differ slightly due to the positioning misalignment of a workpiece that was mounted manually. However, there is the possibility to solve this problem by installing a real-time diameter measurement system or introducing zero adjustments of the workpiece offset position. The additional measurement and turning of the workpiece should achieve the precise control of the diameter at the sub-micrometer level.

The Q-factor measurement was performed by using a wavelength-tunable laser, a polarization controller, and a photodetector. The light was coupled via a tapered fiber with careful adjustment of the gap between the resonator and the fiber waveguide. A calibrated Mach-Zehnder interferometer was used as the frequency reference. Figures 4.9(d) and 4.9(e) show the measured transmission spectra of the fabricated microresonators. The full-width at half-maximum (FWHM) linewidth of the MgF_2 resonator was 1.40 MHz, which corresponds to a loaded $Q = 1.39 \times 10^8$ at a wavelength of 1545 nm. Also, the CaF_2 resonator had a linewidth of 2.53 MHz at 1546 nm, corresponding to $Q = 7.67 \times 10^7$. Noted that the comparably high-Q values were recorded in different wavelength regions for other resonant modes. The obtained Q, which exceeded 100 million, is so far the highest value recorded in a crystalline WGM microresonator

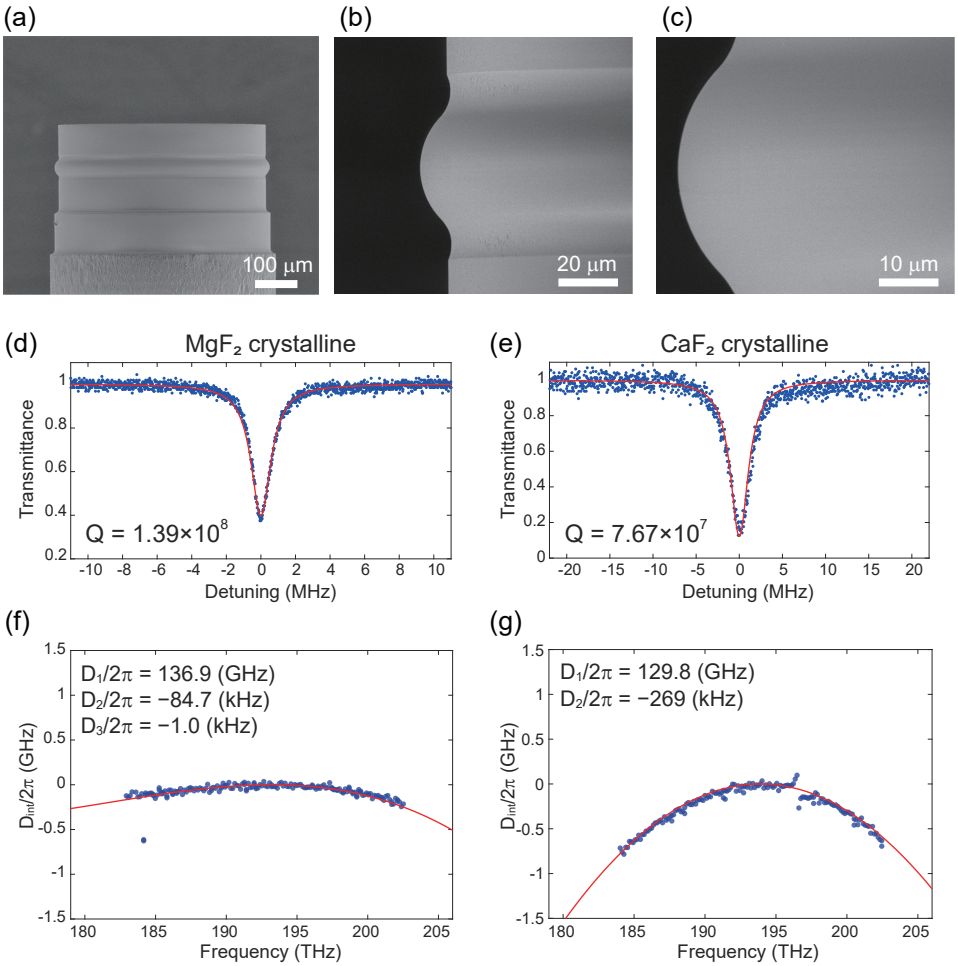

Fig. 4.9: Q-factor and dispersion measurement of crystalline microresonators fabricated by ultra-precise turning. (a) SEM image of a fabricated MgF_2 microresonator with a diameter of 508 μm and a curvature radius of 36 μm. (b), (c) Magnified views of the resonator. (d) Normalized transmission spectra of the fabricated MgF_2 microresonator. The Lorentzian fitting (red line) yield loaded a Q value of 139 million. (e) Normalized transmission spectra of the fabricated CaF_2 microresonator. The fitting curves give a loaded Q for the fundamental mode of 76.7 million. (f), (g) Measured dispersion D_{int} versus frequency. The red curve indicates the calculated dispersion of the fundamental TM mode, which agrees well with the experimental result.

fabricated solely by ultra-precision machining without a conventional polishing process. In other words, this approach has overcome the need for skilled manual techniques throughout the fabrication process to obtain ultrahigh-Q crystalline microresonators.

The dispersion measurement was performed to confirm that the machining process can be compatible with dispersion engineering techniques. Figures 4.9(f) and 4.9(g) show the measured integrated dispersion, D_{int}, versus frequency in each resonator. The dispersion was measured by a wavelength meter method (cf. §3.3.2). The measured dispersion agrees well with the theoretical dispersion calculated with the finite element method (FEM), and these results indicate that ultraprecision turning enables us to obtain the designed resonator shape.

4.4.2 Triangular-shaped WGM microresonator

Figure 4.10(a) and 4.10(b) show SEM images of a fabricated triangular-shaped CaF_2 microresonator whose triangular structure is designed with an apex angle of 120°. The resonator diameter was 502 μm. The experiment was performed in the same manner as the previous section. The Q value was 1.03×10^7 at 1552.2 nm as shown in Fig. 4.10(c). The measured dispersion also agrees with the calculated result, which exhibits strong normal dispersion compared with spherical shaped WGMs [Fig. 4.10(d)]. This fact is attributed to the fragility of the edge of the apex or remaining specks of dust, thereby increasing scattering loss.

4.5 Dispersion engineering and numerical simulation of octave-wide parametric oscillation

Next mission is to realize the large frequency shift parametric oscillation in a manufactured microresonator. Here, the principle of dispersion engineering and numerical simulation will be discussed. The presence of dispersion in a microresonator changes the relative position of the resonance frequencies. Assuming that μ represents the relative mode number (pump mode is $\mu = 0$), all the resonance frequencies are given by the Taylor expression: $\omega_\mu = \omega_0 + \sum(D_j\mu^j)/(j!)$ $(j \geq 1)$. Consequently, integrated dispersion D_{int} is used to express the dispersion with a function of μ,

$$D_{\text{int}} = \omega_\mu - \omega_0 - \mu D_1 = \frac{1}{2}D_2\mu^2 + \frac{1}{6}D_3\mu^3 + \frac{1}{24}D_4\mu^4 + \cdots, \tag{4.2}$$

as introduced in Eq. (3.15). Higher than fourth-order dispersion (D_5, $D_6, \cdots$) is less important in this work, and therefore disregarded here. As explained in §3.4.2, the phase-matched mode number for initial parametric sidebands can be estimated simply by using frequency difference value defined as $(\omega_{0+\mu} + \omega_{0-\mu} -$

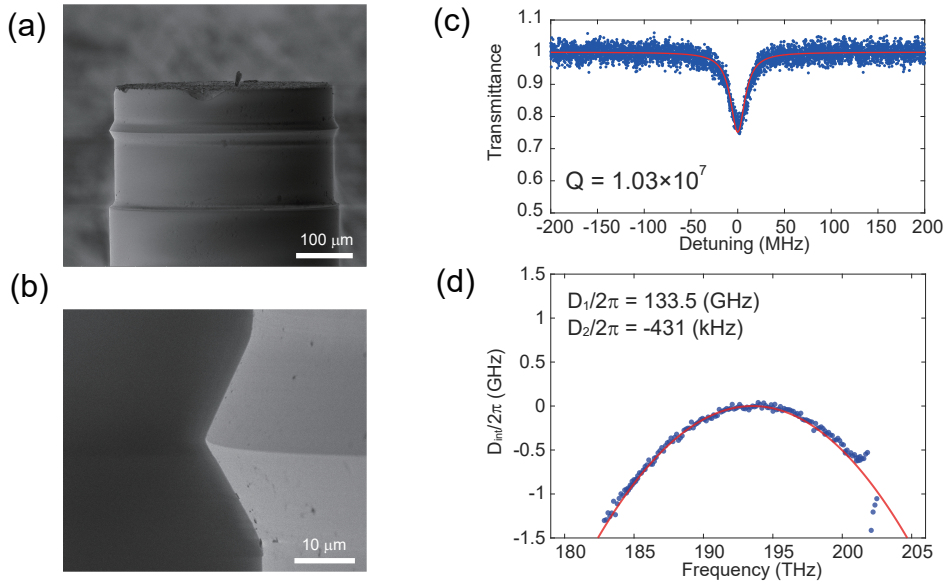

Fig. 4.10: (a) and (b) SEM images of fabricated triangular-shaped CaF_2 microresonator with an apex angle of 120°. (c) Normalized transmission spectrum, yielding a loaded Q of 10.3 million. (d) Measured dispersion D_{int} versus frequency showing good agreement with the calculated dispersion for the fundamental mode (red curve).

$2\omega_0) = D_2\mu^2 + (1/12)D_4\mu^4$, where the the sign of D_2 is negative (i.e., normal dispersion) and that of D_4 is positive. To satisfy the phase-matching condition, second-order dispersion must be normal but weak because the fourth-order dispersion compensates the normal dispersion far from the pump mode. Thus, a weak normal dispersion, which is close to the zero dispersion regime, is a critical condition for the phase-matching. As shown in Fig. 3.6, an upper limit of the resonator radius of an MgF_2 resonator to be in the normal dispersion regime is given as 350 μm, and therefore the resonator diameter should be lower than 700 μm in terms of dispersion engineering. Noted that the calculation method introduced in §3.1.4 was adopted in order to simulate microresonator dispersion. The dispersion calculation yields the desired resonator diameter of ∼500 μm to achieve an octave-wide FWM by using a 1550 nm pump.

To obtain the parametric oscillation, the bandwidth of the parametric gain envelope must overlap the resonant modes in the resonator. Parametric gain bandwidth in a microresonator has been analytically studied in Ref. [67], and it was shown that the gain bandwidth tends to decrease as the frequency shift becomes large. If the gain bandwidth falls below 1-FSR of the resonator, the possibility of phase-matched FWM also significantly decreases. Then, a numerical simulation was conducted using the LLE to confirm the possibility of the parametric oscillation. The LLE including higher-order dispersion is given as Eq. (2.48).

Figure 4.11(a) shows the dispersion used in the LLE simulation. The solid red

line and the solid green line show the integrated dispersion and the frequency difference value (i.e., phase-matching condition), respectively. The quality factor in this simulation follows our experimental result that will be described later, and other parameters are obtained by FEM calculation and from physical values. From the zero-cross point of the solid green line, it is possible to estimate the position of the primary sidebands via degenerate-FWM, which is approximately at mode number $\mu = \pm 510$. The values correspond to the frequency shift of 70 THz from the pump frequency, and they reach a one-octave frequency shift with 1550 nm pumping. Figure 4.11(b) shows the simulated spectra at different normalized detuning values $t_R\delta_0$. When the detuning reached the threshold, primary sidebands were generated at the theoretically predicted wavelength that corresponds to the mode number $\mu = \pm 510$. Finally, the pump and the oscillated sidebands formed three clustered combs as expected.

Even though the clustered comb can be generated via degenerate-FWM from each primary line, the high-frequency side of primary sidebands is located in a strong normal dispersion regime where FWM could not be generated due to a lack of modulation instability (MI) gain. However, the formation scheme for a clustered comb is explained as follows: after primary sideband (signal and idler pair) generation, secondary sidebands are generated via degenerate-FWM from one primary sideband experiencing anomalous dispersion, which is ordinarily lower frequency (longer wavelength) signal light. Once the secondary sidebands have been generated, non-degenerate FWM will occur and form other comb lines in the vicinity of the idler and pump lights.

4.6 Experimental demonstration in a dispersion engineered crystalline microresonator

With the numerical simulation in mind, an experimental demonstration was performed in an MgF_2 crystalline microresonator that was fabricated by using ultra-precision machining.

4.6.1 Characterization of crystalline magnesium fluoride microresonator

The MgF_2 microresonator has a diameter of 508 μm and a curvature radius of 36 μm, corresponding to a 137 GHz FSR, as described in §4.4. First, the precise dispersion measurement (cf. §3.3.3) was performed to evaluate the dispersion again, and more importantly, to identify the desired transverse mode that meets the condition of parametric generation. Figure 4.12(a) shows the transmission spectrum around 1550 nm measured with a wavelength-tunable laser. There are several different mode families, and the FSR of the fundamental mode is indicated as red circles. The measured Q-factor of the pump mode (i.e., $\mu = 0$) was 8×10^7. Figure 4.12(b) shows the mode structure of all the resonance modes,

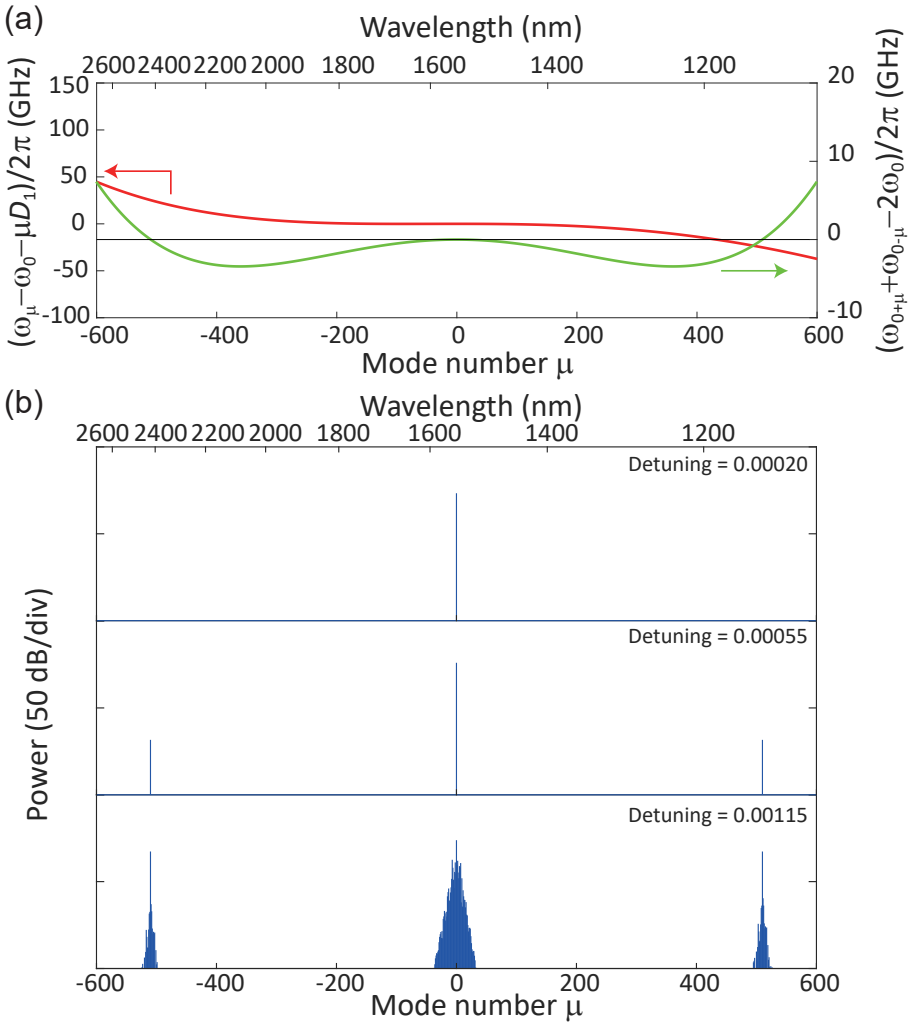

Fig. 4.11: (a) Calculated integrated dispersion D_{int} (solid red line) and frequency difference value $(\omega_{0+\mu} + \omega_{0-\mu} - 2\omega_0)$ (solid green line) of fundamental TE mode. The points at which the green line crosses black reference line predict the phase-matched wavelength. (b) Simulation results with increasing pump detuning. The used parameters are as follows; $Q_{\text{int}} = 1 \times 10^8$, $Q_{\text{ext}} = 4 \times 10^8$, $n = 1.37$, $n_2 = 0.9 \times 10^{-20}$ m^2/W, $A_{\text{eff}} = 34.8$ μm^2, and $P_{\text{in}} = 300$ mW. The FSR and dispersion values are $D_1/2\pi = 136.9$ GHz, $D_2/2\pi = -52.9$ kHz, $D_3/2\pi = -1.14$ kHz, and $D_4/2\pi = 2.45$ Hz.

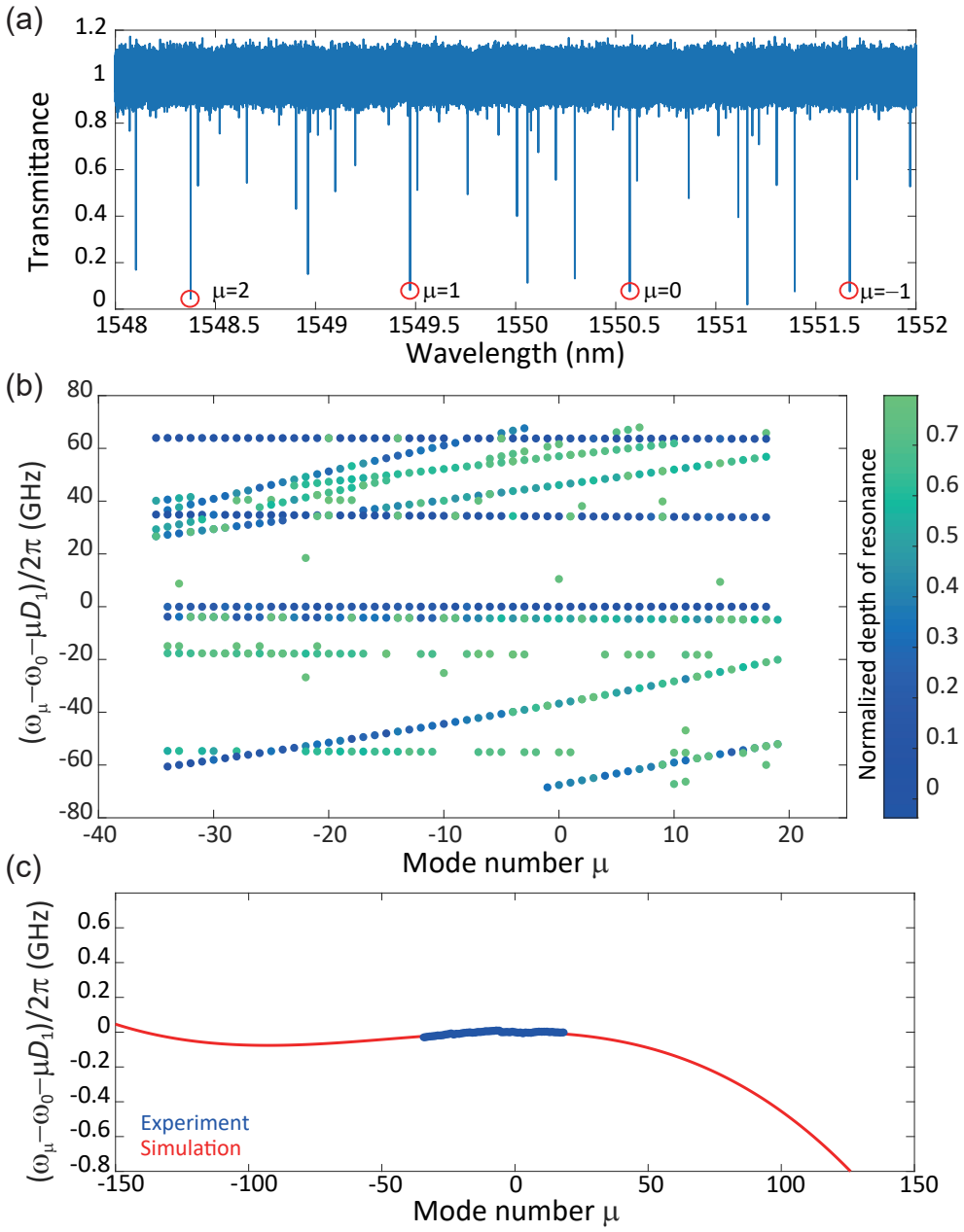

Fig. 4.12: (a) Transmission spectrum of fabricated MgF_2 microresonator. Red circles indicate resonances belonging to the same mode family that we used as pump mode in the comb experiment. (b) Experimentally observed mode structure, where dots show the position of resonances, in a wavelength from 1530 nm to 1590 nm, limited by the bandwidth of mode-locked fiber comb source. (c) The calculated dispersion and the measured result of 55 resonances for fundamental TE mode.

and it enables us to identify the pump mode. The experimental (blue dots) and simulated dispersion (solid red line) of a fundamental TE mode are plotted in Fig. 4.12(c). The measured dispersion agrees well with the calculated dispersion $(\omega_\mu - \omega_0 - D_1\mu)/2\pi$, which confirmed that the technique of ultraprecision machining made it possible to fabricate a pre-designed resonator shape.

4.6.2 Observation of octave-wide optical parametric oscillations and clustered combs

Figure 4.13 shows the experimental setup for the observation of optical parametric oscillation. The input CW laser was amplified using an EDFA, and the polarization was adjusted using a polarization controller. After splitting the output light with optical couplers, three OSAs were used to cover the octave-wide wavelength. For only above 2400 nm wavelength, the low-loss mid-infrared optical fiber was used that shows broad transmission up to 4.5 μm. First, the resonant mode $\mu = 0$ (1550.56 nm) was pumped with an input power of 350 mW. With careful tuning of the pump wavelength, stable idler and signal sidebands were observed at the wavelengths of 1140 and 2425 nm, respectively, as shown in Fig. 4.14(a). Figure 4.14(b) shows a magnification of spectra of interest, and it confirms that high-frequency sidebands formed a clustered comb with a 1-FSR mode spacing. Unfortunately, the secondary sidebands in the vicinity of the pump line were concealed by the amplifier noise of the EDFA. Next, the primary sidebands were observed with wavelengths of 1137 and 2433 nm with the further tuning of the laser wavelength to the adjacent resonant mode of the same mode family, namely $\mu = 1$ (1549.47 nm) [Fig. 4.14(c)]. These experimental observations agree well with the simulation results, and the frequency shift of the FWM sidebands exceeds one-octave, which is the largest frequency difference up to 140 THz in this experiment.

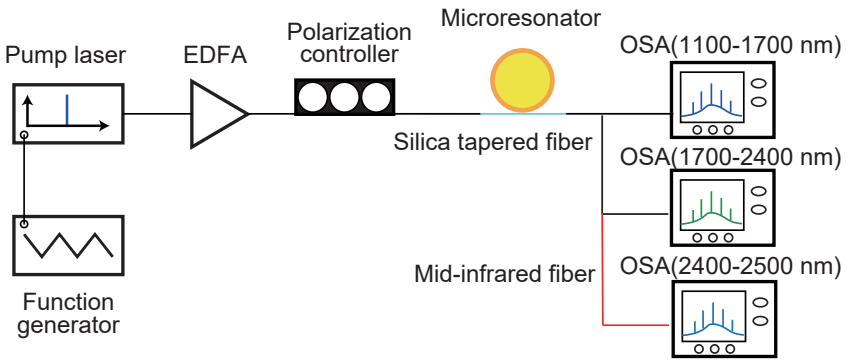

Fig. 4.13: Experimental setup for observation of octave-wide parametric generation. EDFA, erbium-doped fiber amplifier. OSA, optical spectrum analyzer. Mid-infrared fiber was used above a 2.4 μm wavelength to avoid unwanted attenuation.

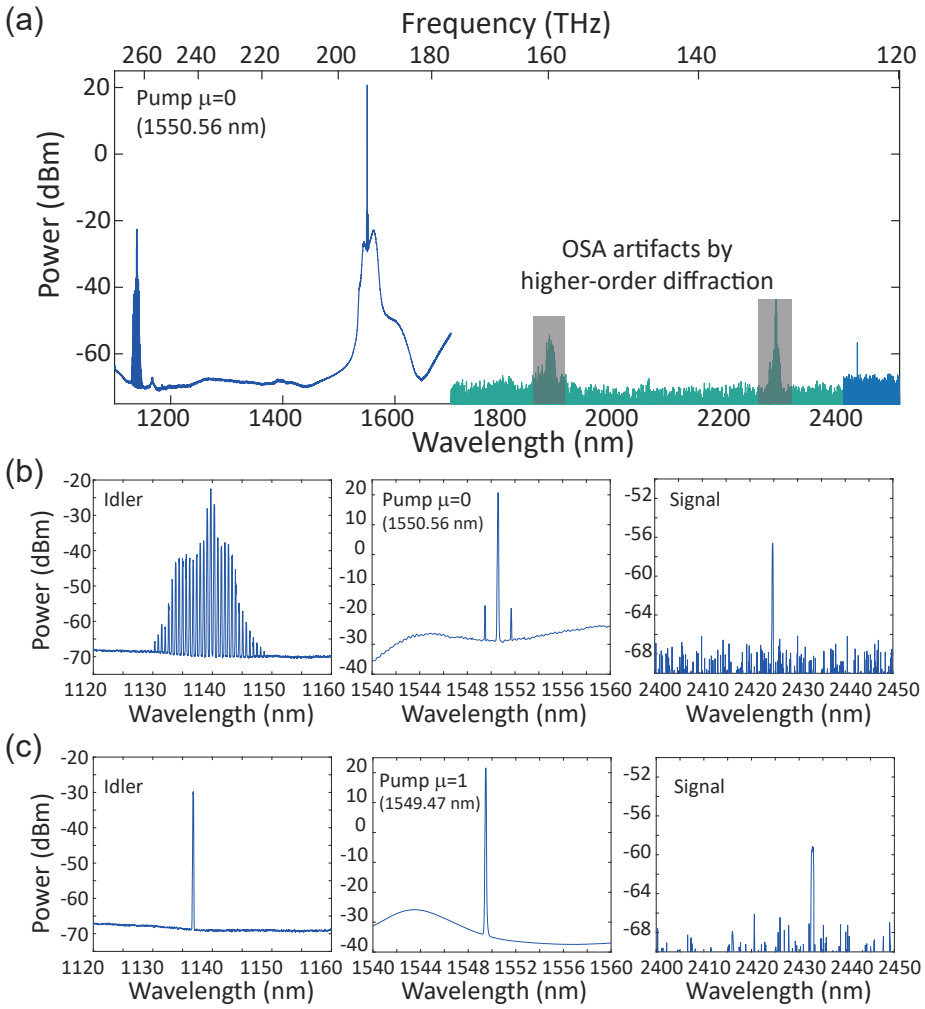

Fig. 4.14: (a) Experimentally observed spectrum at a pump mode $\mu = 0$ (1550.56 nm) when using different OSAs (depicted in different colors). The gray shaded signals indicate the OSA artifact noises. (b) Detailed spectra of interest, which show a clustered comb formation in the vicinity of 1140 nm and the pump wavelength, and that also confirmed the signal wavelength at 2425 nm. (c) Observed spectra when pumping in an adjacent mode $\mu = 1$ (1549.47 nm), indicating an FWM pair of 1137 and 2433 nm.

Figure 4.15 shows the comparison of the theoretically predicted phase-matched wavelength and the experimentally measured wavelengths (blue and red circles). These results confirmed that the oscillation wavelength could be tunable by only changing the pump wavelength, as reported in previous works [64, 67]. In this experiment, the pump wavelength is limited to only around 1550 nm because of the wavelength range of the used narrow-linewidth laser; however, in practice, there is the potential for obtaining larger frequency sideband as the theoretical prediction[*c].

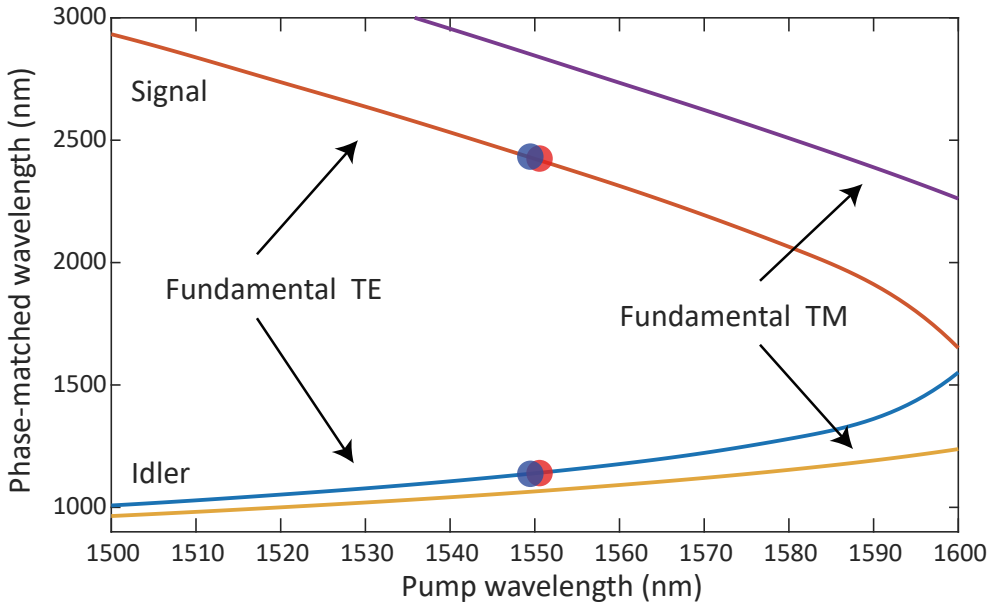

Fig. 4.15: Simulated phase-matched wavelength of fundamental mode (solid lines) as a function of the pump wavelength in MgF_2 used in this work. Experimental plots are shown as blue and red circles.

4.7 Discussion and summary

4.7.1 Towards further Q-factor improvement in ultraprecision machining

Theoretical limitation by surface roughness

This part addresses the possibility of further improvement of the *Q*-factor in ultraprecision machining. When omitting the coupling rate between the resonator and the waveguide, the intrinsic *Q*-factor is determined by several contributions

[*c]Almost at the same time as this work, Ref. [66] reported the observation of discrete wavelength tunability over an optical octave from 1083 nm to 2670 nm, and the signatures of spectral components over 3800 nm.

as,

$$Q_{\text{int}}^{-1} = Q_{\text{mat}}^{-1} + Q_{\text{surf}}^{-1} + Q_{\text{scatt}}^{-1} + Q_{\text{rad}}^{-1}, \tag{4.3}$$

where Q_{mat}^{-1} is determined by material absorption, Q_{surf}^{-1} and Q_{scatt}^{-1} are determined by surface absorption and scattering loss, respectively. In particular, scattering loss is mainly induced by surface roughness, dust particles, and subsurface damages. The radiation (tunneling) loss is given by Q_{rad}^{-1} that is linked to the curvature radiation limit, and this loss is significant only with resonators having a diameter of several micrometers. Since measured Q-factor can readily reach 10^9 by polishing millimeter-scale fluoride crystalline resonators, the effect of Q_{mat}^{-1}, Q_{rad}^{-1}, can be negligible [6]. Hence, Q_{surf}^{-1} is one possible reason for this, but single crystals such as MgF_2 and CaF_2 inhibit the diffusion of water into the crystal lattice, which makes Q_{surf}^{-1} negligible in our case [7].

Therefore, Q_{scatt}^{-1} should be focused as a fundamental limitation of ultra-precision machining. The maximum Q-factor as regards surface roughness can be estimated theoretically as [7, 182]:

$$Q_{\text{scatt}} \approx \frac{3\lambda^3 R}{8n\pi^2 B^2 \sigma^2} \tag{4.4}$$

where R is the resonator radius, n is the refractive index, B is the correlation length, and σ is the surface roughness (RMS). Figure 4.16 shows the maximum Q-factor versus surface roughness and correlation length of an MgF_2 resonator. Theoretically achievable values for ultra-precision machining correspond to Q values of $10^7 - 10^9$, which are consistent with measured Q-factors. It should be noted that the surface roughness is an experimentally observable parameter, whereas the correlation length is rather difficult to observe directly due to the spatial resolution of the instrument. Then, Figure 4.16 employs the correlation length value in the range of a few tens to hundreds of nanometers, as discussed in [183]. This result indicates that the roughness of the machined surface could limit the present Q. A possible way to improve the surface roughness and the correlation length is to optimize the cutting parameters, for example, by using a smaller depth of cut and a lower feed rate. Specifically, ideal conditions are believed to realize an ultrasmooth surface for the entire cylindrical position, and consequently eliminate the effect of crystal anisotropy.

Subsurface damage caused by diamond turning

Subsurface damage can occur during machining of a single crystal, and so it has been intensively studied in the field of micromachining and material science [185]. Such underlayer damage could degrade Q in the same way as surface scattering; therefore, not only the surface but also the underlayer should be investigated for the detailed discussion. The surface and the subsurface damage of the machined resonator were observed using an SEM and a transmission electron microscope (TEM). And the results were compared with the polishing results. For TEM measurement, the samples were cut into pieces of approximately

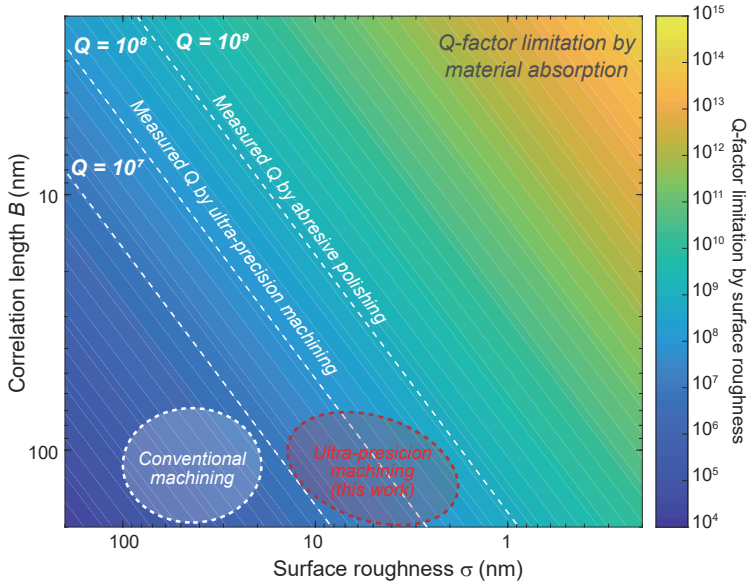

Fig. 4.16: Q-factor limitation caused by surface scattering loss in MgF_2 crystalline microresonators derived from Eq. (4.4) (λ=1550 nm and $R = 250$ μm). The dashed contours show roughly estimated value from our measurement and previous studies [7, 182, 183].

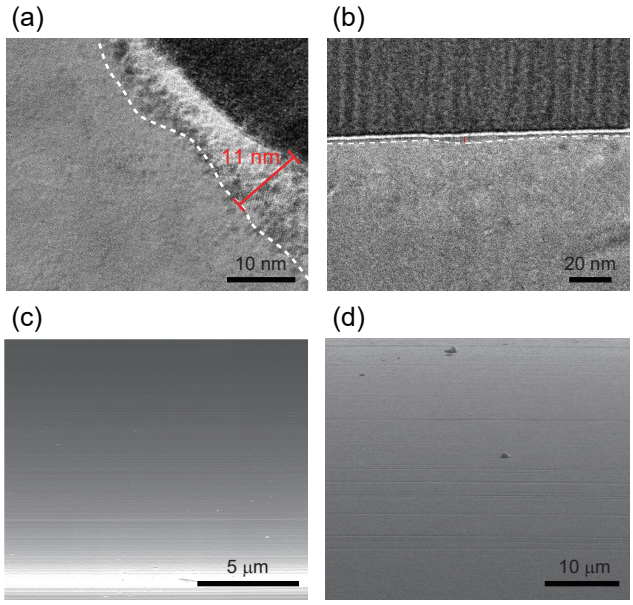

Fig. 4.17: (a), (b) TEM images of the subsurface damage of machined and polished single crystal samples, respectively. The subsurface damage is described in detail in Ref. [184]. (c), (d) SEM images of the surface condition after the machining and polishing processes, respectively.

0.1 mm×0.1 mm from the cylinder workpieces. For comparison, a polished CaF_2 microresonator, yielding a Q of 1×10^9, was prepared.

Figures 4.17(a) and 4.17(b) are TEM images of a machined surface and a polished surface, respectively. The subsurface damage with a depth of 11 nm was clearly observed in the machined sample; on the other hand, no significant damage was observed in the sample fabricated with polishing. These results suggest that the difference in the subsurface layer could influence the Q-factor obtained with the ultra-precision turning and polishing method. Figures 4.17(c) and 4.17(d) show the SEM images of machined and polished surfaces, respectively. On the machined surface, one can see that chips have adhered, and there are periodic tracks caused by the regular motion of the ultraprecision lathe. However, the polished surface is very smooth, although a few grooves are irregularly observed as the evidence of the manual process. It is generally known that the subsurface damage mechanism strongly depends on the crystal properties and cutting condition, and the efforts to reduce the subsurface damage are described elsewhere [186]. The reduction of underlayer damage could also help to improve the present Q.

4.7.2 Conversion efficiency and measurable power of parametric oscillation

Experimentally observed power of the lower frequency (longer wavelength) sidebands ranges from very weak to barely measurable compared with that on the pump and higher frequency sideband, whereas the optical power in the simulation is at the same level as a high-frequency side. In fact, the power of the longer wavelength component is about three orders of magnitude lower than that of a shorter wavelength component. The reason for this can be explained as follows: the most probable reason is the strong material absorption of silica above 1.9 μm. Although the fluoride material used as a resonator is transparent even at mid-infrared wavelengths, the tapered fiber and optical coupler mainly used in this experiment were made of silica. The attenuation of standard silica fiber at 2.4 μm is typically 1000 times stronger than at 1.55 μm. (>1000 dB/km at 2.4 μm and <1 dB/km at 1.55 μm). Although the length of the tapered region was about 5 ∼ 10 cm, the rest of the fiber in this experiment is several meters long and contributes to the strong attenuation of the signal. Unfortunately, there has been little study on the attenuation of mid-infrared light in silica *tapered* fiber, but the signal around 2.4 μm would be attenuated while propagating thorough the silica fiber. The second reason is the phase-mismatch between the tapered fiber and the WG mode because the waist of the tapered fiber is optimized for a 1550 nm pump wavelength. Therefore, the coupling efficiency decreases at wavelengths far from the pump mode. Wavelength dependent coupling efficiency can be simply estimated from the difference of effective refractive indices for tapered fiber and WG mode. For the 1.55 μm band, a difference of effective index Δn is 0.007 (where $n_{\mathrm{fiber}} = 1.354$, $n_{\mathrm{WGM}} = 1.361$). On the other hand,

for 2.4 μm band, Δn is 0.098 (where $n_{\text{fiber}} = 1.257$, $n_{\text{WGM}} = 1.355$). This result describes the value of phase-mismatch between tapered fiber and WG mode is larger in the 2.4 μm band than in the 1.55 μm, and thus the coupling efficiency is also smaller at 2.4 μm.

A simple way to overcome the problem is to utilize low-OH silica fiber as a tapered fiber coupler as in a previous work that reported Kerr comb generation at a wavelength of 2.45 μm [187]. However, the tapered region should be optimized for the pump wavelength even with this method. Another solution, although it demands a more complex setup, would be to employ an add-drop system utilizing a tapered silica fiber for the pump (add side) and a waist optimized low-OH or chalcogenide (ChG) tapered fiber for low-frequency light (drop side). In particular, ChG tapered fiber is more suitable for the mid-infrared region above 2 μm [188].

4.7.3 Summary

In conclusion, this chapter demonstrated all-precision machining fabrication of ultrahigh-Q crystalline microresonators. The Q value exceeds 100 million without a subsequent polishing process that is generally required to raise the Q of crystalline microresonators. The preliminary experiments revealed an ideal cutting condition for realizing an ultrasmooth surface for the whole resonator surface. Indeed, the fully computer-controlled machining has an advantage for the dispersion engineering for nonlinear experiments over the conventional polishing process. The described fabrication and cleaning procedure promises to raise the potential of crystalline microresonators for various applications. Also, this chapter provides the scheme of octave-wide phase-matched optical parametric oscillation in a crystalline MgF_2 microresonator that is designed to realize clustered comb generation via octave-wide separated FWM simultaneously. In fact, an octave-wide optical parametric oscillation has been demonstrated by using a fabricated microresonator with machining solely. Although identification of the resonance mode is generally tricky because it is close to zero dispersion, the employed precise dispersion measurement enabled to pick up specific mode family for the pump. The theoretical analysis of phase-matching condition including higher-order dispersion and numerical simulation supported the experimental observation of clustered comb formation in both 1.1 μm and 2.4 μm wavelengths, which could promise the localized microcomb formation in an unexplored wavelength region, for example, the T-band (1.0–1.26 μm), O-band (1.26–1.36 μm) and mid-infrared region, from compact Kerr nonlinear devices.

Chapter 5

Third-harmonic blue light emission via Kerr clustered combs and dispersive waves

This chapter presents the experimental demonstration of broadband visible light emission via Kerr clustered combs and dispersive waves. In particular, the extension of bandwidth, such as into the blue light wavelength region, is of interest in the field of microresonator nonlinear optics. This chapter presents two approaches to obtaining broad bandwidth visible light by engineering the dispersion in the pump wavelength band, namely the near-infrared region. One is based on third-order frequency conversion from a clustered comb, and the other employs a dispersive wave, and thereby yields visible light emission over a broad bandwidth ranging from 438 to 612 nm[*a].

5.1 Introduction and motivation

Broadband visible light generation by using the THG and TSFG process is of interest as well as the study on microresonator frequency comb. Although some previous studies have proposed approaches to visible light generation such as yellow, orange, and red wavelength bands, by using both stimulated Raman scattering (SRS) and FWM process, there are still challenges with respect to third-harmonic generation in a shorter wavelength regime (i.e., blue or ultraviolet) and the deterministic generation of visible wavelength light from the infrared pump. Here, the first motivation of this work is to experimentally demonstrate blue light emission via THG and TSFG in a silica toroid microresonator. The second motivation is to achieve deterministic generation of visible wavelength light by managing the microresonator dispersion, which is the main topic of this thesis.

[*a]Contents described in this chapter has been published in "Third-harmonic blue light generation from Kerr clustered combs and dispersive waves," Optics Letters, **42**, 10, 2010–2013 (2017).

5.2 Analysis of phase-matching condition for efficient third-harmonic generation

5.2.1 Phase-matched transverse mode in visible wavelength

To achieve third-harmonic conversion, the phase matching between the pump and third-harmonic modes must be satisfied [70]. First, momentum conservation must be considered, which requires the wavenumber of the pump mode k_p to be three times smaller than that of the TH mode k_{TH} ($k_{TH} = 3k_p$). When the momentum conservation requirement is met, the energy conservation $\omega_{TH} = 3\omega_p$ should be taken into account. It should be noted that the energy conservation requirement is not automatically met even when momentum conservation is fulfilled, due to dispersive resonance mode. Therefore, it is usually difficult to achieve the phase matching condition when only considering the condition for the fundamental transverse mode. Then, the use of a higher-order transverse mode provides the possibility of the phase-matching for the visible light mode. This will compensate for the frequency mismatch, which is defined as $\Delta\omega = 3\omega_p - \omega_{TH}$. The frequency mismatch is defined as the difference between the resonance frequency of TH and the mathematically triple frequency of the corresponding pump mode as shown in Fig. 5.1. The frequency mismatch needs to be close to zero to realize efficient conversion (solid green line in Fig. 5.1). It should be noted that the efficiency also depends on the spatial mode overlap between the pump and TH modes in addition to the frequency mismatch.

5.2.2 Mode analysis in blue light wavelength regime

To obtain third-harmonic blue light, it is necessary to generate infrared light around 1.3 μm wavelength region by using a 1550 nm pump. Before the phase-matching analysis in the infrared regime, the effect of the momentum and energy matching conditions on the generation of a blue light wavelength has to be investigated. In the same way as in Fig. 5.1, the resonance frequency from 400 to 480 nm was calculated by the FEM simulation, and the result was compared with the resonance frequencies of the pump mode, whose azimuthal mode number is equal to one-third of the mode number of the corresponding TH mode. Here, the fundamental WG mode is defined as $q = 1$ and $p = 0$ [i.e. TE(1,0)] where q and p are the mode number in the radial and polar directions, respectively [159]. Figure 5.2(a) shows the normalized frequency mismatches between the TE(1,0) (fundamental) pump mode and different modes at visible wavelengths. Figure 5.2(b) is the same as (a) but with TE(1,1) (second-order) pump modes. Figure 5.2(a) shows that the optimum TH mode is TE(2,4) when pumping the TE(1,0) mode. Also, the optimum mode is TE(2,7) when pumping TE(1,1) mode. From these results, one can see that a TH mode that satisfies momentum and energy matching is usually present regardless of the pump mode.

In addition, the variation in the mismatch as a function of the wavelength is

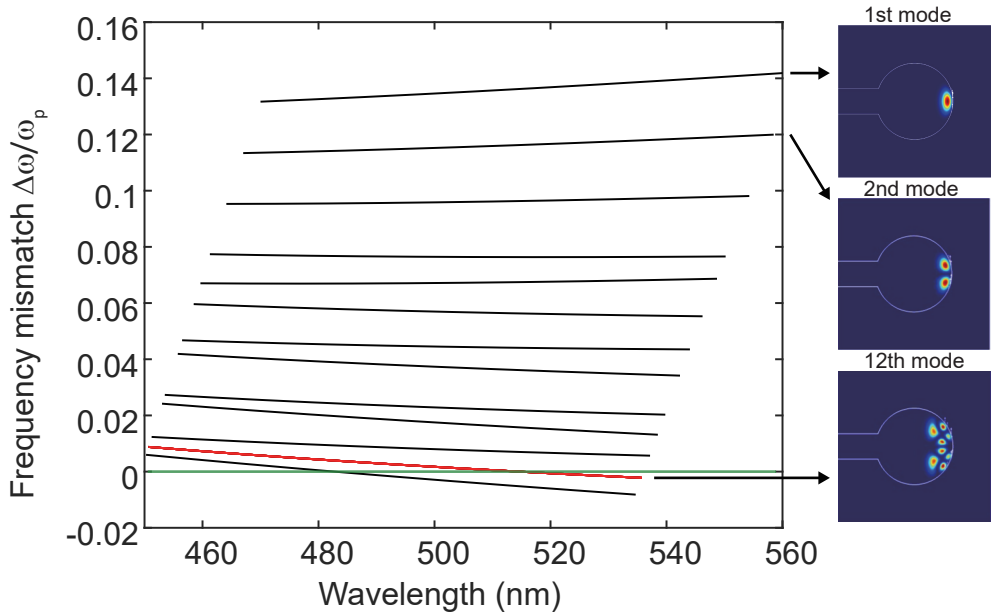

Fig. 5.1: (a) Calculated normalized frequency mismatch between the pump mode and visible modes around TH wavelength in a silica microtoroid with a major diameter of 50 μm and a minor diameter of 6 μm. Multiple black lines correspond to simulated visible transverse modes. Right panels show the mode profiles of 1st mode, 2nd mode, and 12th mode (solid red line), respectively. The green line corresponds to perfect phase-matching ($\Delta\omega/\omega_p = 0$) and this result indicates that the 12th mode satisfies the phase-matching condition at 517 nm for 1550 nm pumping.

smaller in Fig. 5.2(b) than in 5.2(a), which indicates that pumping at higher-order modes enables us to achieve phase matching in a broader wavelength regime. The mode overlap integral $\int E_{\mathrm{p}}^{3} E_{\mathrm{TH}}^{*}\, \mathrm{d}A$ for the pump and TH modes is also calculated to investigate the conversion efficiency. The results show that a pair consisting of TE(1,1) and TE(2,7) has 3.1 times larger overlap than a pair consisting of TE(1,0) and TE(2,4). The reason for such a large difference in the conversion efficiency can be found when looking at the mode profiles. Figure 5.2(c) and 5.2(d) are the mode cross-sections of TE(1,0) and TE(2,4), and Figure 5.2(e) shows the overlap between the pump and TH modes. Also, the mode cross-sections for TE(1,1), TE(2,7), and the mode overlap are shown in Figs. 5.2(f)-5.2(h). These results indicate that the use of a higher-order mode as a pump is more advantageous than using a lower order pump mode in terms of the conversion efficiency as well as the small frequency mismatch between infrared mode and TH mode.

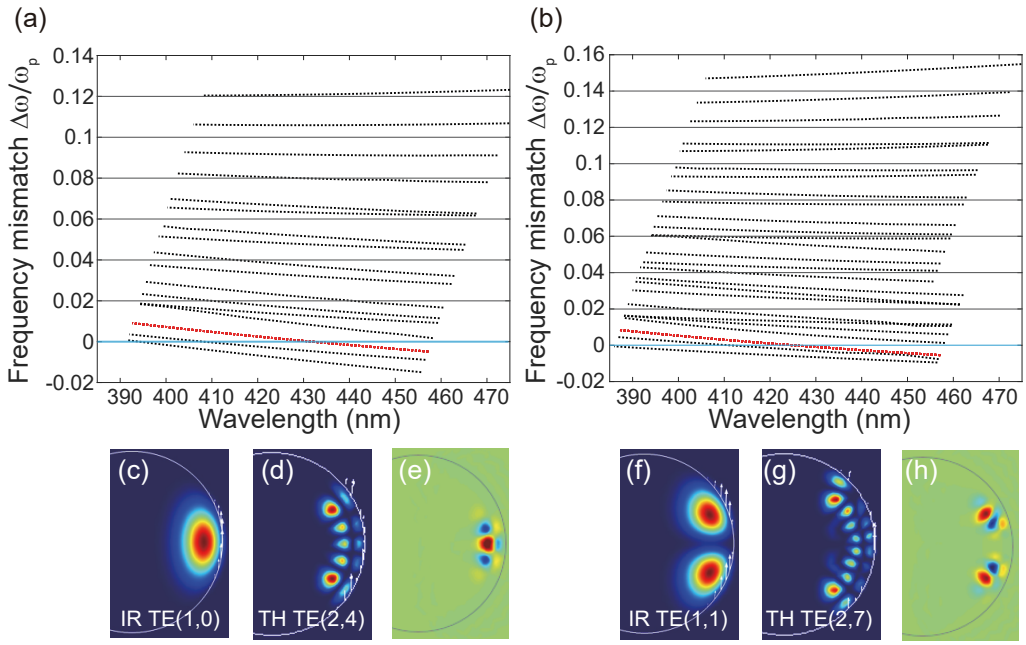

Fig. 5.2: (a) and (b) Calculated normalized frequency mismatch $\Delta\omega/\omega_p$ between the pump modes [TE(1,0) and TE(1,1)] and several visible modes in the blue wavelength regime, respectively, in a silica microtoroid with a major diameter of 54 μm and a minor diameter of 8 μm. The phase-matched TH modes are shown in the red. (c), (d), (f), and (g) Mode profiles for the infrared pump modes and the phase-matched TH modes. (e) and (h) Mode overlap of the mode field distribution between the respective pump and TH modes.

5.3 Dispersion engineering and numerical simulation in a silica microtoroid

On the basis of the analysis in §5.2.2, pumping with a second-order mode, namely the TE(1,1) mode, is suitable for obtaining both a broad bandwidth and efficient TH conversion. Since TH modes that obey the conservation laws are usually present, the dispersion of the TE(1,1) mode at telecom wavelength is of interest regarding the phase-matching condition for optical parametric oscillation. As mentioned earlier, it is necessary to generate sufficiently strong infrared light around 1.3 μm to be converted to TH blue light. Hence, the scheme of the clustered combs and the dispersive waves enables the bandwidth extension to that wavelength regime (cf. §3.4). Here, the clustered comb scheme is mainly discussed because it is more suitable to obtain a pure optical parametric oscillation accompanying only signal and idler light, thereby obtaining single frequency blue light.

First, the dispersion calculation was performed to obtain the phase-matching point for the optical parametric oscillation in a silica toroid microresonator whose

major and minor diameters are 54 μm and 8 μm, respectively. It should be noted that the second-order TE mode is assumed as a pump mode with the above discussion in mind. Figure 5.3(a) shows the value of the frequency difference $(\omega_{0+\mu} + \omega_{0-\mu} - 2\omega_0)$ as a function of pump wavelength, where the comb lines will be generated at the point where the value is close to zero. Phase-matched wavelength versus pump wavelength is shown in Fig. 5.3(b). When one pumps the shorter resonant wavelength, a parametric oscillation and subsequently clustered comb are generated at the wavelength even far from the pump mode. In

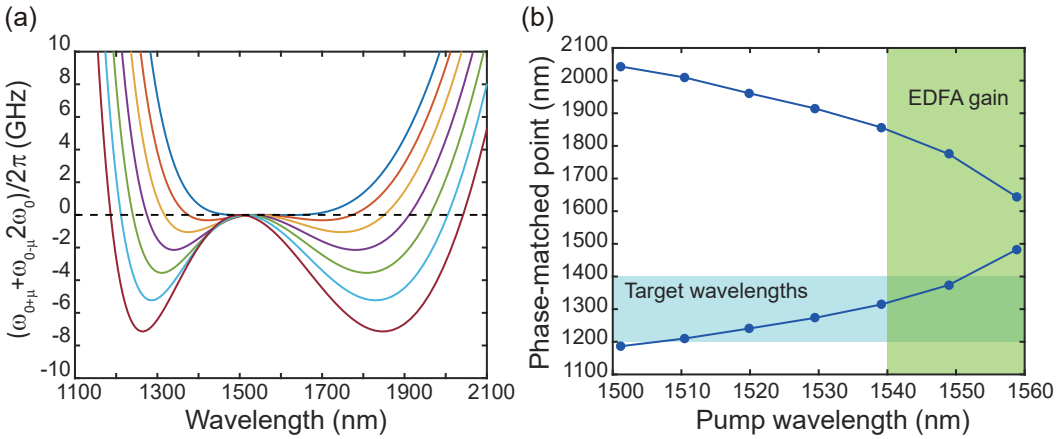

Fig. 5.3: (a) FEM calculation results of frequency difference $(\omega_{0+\mu} + \omega_{0-\mu} - 2\omega_0)$ of a second-order TE mode in a silica microtoroid with a major diameter of 54 μm and a minor diameter of 8 μm. (b) Phase-matched wavelength as a function of the pump wavelength. Blue and green shaded regions indicate the target wavelengths for TH blue light and EDFA gain, respectively.

practice, nevertheless, the pump wavelength is limited by the gain bandwidth of the erbium-doped fiber amplifier (EDFA) used for the experiment.

Next, the Lugiato-Lefever equation (LLE) given in Eq. (2.48) provides a more detailed investigation regarding the possibility of the parametric oscillation. Figure 5.4(a) shows the calculated integrated dispersion $D_{\rm int} = (1/2)D_2\mu^2 + (1/6)D_3\mu^3 + (1/24)D_4\mu^4$ of the TE(1,1) mode when the pump wavelength of 1539 nm is assigned as the center mode $\mu = 0$. Figure 5.4(b) shows the frequency difference value (i.e., the phase-matching condition) calculated from Fig. 5.4(a). The primary sidebands will generate at the mode number $\mu = 27$, which are 33.3 THz (225 nm blue-shifted) from the pump line. Figure 5.4(c) and 5.4(d) show the numerical simulation results by solving LLE. One can see that the larger detuning yields the broader optical spectrum as a result of the cascade FWM process. These results show that the primary comb lines are generated at the mode number $\mu = \pm 27$, and thereby a blue light emission should be obtained as a result of third-harmonics of the idler light at a wavelength of $\sim$ 1300 nm.

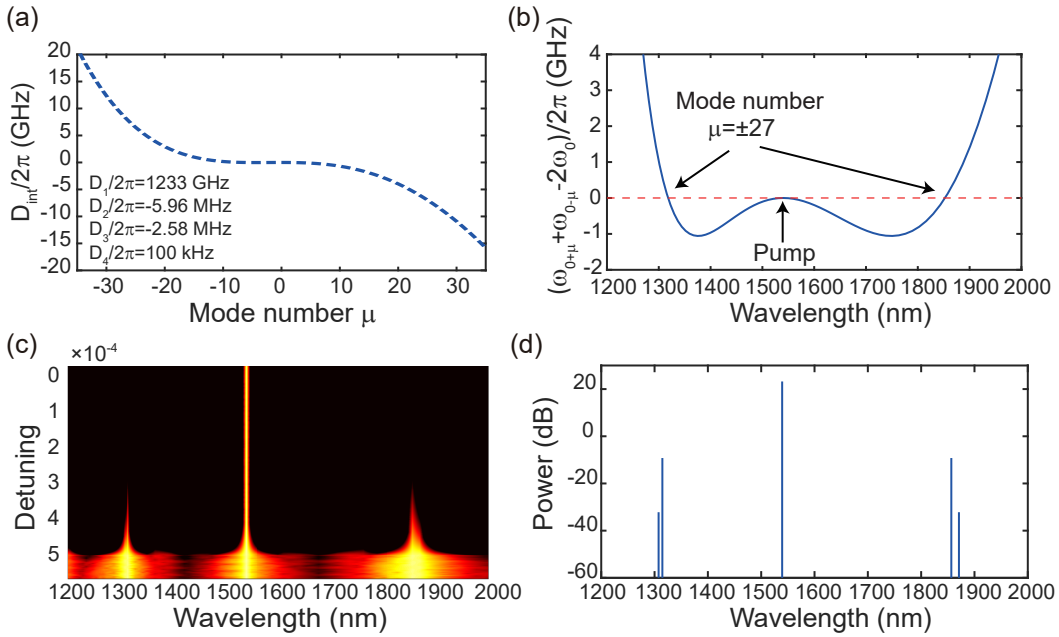

Fig. 5.4: (a) Calculated dispersion D_{int} as a function of mode number. (b) Corresponding frequency difference value $(\omega_{0+\mu}+\omega_{0-\mu}-2\omega_0)$ as a function of wavelength. (c) and (d) Simulated results of the optical parametric oscillation and the clustered comb formation in a silica microtoroid as a function of wavelength. The used parameters are as follows; $\lambda_p = 1539$ nm, $Q_{\text{int}} = 2 \times 10^7$, $Q_{\text{ext}} = 2 \times 10^7$, $n = 1.44$, $n_2 = 2.2 \times 10^{-20}$ m^2/W, $A_{\text{eff}} = 5$ μm^2, and $P_{\text{in}} = 100$ mW. The FSR and dispersion values are shown in (a).

5.4 Experimental demonstration in a silica toroid microresonator

5.4.1 Mode identification using dispersion measurement

A silica toroid microresonator was fabricated by using the CMOS process and CO_2 laser reflow (cf. §2.1.5). The major diameter and the minor diameter are ∼54 μm and ∼8 μm, respectively. Although precise geometry control of the microtoroid is rather difficult in general, the desired resonator size could be finally fabricated through a number of trials. The size of a fabricated device (i.e., major and minor diameters) was measured with an optical microscope. First, a dispersion measurement was performed to specify the TE(1,1) mode to use as the pump mode.

Figure 5.5(a) shows the transmission spectrum of a silica microtoroid used in this experiment. TE(1,0) (fundamental) and TE(1,1) (second-order) modes are indicated as the green triangle and the orange circle, respectively. Figures 5.5(b) and 5.5(c) show the experimental results of dispersion measurements (red circles) for each mode which agree well with the calculation results (blue dashed

lines). These results enable us to distinguish the target pump mode experimentally. The variation between the experimental and the theoretical results is mainly attributed to the anti-mode crossing behavior with other mode families.

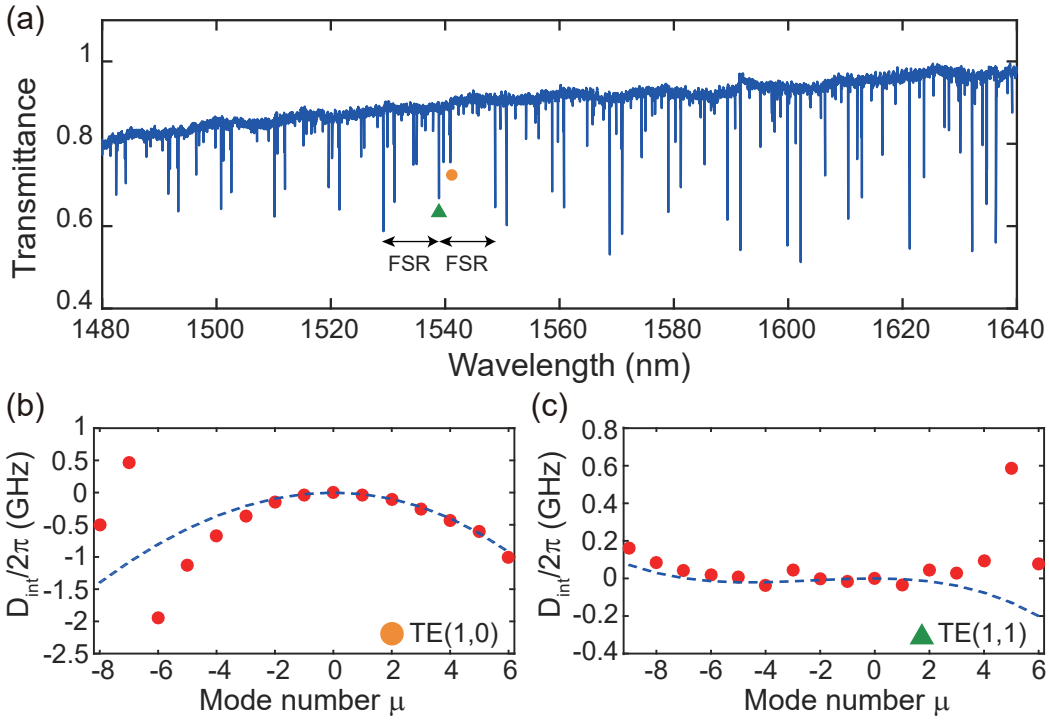

Fig. 5.5: (a) Transmission spectrum of fabricated silica microtoroid. The orange circle indicates the fundamental mode TE(1,0), and the green triangle denotes the pump mode. (b) and (c) Measured and calculated dispersion results of the TE(1,0) and TE(1,1) modes, respectively.

5.4.2 Observation of blue light emission and broadband visible light emission

Blue light emission via Kerr clustered combs

Figure 5.6 shows the experimental setup for observation of blue light emission and optical parametric oscillation. A tapered fiber with a diameter of 1 μm was used to couple the amplified pump light, and a polarization controller was used to adjust the polarization. Third-harmonic visible light was collected with a fiber-coupled spectrometer (USB2000+, Ocean Optics) aligned with a focusing lens. A CMOS camera was also used to image the light emission. The infrared output was measured using an optical spectrum analyzer (OSA) (AQ6375B, Yokogawa).

When the TE(1,1) mode was pumped at a wavelength of 1539 nm with an input power of 380 mW, bright blue light emission was observed on the CMOS camera. The loaded Q of the pump mode was 6×10^6. Figure 5.7(a) shows

the recorded infrared and visible spectra when the blue light emission and the optical parametric oscillation were observed. The blue light has a wavelength of 438 nm, and this agrees perfectly with the TH light of the 1314 nm idler light obtained in the infrared wavelength region. In the infrared region, pure signal and idler pair are generated via degenerate FWM far away from the pump, exactly 27-FSR from the pump mode, which is in perfect agreement with the predicted mode number in the calculation as shown in Fig. 5.4. With a slight detuning change of the pump towards the red wavelength side, new sidebands (i.e., a clustered comb) were generated near the primary comb lines, as shown in Fig. 5.7(b). The generation of 457 nm light is the result of the sum-frequency mixing of two photons at mode number $\mu = 26$ and one photon at $\mu = 6$, where the contributing lines are shown in pink in the left panel of Fig. 5.7(b).

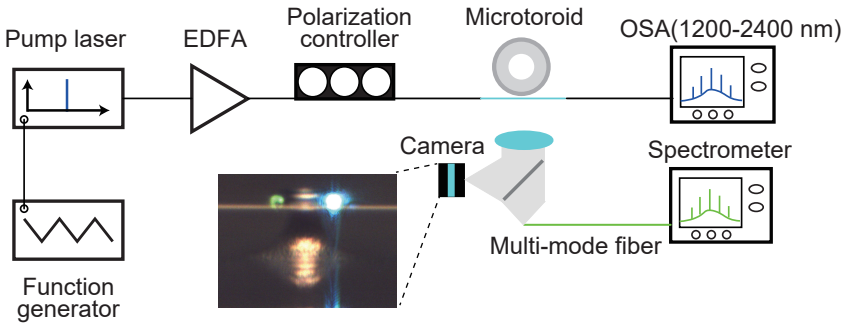

Fig. 5.6: Experimental setup for observation of visible light and infrared light. EDFA, erbium-doped fiber amplifier. OSA, optical spectrum analyzer. The scattered TH light is monitored by using both a camera and a spectrometer.

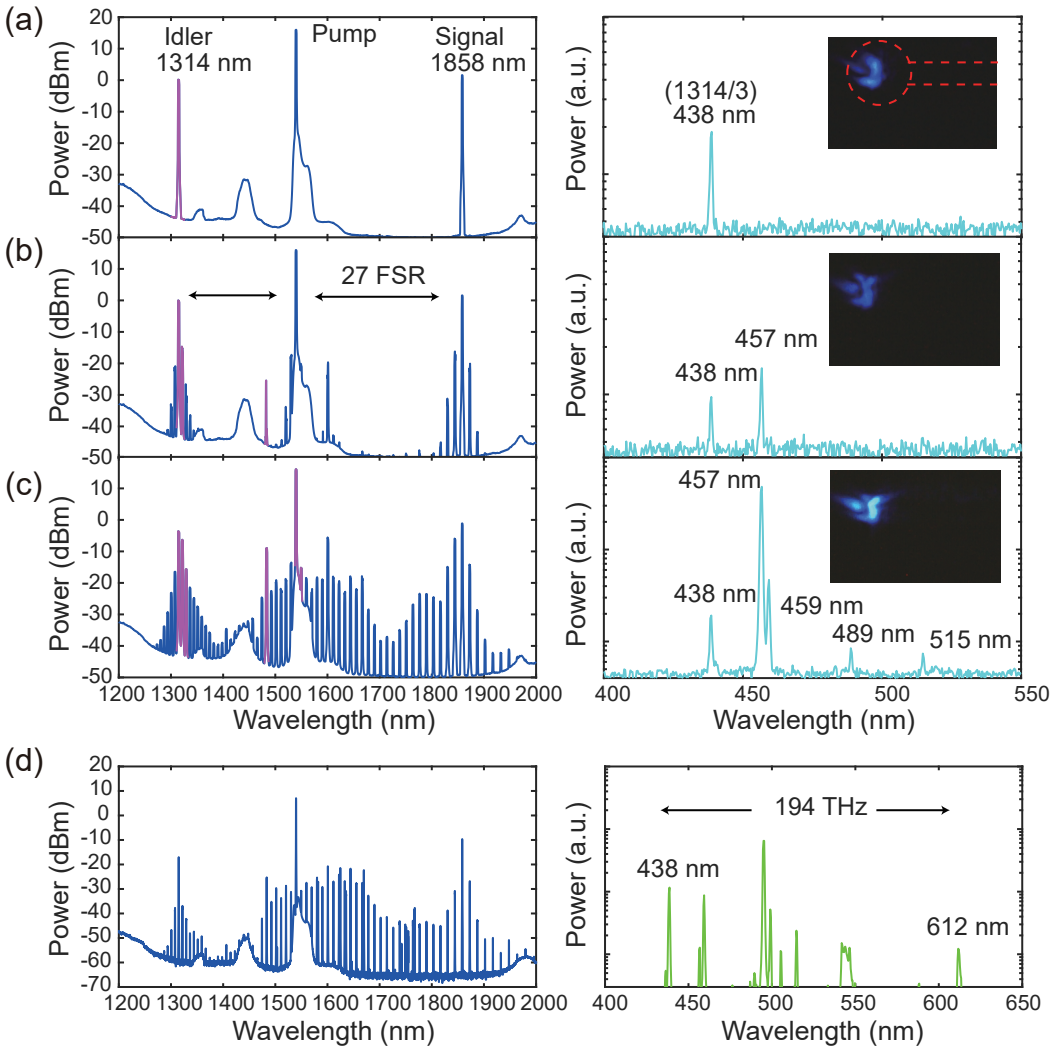

Fig. 5.7: Experimentally observed infrared and visible optical spectra at a pump wavelength of 1539 nm. (a) A large frequency shift optical parametric oscillation was generated at 27-FSR from the pump, and then a CW blue light emission is recorded at a wavelength of 438 nm via the THG process of idler light. The red dashed line represents the approximate geometry of the toroid cross-section. (b) and (c) With a slightly red-detuning of the pump, a clustered comb enables multi-wavelength blue light emission via THG and TSFG processes. The emitted visible light becomes clearer (see pictures of insets). (d) Under a different pump condition (but the same pump mode), broad bandwidth visible light ranging from 438 to 612 nm was observed.

Even broad bandwidth infrared combs spanning half an octave, and five peaks (438, 457, 459, 489, and 515 nm) were generated via THG and TSFG in the visible region with further detuning of the pump towards a longer wavelength [Fig. 5.7(c)]. The asymmetric shape in the infrared spectrum at 1.6–1.8 μm is due to the stimulated Raman scattering. By changing the coupling between the tapered fiber and the resonator, and the detuning of the pump, the spectrum finally changed to very broad bandwidth light ranging from 438 to 612 nm, which covers the entire visible wavelength regime as shown in Fig. 5.7(d). Indeed, a spectrally broad Kerr comb enabled us to observe broad visible light via simultaneous THG and TSFG process. In this case, different transverse TH modes are believed to contribute to satisfying the phase matching condition.

Broadband visible light emission via dispersive waves

Although dispersion engineered FWM and a clustered comb can be used to obtain visible light emission as above, a dispersive wave also provides an alternative method to realize broadband TH light. In the same manner as a clustered comb, the frequency at which a dispersive wave is generated can be controlled by engineering the microresonator dispersion. Based on the simulation, a silica microtoroid was fabricated, whose major and minor diameters are 57.4 μm and 6.6 μm, respectively. Here, the TE(1,1) mode of the resonator supports the dispersive wave around 1100 nm assisted by the third-order dispersion. A numerical result for the integrated dispersion D_{int} is shown in Fig. 5.8(a), which indicates that a dispersive wave can be generated around 1100 nm corresponding to mode number $\mu \simeq 64$. Figure 5.8(b) and 5.8(c) show spectra observed in the infrared and visible regions, respectively. Comb lines at $\mu \simeq 64$ in the 1.0 to 1.2 μm wavelength region are attributed to a dispersive wave as predicted by the calculation. Indeed, strong blue light emission was confirmed at a wavelength of 478 nm thanks to the TSFG of the dispersive wave lines and Raman lines. Interestingly, the dominant comb mode in the infrared spectrum is not the Kerr comb in the vicinity of the pump but a Raman comb centered around 1700 nm despite the anomalous dispersion regime. These experiments showed that the higher-order dispersion engineering made it possible to demonstrate short-wavelength third-harmonic generation in a silica toroid microresonator.

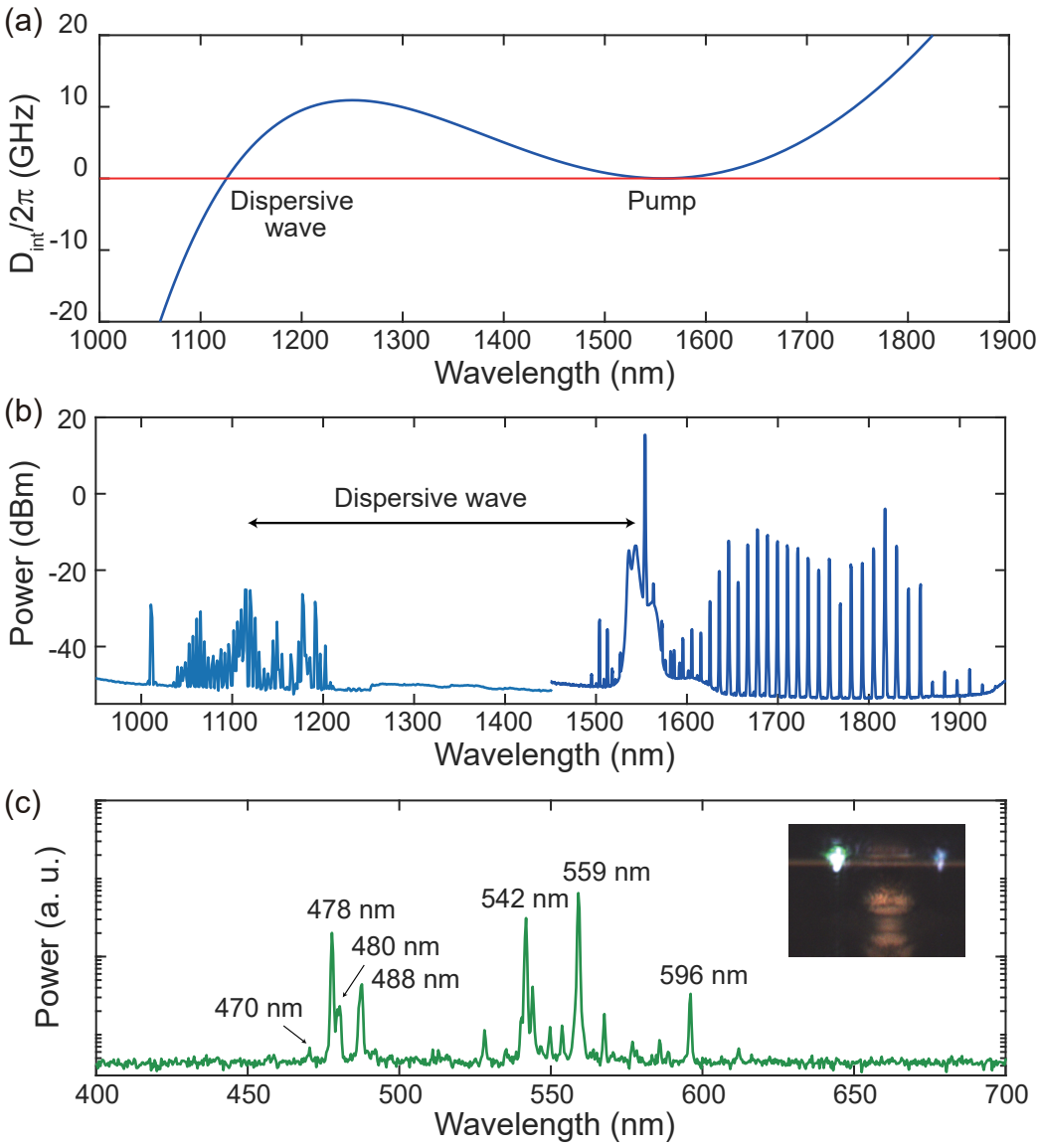

Fig. 5.8: (a) Calculated integrated dispersion of the TE(1,1) mode in a silica microtoroid with a major diameter of 57.4 μm and a minor diameter of 6.6 μm. The point of dispersive emission can be predicted as mode number $\mu \simeq 64$. The dispersion parameters are as follows: $D_1/2\pi =$ 1156 GHz, $D_2/2\pi = 44$ MHz, and $D_3/2\pi = -2.6$ MHz. (b) Observed infrared spectrum with a pump wavelength of 1553.6 nm. The dispersive wave was generated around 1100 nm. (c) Observed visible spectrum, where the blue light emissions (470, 478, 480, and 488 nm) are generated by the frequency mixing process among dispersive wave, pump, and Raman comb. Especially, the generation of 478 nm light is the result of TSFG from the light at 1114 nm, 1554 nm and 1818 nm.

5.5 Discussion and summary

This work demonstrated the deterministic THG and SFG based visible light emission by utilizing clustered combs and dispersive waves. The dispersion engineering — characterizing the dispersion of the pump mode and generating controlled Kerr comb spectra — enabled us to generate the desired wavelength light at visible wavelengths using a top-down approach from simulation to fabrication and experiment.

In addition, it should be noted that another possible approach is via anti-Stokes light of stimulated Raman scattering [189]. Since the SRS gain in silica is very broad, some of the gain bands are centered around 1000 cm^{-1} [189, 190]. However, it is considered challenging to observe a strong emission due to the weak gain of these Raman modes. Moreover, an anti-Stokes signal is generally much weaker than a Stokes signal. Also, this scheme is not so viable for a view to a top-down approach by using dispersion engineering.

In conclusion, a well-designed dispersion in a pump wavelength regime enabled the first observation of deterministic blue light third-harmonic emission and unprecedented broad bandwidth visible light generation ranging from 438 to 612 nm with a single CW pump. Moreover, a numerical simulation, which was to calculate the phase-matching condition between pumped mode and third-harmonic mode, identified the phase-matched transverse mode in the blue light wavelength regime. Continuous blue light emission from an infrared CW pump is an important factor for realizing an on-chip light source supporting the entire bandwidth. This result will help expand visible comb generation to the blue spectral region. Also, this work paves the way for achieving arbitrary generation of broad bandwidth light deterministically by controlling the dispersion of the microresonator system.

Chapter 6

Numerical investigation of Kerr frequency comb generation in mode coupled microresonators

This chapter describes numerical simulations of anti-mode crossing assisted normal dispersion Kerr frequency comb generation in mode coupled microresonators. A set of nonlinear coupled mode equations permits us to simulate complex comb formation dynamics between two different mode families, and theoretical analysis for the phase-matching condition gives suitable parameters for free-spectral range (FSR) selectable comb formation. This work also found that an oscillating behavior of intracavity power is present, depending on pump detuning. The systematic and rigorous numerical modeling proposed in this work will provide a powerful tool for assisting future work in terms of dispersion engineering for Kerr comb generation and frequency tuning for deterministic mode-locked comb generation[*a].

6.1 Introduction and motivation

Kerr frequency comb generation with mode coupling effect

The effect of mode coupling itself has been studied since the beginning or early stages of the research on high-Q optical microresonators [182, 191, 192]. Indeed, a phenomenon of mode coupling is not limited to optical microresonators; on the contrary, it has been a well-known phenomenon in a coupled pendulum, coupled LC circuit, and so on. The mode coupling between the counter-propagating modes, namely clockwise and counter-clockwise (CW-CCW) mode coupling, is usually induced by the backward scattering. The observation of CW-CCW mode coupling, which exhibits as the mode splitting of resonance mode,

[*a]Contents presented in this chapter has been published in "Analysis of mode coupling assisted Kerr comb generation in normal dispersion system," IEEE Photonics Journal, **10**, 5, 4501511 (2018).

has already been reported in a high-Q silica microsphere in 1995 [191]. Subsequently, there have been many theoretical and experimental studies [182, 192, 193] and demonstration for practical sensing application [194]. Besides, the strong coupling between different resonance modes produces an anti-crossing behavior or Fano-like resonance and thereby plays an essential role in various applications such as parity-time symmetry [195], all-optical logic operation [196], and electromagnetically induced transparency (EIT) [197].

From the viewpoint of the microresonator frequency comb, a deep relationship between the mode coupling and frequency comb generation has been explored [167, 171, 172]. Indeed, the mode coupling has created novel functions and rich dynamics with microcomb formation. The mode interactions in counter-propagating modes or different spatial modes are particular interests since they can be easily observed in optical microcavities for which the waveguide yields multi-modes. The strong mode coupling induces the mode frequency shift of a particular resonance mode, which indicates that the mode coupling can disturb the microresonator dispersion. A CW-CCW mode coupling strongly affects the soliton formation in the pump mode, as is the case for the mode interaction inhibiting the soliton formation. Figure 6.1(a) and 6.1(b) show a schematic illustration and a transmission spectrum for the CW-CCW model. The simulation results of soliton generation under strong CW-CCW coupling are shown in Figs. 6.1(c)-6.1(f). The simulation assumed the constant coupling for all modes, $\Gamma = 1.0$, where $\Gamma = \kappa/\gamma$ is given by the ratio of coupling rate to decay rate. The probability of soliton formation significantly decreases when the mode coupling becomes stronger as shown in Figs. 6.1(g) and 6.1(h), and these results suggest that the mode coupling should be circumvented for the reliable soliton generation (Further details of the effect of CW-CCW mode coupling on Kerr comb generation are presented in Appendix. B).

On the other hand, the drawback can also be useful if it is possible to control the mode shift, namely local dispersion engineering. Indeed, the avoided mode crossing could be utilized for deterministic soliton generation [167] and dispersive wave emission [168] (cf. §3.4). The sophisticated mode interaction achieved by a continuous tuning of resonance could leverage Kerr frequency comb in the normal dispersion regime, which is the main topic of this chapter.

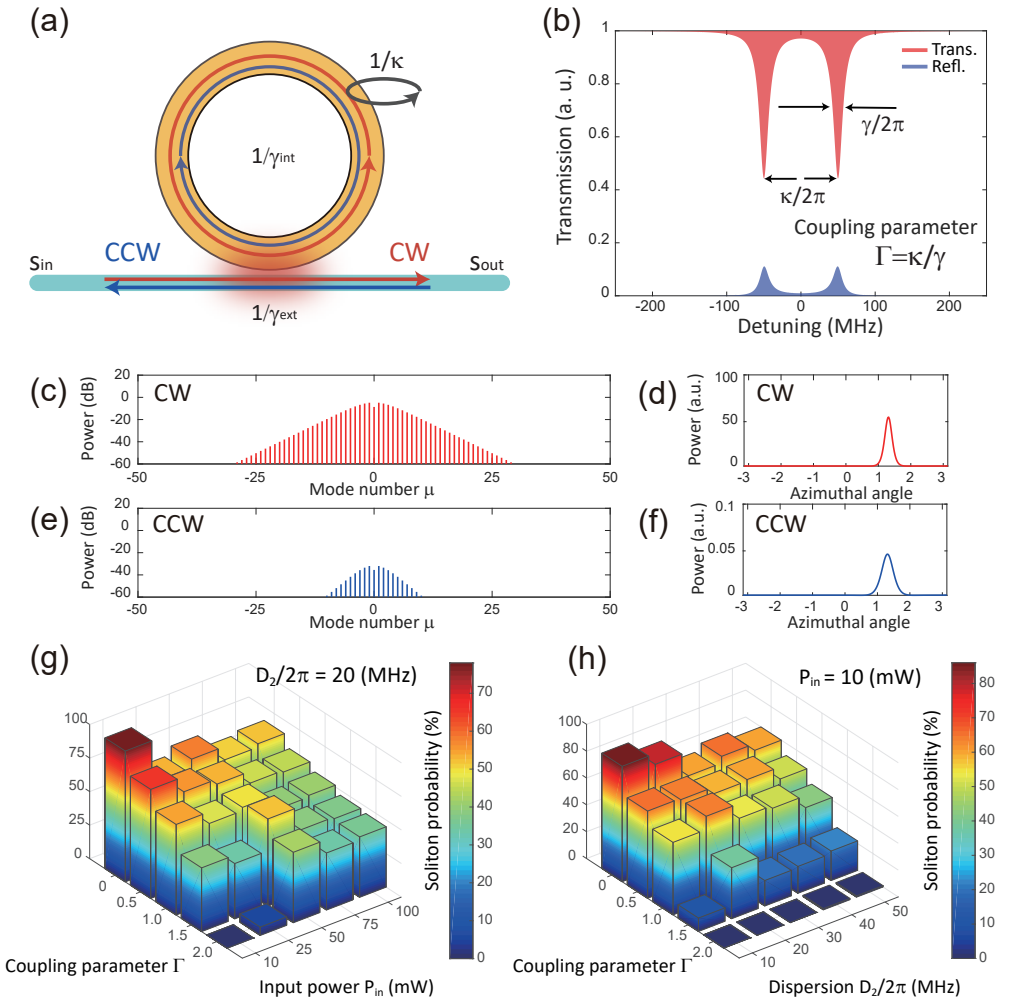

Fig. 6.1: (a) Schematic illustration of CW-CCW mode coupling model. (b) Calculated transmission (red) and reflection (blue) spectra with strong mode coupling. The intrinsic decay rate, the coupling rate, and the splitting width are $(\gamma_{\mathrm{int}}, \gamma_{\mathrm{ext}}, \kappa)/2\pi$=(10, 5, 100) MHz, respectively. (c)-(f) Calculated optical spectra and temporal waveforms in the CW and CCW directions with the constant coupling $\Gamma = 1.0$ and input power 10 mW. The intrinsic and coupling Qs were 1×10^7 and 2×10^7, respectively. The other parameters are assumed for a silicon nitride microring whose FSR is 1000 GHz. (g), (h) Calculated probability of soliton formation in the CW direction when the input power, and second-order dispersion are changed.

Model of coupled cavity system

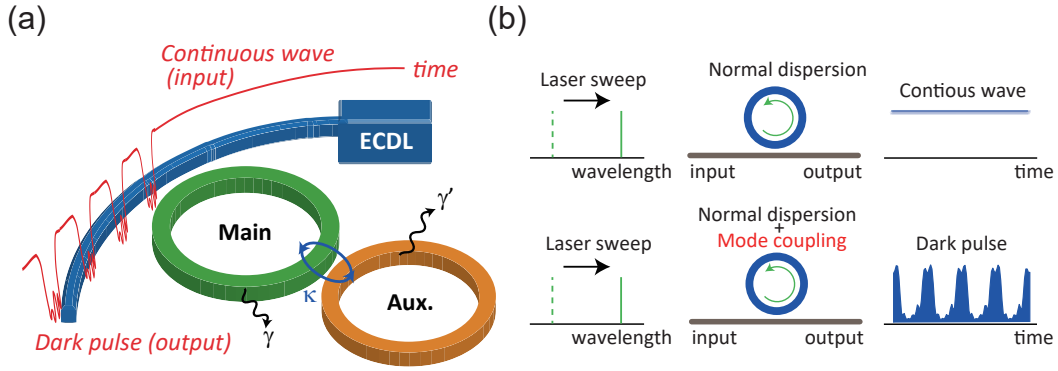

Fig. 6.2: (a) Schematic illustration describing the model of the coupled cavity system used for this study. The Main cavity is pumped by a continuous-wave laser, and the Aux. cavity is used to induce mode coupling. (b) Without mode coupling, no comb is generated due to the lack of parametric gain in a normal dispersion. However, mode coupling induced local dispersion change enables dark pulse formation in spite of normal dispersion system.

Figure 6.2(a) is a schematic illustration of the coupled cavity system of interest in this study. The Main cavity is coupled with both an external waveguide and an Auxiliary (Aux.) cavity. The coupling rate between the Main and Aux. cavity modes is given by κ. The field amplitudes of the Main and Aux. cavity modes are denoted with a and b, respectively. Also, γ and γ' are the loaded decay rates of the two cavities, where the coupling rate with the external waveguide is also taken into account for γ. In the scheme of anti-mode crossing assisted microcomb generation, the Aux. cavity is used to achieve mode coupling with the Main cavity [see also Fig. 6.2(b)].

Figure 6.3 shows a schematic diagram of the spectrum of the Main and Aux. cavities when two cavities are coupled at mode $\mu = -1$, where μ is given by an integer number showing the relative longitudinal mode number. Here, ω_μ and ω'_μ are the resonant frequencies of the longitudinal modes at mode number μ for the Main and Aux. cavities, respectively. The mode coupling induces two new supermode resonances with frequencies denoted by $\omega_\mu^{(-)}$ and $\omega_\mu^{(+)}$, where $\omega_\mu^{(-)}$ is the symmetric mode, and $\omega_\mu^{(+)}$ is the anti-symmetric mode. It should be noted that the free-spectral range (FSR) is not equidistance when the cavity system has dispersion. The dispersion introduces the resonance asymmetry factor Δ_{as} of positive ($\Delta_{as} > 0$) for an anomalous dispersion and negative ($\Delta_{as} < 0$) for a normal dispersion, when it is defined as $\Delta_{as} = \left(\omega_\mu - \omega_0\right) - \left(\omega_0 - \omega_{-\mu}\right)$. The definition is the same way as in Ref. [158]. In this study, the two cavities are both in a normal dispersion at the pump mode ($\Delta_{as} < 0$) but have slightly different FSRs and dispersions. To obtain mode coupling at the desired μ, a slight

offset between the Aux. and Main resonance frequencies is introduced with a frequency offset of $\Delta\omega$ at the pump mode $\mu = 0$.

When the dispersion of the Main cavity is given, the resonance frequency of a coupled Main cavity is expressed as a function of μ as, $\omega_\mu = \omega_0 + \mu D_1 + (1/2)\mu^2 D_2$, where D_1 is the FSR, and D_2 represents the second-order dispersion (dispersion is normal with $D_2 < 0$). Hence, the resonant frequencies of the Aux. cavity is shifted by $\Delta\omega$ from the Main cavity, for example $\omega'_\mu = (\omega_0 + \Delta\omega) + \mu D'_1 + (1/2)\mu^2 D'_2$ (the higher-order dispersions are neglected in this model). When the offset frequency $\Delta\omega$ is zero, the center modes ($\mu = 0$) of Main and Aux. are coupled with each other. On the other hand, when the offset frequency has a nonzero value, the location at which the strong interaction occurs changes. Although the overall dispersion is normal in the main mode, the mode coupling between the Main and Aux. cavity modes causes local anomalous dispersion ($\Delta_{as} > 0$) and make it possible to trigger the generation of normal dispersion Kerr frequency comb.

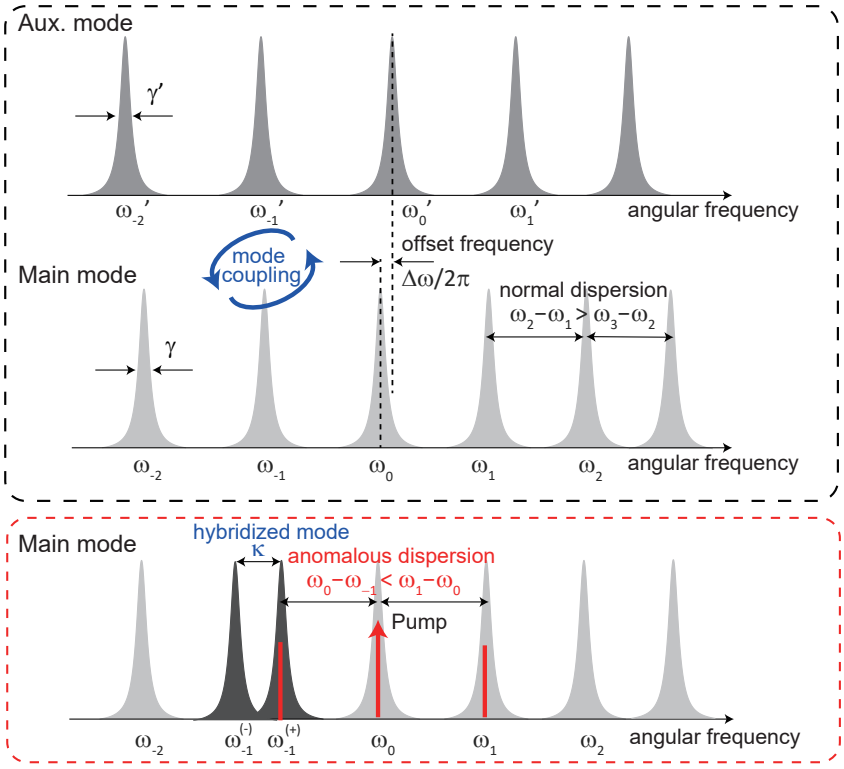

Fig. 6.3: Schematic diagram of mode coupling induced local dispersion change. When the two cavity modes are coupled at $\mu = -1$, they formed a hybridized mode and thereby induced a local anomalous dispersion among the modes of ω_{-1}, ω_0, and ω_1.

Motivation

This motivation of this study is to provide a rigorous model and simulate mode coupling assisted normal dispersion Kerr comb generation in a coupled cavity system using nonlinear coupled mode equations (NCMEs). Although numerical simulations including the mode coupling effect have been conducted using Lugiato-Lefever equations [76, 168, 198] and nonlinear coupled mode equations [166, 173, 199], there has been little work that has rigorously modeled the dynamic effect of mode coupling induced phase-matching on Kerr comb generation using two-mode equations. Even though a model with only a single mode equation is rather simple and reduces calculation cost, the proposed model here (i.e., comb evolution including two different mode families) enabled us to simulate in a more rigorous way and obtain optimized parameters in a practical experiment. In addition to reproducing the preceding experimental results, the calculation results indicate new findings related to the oscillating and non-oscillating behaviors of the optical spectrum during Kerr comb evolution, which are sensitive to the chosen parameters.

6.2 Theoretical analysis

6.2.1 Supermode resonance by anti-mode crossing effect

The most simple case, where a single mode is considered in Main and Aux. cavities, takes only decay rates and a mode coupling at a coupling rate of κ into account. Since a mode coupling between two cavities is of interest, the effect of the external waveguide is omitted here. Then the coupled mode equations are given as [79, 200],

$$\frac{da}{dt} = \left(j\omega - \frac{\gamma}{2}\right)a + j\frac{\kappa}{2}b, \tag{6.1}$$

$$\frac{db}{dt} = \left(j\omega' - \frac{\gamma'}{2}\right)b + j\frac{\kappa}{2}a, \tag{6.2}$$

where a and b are the field amplitudes of Main and Aux. mode, respectively. In a steady state, the eigenvalues $\omega^{(\pm)}$ of the Eqs. (6.1) and (6.2) are given as,

$$\omega^{(\pm)} = \frac{\omega+\omega'}{2} + \frac{j}{2}\left(\frac{\gamma}{2}+\frac{\gamma'}{2}\right) \pm \sqrt{\left[\frac{\omega-\omega'}{2} + \frac{j}{2}\left(\frac{\gamma}{2}-\frac{\gamma'}{2}\right)\right]^2 + \left|\frac{\kappa}{2}\right|^2}. \tag{6.3}$$

Figure 6.4 shows the theoretical transmission spectrum with and without a mode coupling effect when changing the detuning of the Aux. mode. (To be precise, the vertical axes represent $|1-\tilde{a}-\tilde{b}|^2$ and $|1-\tilde{a}|^2$ for Figs. 6.4(a) and 6.4(b), respectively. $\tilde{a}$ and $\tilde{b}$ are the Fourier transformed spectra of the field amplitudes a and b, respectively.) The main mode is not affected when there is no mode coupling ($\kappa = 0$), and thus the resonant frequency does not

exhibit anti-crossing behavior, as shown in Fig. 6.4(a). When mode coupling of $\kappa/2\pi = 1000$ MHz is present, anti-crossing behavior is clearly observed. The frequencies of the hybridized resonances are located at positions that are red- ($\omega^{(-)}$) and blue- ($\omega^{(+)}$) shifted in relation to the original resonance position as shown in Fig. 6.4(b). When the detuning between two resonances is zero (see green line), the width of mode splitting ($= \omega_{\mu}^{(+)} - \omega_{\mu}^{(-)}$) perfectly agrees with a coupling rate of κ .

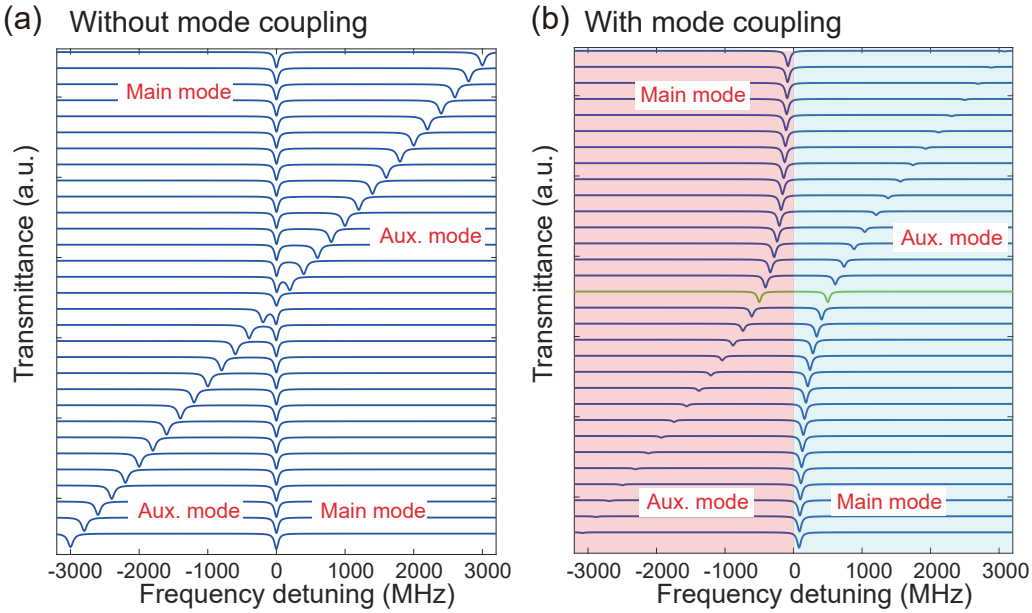

Fig. 6.4: Calculated transmittance (a) without and (b) with mode coupling ($\kappa/2\pi = 1000$ MHz) when changing the frequency detuning of the auxiliary (AUX.) mode. The intrinsic Q-factors of the Main and Aux. modes are 5×10^6 and 3×10^6, respectively, and the coupling rate with the waveguide is 7×10^6. Transmittance spectrum with the same detuning of two resonances mode is shown by the green line in (b), where the splitting width agrees with the mode coupling rate of κ.

6.2.2 Phase-matching condition by anti-mode crossing in normal dispersion microresonators

Here, the relationship between three modes, namely the pump ω_0, signal $\omega_{-\mu}$ and idler ω_{μ} modes, are investigated in terms of the resonance asymmetry factor Δ_{as}, which must be positive to satisfy the phase-matching condition. If the overall dispersion is normal, the local anomalous dispersion ($\Delta_{as} > 0$) leads to MI gain at the desired mode number μ, and primary sidebands start to appear. Importantly, the location of the local dispersion change can be selected by changing the frequency offset $\Delta\omega$ by continuously tuning the resonance frequency of

the Aux. mode. For instance, when $\Delta\omega$ is tuned in such a way that the mode coupling occurs at $\mu = 3$, the primary sidebands start to appear at a distance of 3-FSRs from the pump mode ($\mu = 0$); and with the help of the cascade process, a mode-locked comb with a 3-FSR spacing can be formed. Hence, one can control the location of the initial comb lines arbitrarily, which in turn enables one to realize an FSR-selectable mode-locked Kerr comb in a normal dispersion. The above scheme has been experimentally demonstrated by using integrated heaters to tune the resonance frequency via the thermo-optic effect [158].

Figure 6.5 shows the asymmetry factor Δ_{as} at different μ, as a function of $\Delta\omega$. The coupling rate κ is fixed at a constant value ($\kappa/2\pi$ =3.34 GHz), and the other parameters are taken from Ref. [158]. The condition for the anomalous dispersion ($\Delta_{as} > 0$), which is necessary to obtain MI gain, is shown in white, whereas the gray shaded region indicates the absence of MI gain due to the normal dispersion of the system. One can see that the phase-matched mode number μ increases as the increase of the offset frequency $\Delta\omega$. The vertical black dotted line represents $\Delta\omega$, when the Main and Aux. modes at μ perfectly overlap its resonant frequencies (i.e., $\omega_\mu = \omega'_\mu$) and couple. This indicates that the frequency separation between "A" and "B" in Fig. 6.5 is equal to $\kappa/(2\pi)$. When $\Delta\omega/(2\pi)$ approaches 12.5 GHz, the splitting ($\omega_{-1}^{(+)} - \omega_{-1}^{(-)}$) approaches the maximum value, and thus Δ_{as} is at its largest. This is because the anti-symmetric mode ($\omega_{-1}^{(+)}$) is shifted to its maximum from the original frequency ω_{-1}, and its mode is of interest because it will contribute to the positive Δ_{as}. When $\Delta\omega/(2\pi) = 12.5$ GHz, the energy of the hybridized mode is equally distributed between the Main and Aux. cavities (i.e., at "A" and "B"). However, when $\Delta\omega/(2\pi)$ is larger than 12.5 GHz, the anti-symmetric mode ($\omega_{-1}^{(+)}$) is no longer coupled efficiently with the Main cavity (the blue dashed line of "A"). Therefore, it is then necessary to focus on the symmetric mode ($\omega_{-1}^{(-)}$), which contributes to the normal dispersion of the system (the solid blue line of "B").

When $\Delta\omega$ is small, one can always find a coupled mode exhibiting a local anomalous dispersion. However, when $\Delta\omega$ is large, some ranges, not satisfying $\Delta_{as} > 0$, appear. These features suggest that precise frequency tuning is needed if one requires a local normal dispersion for large-FSR (i.e., 5-FSR, 6-FSR) comb generation. On the other hand, the asymmetry factor for each mode number increases significantly when the offset frequency is close to zero (red shaded region in Fig. 6.5), where the two center frequency modes ($\mu = 0$) are strongly coupled. In this region, the position of the initial comb sidebands can not be selected because the competition occurs between the MI gains of different mode numbers μ.

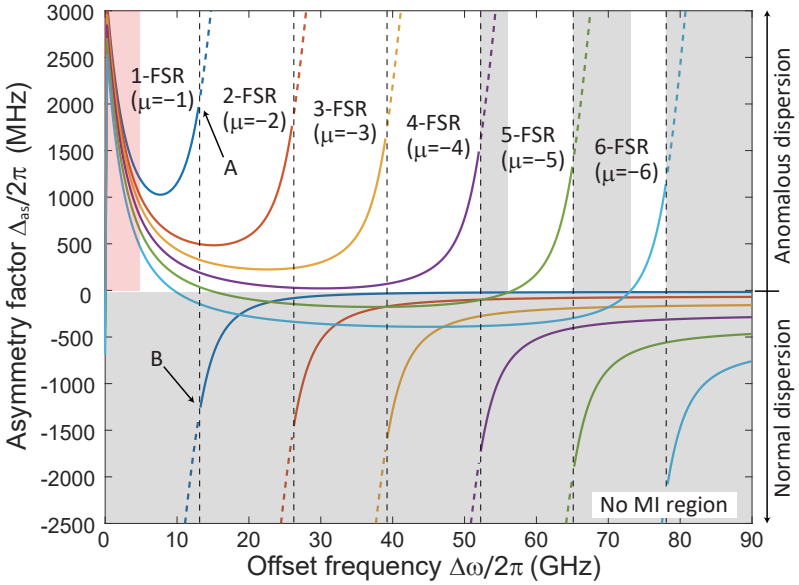

Fig. 6.5: Theoretical analysis of the asymmetry factor versus the offset frequency of the Aux. mode for each mode. The gray shaded region indicates no MI region because of the local dispersion being normal. The asymmetry factor increases greatly for each mode number μ in the red shaded region ($\Delta\omega/(2\pi) = 0 \sim 5$ GHz).

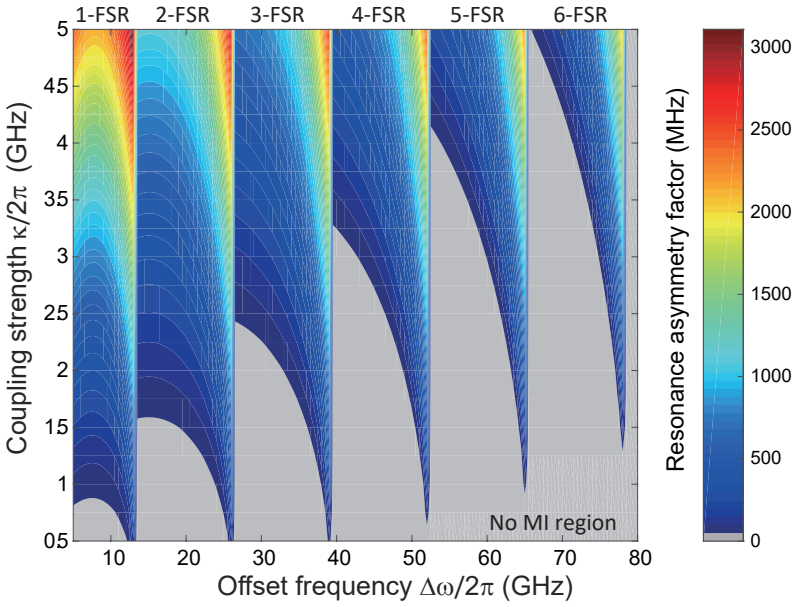

Fig. 6.6: Mapping of asymmetry factor versus offset frequency and coupling strength for different FSRs. The gray shaded region indicates the no MI region because of the local dispersion being normal. As the coupling strength increases, the no MI region becomes narrower because the phase-matching condition is easily satisfied.

Figure 6.6 shows further analysis of the phase-matching condition as a function of the mode coupling strength κ. This map shows that strong coupling (large mode splitting) makes it possible to have a large asymmetry factor and narrows the region with no MI gain. These analyses give the information to determine the critical condition as regards frequency tuning for FSR-selectable comb generation. The offset frequency gap from the 1-FSR to 6-FSR region is about 65 GHz when $\kappa/2\pi = 3.34$ GHz, which agrees well with an experimental report on the frequency shift of the auxiliary mode $\sim$ 64.8 GHz roughly estimated from the thermal heater power and the thermal shifting efficiency in Ref. [158].

6.3 Numerical simulation

6.3.1 Nonlinear coupled mode equations with mode coupling effect

The nonlinear coupled mode equations that takes the mode coupling term into account are described as,

$$\frac{\partial A_\mu}{\partial t} = -\left[\frac{\gamma}{2} + i\left(\omega_\mu - \omega_p - \mu D_1\right)\right]A_\mu + ig\sum_{j,k} A_j A_k A^*_{j+k-\mu} + i\frac{\kappa}{2}B_\mu + f\,\delta_{\mu 0}, \quad (6.4)$$

$$\frac{\partial B_\mu}{\partial t} = -\left[\frac{\gamma'}{2} + i\left(\omega'_\mu - \omega_p - \mu D'_1\right)\right]B_\mu + ig'\sum_{j,k} B_j B_k B^*_{j+k-\mu} + i\frac{\kappa}{2}A_\mu, \quad (6.5)$$

where A_μ (Main) and B_μ (Aux.), respectively are the slowly varying amplitude of each comb mode. Each term of the equations was introduced in §2.4.1. The calculation is performed with a total of 201 modes using the 4th-order Runge-Kutta method and a fast Fourier transform acceleration algorithm [201][*b]. Table 6.1 shows the parameters used in the following simulations that assumed coupled silicon nitride microresonators. The radii of the two microrings are 60 μm (Main) and 58 μm (Aux.), respectively, and the waveguide cross-section dimension is 1300 nm×600 nm [158].

[*b]The number of modes should be large enough for a simulated comb bandwidth.

Table. 6.1: Parameters used for the numerical simulation. They are taken from physical constants and Ref. [158]

Parameters	Symbol	Values (Main)	Values (Aux.)	Units
Refractive index	n_0	1.98	1.98	–
Nonlinear refractive index	n_2	2.4×10^{-19}	2.4×10^{-19}	m^2/W
Center frequency	$\omega_0/2\pi$	191.9	191.9	THz
Offset frequency	$\Delta\omega/2\pi$	–	variable	GHz
Cavity FSR	$D_1/2\pi$	378	391	GHz
Dispersion	$D_2/2\pi$	–16	–17	MHz
Effective mode area	A_{eff}	1.10	1.10	μm^2
Loaded quality factor	Q	7.5×10^5	3.7×10^5	–
External quality factor	Q_{ext}	3.5×10^6	–	–
Mode coupling rate	$\kappa/2\pi$	3.34	3.34	GHz
Input power	P_{in}	500	–	mW

6.3.2 Numerical simulation on FSR-selectable comb and deterministic dark pulse formation

Figure 6.7 shows the simulation results of 3-FSR microcomb generation, where the offset frequency $\Delta\omega/(2\pi)$ is 36 GHz, determined by the theoretical curve in Fig. 6.5. Figure 6.7(a) shows the cavity dispersion ($\omega_\mu - \omega_0 - \mu D_1$) of the coupled Main cavity, with (red) and without (green) mode couplings, indicating that a strong mode interaction is present in three modes apart from the pump mode. Figure 6.7(b), 6.7(c), and 6.7(d), respectively show the average intracavity power, the evolution of the optical spectrum, and the temporal waveform at different normalized pump detunings $t_R(\omega_0 - \omega_p)$ (t_R is the roundtrip time of the Main cavity). Here, the initial comb sidebands are generated at 3-FSR apart from the pump, where strong mode coupling occurred, and then a stable 3-FSR comb is formed without passing through a chaotic state. Even when adopting different initial noise, the trajectory of the intracavity power followed the same path, which proved numerically that deterministic mode-locked dark pulse generation is indeed possible by using this scheme, as reported in the previous work [158].

Optical spectra and temporal waveforms at different pump detunings are shown in Figs. 6.7(e)-6.7(g), where the red and blue lines represent the Main and Aux. modes, respectively. When the pump detuning is increased, the pulse duration of dark state and spectrum bandwidth became broader. As a result, the waveform had the appearance of a bright pulse-like state with periodic oscillatory tails. Although such spectra are known as a platicon [173], there are certain differences between the platicon and the results that exhibit an asymmetrical shape with respect to the pump mode. Such trends are usually induced by the effect of higher-order dispersion (e.g., dispersive waves), whereas this study is only considering the second-order dispersion. This fact suggests that the model rigorously simulates the dynamic mode coupling that affects the effective dispersion profile of the Main cavity, and thereby enabling the accurate reproduction of the asymmetric comb spectrum and the temporal waveform. These results demonstrate the advantage of using a rigorous model instead of the more simple model taking the mode shift into account as the perturbated dispersion $\omega_\mu = \omega_0 - \delta_{\mu 0}\Delta_\mu + D_1\mu + (1/2)D_2\mu^2$, where Δ_μ is the mode shift frequency at mode number μ.

Figure 6.8 shows the calculated results of the FSR-selectable comb generation. The arbitrary-FSR comb generation can be obtained only by changing the offset frequency from 5.5 GHz to 76 GHz, which again agrees well with reported experimental results [158]. These results confirmed that the rigorous modeling is well suited for the simulation of normal dispersion Kerr comb generation in a coupled cavity system.

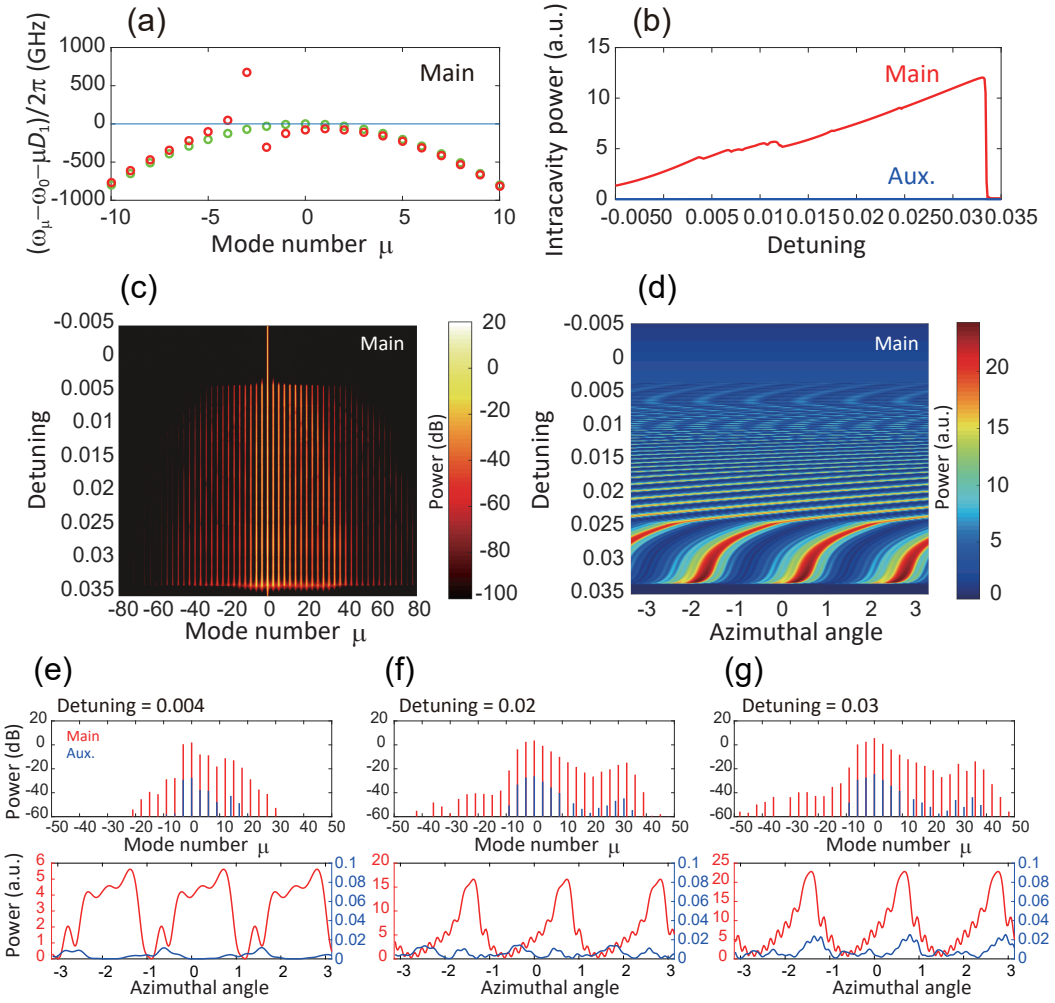

Fig. 6.7: (a) Cavity dispersion of the main mode with mode coupling (red circles) and without mode coupling (green circles). A strong mode interaction occurs at the mode number $\mu = -3$. (b) Average intracavity power versus normalized pump detuning $t_R(\omega_0 - \omega_p)$ during pump sweeping from blue-side to red-side. The trajectory of the main mode follows the same path when the calculation is repeated with different initial noise conditions. (c) and (d) Evolution of the optical spectrum and time domain waveform versus pump detuning. (e), (f), and (g) Simulated optical spectra and temporal waveforms of the main (red) and auxiliary (blue) modes with different detunings. Further detuning of pump results in the broader pulse duration of dark state and spectrum bandwidth.

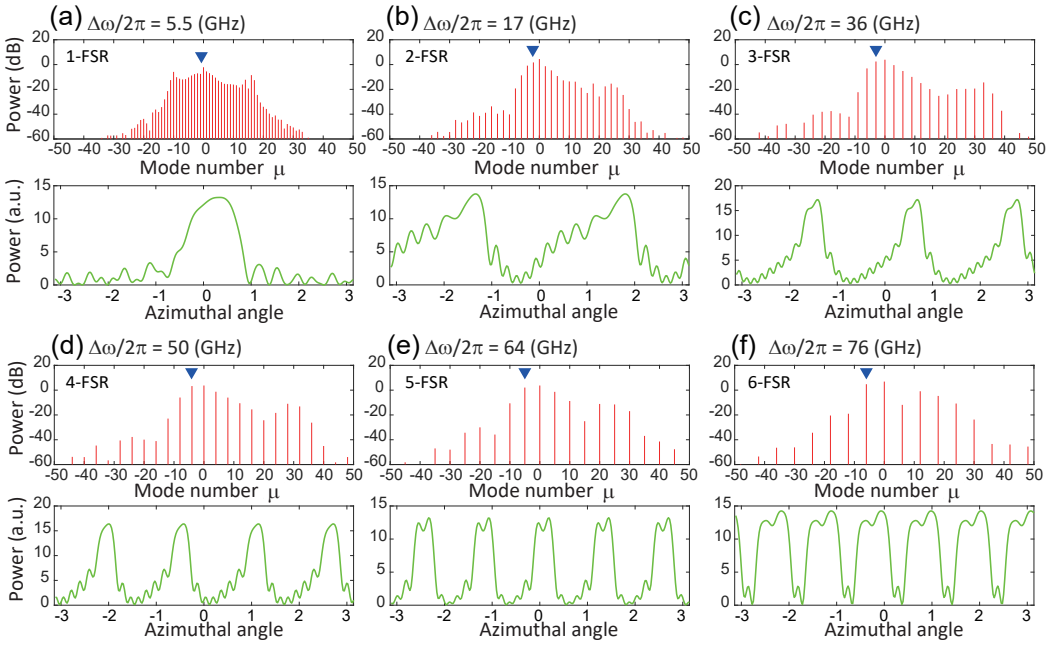

Fig. 6.8: Simulated optical spectra and temporal waveforms with different offset frequencies $\Delta\omega/(2\pi)$. The blue arrows indicate the locations of strong mode coupling. (a) 1-FSR; $\Delta\omega/(2\pi) = 5.5$ GHz. (b) 2-FSR; $\Delta\omega/(2\pi) = 17$ GHz. (c) 3-FSR; $\Delta\omega/(2\pi) = 36$ GHz. (d) 4-FSR; $\Delta\omega/(2\pi) = 50$ GHz. (e) 5-FSR; $\Delta\omega/(2\pi) = 64$ GHz. (f) 6-FSR; $\Delta\omega/(2\pi) = 76$ GHz.

6.3.3 Mode coupling induced oscillating behavior in 1-FSR comb generation

This section describes 1-FSR comb generation with different offset frequencies in more detail. Figure 6.9(a) is a magnified view of Fig. 6.5 for $\mu = -1$ (1-FSR), which shows the relation between the asymmetry factor Δ_{as} and the offset frequency $\Delta\omega$. First, the four different offsets ($\Delta\omega/2\pi = 5.25$, 7.75, 10.0, and 12.5 GHz) were chosen for the comb simulation. Figure 6.9(b) shows the calculated average intracavity power. Notably, such randomly oscillating behaviors are observed whatever the offset frequency (gray shaded region). These behaviors have never before been observed for 3-FSR comb generation [see Fig. 6.7(b)], and the oscillating region is strongly dependent on the detuning and offset frequency. Figure 6.9(c) shows the evolution of the optical spectrum when we swept the pump detuning while setting $\Delta\omega/(2\pi)$ at 7.75 GHz. Snapshots of the spectrum and the waveform are shown in Fig. 6.9(d). In the initial state (I) (detuning $= 0.004 \sim 0.012$), the comb spectrum is stable but the bandwidth is relatively narrow. After the initial state, the optical spectrum becomes highly unstable. In addition, the intracavity power exhibits clear oscillations with the detuning of $0.012 \sim 0.017$ (II). Finally, it becomes stable again when detuning reaches 0.017. In this state, the intracavity power exhibits small steps, and the

comb spectrum and temporal waveform show discrete transitions. These small steps have been observed experimentally in a normal dispersion system [76]; however, it is different from the soliton step usually observed in an anomalous dispersion system (corresponding to the change in soliton number). In this condition, the comb repetition rate does not change from 1-FSR from start to end, and the temporal waveform in (III) is always in a mode-locked state even though the shape of the temporal waveform is similar to that of platicons.

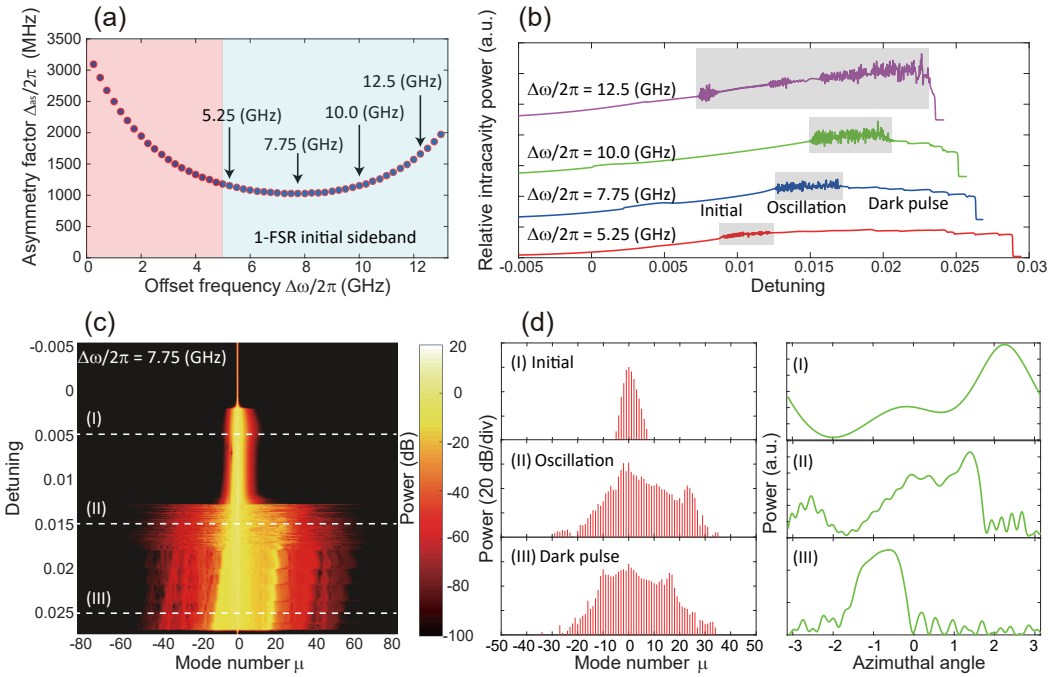

Fig. 6.9: (a) Asymmetry factor versus offset frequency in the 1-FSR comb region. A 1-FSR sideband is generated as the initial comb in the blue shaded region, whereas multi-FSR initial comb lines (e.g., 1-FSR and 2-FSR sidebands) can be generated simultaneously with the pump in the red shaded region. (b) Relative average intracavity powers with different offset frequencies. Oscillation behaviors were observed depending on the chosen offset frequency. (c) Evolution of optical spectrum versus detuning with $\Delta\omega/(2\pi) = 7.75$ GHz. A stable and narrow bandwidth primary comb was generated at the initial state (I). With further detuning, the comb transformed into a highly unstable state, as shown in the gray shaded region of (b). After the oscillation regime, the comb became stable again and formed a dark pulse. Interestingly, the optical spectrum repeated a bandwidth expansion and its narrowing with small steps of intracavity power. (d) Simulated optical spectra and temporal waveforms in each state indicated in (c).

When the offset frequency is in the blue shaded region in Fig. 6.9(a), initial sidebands are generated at 1-FSR. This is expected behavior since the 1-FSR resonant mode is the point where a local dispersion change occurs. However, the simulation shows a different trend (i.e., initial sidebands are generated at multi-FSRs) when choosing an offset frequency in the red shaded region. In this region, many resonant modes satisfy the phase-matching condition simultaneously (see the red shaded region in Fig. 6.5) because the pump mode exhibits a large red-shift due to the strong mode interaction between two center frequencies.

6.4 Discussion and summary

6.4.1 Discussion

The rigorous simulation model presented here not only provides a more accurate reproduction of experimental results but new findings regarding oscillation behaviors prior to the mode-locking transition. It should be noted that some of the features observed in this simulation were discussed in recent theoretical studies; oscillatory tails [198], and the change in angular pulse velocity depending on pump detuning [202]. In particular, the study reported by V. Lobanov *et al.* [173] that undertook a numerical study of the generation of platicons is relevant to this work. Although the work reported valuable results and findings, they performed the calculation only for the Main cavity mode by introducing the frequency shift of one of the modes. In contrast, this work fully calculated the two cavity modes and thereby taking the energy transfer between the two cavity modes into account. Moreover, recent studies have revealed that an intermodal interaction induces breather solitons accompanied by an oscillation of the pulse duration [203], and Kerr interaction between the two optical modes results in the oscillatory regimes depending on the detuning [204]. In addition, it has been known that the comb passed a noisy MI state even when pumping the mode belonging to the strong local anomalous dispersion overall normal dispersion system [205]. These phenomena are similar to our observations (i.e., unstable, oscillating behavior) rather than the previous demonstrations for deterministic dark pulse generation [76, 158, 172]. Although it needs further analysis to understand the complex dynamics, our model will help us to study the formation of the comb spectrum and time domain waveform in a realistic system in a more rigorous way.

6.4.2 Summary

In summary, this chapter studied nonlinear coupled mode equations (NCMEs) to simulate mode coupling assisted Kerr comb generation in a normal dispersion system. The FSR-selectable comb generation was investigated by employing a theoretical analysis, and our calculation results agree well with experimental

results reported in previous works. Moreover, the simulation provided the findings of oscillating behavior during detuning sweeping, and the behaviors are very sensitive to the chosen parameter. The proposed model and analysis will aid in practical experiments on mode coupling assisted normal dispersion Kerr comb generation, in particular, the engineering and design of coupled cavities to obtain a desired Kerr frequency comb spectrum. Also, the analysis of the phase-matching condition can help to deal with practical experiments, and prior examination of optical spectra and temporal waveforms.

Chapter 7

Summary and outlook

This chapter summarizes the thesis and gives a brief outlook of research on microresonator frequency comb and future aspects of dispersion engineering.

7.1 Summary

This thesis studied the dispersion engineering of high-Q optical microresonators with a view to frequency comb generation. The research for this thesis, was drive by the desire to explore the underlying physics of the microresonator-based frequency comb, namely the possibility offered by dispersion engineering, to realize broader and more controllable microcomb generation. One specific limitation of dispersion engineering is its accuracy when fabricating whispering gallery mode resonators. Abrasive polishing and a laser reflow process cannot control the precise resonator geometry, resulting in a lack of dispersion controllability compared with lithography-based waveguide resonators. However, precision machining opens the possibility of overcoming this limitation. Indeed, microcomb generation has been realized in a fabricated crystalline microresonator by machining alone. The obtained large-frequency-shift microcomb achieves one octave for the first time, and the spectral position perfectly agrees with the prediction based on numerical analysis. These results will have a great impact on microcomb studies from the perspective of the geometry dispersion engineering of whispering gallery mode resonators. Dispersion engineering techniques have been applied to deterministic visible light emission in on-chip silica toroid microresonators and even in a coupled resonator system designed to induce local dispersion. These studies show the potential for realizing reliable microcomb generation in the normal dispersion regime. The entire work is motivated by the idea that the spectral bandwidth can be extended into the unexplored wavelength region by employing dispersion engineering.

As a summary of this work, the following list presents an overview of the main achievements in this thesis.

- The principles and strategies for dispersion engineering are revealed, fea-

turing whispering gallery mode microresonators. The methods for simulation and measurement of dispersion can be applicable for other types of microresonators and could be helpful for various applications, not limited to microcombs. The role of dispersion in the microcomb spectrum is also shown.

- All-precision machining fabrication of ultrahigh-*Q* crystalline microresonator has been demonstrated. The computer-controlled ultraprecision machining achieved an ultrahigh-*Q* exceeding 100 million, for the first time, without a subsequent polishing process. Since the machining process readily offers the dispersion engineering and size control of manufactured devices, this method makes it possible to manage both an ultrahigh-*Q* and dispersion engineering.

- Octave-wide phase-matched four-wave mixing and clustered comb generation have been demonstrated for the first time. The dispersion engineered microresonator enabled the primary sideband generation with a frequency shift up to 140 THz. By using a 1550 nm pump, a magnesium fluoride microresonator started to oscillate at 1.1 μm and 2.4 μm. Subsequently, it formed localized microcomb formation in the wavelength region, which has not been much explored thus far.

- Third-harmonic blue light emission has been reported in a silica microtoroid resonator. The cascade third-order nonlinear processes, namely four-wave mixing, stimulated Raman scattering, and third-harmonic generation, enabled the first observation of deterministic multi-color visible light generation. It has also been revealed that the higher-order dispersion plays a key role in the phase-matching process ranging from visible to near-infrared wavelength regime.

- Nonlinear coupled mode equations to simulate mode coupling assisted frequency comb generation has been presented. Besides the geometrical dispersion engineering, local dispersion control can be used to generate mode-locked microcomb in a normal dispersion regime. The numerical simulation provides more rigorous simulation by taking dynamic phase shift by mode coupling into account.

7.2 Outlook

Visible and mid-infrared microcombs

Microresonator frequency combs so far have been developed with a focus on telecommunication wavelength. There are many reasons, such as instrumental limitations and target applications; nevertheless, the one critical problem for overcoming wavelength bandwidth is the microresonator dispersion. Strong material dispersion dominates the overall dispersion and inhibits the visible and

mid-infrared microcomb generation in the same manner as the telecom band. The visible and ultraviolet wavelength bands are highly attractive spectral regions because they would benefit optical atomic clock [206], bioimaging [207], and astronomical calibration [208]. Besides, the shorter wavelength microcombs can replace mode-locked titanium sapphire lasers, which are used for many applications, by small devices. The mid-infrared regime, which is known as the finger-print region, is also fascinating for particular applications in molecular spectroscopy and chemical sensing [209]. In this respect, dispersion engineering presented in this thesis will play a key role in obtaining visible and mid-infrared frequency comb by tailoring a resonator geometry, selecting a resonator material, and hybridization of resonance modes. Recently, many studies show the potential of spectral extension with sophisticated dispersion engineering and resonator fabrication [161, 210–212].

Ultraprecision machining for geometry dispersion engineering
Ultraprecision machining overcomes the limitation of geometric dispersion in crystalline microresonators. Moreover, precise control of the resonator size and reproducibility may become great advantages for various applications, including dual-comb spectroscopy and LiDAR. Especially, computer-controlled machining provides the geometry controllability, and thereby realizing triangular and rectangular resonator cross-sections, which has not been achieved with manual fabrication methods. These features will definitely contribute to microcomb spectral extension and applications.

Merging of different materials for dispersion engineering
Merging of different materials would impact dispersion engineering. In the present, the difficulty of fabrication may inhibit the realization. However, hybrid-material resonators can give the possibility of dispersion engineering shortly, not limiting to geometry tailoring. These techniques could include the functionalization of the monolithic resonator by combining different materials such as monolayer semiconductors and graphene.

Miniaturization of passively mode-locked lasers
The development of dissipative Kerr soliton brought a revolution in the study on microresonator frequency comb. However, there are still subjects to be solved, such as low conversion efficiency, bandwidth extension, stochastic soliton formation, and integration with waveguide, etc. In particular, the strong pump is required for comb generation, and in principle, the pump remains at the transmitted comb light. This is a challenge because the strong pump is usually unwanted for many applications; therefore, the transmitted pump is rejected by using an additional filter. In this respect, the use of active resonators, namely a gain-doped microresonator and the combination with a saturable absorber (i.e., carbon nanotube, graphene), will be the solution. Noted that this idea is similar to that of the conventional mode-locked lasers.

Appendix A

Gain transition between four-wave mixing and Raman effect in silica microresonators

The effects of four-wave mixing (FWM) and Raman gain coexist and compete in optical microresonators. A silica microresonator, especially with a large free-spectral range, exhibits the selectable transition between modulation instability (MI) and Raman gain with only changing pump power or pump detuning. Such a transition is attributed to the dynamic appearance and disappearance of FWM gain inhibiting discrete resonance modes. Steady-state analysis and numerical simulation using a Lugiato-Lefever equation with Raman effect revealed that the Raman-dominant region is present between transitions of FWM with different free-spectral range spacings. Also, an experimental observation confirms the controllable switching of intracavity field between a stable Kerr comb and a stable Raman state in a silica toroid microresonator[*a].

A.1 Theory and analysis of FWM and Raman gain in a silica microresonator

Modulation instability gain, namely FWM gain, originates in the Kerr effect and induces a parametric oscillation from vacuum fluctuations in nonlinear materials. When the system is pumped with a continuous wave input, new frequency sidebands are generated as a result of the cascade FWM process. The gain spectrum $g(\Omega)$ of the MI including the loss in an optical fiber is derived from the nonlinear Schrödinger equation (NLSE), as described in [114],

$$g_{\text{fib}}(\Omega) = -\alpha_{\text{fib}} + |\beta_2 \Omega| \sqrt{\Omega_c^2 - \Omega^2}, \tag{A.1}$$

[*a]Part of the contents of this chapter was published in "Transition between Kerr comb and stimulated Raman comb in a silica whispering gallery mode microcavity," Journal of the Optical Society of America B, **35**, 1, 100–106 (2018).

where, $\Omega_c^2 = 4\gamma P_0/\beta_2$ is the frequency of the gain peak. Ω, β_2, γ_{NL}, α_{fib}, and P_0 are the modulation frequency, second-order dispersion, nonlinear coefficient, propagation loss, and optical power, respectively. On the other hand, MI gain in an optical microresonator is obtained from the LLE [113], which is an expansion of the NLSE used to describe the linear and nonlinear dynamics in an optical cavity. The equation is given as [213, 214],

$$g_{\mathrm{cav}}(\Omega) = -\alpha_{\mathrm{cav}} + \sqrt{(\gamma L P_0)^2 - (\delta_{\mathrm{miss}})^2}, \tag{A.2}$$

where,

$$\delta_{\mathrm{miss}} = \delta_0 - \frac{\beta_2}{2} L\Omega^2 - 2\gamma L P_0, \tag{A.3}$$

represents the phase-mismatch due to the detuning, dispersion and nonlinear phase shift. α_{cav}, L, and $\delta_0 = t_R(\omega_0 - \omega_p)$, are the loss of the cavity per roundtrip, the cavity length, and the phase detuning of the input frequency ω_p to the resonance frequency ω_0 (t_R is the roundtrip time). In both cases, the higher order dispersions are neglected to simplify the discussion.

A silica-based microresonator easily shows stimulated Raman scattering (SRS) owing to a large and broad Raman gain. The Raman gain g_{R} per roundtrip is given as [114],

$$g_{\mathrm{R}} = -\alpha + g_{\mathrm{bulk}}^{\mathrm{R}} \frac{P_0}{A_{\mathrm{eff}}} L_{\mathrm{eff}}, \tag{A.4}$$

$$L_{\mathrm{eff}} = \frac{1}{\alpha}[1 - \exp(-\alpha L)], \tag{A.5}$$

where $g_{\mathrm{bulk}}^{\mathrm{R}} = 0.6 \times 10^{-13}$ m/W [114] is the bulk Raman gain of silica at a pump wavelength of 1550 nm, and A_{eff} is the effective mode area. L_{eff} is the effective length determined by the propagation loss α. Since the Raman gain spectrum is broad and its full-width at half-maximum (FWHM) covers more than 10 THz, the Raman gain spectrum always covers multi-FSRs of the microresonator resonances even when the resonator size (diameter) is relatively small. This is a significant difference between MI gain and Raman gain since, with a small microresonator (i.e., a large FSR system), there is a possibility that the MI gain can be located between the longitudinal modes, thereby suppressing FWM generation. Figure A.1 shows a schematic illustration of the gain competition between the FWM and SRS discussed above.

To obtain an intracavity power P_0 from an input power P_{in}, the bistable condition of nonlinear resonator is considered as,

$$\theta P_{\mathrm{in}} = (\gamma_{\mathrm{NL}} L)^2 P_0^3 - 2\delta_0 \gamma_{\mathrm{NL}} L P_0^2 + (\delta_0^2 + \alpha^2) P_0, \tag{A.6}$$

where θ is the coupling coefficient between the cavity and the input waveguide. Eq. A.6 gives P_0 at P_{in} and δ_0, which enable to calculate the MI and Raman gain as a function of the input power by using Eqs. (A.2) and (A.4).

Figure A.2(a) shows the theoretical values of MI gain at frequencies 1-FSR and 2-FSR from the pump frequency, along with the Raman gain. The parameters are set as follows: pump wavelength λ_p = 1542 nm, refractive index

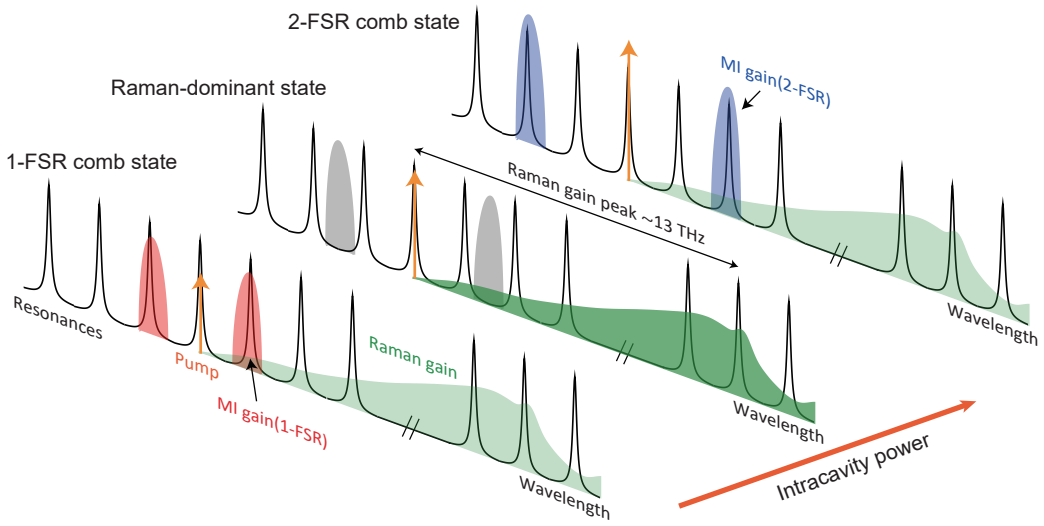

Fig. A.1: Schematic illustration explaining the competition between the MI and Raman gain in a large-FSR silica microresonator system. 1-FSR comb state: The peak of the MI gain overlaps a pair of longitudinal modes 1-FSR from the pump frequency at a low pump power. Since the MI gain is higher than the Raman gain, the FWM generation will be dominant. Raman-dominant state: The peak of the MI gain is between the large FSR's longitudinal modes. Since the longitudinal modes overlap the broad Raman gain, the SRS process can occur instead of FWM generation. 2-FSR comb state: The peak of the MI gain overlaps a pair of longitudinal modes 2-FSR from the pump frequency at a high pump power. Then those resonances receive MI gain and 2-FSR comb is generated.

$n = 1.44$, nonlinear refractive index $n_2 = 2.2 \times 10^{-20}$ m^2/W, nonlinear coefficient $\gamma_{\mathrm{NL}} = 1.79 \times 10^{-2}$ W^{-1}m^{-1} ($\gamma_{\mathrm{NL}} = n_2\omega_0/cA_{\mathrm{eff}}$), intrinsic quality factor $Q_{\mathrm{int}} = 5 \times 10^7$, external (coupling) quality factor $Q_{\mathrm{ext}} = 1 \times 10^8$, and the phase detuning from cold cavity resonance $\delta_0 = -5.4 \times 10^{-8}$. It should be noted that an anomalous dispersion ($\beta_2 < 0$) is required for this scheme to function (because phase-matching is satisfied only when $\beta_2 < 0$ under the condition $\delta_0 \sim 0$), so second-order mode of a silica microtoroid is assumed as the pump mode. Major and minor diameters are ≈50 μm and ≈7 μm, respectively. The cavity FSR $D_1/2\pi = 1350$ GHz, the second-order dispersion $\beta_2 = -10$ ps^2/km ($D_2/2\pi = 23.8$ MHz), the effective mode area $A_{\mathrm{eff}} = 5$ μm^2, all of which can be estimated by using the finite element method. Figure A.2(a) indicates that there are three regions present, where 1-FSR MI gain, Raman gain, and 2-FSR MI gain are dominant with respect to the input power. As further increasing of the input power, the resonator experiences through 1-FSR gain, Raman, and 2-FSR gain in order. So the result in Fig. A.2(a) directly supports the explanation in Fig. A.1.

Also, Figure A.2(a) defines the maximum input power at which the gain at 1-FSR is equal to zero as $P_{\text{1-FSR}}$, and the minimum input power at which the

gain at 2-FSR is equal to zero as $P_{2\text{-FSR}}$, indicated as the black arrows. The difference between these two powers $\Delta P_{\text{in}} = P_{2\text{-FSR}} - P_{1\text{-FSR}}$ represents the range of the input power to achieve a Raman-dominant state. Figure A.2(b) shows the ΔP_{in} as a function of the resonator FSR for different coupling rates with the waveguide. When ΔP_{in} is zero, the system has no Raman-dominant region, but the MI gain at 2-FSR is dominant. For example, the calculation shows that the FSR must be larger than 1000 GHz to obtain SRS when the system is operating in a critical coupling condition. Hence, this analysis allows us to obtain important information about the strategy for choosing the cavity diameter to obtain a Raman-dominant state without FWM. The result shows that an under coupling condition ($Q_{\text{ext}} > Q_{\text{int}}$) in addition to the choice of a large-FSR (i.e., a small diameter microresonator) is suitable for obtaining a Raman-dominant region over a broad range.

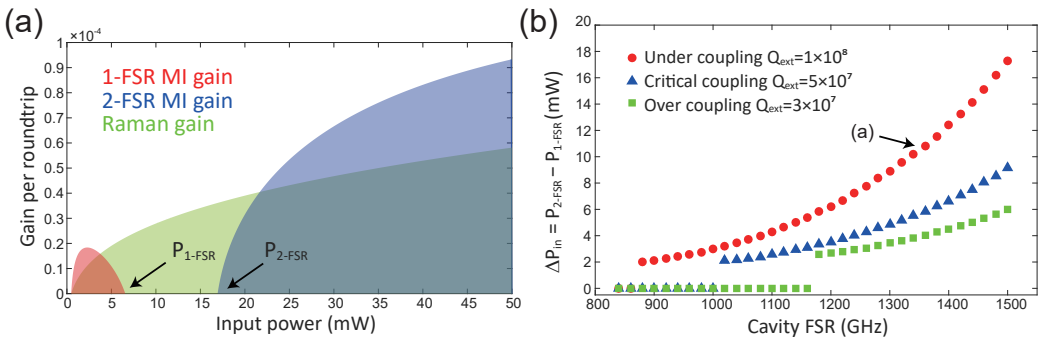

Fig. A.2: (a) Calculated MI gain at two different frequencies (1-FSR and 2-FSR from the pump), and the Raman gain per roundtrip as a function of the input power when Q_{ext} is 1×10^8. Only the Raman gain inhibits the cavity modes when the input power is in the 6.5 $\sim$ 17 mW range, because the MI gain is located between the 1-FSR and 2-FSR resonant modes. (b) ΔP_{in} versus the cavity FSR at three different coupling conditions. $\Delta P_{\text{in}} = P_{2\text{-FSR}} - P_{1\text{-FSR}}$ is the allowed power range for obtaining the Raman-dominant state. The arrow is at the condition for (a).

A.2 Numerical simulation based on Lugiato-Lefever equation

Numerical simulation can be performed by using the LLE model with Raman effect as Eq. (2.52) and the impulse Raman response given as Eq. (2.50). Here, τ_1 and τ_2 are given as 12.2 fs, and $\tau_2 = 32$ fs, respectively [114], and the other parameters are the same as introduced in the previous section. The simulated spectra are shown in Figs. A.3(a)-A.3(c), with changing the input power. Insets show the time domain waveforms. At an input power of 2.5 mW, a stable 1-FSR comb, namely a Turing pattern comb, was generated as expected without any

Raman components. However, only the Raman comb appeared when the input power was 10 mW, and this result is consistent with the analysis in Fig. A.2. Finally, the 2-FSR comb became dominant when the input power was set to 40 mW in which case Raman lines were not observed again. It should be noted that these transitions can be observed by changing different parameters such as the coupling Q or the laser detuning as long as the gain gap similar to ΔP_{in} exists.

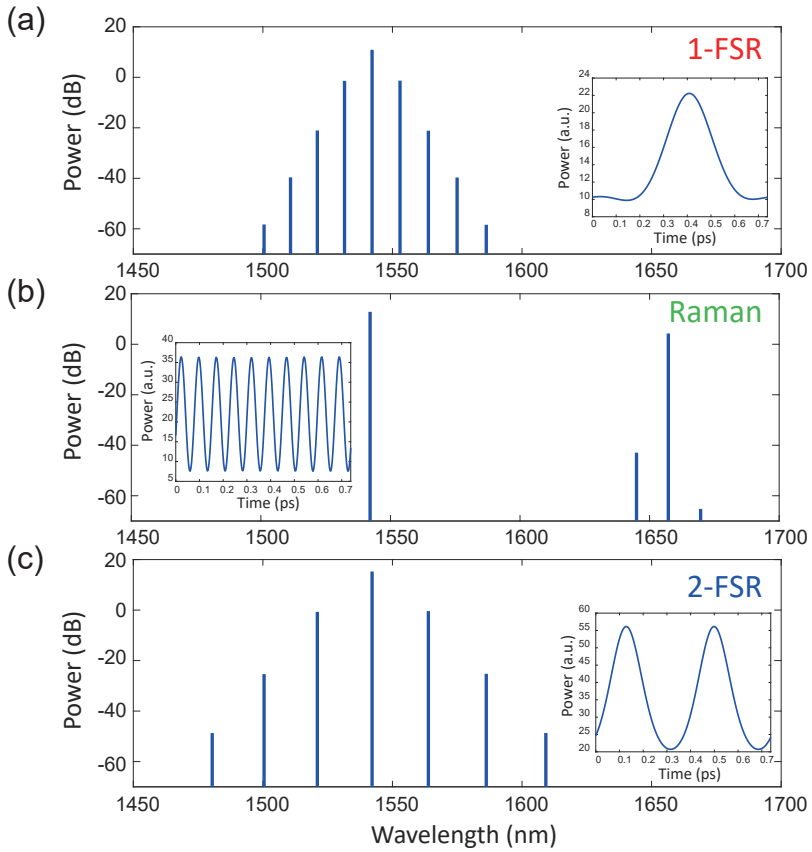

Fig. A.3: Simulated spectra with LLE for different input powers. Insets show simulated temporal waveforms. (a) Output spectrum when the resonator is pumped with a 2.5 mW input. 1-FSR Turing pattern comb is observed. (b) At 10 mW input. The peak of the output spectrum at 1657 nm wavelength corresponds to the peak of the Raman shift of silica. (c) At 40 mW input. A 2-FSR Turing pattern comb is obtained.

A.3 Experimental observation in silica microtoroid

Based on the results of numerical simulation, the experiment was performed using a silica toroid microresonator. The major and minor diameters are ≈50 μm and ≈7 μm, respectively, and the measured Q of the pump mode was 1.8×10^7. In the experiment, the laser detuning is gradually changed instead of pump power

tuning. Since a coupled power depends on both the laser detuning and pump power (and the coupling rate), the laser-detuning is the best way to continuously control the intracavity power. The experiment is performed in the effectively blue-detuned region, and therefore thermally stable. When the laser detuning is increased towards the red-detuned side, the spectrum dynamically changes, as shown in Fig. A.4. The experimental results clearly show the transition from 1-FSR comb to Raman comb, and the back to 2-FSR comb state as the numerical simulation revealed.

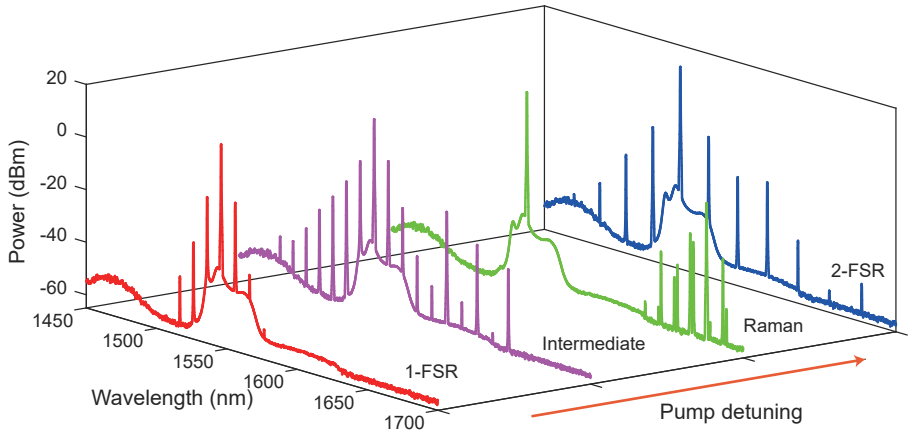

Fig. A.4: Measured output spectra from a silica toroid microresonator pumped at different detunings. The pump power was about 250 mW. The wavelength of the input laser is swept from a shorter to a longer wavelength. When the pump is largely blue detuned, a 1-FSR comb is obtained. The spectral envelope of the 1-FSR became broader, and Raman lines appeared with the smaller detuning. When the detuning is at its smallest, a 2-FSR comb is finally observed.

A.4 Summary

In summary, it has been demonstrated that the gain transition between FWM and Raman-dominant states is present in a silica microresonator that exhibits a broadband Raman gain. Although a Raman comb is of high interest in terms of extending the wavelength regime of the microresonator frequency combs, this study revealed that it is needed to choose the resonator size, the gap between the cavity and the waveguide, and the input power carefully, in order to obtain Raman state selectively. Also, this system, representing the competition between the Kerr and Raman effects, is well related to the microresonator dispersion (e.g., the trade-off relation between the cavity size and anomalous dispersion), and therefore will be interesting subject with regard to the dispersion engineering.

Appendix B

Impact on microcomb formation in a clockwise and counter-clockwise mode coupled microresonator

The impact of inherent mode coupling between clockwise (CW) and counter-clockwise (CCW) modes is a particular underlying problem for Kerr frequency comb generation in optical microresonators. Here, numerical analysis using coupled Lugiato-Lefever equations reveals that the scattering-induced mode coupling affects the formation of soliton microcomb in the pump direction. It also showed that CCW comb power depends on the coupling strength between the CW and CCW modes. The experiment is performed using a silica toroid microresonator that exhibits the strong mode coupling to confirm the simulation results. The understanding of the specific relation between CW-CCW mode coupling and Kerr frequency comb could provide variable information for performers as regards the experiment and measurement of soliton microcomb[*a].

B.1 Numerical simulation based on coupled Lugiato-Lefever equations

Coupled Lugiato-Lefever equations (LLEs) that take CW-CCW mode coupling into account are represented as [168],

$$\frac{\partial A(\phi,t)}{\partial t} = -\left(\frac{\gamma}{2} + i\delta_0\right)A + i\frac{D_2}{2}\frac{\partial^2 A}{\partial \phi^2} + ig|A|^2A + i\frac{\kappa_\mu}{2}B + \sqrt{\gamma_{\text{ext}}}A_{\text{in}}, \tag{B.1}$$

$$\frac{\partial B(\phi,t)}{\partial t} = -\left(\frac{\gamma}{2} + i\delta_0\right)B + i\frac{D_2}{2}\frac{\partial^2 B}{\partial \phi^2} + ig|B|^2B + i\frac{\kappa_\mu}{2}A, \tag{B.2}$$

[*a]Part the contents of this chapter was published in "Effect on Kerr comb generation in a clockwise and counter-clockwise mode coupled microcavity," Optics Express, **25**, 23, 28969–28982 (2017).

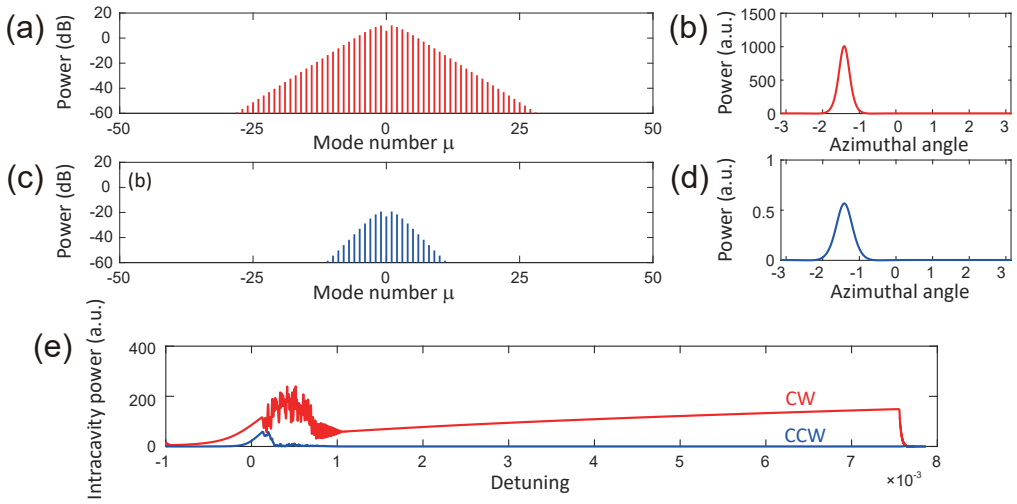

Fig. B.1: Simulation results when the CW-CCW mode coupling is the same for all longitudinal modes with a constant $\Gamma = 1.0$, $P_{\text{in}} = 100$mW. (a), (b) Optical spectrum and temporal waveform of CW direction. (c), (d) Corresponding results of CCW direction. (e) Average intracavity power while the normalized detuning is scanning.

where A and B correspond to CW mode and CCW mode, respectively, and κ_μ is the coupling coefficient between two modes. It should be noted that the decay rate, detuning, and the nonlinear coefficient are the same for both modes due to the mode degeneracy. The cross-phase modulation (XPM) between the two counter-propagating modes since the XPM interaction is weak, and thus neglected in the above equations. In the following simulation, a silica toroid microresonator is assumed as a platform. A silica microtoroid, especially a small diameter resonator, often shows strong CW-CCW mode coupling. The calculation parameters are as follows: input wavelength $\lambda_p = 1542$ nm, refractive index $n = 1.44$, nonlinear refractive index $n_2 = 2.2 \times 10^{-20}$ m^2/W, $Q_{\text{int}} = 2 \times 10^7$, $Q_{\text{ext}} = 2 \times 10^7$ and $A_{\text{eff}} = 5$ μm^2. The cavity free-spectral range (FSR) $D_1/2\pi$ is 1350 GHz, and the second-order dispersion $D_2/2\pi = 23.8$ MHz.

First, the numerical simulation was performed with constant coupling $\Gamma = 1.0$ and input power $P_{\text{in}} = 100$ mW. The result is shown in Fig. B.1. In this condition, the CW comb spectrum and intracavity intensity indicate that the CW comb is not disturbed by mode coupling with $\Gamma = 1.0$. However, one can see some interesting behaviors from the results. Although the intracavity power of both the CW and CCW modes increased until the detuning reached 0.2×10^{-3}, the power of the CCW mode decreased significantly when the CW mode generated a pulse ($> 1 \times 10^{-3}$). These results suggested that the CCW mode receives the power of the CW comb by fixed coupling in the spectrum domain, and there are no nonlinear processes after the soliton formation in the CW direction. As a result, the spectrum and the time domain waveform of the CCW mode are similar to those of the CW mode; however, the peak power exhibits orders of

magnitude smaller than that of the CW mode.

Next, further analysis was conducted by changing the coupling strength and input power. Figure B.2(a) and B.2(b) show the intracavity intensity with $\Gamma = 0.5$, $P_{\text{in}} = 50$ mW and $\Gamma = 3.0$, $P_{\text{in}} = 200$ mW, respectively. And, Figure B.2(c) and B.2(d) show the numerical investigation of the probability of soliton generation when changing input power and dispersion, respectively. With a small Γ value, the CW mode exhibits a stable soliton state; however, with a Γ value of > 2.5, the probability suddenly decreases. When $\Gamma > 3.0$, the CW mode could not be transformed into a soliton state whatever the dispersion value was set. These results indicate that the mode coupling strength affects the probability of soliton formation in the CW mode. Only very strong coupling induces competition between the intracavity powers of the CW and CCW modes and disturbs Kerr comb formation even in the CW mode. In other words, the coupling between the CW-CCW modes will not affect Kerr comb generation in the CW direction as long as the coupling is within the practical strength range.

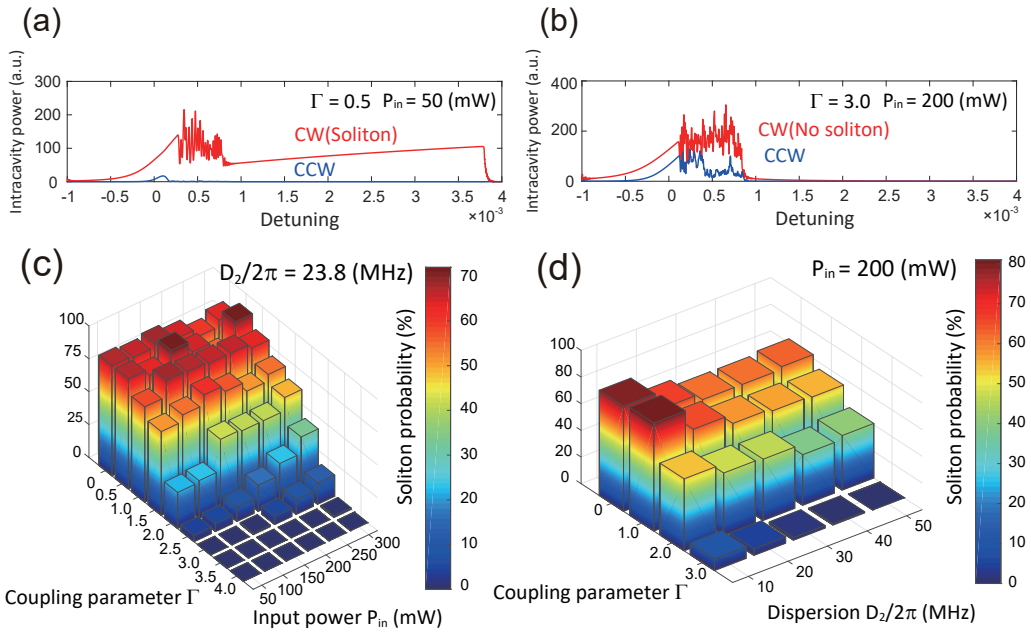

Fig. B.2: (a), (b) Intracavity powers versus normalized detuning with different coupling parameter and input power. (c), (d) Numerical investigation of probability of soliton formation in the CW direction when changing input power and dispersion $D_2/2\pi$, respectively. In each case, the calculations were performed 100 times.

Although constant coupling was thus far assumed, the coupling strength is not always the same for all modes in the real microresonator system. This difference has been observed experimentally and can be explained by the presence of multiple scattering points [194]. Here, the simulation assumes the random coupling parameters of each longitudinal mode. Figure B.3 shows the results with $\Gamma = 0 \sim 4.0$ and $P_{\text{in}} = 100$ mW. The Γ value of each mode is randomly

selected from 0 to 4.0 by a pseudorandom number algorithm whose average value is about 2.0. Calculated spectra and temporal waveforms of the CW and CCW modes are shown in Fig. B.3(a)-B.3(d), respectively. The CCW mode experienced random coupling Γ from 0 to 4.0, as shown in Fig. B.3(e). The comb intensities of CCW modes, particularly $\mu = -7$, 2, and 7, are weaker than those of the other modes depending on the coupling strength Γ. On the other hand, the intensity of some combs (e.g., $\mu = 3, 4$) is correspondingly strong. Even when a CW mode is in a soliton state or a Turing pattern state, the intensity of the CCW mode is weak, and the waveform is not smooth [Fig. B.3(d)]. These results show that the CCW comb teeth are directly affected by the coupling strength and could not be compensated with the nonlinear effect. On the other hand, the CW mode generates a soliton pulse in spite of random coupling.

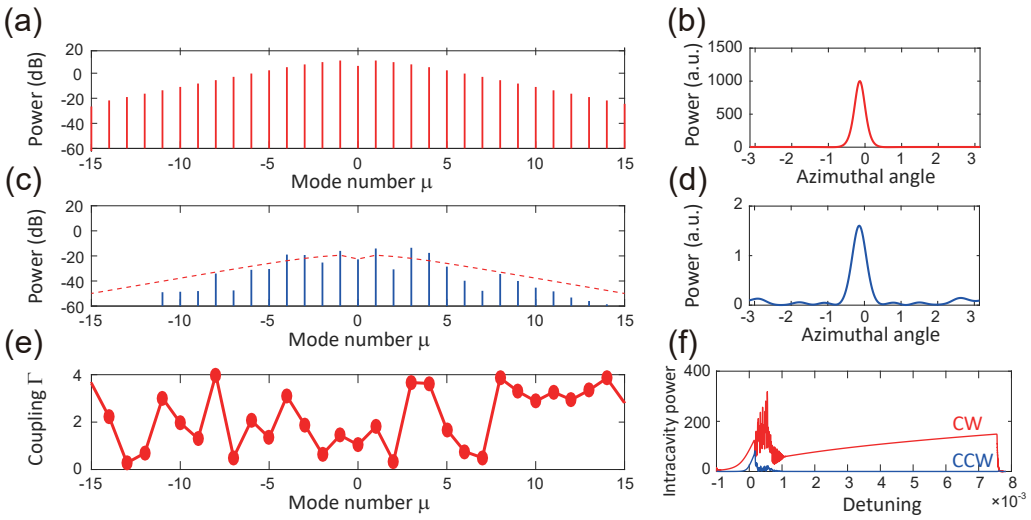

Fig. B.3: (a), (b) Simulated optical spectrum and temporal waveform in the CW direction when the coupling strength is randomly set with Γ =0 to 4.0, as shown in (e). (c), (d) Corresponding results of the CCW direction. The red dashed line indicates the envelope of the soliton comb. (e) Coupling parameter Γ for each longitudinal mode. (f) Average intracavity power and normalized detuning of CW and CCW modes.

B.2 Experimental observation of CW-CCW mode coupled Kerr frequency comb

To confirm the numerical results, an experiment was performed in a silica toroid microresonator that inherently exhibits a strong CW-CCW mode coupling. The transmission spectrum, which gives the coupling strength of each mode, was recorded in advance. Since the diameter of the microtoroid was 45 μm, the higher-order mode was selected as the pump mode from the standpoint of the

dispersion. To observe the CCW comb mode, an optical circulator was inserted before the coupling to the microresonator. Fig. B.4 shows the experimental setup. The combs generated in the CW and CCW directions are simultaneously observed, as shown in Figs. B.4(b) and B.4(c). The CW comb spectrum suggests a low-noise initial state, namely a Turing pattern comb; on the other hand, the CCW direction is also temporally stable but exhibiting an irregular spectrum shape as described in the simulation. Then, the power ratio of the CW and CCW modes (P_μ) can be compared with the strengths of the CW-CCW coupling ($\Gamma = \kappa/\gamma$), which were obtained from the preliminary experiment of transmission measurement. The coupling strength differs for different modes but falls within the 10 to 50 MHz range, and typically measured linewidths imply $Q \sim 1 \times 10^7$. Figure B.4(d) shows the transmission spectrum of the particular mode $\mu = -2$. Here, the power ratio P_μ was calculated by dividing the CCW peak power by the CW peak power. The results of P_μ and Γ for each mode are summarized in Fig. B.4(e), where the two lines show a strong correlation, which indicates that the CCW comb is generated by the scattering of each CW comb component. This, in turn, indicates that the FWM process is dominant in the CW direction, and nonlinear mixing rarely occurs in the CCW direction. The trend of the experimental observation agrees with the numerical simulation in terms of the irregular comb power. Nevertheless, a soliton could not be observed in this experiment, mainly due to the instrumental limitation.

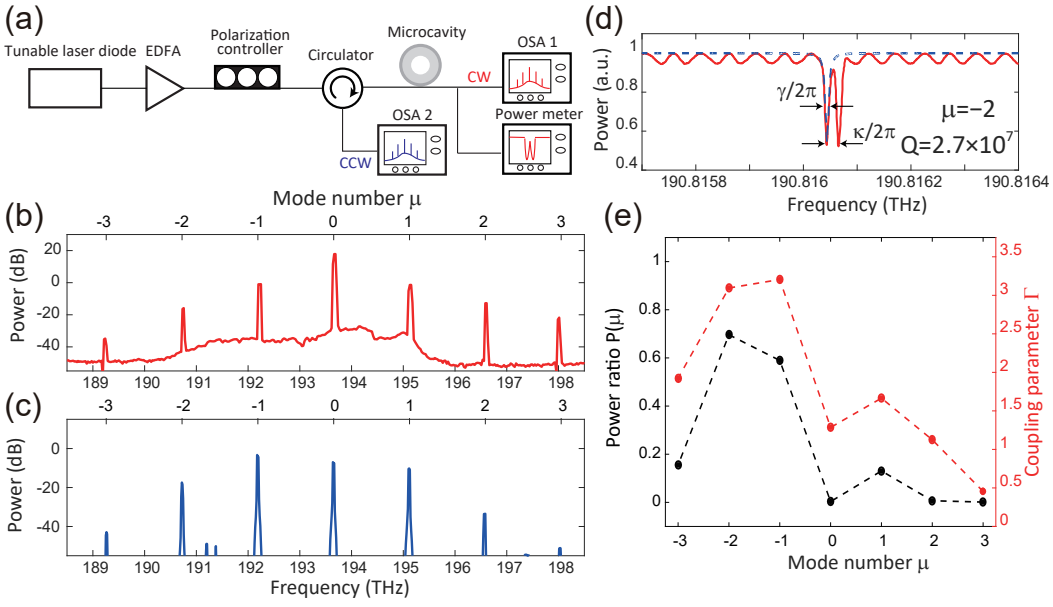

Fig. B.4: (a) Experimental setup used for measuring CW and CCW combs and transmission spectrum. (b) Measured CW comb spectrum. (c) Measured CCW comb spectrum. (d) Transmittance spectrum of a mode ($\mu = -2$). Q is 2.7×10^7 and the splitting width $\kappa/2\pi$ is 22 MHz. (e) Relationship between the normalized power ratio of CW to CCW and the coupling parameter Γ.

B.3 Summary

In summary, the effect of a CW-CCW mode coupling on Kerr comb generation has been investigated both experimentally and theoretically. In the numerical simulation, a model with which to study a CW-CCW mode coupled system was developed based on a Lugiato-Lefever equation. The calculation result suggested that CW-CCW coupling will not degrade the CW comb and soliton formation as long as the system has a sufficiently anomalous dispersion and weak coupling. In the experiment, the contribution of linear scattering to a spectrum in the CCW direction was confirmed.

Bibliography

[1] T. H. Maiman, "Stimulated optical radiation in ruby," Nature **187**, 493–494 (1960).

[2] A. L. Schawlow and C. H. Townes, "Infrared and optical masers," Phys. Rev. **112**, 1940–1949 (1958).

[3] K. J. Vahala, "Optical microcavities," Nature **424**, 839 (2003).

[4] V. Braginsky, M. Gorodetsky, and V. Ilchenko, "Quality-factor and nonlinear properties of optical whispering-gallery modes," Phys. Lett. A **137**, 393–397 (1989).

[5] D. Armani, T. J. Kippenberg, S. Spillane, and K. J. Vahala, "Ultra-high-Q toroid microcavity on a chip," Nature **421**, 925–928 (2003).

[6] M. L. Gorodetsky, A. A. Savchenkov, and V. S. Ilchenko, "Ultimate Q of optical microsphere resonators," Opt. Lett. **21**, 453–455 (1996).

[7] I. S. Grudinin, A. B. Matsko, A. A. Savchenkov, D. Strekalov, V. S. Ilchenko, and L. Maleki, "Ultra high Q crystalline microcavities," Opt. Commun. **265**, 33 – 38 (2006).

[8] P. Rabiei, W. H. Steier, Cheng Zhang, and L. R. Dalton, "Polymer micro-ring filters and modulators," J. Light. Technol. **20**, 1968–1975 (2002).

[9] V. S. Ilchenko, A. A. Savchenkov, A. B. Matsko, and L. Maleki, "Crystalline whispering gallery mode resonators: in search of the optimal material," in "Laser Resonators, Microresonators, and Beam Control XVI," , vol. 8960International Society for Optics and Photonics (SPIE, 2014), vol. 8960, pp. 153 – 162.

[10] M. Borselli, T. J. Johnson, and O. Painter, "Beyond the Rayleigh scattering limit in high-Q silicon microdisks: theory and experiment," Opt. Express **13**, 1515–1530 (2005).

[11] J. Lin, Y. Xu, Z. Fang, M. Wang, J. Song, N. Wang, L. Qiao, W. Fang, and Y. Cheng, "Fabrication of high-Q lithium niobate microresonators using femtosecond laser micromachining," Sci. Rep. **5**, 8072 (2015).

[12] G. Lin and Y. K. Chembo, "Monolithic total internal reflection resonators for applications in photonics," Opt. Mater. X **2**, 100017 (2019).

[13] H. Lee, T. Chen, J. Li, K. Y. Yang, S. Jeon, O. Painter, and K. J. Vahala, "Chemically etched ultrahigh-Q wedge-resonator on a silicon chip," Nat. Photonics **6**, 369 (2012).

[14] W. Liang, A. A. Savchenkov, A. B. Matsko, V. S. Ilchenko, D. Seidel, and L. Maleki, "Generation of near-infrared frequency combs from a MgF_2 whispering gallery mode resonator," Opt. Lett. **36**, 2290–2292 (2011).

[15] P. Del'Haye, S. A. Diddams, and S. B. Papp, "Laser-machined ultra-high-Q microrod resonators for nonlinear optics," Appl. Phys. Lett. **102**, 221119 (2013).

[16] M. Sumetsky, Y. Dulashko, and R. S. Windeler, "Optical microbubble resonator," Opt. Lett. **35**, 898–900 (2010).

[17] S. Xiao, M. H. Khan, H. Shen, and M. Qi, "Compact silicon microring resonators with ultra-low propagation loss in the C band," Opt. Express **15**, 14467–14475 (2007).

[18] J. S. Levy, A. Gondarenko, M. A. Foster, A. C. Turner-Foster, A. L. Gaeta, and M. Lipson, "CMOS-compatible multiple-wavelength oscillator for on-chip optical interconnects," Nat. Photonics **4**, 37–40 (2010).

[19] M. Ferrera, L. Razzari, D. Duchesne, R. Morandotti, Z. Yang, M. Liscidini, J. E. Sipe, S. Chu, B. E. Little, and D. J. Moss, "Low-power continuous-wave nonlinear optics in doped silica glass integrated waveguide structures," Nat. Photonics **2**, 737–740 (2008).

[20] H. Jung, C. Xiong, K. Y. Fong, X. Zhang, and H. X. Tang, "Optical frequency comb generation from aluminum nitride microring resonator," Opt. Lett. **38**, 2810–2813 (2013).

[21] L. Ottaviano, M. Pu, E. Semenova, and K. Yvind, "Low-loss high-confinement waveguides and microring resonators in AlGaAs-on-insulator," Opt. Lett. **41**, 3996–3999 (2016).

[22] B. J. M. Hausmann, I. Bulu, V. Venkataraman, P. Deotare, and M. Lončar, "Diamond nonlinear photonics," Nat. Photonics **8**, 369 (2014).

[23] V. R. Almeida, C. A. Barrios, R. R. Panepucci, M. Lipson, M. A. Foster, D. G. Ouzounov, and A. L. Gaeta, "All-optical switching on a silicon chip," Opt. Lett. **29**, 2867–2869 (2004).

[24] M. R. Foreman, J. D. Swaim, and F. Vollmer, "Whispering gallery mode sensors," Adv. Opt. Photon. **7**, 168–240 (2015).

[25] H. Mabuchi and A. C. Doherty, "Cavity quantum electrodynamics: Coherence in context," Science **298**, 1372–1377 (2002).

[26] D. W. Vernooy, A. Furusawa, N. P. Georgiades, V. S. Ilchenko, and H. J. Kimble, "Cavity QED with high-Q whispering gallery modes," Phys. Rev. A **57**, R2293–R2296 (1998).

[27] M. Aspelmeyer, T. J. Kippenberg, and F. Marquardt, "Cavity optomechanics," Rev. Mod. Phys. **86**, 1391–1452 (2014).

[28] T. J. Kippenberg, R. Holzwarth, and S. A. Diddams, "Microresonator-based optical frequency combs," Science **332**, 555–559 (2011).

[29] R. Holzwarth, T. Udem, T. W. Hänsch, J. C. Knight, W. J. Wadsworth, and P. S. J. Russell, "Optical frequency synthesizer for precision spectroscopy," Phys. Rev. Lett. **85**, 2264–2267 (2000).

[30] S. A. Diddams, D. J. Jones, J. Ye, S. T. Cundiff, J. L. Hall, J. K. Ranka, R. S. Windeler, R. Holzwarth, T. Udem, and T. W. Hänsch, "Direct link between microwave and optical frequencies with a 300 THz femtosecond laser comb," Phys. Rev. Lett. **84**, 5102–5105 (2000).

[31] T. Udem, R. Holzwarth, and T. W. Hansch, "Optical frequency metrology," Nature **416**, 233–237 (2002).

[32] S. A. Diddams, "The evolving optical frequency comb," J. Opt. Soc. Am. B **27**, B51–B62 (2010).

[33] J. L. Hall, "Why it took so long for the laser and the optical comb to be invented: the unmarked trail from concept to experimental reality," J. Opt. Soc. Am. B **34**, 338–346 (2017).

[34] P. Del'Haye, A. Schliesser, O. Arcizet, T. Wilken, R. Holzwarth, and T. J. Kippenberg, "Optical frequency comb generation from a monolithic microresonator," Nature **450**, 1214–1217 (2007).

[35] P. Del'Haye, T. Herr, E. Gavartin, M. L. Gorodetsky, R. Holzwarth, and T. J. Kippenberg, "Octave spanning tunable frequency comb from a microresonator," Phys. Rev. Lett. **107**, 063901 (2011).

[36] P. Del'Haye, O. Arcizet, A. Schliesser, R. Holzwarth, and T. J. Kippenberg, "Full stabilization of a microresonator-based optical frequency comb," Phys. Rev. Lett. **101**, 053903 (2008).

[37] A. A. Savchenkov, A. B. Matsko, V. S. Ilchenko, I. Solomatine, D. Seidel, and L. Maleki, "Tunable optical frequency comb with a crystalline whispering gallery mode resonator," Phys. Rev. Lett. **101**, 093902 (2008).

[38] Y. K. Chembo and N. Yu, "On the generation of octave-spanning optical frequency combs using monolithic whispering-gallery-mode microresonators," Opt. Lett. **35**, 2696–2698 (2010).

[39] A. Pasquazi, M. Peccianti, L. Razzari, D. J. Moss, S. Coen, M. Erkintalo, Y. K. Chembo, T. Hansson, S. Wabnitz, P. Del' Haye, X. Xue, A. M. Weiner, and R. Morandotti, "Micro-combs: A novel generation of optical sources," Phys. Rep. **729**, 1– –81 (2018). Micro-combs: A novel generation of optical sources.

[40] P. Grelu and N. Akhmediev, "Dissipative solitons for mode-locked lasers," Nat. Photonics **6**, 84–92 (2012).

[41] T. Herr, V. Brasch, J. Jost, C. Wang, N. Kondratiev, M. Gorodetsky, and T. J. Kippenberg, "Temporal solitons in optical microresonators," Nat. Photonics **8**, 145–152 (2014).

[42] X. Yi, Q.-F. Yang, K. Y. Yang, M.-G. Suh, and K. J. Vahala, "Soliton frequency comb at microwave rates in a high-Q silica microresonator," Optica **2**, 1078–1085 (2015).

[43] V. Brasch, M. Geiselmann, T. Herr, G. Lihachev, M. H. Pfeiffer, M. L. Gorodetsky, and T. J. Kippenberg, "Photonic chip–based optical frequency comb using soliton Cherenkov radiation," Science **351**, 357–360 (2016).

[44] C. Joshi, J. K. Jang, K. Luke, X. Ji, S. A. Miller, A. Klenner, Y. Okawachi, M. Lipson, and A. L. Gaeta, "Thermally controlled comb generation and soliton modelocking in microresonators," Opt. Lett. **41**, 2565–2568 (2016).

[45] A. G. Griffith, R. K. W. Lau, J. Cardenas, Y. Okawachi, A. Mohanty, R. Fain, Y. H. D. Lee, M. Yu, C. T. Phare, C. B. Poitras, A. L. Gaeta, and M. Lipson, "Silicon-chip mid-infrared frequency comb generation," Nat. Commun. **6**, 6299 (2015).

[46] Z. Gong, A. Bruch, M. Shen, X. Guo, H. Jung, L. Fan, X. Liu, L. Zhang, J. Wang, J. Li, J. Yan, and H. X. Tang, "High-fidelity cavity soliton generation in crystalline AlN micro-ring resonators," Opt. Lett. **43**, 4366–4369 (2018).

[47] Y. He, Q.-F. Yang, J. Ling, R. Luo, H. Liang, M. Li, B. Shen, H. Wang, K. Vahala, and Q. Lin, "Self-starting bi-chromatic $LiNbO_3$ soliton microcomb," Optica **6**, 1138–1144 (2019).

[48] I. S. Grudinin, A. B. Matsko, and L. Maleki, "On the fundamental limits of Q factor of crystalline dielectric resonators," Opt. Express **15**, 3390–3395 (2007).

[49] A. A. Savchenkov, A. B. Matsko, V. S. Ilchenko, and L. Maleki, "Optical resonators with ten million finesse," Opt. Express **15**, 6768–6773 (2007).

[50] A. A. Savchenkov, I. S. Grudinin, A. B. Matsko, D. Strekalov, M. Mohageg, V. S. Ilchenko, and L. Maleki, "Morphology-dependent photonic circuit elements," Opt. Lett. **31**, 1313–1315 (2006).

[51] J. M. Winkler, I. S. Grudinin, and N. Yu, "On the properties of single-mode optical resonators," Opt. Express **24**, 13231–13243 (2016).

[52] I. S. Grudinin, L. Baumgartel, and N. Yu, "Frequency comb from a microresonator with engineered spectrum," Opt. Express **20**, 6604–6609 (2012).

[53] I. S. Grudinin and N. Yu, "Dispersion engineering of crystalline resonators via microstructuring," Optica **2**, 221–224 (2015).

[54] Y. Nakagawa, Y. Mizumoto, T. Kato, T. Kobatake, H. Itobe, Y. Kakinuma, and T. Tanabe, "Dispersion tailoring of a crystalline whispering gallery mode microcavity for a wide-spanning optical Kerr frequency comb," J. Opt. Soc. Am. B **33**, 1913–1920 (2016).

[55] N. G. Pavlov, G. Lihachev, S. Koptyaev, E. Lucas, M. Karpov, N. M. Kondratiev, I. A. Bilenko, T. J. Kippenberg, and M. L. Gorodetsky, "Soliton dual frequency combs in crystalline microresonators," Opt. Lett. **42**, 514–517 (2017).

[56] T. J. Kippenberg, S. M. Spillane, and K. J. Vahala, "Kerr-nonlinearity optical parametric oscillation in an ultrahigh-Q toroid microcavity," Phys. Rev. Lett. **93**, 083904 (2004).

[57] M. Soltani, V. Ilchenko, A. Matsko, A. Savchenkov, J. Schlafer, C. Ryan, and L. Maleki, "Ultrahigh Q whispering gallery mode electro-optic resonators on a silicon photonic chip," Opt. Lett. **41**, 4375–4378 (2016).

[58] M. Anderson, N. G. Pavlov, J. D. Jost, G. Lihachev, J. Liu, T. Morais, M. Zervas, M. L. Gorodetsky, and T. J. Kippenberg, "Highly efficient coupling of crystalline microresonators to integrated photonic waveguides," Opt. Lett. **43**, 2106–2109 (2018).

[59] G. Liu, V. S. Ilchenko, T. Su, Y.-C. Ling, S. Feng, K. Shang, Y. Zhang, W. Liang, A. A. Savchenkov, A. B. Matsko, L. Maleki, and S. J. B. Yoo, "Low-loss prism-waveguide optical coupling for ultrahigh-Q low-index monolithic resonators," Optica **5**, 219–226 (2018).

[60] Y. Zhuang, H. Kumazaki, S. Fujii, R. Imamura, N. A. B. Daud, R. Ishida, H. Chen, and T. Tanabe, "Coupling of a whispering gallery mode to a silicon chip with photonic crystal," Opt. Lett. **44**, 5731–5734 (2019).

[61] C. Lin, W. A. Reed, A. D. Pearson, and H.-T. Shang, "Phase matching in the minimum-chromatic-dispersion region of single-mode fibers for stimulated four-photon mixing," Opt. Lett. **6**, 493–495 (1981).

[62] G. K. L. Wong, S. G. Murdoch, R. Leonhardt, J. D. Harvey, and V. Marie, "High-conversion-efficiency widely-tunable all-fiber optical parametric oscillator," Opt. Express **15**, 2947–2952 (2007).

[63] A. Y. H. Chen, G. K. L. Wong, S. G. Murdoch, R. Leonhardt, J. D. Harvey, J. C. Knight, W. J. Wadsworth, and P. S. J. Russell, "Widely tunable optical parametric generation in a photonic crystal fiber," Opt. Lett. **30**, 762–764 (2005).

[64] A. B. Matsko, A. A. Savchenkov, S.-W. Huang, and L. Maleki, "Clustered frequency comb," Opt. Lett. **41**, 5102–5105 (2016).

[65] N. L. B. Sayson, H. Pham, K. E. Webb, V. Ng, L. S. Trainor, H. G. L. Schwefel, S. Coen, M. Erkintalo, and S. G. Murdoch, "Origins of clustered frequency combs in kerr microresonators," Opt. Lett. **43**, 4180–4183 (2018).

[66] N. L. B. Sayson, T. Bi, V. Ng, H. Pham, L. S. Trainor, H. G. L. Schwefel, S. Coen, M. Erkintalo, and S. G. Murdoch, "Octave-spanning tunable parametric oscillation in crystalline Kerr microresonators," Nat. Photonics **13**, 701–706 (2019).

[67] N. L. B. Sayson, K. E. Webb, S. Coen, M. Erkintalo, and S. G. Murdoch, "Widely tunable optical parametric oscillation in a Kerr microresonator," Opt. Lett. **42**, 5190–5193 (2017).

[68] Y. Tang, Z. Gong, X. Liu, and H. X. Tang, "Widely separated optical kerr parametric oscillation in AlN microrings," Opt. Lett. **45**, 1124–1127 (2020).

[69] X. Lu, G. Moille, A. Singh, Q. Li, D. A. Westly, A. Rao, S.-P. Yu, T. C. Briles, S. B. Papp, and K. Srinivasan, "Milliwatt-threshold visible–telecom optical parametric oscillation using silicon nanophotonics," Optica **6**, 1535–1541 (2019).

[70] T. Carmon and K. J. Vahala, "Visible continuous emission from a silica microphotonic device by third-harmonic generation," Nat. Phys. **3**, 430–435 (2007).

[71] D. Farnesi, A. Barucci, G. C. Righini, S. Berneschi, S. Soria, and G. Nunzi Conti, "Optical frequency conversion in silica-whispering-gallery-mode microspherical resonators," Phys. Rev. Lett. **112**, 093901 (2014).

[72] S. Miller, K. Luke, Y. Okawachi, J. Cardenas, A. L. Gaeta, and M. Lipson, "On-chip frequency comb generation at visible wavelengths via simultaneous second- and third-order optical nonlinearities," Opt. Express **22**, 26517–26525 (2014).

[73] L. Wang, L. Chang, N. Volet, M. H. Pfeiffer, M. Zervas, H. Guo, T. J. Kippenberg, and J. E. Bowers, "Frequency comb generation in the green using silicon nitride microresonators," Laser Photon. Rev. **10**, 631–638 (2016).

[74] H. Jung, R. Stoll, X. Guo, D. Fischer, and H. X. Tang, "Green, red, and IR frequency comb line generation from single IR pump in AlN microring resonator," Optica **1**, 396–399 (2014).

[75] X. Xue, P.-H. Wang, Y. Xuan, M. Qi, and A. M. Weiner, "Microresonator kerr frequency combs with high conversion efficiency," Laser Photon. Rev. **11**, 1600276 (2017).

[76] X. Xue, Y. Xuan, Y. Liu, P.-H. Wang, S. Chen, J. Wang, D. E. Leaird, M. Qi, and A. M. Weiner, "Mode-locked dark pulse Kerr combs in normal-dispersion microresonators," Nat. Photonics **9**, 594–600 (2015).

[77] S.-W. Huang, H. Zhou, J. Yang, J. F. McMillan, A. Matsko, M. Yu, D.-L. Kwong, L. Maleki, and C. Wong, "Mode-locked ultrashort pulse generation from on-chip normal dispersion microresonators," Phys. Rev. Lett. **114**, 053901 (2015).

[78] S. Kim, K. Han, C. Wang, J. A. Jaramillo-Villegas, X. Xue, C. Bao, Y. Xuan, D. E. Leaird, A. M. Weiner, and M. Qi, "Dispersion engineering and frequency comb generation in thin silicon nitride concentric microresonators," Nat. Commun. **8**, 372 (2017).

[79] H. A. Haus and W. Huang, "Coupled-mode theory," Proc. IEEE **79**, 1505–1518 (1991).

[80] S. M. Spillane, T. J. Kippenberg, O. J. Painter, and K. J. Vahala, "Ideality in a fiber-taper-coupled microresonator system for application to cavity quantum electrodynamics," Phys. Rev. Lett. **91**, 043902 (2003).

[81] J. Knight, G. Cheung, F. Jacques, and T. Birks, "Phase-matched excitation of whispering-gallery-mode resonances by a fiber taper," Opt. Lett. **22**, 1129–1131 (1997).

[82] L. Ding, C. Belacel, S. Ducci, G. Leo, and I. Favero, "Ultralow loss single-mode silica tapers manufactured by a microheater," Appl. Opt. **49**, 2441–2445 (2010).

[83] R. Nagai and T. Aoki, "Ultra-low-loss tapered optical fibers with minimal lengths," Opt. Express **22**, 28427–28436 (2014).

[84] M. L. Gorodetsky and V. S. Ilchenko, "Optical microsphere resonators: optimal coupling to high-Q whispering-gallery modes," J. Opt. Soc. Am. B **16**, 147–154 (1999).

[85] Y. A. Demchenko, I. A. Bilenko, and M. L. Gorodetsky, "Optimisation of the prism coupling of optical whispering-gallery-mode microcavities," Quantum Electron. **47**, 743–747 (2017).

[86] G. Lin, J. Fürst, D. V. Strekalov, I. S. Grudinin, and N. Yu, "High-Q UV whispering gallery mode resonators made of angle-cut BBO crystals," Opt. Express **20**, 21372–21378 (2012).

[87] J. U. Fürst, D. V. Strekalov, D. Elser, A. Aiello, U. L. Andersen, C. Marquardt, and G. Leuchs, "Quantum light from a whispering-gallery-mode disk resonator," Phys. Rev. Lett. **106**, 113901 (2011).

[88] V. S. Ilchenko, A. M. Bennett, P. Santini, A. A. Savchenkov, A. B. Matsko, and L. Maleki, "Whispering gallery mode diamond resonator," Opt. Lett. **38**, 4320–4323 (2013).

[89] Y. Pan, G. Lin, S. Diallo, X. Zhang, and Y. K. Chembo, "Design of X-cut and Z-cut lithium niobate whispering-gallery-mode disk-resonators with high quality factors," IEEE Photon. J. **9**, 1–8 (2017).

[90] J. U. Fürst, K. Buse, I. Breunig, P. Becker, J. Liebertz, and L. Bohatý, "Second-harmonic generation of light at 245âĂŁâĂŁnm in a lithium tetraborate whispering gallery resonator," Opt. Lett. **40**, 1932–1935 (2015).

[91] M. H. P. Pfeiffer, J. Liu, M. Geiselmann, and T. J. Kippenberg, "Coupling ideality of integrated planar high-Q microresonators," Phys. Rev. Applied **7**, 024026 (2017).

[92] Y. Xuan, Y. Liu, L. T. Varghese, A. J. Metcalf, X. Xue, P.-H. Wang, K. Han, J. A. Jaramillo-Villegas, A. A. Noman, C. Wang, S. Kim, M. Teng, Y. J. Lee, B. Niu, L. Fan, J. Wang, D. E. Leaird, A. M. Weiner, and M. Qi, "High-Q silicon nitride microresonators exhibiting low-power frequency comb initiation," Optica **3**, 1171–1180 (2016).

[93] X. Ji, F. A. S. Barbosa, S. P. Roberts, A. Dutt, J. Cardenas, Y. Okawachi, A. Bryant, A. L. Gaeta, and M. Lipson, "Ultra-low-loss on-chip resonators with sub-milliwatt parametric oscillation threshold," Optica **4**, 619–624 (2017).

[94] M. H. P. Pfeiffer, J. Liu, A. S. Raja, T. Morais, B. Ghadiani, and T. J. Kippenberg, "Ultra-smooth silicon nitride waveguides based on the Damascene reflow process: fabrication and loss origins," Optica **5**, 884–892 (2018).

[95] R. W. Boyd, Nonlinear optics (Taylor & Francis, 2003).

[96] A. A. Savchenkov, A. B. Matsko, D. Strekalov, M. Mohageg, V. S. Ilchenko, and L. Maleki, "Low threshold optical oscillations in a whispering gallery mode CaF_2 resonator," Phys. Rev. Lett. **93**, 243905 (2004).

[97] T. J. Kippenberg, S. M. Spillane, B. Min, and K. J. Vahala, "Theoretical and experimental study of stimulated and cascaded Raman scattering in ultrahigh-Q optical microcavities," IEEE J. Sel. Topics Quantum Electron. **10**, 1219–1228 (2004).

[98] I. S. Grudinin, A. B. Matsko, and L. Maleki, "Brillouin lasing with a CaF_2 whispering gallery mode resonator," Phys. Rev. Lett. **102**, 043902 (2009).

[99] T. Carmon, L. Yang, and K. J. Vahala, "Dynamical thermal behavior and thermal self-stability of microcavities," Opt. Express **12**, 4742–4750 (2004).

[100] L. He, Y.-F. Xiao, J. Zhu, S. K. Ozdemir, and L. Yang, "Oscillatory thermal dynamics in high-Q PDMS-coated silica toroidal microresonators," Opt. Express **17**, 9571–9581 (2009).

[101] A. J. DeMaria, D. A. Stetser, and H. Heynau, "Self mode-locking of lasers with saturable absorbers," Appl. Phys. Lett. **8**, 174–176 (1966).

[102] Y. K. Chen, M. C. Wu, T. Tanbun-Ek, R. A. Logan, and M. A. Chin, "Subpicosecond monolithic colliding-pulse mode-locked multiple quantum well lasers," Appl. Phys. Lett. **58**, 1253–1255 (1991).

[103] D. J. Jones, S. A. Diddams, J. K. Ranka, A. Stentz, R. S. Windeler, J. L. Hall, and S. T. Cundiff, "Carrier-envelope phase control of femtosecond mode-locked lasers and direct optical frequency synthesis," Science **288**, 635–639 (2000).

[104] M. Kourogi, K. Nakagawa, and M. Ohtsu, "Wide-span optical frequency comb generator for accurate optical frequency difference measurement," IEEE J. Quantum Electron. **29**, 2693–2701 (1993).

[105] N. R. Newbury, "Searching for applications with a fine-tooth comb," Nat. Photonics **5**, 186–188 (2011).

[106] S. A. Diddams, J. C. Bergquist, S. R. Jefferts, and C. W. Oates, "Standards of time and frequency at the outset of the 21st century," Science **306**, 1318–1324 (2004).

[107] S. A. Diddams, L. Hollberg, and V. Mbele, "Molecular fingerprinting with the resolved modes of a femtosecond laser frequency comb," Nature **445**, 627–630 (2007).

[108] I. Coddington, N. Newbury, and W. Swann, "Dual-comb spectroscopy," Optica **3**, 414–426 (2016).

[109] T. M. Fortier, M. S. Kirchner, F. Quinlan, J. Taylor, J. C. Bergquist, T. Rosenband, N. Lemke, A. Ludlow, Y. Jiang, C. W. Oates, and S. A. Diddams, "Generation of ultrastable microwaves via optical frequency division," Nat. Photonics **5**, 425–429 (2011).

[110] Y. K. Chembo and N. Yu, "Modal expansion approach to optical-frequency-comb generation with monolithic whispering-gallery-mode resonators," Phys. Rev. A **82**, 033801 (2010).

[111] Y. K. Chembo and C. R. Menyuk, "Spatiotemporal Lugiato-Lefever formalism for Kerr-comb generation in whispering-gallery-mode resonators," Phys. Rev. A **87**, 053852 (2013).

[112] S. Coen, H. G. Randle, T. Sylvestre, and M. Erkintalo, "Modeling of octave-spanning Kerr frequency combs using a generalized mean-field Lugiato-Lefever model," Opt. Lett. **38**, 37–39 (2013).

[113] L. A. Lugiato and R. Lefever, "Spatial dissipative structures in passive optical systems," Phys. Rev. Lett. **58**, 2209 (1987).

[114] G. P. Agrawal, Nonlinear Fiber Optics (Academic, 2007).

[115] Y. K. Chembo, I. S. Grudinin, and N. Yu, "Spatiotemporal dynamics of Kerr-Raman optical frequency combs," Phys. Rev. A **92**, 043818 (2015).

[116] M. R. E. Lamont, Y. Okawachi, and A. L. Gaeta, "Route to stabilized ultrabroadband microresonator-based frequency combs," Opt. Lett. **38**, 3478–3481 (2013).

[117] T. Herr, K. Hartinger, J. Riemensberger, C. Wang, E. Gavartin, R. Holzwarth, M. Gorodetsky, and T. J. Kippenberg, "Universal formation dynamics and noise of Kerr-frequency combs in microresonators," Nat. Photonics **6**, 480–487 (2012).

[118] A. B. Matsko, A. A. Savchenkov, D. Strekalov, V. S. Ilchenko, and L. Maleki, "Optical hyperparametric oscillations in a whispering-gallery-mode resonator: Threshold and phase diffusion," Phys. Rev. A **71**, 033804 (2005).

[119] T. Hansson, D. Modotto, and S. Wabnitz, "Dynamics of the modulational instability in microresonator frequency combs," Phys. Rev. A **88**, 023819–1 – 023819–8 (2013).

[120] V. Brasch, M. Geiselmann, M. H. P. Pfeiffer, and T. J. Kippenberg, "Bringing short-lived dissipative Kerr soliton states in microresonators into a steady state," Opt. Express **24**, 29312–29320 (2016).

[121] X. Yi, Q.-F. Yang, K. Y. Yang, and K. Vahala, "Active capture and stabilization of temporal solitons in microresonators," Opt. Lett. **41**, 2037–2040 (2016).

[122] J. R. Stone, T. C. Briles, T. E. Drake, D. T. Spencer, D. R. Carlson, S. A. Diddams, and S. B. Papp, "Thermal and nonlinear dissipative-soliton dynamics in Kerr-microresonator frequency combs," Phys. Rev. Lett. **121**, 063902 (2018).

[123] S. Zhang, J. M. Silver, L. D. Bino, F. Copie, M. T. M. Woodley, G. N. Ghalanos, A. Ø. Svela, N. Moroney, and P. Del'Haye, "Sub-milliwatt-level microresonator solitons with extended access range using an auxiliary laser," Optica **6**, 206–212 (2019).

[124] H. Zhou, Y. Geng, W. Cui, S.-W. Huang, Q. Zhou, K. Qiu, and C. Wei Wong, "Soliton bursts and deterministic dissipative Kerr soliton generation in auxiliary-assisted microcavities," Light Sci. Appl. **8**, 50 (2019).

[125] R. W. P. Drever, J. L. Hall, F. V. Kowalski, J. Hough, G. M. Ford, A. J. Munley, and H. Ward, "Laser phase and frequency stabilization using an optical resonator," Appl. Phys. B **31**, 97–105 (1983).

[126] E. Obrzud, S. Lecomte, and T. Herr, "Temporal solitons in microresonators driven by optical pulses," Nat. Photonics **11**, 600–607 (2017).

[127] S. J. Herr, V. Brasch, J. Szabados, E. Obrzud, Y. Jia, S. Lecomte, K. Buse, I. Breunig, and T. Herr, "Frequency comb up- and down-conversion in synchronously driven $\chi^{(2)}$ optical microresonators," Opt. Lett. **43**, 5745–5748 (2018).

[128] M. Zhang, B. Buscaino, C. Wang, A. Shams-Ansari, C. Reimer, R. Zhu, J. M. Kahn, and M. Lončar, "Broadband electro-optic frequency comb generation in a lithium niobate microring resonator," Nature **568**, 373–377 (2019).

[129] C. Wang, M. Zhang, M. Yu, R. Zhu, H. Hu, and M. Loncar, "Monolithic lithium niobate photonic circuits for Kerr frequency comb generation and modulation," Nat. Commun. **10**, 978 (2019).

[130] A. Martinez and S. Yamashita, "Multi-gigahertz repetition rate passively mode-locked fiber lasers using carbon nanotubes," Opt. Express **19**, 6155–6163 (2011).

[131] A. S. Mayer, C. R. Phillips, and U. Keller, "Watt-level 10-gigahertz solid-state laser enabled by self-defocusing nonlinearities in an aperiodically poled crystal," Nat. Commun. **8**, 1673 (2017).

[132] S. Kimura, S. Tani, and Y. Kobayashi, "Kerr-lens mode locking above a 20 Ghz repetition rate," Optica **6**, 532–533 (2019).

[133] J. Pfeifle, A. Coillet, R. Henriet, K. Saleh, P. Schindler, C. Weimann, W. Freude, I. V. Balakireva, L. Larger, C. Koos, and Y. K. Chembo, "Optimally coherent kerr combs generated with crystalline whispering gallery mode resonators for ultra-high capacity fiber communications," Phys. Rev. Lett. **114**, 093902 (2015).

[134] P. Marin-Palomo, J. N. Kemal, M. Karpov, A. Kordts, J. Pfeifle, M. H. P. Pfeiffer, P. Trocha, S. Wolf, V. Brasch, M. H. Anderson, R. Rosenberger, K. Vijayan, W. Freude, T. J. Kippenberg, and C. Koos, "Microresonator-based solitons for massively parallel coherent optical communications," Nature **546**, 274–279 (2017).

[135] M.-G. Suh, Q.-F. Yang, K. Y. Yang, X. Yi, and K. J. Vahala, "Microresonator soliton dual-comb spectroscopy," Science **354**, 600–603 (2016).

[136] A. Dutt, C. Joshi, X. Ji, J. Cardenas, Y. Okawachi, K. Luke, A. L. Gaeta, and M. Lipson, "On-chip dual-comb source for spectroscopy," Sci. Adv. **4**, e1701858 (2018).

[137] M. Yu, Y. Okawachi, A. G. Griffith, N. Picque, M. Lipson, and A. L. Gaeta, "Silicon-chip-based mid-infrared dual-comb spectroscopy," Nat. Commun. **9**, 1869 (2018).

[138] P. J. Marchand, J. C. Skehan, J. Riemensberger, J.-J. Ho, M. H. P. Pfeiffer, J. Liu, C. Hauger, T. Lasser, and T. J. Kippenberg, "Soliton microcomb based spectral domain optical coherence tomography," arXiv:1902.06985 (2019).

[139] M.-G. Suh and K. J. Vahala, "Soliton microcomb range measurement," Science **359**, 884–887 (2018).

[140] P. Trocha, M. Karpov, D. Ganin, M. H. P. Pfeiffer, A. Kordts, S. Wolf, J. Krockenberger, P. Marin-Palomo, C. Weimann, S. Randel, W. Freude, T. J. Kippenberg, and C. Koos, "Ultrafast optical ranging using microresonator soliton frequency combs," Science **359**, 887–891 (2018).

[141] E. Obrzud, M. Rainer, A. Harutyunyan, M. H. Anderson, J. Liu, M. Geiselmann, B. Chazelas, S. Kundermann, S. Lecomte, M. Cecconi, A. Ghedina, E. Molinari, F. Pepe, F. Wildi, F. Bouchy, T. J. Kippenberg, and T. Herr, "A microphotonic astrocomb," Nat. Photonics **13**, 31–35 (2019).

[142] M.-G. Suh, X. Yi, Y.-H. Lai, S. Leifer, I. S. Grudinin, G. Vasisht, E. C. Martin, M. P. Fitzgerald, G. Doppmann, J. Wang, D. Mawet, S. B. Papp, S. A. Diddams, C. Beichman, and K. Vahala, "Searching for exoplanets using a microresonator astrocomb," Nat. Photonics **13**, 25–30 (2019).

[143] V. Brasch, E. Lucas, J. D. Jost, M. Geiselmann, and T. J. Kippenberg, "Self-referenced photonic chip soliton Kerr frequency comb," Light Sci. Appl. **6**, e16202–e16202 (2017).

[144] S. B. Papp, K. Beha, P. Del'Haye, F. Quinlan, H. Lee, K. J. Vahala, and S. A. Diddams, "Microresonator frequency comb optical clock," Optica **1**, 10–14 (2014).

[145] W. Liang, D. Eliyahu, V. S. Ilchenko, A. A. Savchenkov, A. B. Matsko, D. Seidel, and L. Maleki, "High spectral purity Kerr frequency comb radio frequency photonic oscillator," Nat. Commun. **6**, 7957 (2015).

[146] D. T. Spencer, T. Drake, T. C. Briles, J. Stone, L. C. Sinclair, C. Fredrick, Q. Li, D. Westly, B. R. Ilic, A. Bluestone, N. Volet, T. Komljenovic, L. Chang, S. H. Lee, D. Y. Oh, M.-G. Suh, K. Y. Yang, M. H. P. Pfeiffer, T. J. Kippenberg, E. Norberg, L. Theogarajan, K. Vahala, N. R. Newbury, K. Srinivasan, J. E. Bowers, S. A. Diddams, and S. B. Papp, "An optical-frequency synthesizer using integrated photonics," Nature **557**, 81–85 (2018).

[147] S. Droste, G. Ycas, B. R. Washburn, I. Coddington, and N. R. Newbury, "Optical frequency comb generation based on erbium fiber lasers," Nanophotonics **5**, 196 – 213 (2016).

[148] W. Sellmeier, "Ueber die durch die Aetherschwingungen erregten Mitschwingungen der KÃűrpertheilchen und deren RÃijckwirkung auf die ersteren, besonders zur ErklÃđrung der Dispersion und ihrer anomalien," Ann. der Physik **223**, 386–403 (1872).

[149] M. J. Weber, Handbook of optical materials (CRC press, 2002).

[150] K. Luke, Y. Okawachi, M. R. E. Lamont, A. L. Gaeta, and M. Lipson, "Broadband mid-infrared frequency comb generation in a Si_3N_4 microresonator," Opt. Lett. **40**, 4823–4826 (2015).

[151] Y. A. Demchenko and M. L. Gorodetsky, "Analytical estimates of eigenfrequencies, dispersion, and field distribution in whispering gallery resonators," J. Opt. Soc. Am. B **30**, 3056–3063 (2013).

[152] I. Breunig, B. Sturman, F. Sedlmeir, H. G. L. Schwefel, and K. Buse, "Whispering gallery modes at the rim of an axisymmetric optical resonator: Analytical versus numerical description and comparison with experiment," Opt. Express **21**, 30683–30692 (2013).

[153] M. Oxborrow, "How to simulate the whispering-gallery modes of dielectric microresonators in FEMLAB/COMSOL," Proc. SPIE **6452**, 6452–1 – 6452–12 (2007).

[154] S. M. Spillane, T. J. Kippenberg, K. J. Vahala, K. W. Goh, E. Wilcut, and H. J. Kimble, "Ultrahigh-Q toroidal microresonators for cavity quantum electrodynamics," Phys. Rev. A **71**, 013817 (2005).

[155] K. Y. Yang, K. Beha, D. C. Cole, X. Yi, P. Del'Haye, H. Lee, J. Li, D. Y. Oh, S. A. Diddams, S. B. Papp, and K. J. Vahala, "Broadband dispersion-engineered microresonator on a chip," Nat. Photonics **10**, 316–320 (2016).

[156] J. Riemensberger, K. Hartinger, T. Herr, V. Brasch, R. Holzwarth, and T. J. Kippenberg, "Dispersion engineering of thick high-Q silicon nitride ring-resonators via atomic layer deposition," Opt. Express **20**, 27661–27669 (2012).

[157] L. Zhang, Y. Yue, R. G. Beausoleil, and A. E. Willner, "Flattened dispersion in silicon slot waveguides," Opt. Express **18**, 20529–20534 (2010).

[158] X. Xue, Y. Xuan, P.-H. Wang, Y. Liu, D. E. Leaird, M. Qi, and A. M. Weiner, "Normal-dispersion microcombs enabled by controllable mode interactions," Laser Photon. Rev. **9**, L23–L28 (2015).

[159] G. Lin and Y. K. Chembo, "On the dispersion management of fluorite whispering-gallery mode resonators for Kerr optical frequency comb generation in the telecom and mid-infrared range," Opt. Express **23**, 1594–1604 (2015).

[160] G. Li, P. Liu, X. Jiang, C. Yang, J. Ma, H. Wu, and M. Xiao, "High-Q silica microdisk optical resonators with large wedge angles on a silicon chip," Photon. Res. **3**, 279–282 (2015).

[161] S. H. Lee, D. Y. Oh, Q.-F. Yang, B. Shen, H. Wang, K. Y. Yang, Y.-H. Lai, X. Yi, X. Li, and K. Vahala, "Towards visible soliton microcomb generation," Nat. Commun. **8**, 1295 (2017).

[162] J. Li, H. Lee, K. Y. Yang, and K. J. Vahala, "Sideband spectroscopy and dispersion measurement in microcavities," Opt. Express **20**, 26337–26344 (2012).

[163] P. Del'Haye, O. Arcizet, M. L. Gorodetsky, R. Holzwarth, and T. J. Kippenberg, "Frequency comb assisted diode laser spectroscopy for measurement of microcavity dispersion," Nat. Photonics **3**, 529–533 (2009).

[164] J. Liu, V. Brasch, M. H. P. Pfeiffer, A. Kordts, A. N. Kamel, H. Guo, M. Geiselmann, and T. J. Kippenberg, "Frequency-comb-assisted broadband precision spectroscopy with cascaded diode lasers," Opt. Lett. **41**, 3134–3137 (2016).

[165] S. B. Papp, P. Del'Haye, and S. A. Diddams, "Parametric seeding of a microresonator optical frequency comb," Opt. Express **21**, 17615–17624 (2013).

[166] T. Herr, V. Brasch, J. D. Jost, I. Mirgorodskiy, G. Lihachev, M. L. Gorodetsky, and T. J. Kippenberg, "Mode spectrum and temporal soliton formation in optical microresonators," Phys. Rev. Lett. **113**, 123901 (2014).

[167] C. Bao, Y. Xuan, D. E. Leaird, S. Wabnitz, M. Qi, and A. M. Weiner, "Spatial mode-interaction induced single soliton generation in microresonators," Optica **4**, 1011–1015 (2017).

[168] X. Yi, Q.-F. Yang, X. Zhang, K. Y. Yang, X. Li, and K. J. Vahala, "Single-mode dispersive waves and soliton microcomb dynamics," Nat. Commun. **8**, 14869 (2017).

[169] D. C. Cole, E. S. Lamb, P. Del'Haye, S. A. Diddams, and S. B. Papp, "Soliton crystals in Kerr resonators," Nat. Photonics **11**, 671–676 (2017).

[170] H. Taheri, A. B. Matsko, and L. Maleki, "Optical lattice trap for Kerr solitons," Eur. Phys. J. D **71**, 153 (2017).

[171] A. A. Savchenkov, A. B. Matsko, W. Liang, V. S. Ilchenko, D. Seidel, and L. Maleki, "Kerr frequency comb generation in overmoded resonators," Opt. Express **20**, 27290–27298 (2012).

[172] Y. Liu, Y. Xuan, X. Xue, P.-H. Wang, S. Chen, A. J. Metcalf, J. Wang, D. E. Leaird, M. Qi, and A. M. Weiner, "Investigation of mode coupling in normal-dispersion silicon nitride microresonators for Kerr frequency comb generation," Optica **1**, 137–144 (2014).

[173] V. Lobanov, G. Lihachev, T. J. Kippenberg, and M. Gorodetsky, "Frequency combs and platicons in optical microresonators with normal GVD," Opt. Express **23**, 7713–7721 (2015).

[174] R. E. Newnham, Properties of materials: anisotropy, symmetry, structure (Oxford University Press on Demand, 2005).

[175] C. Kittel, Introduction to solid state physics, vol. 8 (Wiley New York, 1976).

[176] P. N. Blake and R. O. Scattergood, "Ductile-regime machining of germanium and silicon," J. Am. Ceram. Soc. **73**, 949–957 (1990).

[177] S. Azami, H. Kudo, Y. Mizumoto, T. Tanabe, J. Yan, and Y. Kakinuma, "Experimental study of crystal anisotropy based on ultra-precision cylindrical turning of single-crystal calcium fluoride," Precis. Eng. **40**, 172–181 (2015).

[178] Y. Kakinuma, S. Azami, and T. Tanabe, "Evaluation of subsurface damage caused by ultra-precision turning in fabrication of CaF_2 optical micro resonator," CIRP Annals **64**, 117 – 120 (2015).

[179] W. Blackley and R. Scattergood, "Ductile-regime machining model for diamond turning of brittle materials," Precis. Eng. **13**, 95 – 103 (1991).

[180] K. Liu, D. Zuo, X. P. Li, and M. Rahman, "Nanometric ductile cutting characteristics of silicon wafer using single crystal diamond tools," J. Vac. Sci. Technol **27**, 1361–1366 (2009).

[181] A. Aramcharoen and P. Mativenga, "Size effect and tool geometry in micromilling of tool steel," Precis. Eng. **33**, 402 – 407 (2009).

[182] M. L. Gorodetsky, A. D. Pryamikov, and V. S. Ilchenko, "Rayleigh scattering in high-Q microspheres," J. Opt. Soc. Am. B **17**, 1051–1057 (2000).

[183] G. Lin, R. Henriet, A. Coillet, M. Jacquot, L. Furfaro, G. Cibiel, L. Larger, and Y. K. Chembo, "Dependence of quality factor on surface roughness in crystalline whispering-gallery mode resonators," Opt. Lett. **43**, 495–498 (2018).

[184] Y. Mizumoto, H. Kangawa, Y. Nakagawa, H. Itobe, T. Tanabe, and Y. Kakinuma, "Influence of nose radius on surface integrity in ultra-precision cylindrical turning of single-crystal calcium fluoride," Procedia CIRP **45**, 139 – 142 (2016). 3rd CIRP Conference on Surface Integrity.

[185] J. Yan, T. Asami, H. Harada, and T. Kuriyagawa, "Fundamental investigation of subsurface damage in single crystalline silicon caused by diamond machining," Precis. Eng. **33**, 378 – 386 (2009).

[186] Y. Mizumoto, H. Amano, H. Kangawa, K. Harano, H. Sumiya, and Y. Kakinuma, "On the improvement of subsurface quality of CaF_2 single crystal machined by boron-doped nano-polycrystalline diamond tools," Precis. Eng. **52**, 73 – 83 (2018).

[187] C. Y. Wang, T. Herr, P. Del'Haye, A. Schliesser, J. Hofer, R. Holzwarth, T. Hänsch, N. Picqué, and T. J. Kippenberg, "Mid-infrared optical frequency combs at 2.5 μm based on crystalline microresonators," Nat. Commun. **4**, 1345 (2013).

[188] C. Lecaplain, C. Javerzac-Galy, M. L. Gorodetsky, and T. J. Kippenberg, "Mid-infrared ultra-high-Q resonators based on fluoride crystalline materials," Nat. Commun. **7**, 13383 (2016).

[189] D. Farnesi, F. Cosi, C. Trono, G. C. Righini, G. N. Conti, and S. Soria, "Stimulated anti-Stokes Raman scattering resonantly enhanced in silica microspheres," Opt. Lett. **39**, 5993–5996 (2014).

[190] D. Hollenbeck and C. D. Cantrell, "Multiple-vibrational-mode model for fiber-optic Raman gain spectrum and response function," J. Opt. Soc. Am. B **19**, 2886–2892 (2002).

[191] D. Weiss, V. Sandoghdar, J. Hare, V. Lefevre-Seguin, J.-M. Raimond, and S. Haroche, "Splitting of high-Q Mie modes induced by light backscattering in silica microspheres," Opt. Lett. **20**, 1835–1837 (1995).

[192] T. J. Kippenberg, S. Spillane, and K. Vahala, "Modal coupling in traveling-wave resonators," Opt. Lett. **27**, 1669–1671 (2002).

[193] J. Zhu, Ş. K. Özdemir, L. He, and L. Yang, "Controlled manipulation of mode splitting in an optical microcavity by two Rayleigh scatterers," Opt. Express **18**, 23535–23543 (2010).

[194] J. Zhu, Ş. K. Özdemir, Y.-F. Xiao, L. Li, L. He, D.-R. Chen, and L. Yang, "On-chip single nanoparticle detection and sizing by mode splitting in an ultrahigh-Q microresonator," Nat. Photonics **4**, 46–49 (2010).

[195] B. Peng, a. K. Ozdemir, F. Lei, F. Monifi, M. Gianfreda, G. L. Long, S. Fan, F. Nori, C. M. Bender, and L. Yang, "Parity-time-symmetric whispering-gallery microcavities," Nat. Phys. **10**, 394 EP – (2014).

[196] W. Yoshiki, Y. Honda, T. Tetsumoto, K. Furusawa, N. Sekine, and T. Tanabe, "All-optical tunable buffering with coupled ultra-high Q whispering gallery mode microcavities," Sci. Rep. **7**, 10688 (2017).

[197] B. Peng, Ş. K. Özdemir, W. Chen, F. Nori, and L. Yang, "What is and what is not electromagnetically induced transparency in whispering-gallery microcavities," Nat. Commun. **5**, 5082 EP – (2014).

[198] J. K. Jang, Y. Okawachi, M. Yu, K. Luke, X. Ji, M. Lipson, and A. L. Gaeta, "Dynamics of mode-coupling-induced microresonator frequency combs in normal dispersion," Opt. Express **24**, 28794–28803 (2016).

[199] A. B. Matsko, W. Liang, A. A. Savchenkov, D. Eliyahu, and L. Maleki, "Optical Cherenkov radiation in overmoded microresonators," Opt. Lett. **41**, 2907–2910 (2016).

[200] W. Yoshiki, A. Chen-Jinnai, T. Tetsumoto, and T. Tanabe, "Observation of energy oscillation between strongly-coupled counter-propagating ultra-high Q whispering gallery modes," Opt. Express **23**, 30851–30860 (2015).

[201] T. Hansson, D. Modotto, and S. Wabnitz, "On the numerical simulation of Kerr frequency combs using coupled mode equations," Opt. Commun. **312**, 134–136 (2014).

[202] V. E. Lobanov, A. V. Cherenkov, A. E. Shitikov, I. A. Bilenko, and M. L. Gorodetsky, "Dynamics of platicons due to third-order dispersion," Eur. Phys. J. D **71**, 185–1 – 185–55 (2017).

[203] H. Guo, E. Lucas, M. H. P. Pfeiffer, M. Karpov, M. Anderson, J. Liu, M. Geiselmann, J. D. Jost, and T. J. Kippenberg, "Intermode breather solitons in optical microresonators," Phys. Rev. X **7**, 041055–1 – 041055–10 (2017).

[204] M. T. M. Woodley, J. M. Silver, L. Hill, F. m. c. Copie, L. Del Bino, S. Zhang, G.-L. Oppo, and P. Del'Haye, "Universal symmetry-breaking dynamics for the Kerr interaction of counterpropagating light in dielectric ring resonators," Phys. Rev. A **98**, 053863 (2018).

[205] M. Karpov, M. H. P. Pfeiffer, J. Liu, A. Lukashchuk, and T. J. Kippenberg, "Photonic chip-based soliton frequency combs covering the biological imaging window," Nat. Commun. **9**, 1146–1 – 1146–8 (2018).

[206] S. A. Diddams, T. Udem, J. C. Bergquist, E. A. Curtis, R. E. Drullinger, L. Hollberg, W. M. Itano, W. D. Lee, C. W. Oates, K. R. Vogel, and D. J. Wineland, "An optical clock based on a single trapped 199Hg+ ion," Science **293**, 825–828 (2001).

[207] W. Denk, J. Strickler, and W. Webb, "Two-photon laser scanning fluorescence microscopy," Science **248**, 73–76 (1990).

[208] R. A. McCracken, J. M. Charsley, and D. T. Reid, "A decade of astrocombs: recent advances in frequency combs for astronomy," Opt. Express **25**, 15058–15078 (2017).

[209] A. Schliesser, N. Picque, and T. W. Hansch, "Mid-infrared frequency combs," Nat. Photonics **6**, 440–449 (2012).

[210] Y. Yang, X. Jiang, S. Kasumie, G. Zhao, L. Xu, J. M. Ward, L. Yang, and S. Nic Chormaic, "Four-wave mixing parametric oscillation and frequency comb generation at visible wavelengths in a silica microbubble resonator," Opt. Lett. **41**, 5266–5269 (2016).

[211] M. Yu, Y. Okawachi, A. G. Griffith, M. Lipson, and A. L. Gaeta, "Mode-locked mid-infrared frequency combs in a silicon microresonator," Optica **3**, 854–860 (2016).

[212] Y. Zhao, X. Ji, B. Y. Kim, P. S. Donvalkar, J. K. Jang, C. Joshi, M. Yu, C. Joshi, R. R. Domeneguetti, F. A. S. Barbosa, P. Nussenzveig, Y. Okawachi, M. Lipson, and A. L. Gaeta, "Visible nonlinear photonics via high-order-mode dispersion engineering," Optica **7**, 135–141 (2020).

[213] V. Torres-Company, D. Castelló-Lurbe, and E. Silvestre, "Comparative analysis of spectral coherence in microresonator frequency combs," Opt. Express **22**, 4678–4691 (2014).

[214] M. Haelterman, S. Trillo, and S. Wabnitz, "Additive-modulation-instability ring laser in the normal dispersion regime of a fiber," Opt. Lett. **17**, 745–747 (1992).

List of publications and presentations

Publications (related to this thesis)

1. S. Fujii, Y. Hayama, K. Imamura, H. Kumazaki, Y. Kakinuma, and T. Tanabe, "All-precision-machining fabrication of ultrahigh-*Q* crystalline optical microresonators," Optica **7**, 694–701 (2020).

2. S. Fujii and T. Tanabe, "Dispersion engineering and measurement of whispering gallery mode microresonator for Kerr frequency comb generation," Nanophotonics **9**, 1087–1104 (2020).

3. S. Fujii, S. Tanaka, M. Fuchida, H. Amano, Y. Hayama, R. Suzuki, Y. Kakinuma, and T. Tanabe, "Octave-wide phase-matched four-wave mixing in dispersion engineered crystalline microresonators," Opt. Lett. **44**, 3146–3149 (2019).

4. S. Fujii, Y. Okabe, R. Suzuki, T. Kato, A. Hori, Y. Honda, and T. Tanabe, "Analysis of mode coupling assisted Kerr comb generation in normal dispersion system," IEEE Photon. J. **10**, 4501511 (2018).

5. 藤井 瞬, 鈴木 良, 堀 敦裕, 久保田 啓寛, 田邉 孝純,「微小共振器におけるカーコムの数値シミュレーション法」, レーザー研究 **46**, 97–102 (2018).

6. S. Fujii, T. Kato, R. Suzuki, A. Hori, and T. Tanabe, "Transition between Kerr comb and stimulated Raman comb in a silica whispering gallery mode microcavity," J. Opt. Soc. Am. B **35**, 100–106 (2018).

7. S. Fujii, A. Hori, T. Kato, R. Suzuki, Y. Okabe, W. Yoshiki, A. C.-Jinnai, and T. Tanabe, "Effect on Kerr comb generation in a clockwise and counter-clockwise mode coupled microcavity," Opt. Express **25**, 28969–28982 (2017).

8. S. Fujii, T. Kato, R. Suzuki, and T. Tanabe, "Third-harmonic blue light generation from Kerr clustered combs and dispersive waves," Opt. Lett. **42**, 2010–2013 (2017).

Other publications

1. Y. Zhuang, H. Kumazaki, S. Fujii, R. Imamura, N. A. B. Daud, R. Ishida, H. Chen, and T. Tanabe, "Coupling of a whispering gallery mode to a silicon chip with photonic crystal" Opt. Lett. **44**, 5731–5734 (2019).

2. T. Tanabe, S. Fujii, and R. Suzuki, "Review on microresonator frequency comb" Jpn. J. Appl. Phys. **58**, SJ–0801 (2019).

3. R. Suzuki, S. Fujii, A. Hori, and T. Tanabe, "Theoretical study on dual-comb generation and soliton trapping in a single microresonator with orthogonally polarized dual pumping," IEEE Photon. J. **11**, 6100511 (2019).

4. Y. Honda, W. Yoshiki, T. Tetsumoto, S. Fujii, K. Furusawa, N. Sekine, and T. Tanabe, "Brillouin lasing in coupled silica toroid microcavities," Appl. Phys. Lett. **112**, 201105 (2018).

5. R. Suzuki, A. Kubota, A. Hori, S. Fujii, and T. Tanabe, "Broadband gain induced Raman comb formation in a silica microresonator," J. Opt. Soc. Am. B **35**, 933–938 (2018).

6. 田邉 孝純, 鈴木 良, 藤井 瞬, 久保田 啓寛, 堀 敦裕, 「微小光共振器によるマイクロコム発生」, レーザー研究 **46**, 86–91 (2018).

7. T. Kato, A. Hori, R. Suzuki, S. Fujii, T. Kobatake, and T. Tanabe, "Transverse mode interaction via stimulated Raman scattering comb in a silica microcavity," Opt. Express **25**, 857–866 (2017).

8. A. C.-Jinnai, T. Kato, S. Fujii, T. Nagano, T. Kobatake, and T. Tanabe, "Broad bandwidth third-harmonic generation via four-wave mixing and stimulated Raman scattering in a microcavity," Opt. Express **24**, 26322-26331 (2016).

Presentations

1. S. Fujii, and T. Tanabe*, "Experimental and numerical demonstration of tunable octave-wide four-wave mixing in dispersion engineered microresonators," SPIE Photonics West 2020, 11274-19, San Fransisco, USA, February 1–6 (2020). (Invited)

2. S. Fujii, Y. Hayama, S. Tanaka, S. Sota, K. Wada, Y. Kakinuma, and T. Tanabe, "Dispersion engineering of crystalline microresonator fabricated with computer-controlled diamond turning," Frontiers in Optics/Laser Science Conference (FiO/LS), FTu5C.5, Washington DC, USA, September 15–19 (2019).

3. S. Fujii, M. Fuchida, H. Amano, S. Tanaka, R. Suzuki, Y. Kakinuma, and T. Tanabe, "Precisely dispersion tailored crystalline microresonator with a Q exceeding 10^8 fabricated by computer-controlled machining," Conference on Lasers and Electro-Optics – European Quantum Electronics Conference (CLEO/Europe–EQEC 2019), CK-5.6, Munich, Germany, June 23–27 (2019).

4. S. Fujii, M. Fuchida, H. Amano, R. Suzuki, Y. Kakinuma, and T. Tanabe, "Ultrahigh-Q crystalline microresonator fabricated with computer-controlled machining without polishing," Conference on Lasers and Electro-Optics (CLEO), STh4J.6, San Jose, USA, May 5–10 (2019).

5. S. Fujii, R. Suzuki, M. Hasegawa, and T. Tanabe, "Kerr comb generation under weak dispersion regime in high-Q silica microtoroids,"Conference on Lasers and Electro-Optics Pacific Rim 2018, Tu3H.4, Hong Kong, July 29–August 3 (2018).

6. S. Fujii, M. Hasegawa, R. Suzuki, and T. Tanabe, "Nonlinear parametric oscillation phase-matched via high-order dispersion in high-Q silica toroid microresonators,"The 7th Advances Lasers and Photon Sources Conference (ALPS'18), ALPS5-I1-7, Yokohama, Japan, April 24–27 (2018).

7. S. Fujii, Y. Okabe, T. Kato, R. Suzuki, A. Hori, and T. Tanabe, “Nonlinear coupled mode equations for Kerr comb generation in coupled microcavity system,” Frontiers in Optics/Laser Science Conference (FiO/LS), FTu2D.3, Washington DC, USA, September 17–21 (2017).

8. 藤井 瞬，岡部 悠介，加藤 拓巳，鈴木 良，堀 敦裕，田邉 孝純，「非線形結合モード方程式を用いた結合共振器モデルにおけるマイクロコムシミュレーション」，第 78 回応用物理学会秋季学術講演会，7a-PA4-1，福岡国際会議場，平成 29 年 9 月 5 日–8 日．

9. 藤井 瞬，加藤 拓巳，鈴木 良，堀 敦裕，田邉 孝純，「シリカ微小光共振器における四光波混合と誘導ラマン散乱間で発生する利得競合の観測」，第 78 回応用物理学会秋季学術講演会，6p-S45-20，福岡国際会議場，平成 29 年 9 月 5 日–8 日．

10. S. Fujii, Y. Okabe, T. Kato, R. Suzuki, Y. Honda, A. Hori, and T. Tanabe, “Numerical simulation of dark soliton generation in coupled microcavity system,” The 24th Congress of the International Commissions for Optics (ICO-24), M1E-07, Tokyo, Japan, August 21–25 (2017).

11. S. Fujii, T. Kato, A. C.-Jinnai, R. Suzuki, and T. Tanabe, “Broad bandwidth visible light generation via third-order nonlinear interaction in silica toroid microcavity,” The 6th Advances Lasers and Photon Sources Conference (ALPS’17), ALPSp14-03, Yokohama, Japan, April 18–21 (2017).

12. 藤井 瞬，陣内 哲倫，加藤 拓巳，鈴木 良，田邉 孝純，「シリカトロイド共振器における三次非線形光学効果を介した広帯域可視光発生」，第 64 回応用物理学会春季学術講演会，16p-311-20，パシフィコ横浜，平成 29 年 3 月 14 日–17 日．

13. S. Fujii, T. Kato, A. Hori, Y. Okabe, A. Kubota, and T. Tanabe, “Blue light emission via harmonic generation by stimulated Raman scattering in a silica toroid microcavity,” Frontiers in Optics/Laser Science Conference (FiO/LS), FTh5G.5, Rochester, USA, October 17–21 (2016).

14. S. Fujii, Y. Okabe, W. Yoshiki, T. Kato, A. C.-Jinnai, T. Kobatake, and T. Tanabe, “The effect on Kerr comb generation in mode coupled WGM microcavity,” Conference on Lasers and Electro-Optics (CLEO), STu3Q.1, San Jose, USA, June 5–10 (2016).

15. 藤井 瞬，加藤 拓巳，吉岐 航，陣内 哲倫，小畠 知也，岡部 悠介，田邉 孝純，「WGM 微小共振器における CW-CCW 結合の光カーコム発生への影響」，第 63 回応用物理学会春季学術講演会，20p-P3-6，東工大大岡山キャンパス，平成 28 年 3 月 19 日–22 日．

Acknowledgment

本研究は，慶應義塾大学大学院理工学研究科総合デザイン工学専攻田邉研究室において，田邉孝純教授のご指導の下で行われました．本論文の執筆にあたり，多くの人からのご指導，ご支援をいただいたことに感謝の意を述べさせていただきます．はじめに，本論文の主査であり，指導教官である田邉孝純教授に心より深く感謝申し上げます．筆者が田邉研究室を志望したのは，学部生のとき田邉教授と会話する機会を得られたときにかけていただいたお言葉がきっかけでした．田邉教授との出会いは研究者への漠然とした憧れがありながらも，将来への方向性を決めかねていた筆者にとって大きな転換点だったと感じています．研究者としての姿勢や深く広い知識のみならず，人への接し方，話し方にいたるまで沢山のことを学ばせていただきました．数多くの研究発表のチャンスをいただけたこと，留学の機会に恵まれたことをはじめ，筆者は数年間もの間，自由に好きな研究をしてきましたが，これらはひとえに田邉教授のご尽力あってのものです．田邉研究室で経験したこと，学んだことは筆者の人生にとってかけがえのないものであることは疑う余地もありません．改めて深く感謝申し上げます．

本論文の審査にあたり，快く副査を引き受けていただいた，慶應義塾大学理工学部の神成文彦教授，津田裕之教授，渡邉紳一教授，沖縄科学技術大学院大学（OIST）の Prof. Sile Nic Chormaic に感謝いたします．神成文彦教授には，本論文のみならずこれまでも学内で研究発表をさせていただく機会が多くあり，そのたびに本質的かつ鋭いご指摘をいただきました．神成教授の授業がきっかけでレーザー光学に興味をもった筆者にとって，自身の研究に関してご意見をいただけたことは本当に貴重な経験になりました．津田裕之教授には特に光源としての実用性の観点から多くの貴重なご指摘をいただきました．また，学内発表に際して研究手法に関する多くのご助言をいただいたことは強く記憶に残っています．渡邉紳一教授には，本論文の構成から表現に至るまで多くのご助言をいただきました．また，ファイバレーザーの実験系を見学させていただき，専門的な知識を与えていただきました．I would like to express great appreciation to Prof. Nic Chormaic for reviewing my thesis. She has carefully read this thesis and given a lot of valuable comments and advice from the standpoint of microcavity optics.

また，筆者が研究を行うにあたり，多くの共同研究者に恵まれました．特に慶應義塾大学理工学部の柿沼康弘教授と天野光氏，葉山優花氏をはじめとする柿沼研究室の方々には大変お世話になりました．本論文の第四章に関する研究は教授と氏らの存在なくしてはありえません．深く感謝申し上げます．佐々

田博之博士（慶應義塾大学元教授）にはモード同期ファイバーコム技術に関して多くのことを学ばせていただき，筆者の実験にも何度も使用させていただきました．宮路智行博士（現 京都大学准教授）には定期的にディスカッションする機会をいただき，数学者としての深い知見から理論面における多くのご助言をいただきました．筆者の稚拙な質問にも丁寧にお答えいただけたことは研究を進める上での大きな財産となりました．感謝いたします．橋本洋輔博士（現 JAXA）とは後期博士課程になってから，光周波数コムの安定化やプリズム結合系に関して多くの議論と実験をともにしました．氏の電気部品に対する知識や周波数安定化技術における圧倒的な知見には，多くのことを学ばせていただきました．

田邉研究室には 5 年半在籍することになりましたが，その中で素晴らしい先輩，同期，後輩，研究員や留学生，秘書の方々と出会うことができました．全員に対して謝辞を述べたいところですが，ここでは特に関わりの深かった方たちを中心に書かせていただきます．博士課程の先輩でもあり，研究室の第 1 期生である吉岐航氏と加藤拓己氏，そして第 2 期生である鈴木良氏，鐵本智大氏には研究に関する全てを学ばせていただきました．筆者が研究室に配属されてすぐに研究を始めることができたのはひとえに氏らのご尽力とご指導のおかげです．尊敬できる博士課程の先輩が身近にいたことは筆者の進路を決定づける大きな要因となりました．特に加藤氏には同じ研究テーマに取り組む中で多くのご助言をいただきました． 氏の発想力や実行力がきっかけとなって停滞する研究が動き出すのを何度見たことか分かりません．研究の楽しさ，面白さを教えてくれたかけがえのない存在です．鈴木氏とは研究生活において最も長い時間をともに過ごさせていただきました．丁寧な実験と入念な理論検討から生み出された氏の研究結果と細部まで作り込まれた発表資料は，常に筆者の目標でした．柔らかい物腰から研究室の全員に慕われる人格者であり，困ったときにはいつも頼ってばかりだったと回想します．ご卒業された今でも加藤氏，鈴木氏との交流が続いていることは筆者の人生における幸運の一つです．

同期の堀敦裕氏とは学部時代からの友人でありながら，同じテーマに取り組む仲間として貴重な時間を過ごさせていただきました．特に氏のシミュレーションに関する能力は飛び抜けており，本論文に関しても多大な貢献をしていただきました．氏の現在のご活躍は筆者の大きな刺激になっています．熊崎基氏とも，友人として同期として，思いがけず長い時間を過ごすことになりました． どんな話にも耳を傾け，真摯に聞いてくれる人柄と何事にも精通した知識と技術力にはいつも助けられてばかりでした．後輩である上岡直隆氏，岡村拓氏，本多祥大氏，久保田啓寛氏，今村陸氏とは研究室内に限らず，友人としていつも楽しい時間を過ごさせていただきました．氏らとの思い出は挙げればきりがないですが，ともに行ったドイツやアメリカの学会は特に印象に残っています．同じチームで研究をした陣内哲倫氏，小畠知也氏，岡部悠介氏，長野拓真氏，渕田美夏氏，長谷川穂氏にも大変お世話になりました．感謝申し上げます．また，半田浩一朗氏，大塚民貴氏，田中脩矢氏，曽田昇汰氏，和田幸四郎氏には先輩としてときに厳しく指導することもありましたが，それを跳ね返す成長にはいつも驚かされ，同時に喜びを感じていました．田坂駿氏，木暮蒼真氏，菅原漱人氏とは非常に短い時間となってしまいましたが，初心を思い出

させてくれる貴重な存在でした．各々が長所を生かし，伸び伸びと楽しく研究をしてくれればこれに優るものはありません．

I would like to thank Dr. Pascal Del'Haye who accepted me as a short-term researcher in Max Planck Institute for the Science of Light. He is not only a great researcher in microresonator frequency combs but also a kind and intelligent mentor. I also thank Jonathan, Shuangyou, Leonardo, Michael, George, Niall, and Toby. Thanks to them, I had an enjoyable time and a lot of experience in Germany. I am looking forward to seeing them again.

最後になりましたが，地元から遠く離れた私立大学への入学のみならず，博士課程への進学に理解を示し，どんなときでも味方であり支えてくれた両親と妹，祖父母，親戚の方々に深く感謝いたします．筆者が何ひとつ不自由なく学生をつづけてこられたのは，小さいころから応援し，見守ってくれた家族，親族のおかげです．そして，筆者のどんな決断にも理解を示してくれた妻と今年の 2 月に生まれてきてくれた娘にも感謝いたします．本論文の完成はそんな唯一無二の家族へ捧げます．

2020 年 7 月 8 日 藤井瞬